Universitat Autònoma de Barcelona

3D surface shape measurement using stereoscopic camera based structured light systems

Haolin Zhang

3D surface shape measurement using stereoscopic camera based structured light systems

Haolin Zhang

Submitted in fulfillment of

the requirements for the degree of

Doctor of Physics

Thesis supervisors:

Dr. Juan Campos

Dr. Josep Nicolas

Departament de Física

Universitat Autònoma de Barcelona

Bellaterra, 2019

Acknowledgements

I would like to take this chance to thank everyone who has helped me during my academic career.

First and foremost, I would like to express my deepest gratitude to my advisor, Dr. Juan Campos, for his advising on my research for the last four years. It has been an amazing experience to work with such an innovative leader to pursue my highest degree. Dr. Campos's expertise and insight have greatly inspired me to finish this project. His encouragement and patience have backed me up numerous times when I face challenges. Without his support, I could not imagine how could I finish this thesis and successfully find my dream postdoc position.

I also want to express my gratitude to Dr. Josep Nicolas. Dr. Nicolas has given me great freedom and trust to perform my experiments in his laboratory in ALBA Synchrotron. His suggestions and advices on optical metrology are greatly valued. Without his help, it is impossible for me to perform the experimental measurements demonstrated in this thesis.

Moreover, I also want to say thanks to Dr. Angel Lizana. Dr. Lizana has helped me a lot during these four years in both my research and my personal growth. He has instructed me to prepare all my manuscripts, from which I have a fruitful publication list. He has also given me great trust to participate in some other research projects apart from the one that is demonstrated in this thesis, and this has greatly helped me to enrich my research experience. Finally, I also appreciate his support during these four years, I can still remember my first day in Barcelona when Dr. Angel and Dr. Estévez picked me up in the airport.

Next, I would like to thank Dr. María Josefa Yzuel. Dr. Yzuel has shared her experience in research and teaching with me, and these are extremely important to

develop my career at my early stage. I also want to acknowledge Dr. Juan Carlos Escalera for his support and advice.

I, of course, want to thank my colleagues Dr. Irene Estévez and Albert Van Eeckhout. We shared a great time together in our office and it is really lucky for me to meet you. You really helped me a lot especially when I was not quite fluent in Spanish.

I would like to thank my colleagues in ALBA Synchrotron. First of all, I own my gratitude to Dr. Igors Šics, for Dr. Šics has helped me prepare the experimental setup and the mechanical hardwares used in this thesis. I also want to thank Dr. Jon Ladrera and Dr. Marta Llonch for their help during the system calibration. Moreover, thanks to Dr. Pablo Pedreira for his assist in my experimental preparation.

I would like to thank all professors in Grupo de Optica. Dr. Jordi Mompart, Dr. Verònica Ahufinger, Dr. Todor Kirilov Kalkandjiev, Dr. Francecs Pi, and Dr. Gaspar Orriols. Thank you for your support and help during my staying in Grupo de Optica.

Then, I would like to thank my grandfather Prof. Zhu Liang, who is also a professor in the area of optics. His encouragement has led me into this amazing field.

I would like to thank my companion Miao Zhang. She has always been the sunshine of my life the first moment I met her.

Finally, I would like to thank my parents Shuping Liang and Li Zhang for everything they have given me.

Abstract

Surface shape measurement allows us to obtain three-dimensional information of an object. Thus, it finds extensive applications in various areas such as industrial manufacturing inspection, optical metrology, object recognition, non-destructive evaluation, etc. Within numerous surface shape measurement techniques, structured light measurement presents its great advantage in obtaining the surface shape as it provides a high measurement accuracy with an easy implemented system. Moreover, by projecting digital fringe patterns to the measured object, structured light guarantees a flexible surface measurement, which satisfies the measurement of different shapes, such as plane surfaces, curved surfaces and irregular surfaces. On the other hand, structured light measurement also allows us to measure both specular objects and diffuser objects. For specular object measurement, deflectometry is introduced. Here, the fringe patterns are generated by a commercial liquid crystal display (LCD). For diffuser object measurement, profilometry is used to determine the surface shape. In this technique, the fringe patterns are projected to the object by a video projector.

In this thesis, we firstly propose a stereoscopic phase measuring deflectometry (SPMD) system, which contains two cameras and a commercial LCD, to fulfill the specular object measurement. In particular, by introducing the stereoscopic camera, the undesired height-normal ambiguity is eliminated without moving any deflectometry system component. Within this system, we propose a phase error minimization algorithm, which is fulfilled by searching the minimum phase difference between the corresponding pixels of the LCD and the camera, to simultaneously determine the surface normal and the surface height. What is more, to accomplish an efficient phase minimization, we use a polynomial fitting method. Finally, two-dimensional Fourier integration is used to reconstruct the specular surface shape. Based on this stereoscopic phase measuring deflecectometry system, we measure different specular objects such as a plane mirror, a spherical mirror and even a discontinuous specular disk.

Apart from the specular surface measurement with deflectometry, we also propose a stereoscopic fringe projection profilometry (SFPP) system to accomplish the diffuser

object surface shape measurement. In particular, an SFPP system uses the same stereoscopic camera as in the deflectometry set-up, but it adopts a video projector to replace the LCD to project the fringe patterns. By introducing the stereoscopic camera, we totally avoid the complex video projector calibration, which is represented as the gamma calibration and the video projector position calibration. Under this scenario, a great system flexibility is achieved. For surface reconstruction, geometric triangulation is implemented by performing a 2D sub-pixel interpolation, from which we improve the surface reconstruction accuracy. Based on this stereoscopic profilometry system, the surface shapes of different diffuser objects are measured.

The aforementioned two systems (i.e., deflectometry system and profilometry system) enable us only to measure the surface shape of either a specular or a diffuser object, but they show inadequacies to measure a specular-diffuser hybrid object. Under this scenario, we aim at combining both systems to perform the specular-diffuser hybrid object measurement, as such objects are commonly used in industrial fields. Thanks to the introduction of the stereoscopic camera, we then combine stereoscopic deflectometry with stereoscopic profilometry to measure the surface shape of a specular-diffuser hybrid object. Here, a stereoscopic deflectometry-profilometry hybrid (SDPH) system contains the stereoscopic camera, an LCD and a video projector. In this case, this hybrid system greatly overcomes the inadequacy of single projection structured light systems, as this hybrid system not only ensures to measure specular or diffuser object, but it also allows the measurement of specular-diffuser hybrid objects. Hence, the application of structured light measurement is further broadened.

In summary, we demonstrate in this thesis three stereoscopic camera based structured light systems to perform three-dimensional surface shape measurement. These stereoscopic structured light systems reveal great potential as they are able to measure the surface shapes of specular objects, diffuser objects and even specular-diffuser hybrid objects with high resolution. The proposed stereoscopic structured light systems could be beneficial in various industrial applications, where an accurate surface shape measurement system with an easy implemented scheme is required.

Contents

Chapter 1 Introduction 1

1.1 Motivation 2

1.1.1 Optical metrology 2

1.1.2 Manufacturing inspection 4

1.2 Deflectometry 6

1.2.1 Principle of deflectometry 6

1.2.2 Development of deflectometry 8

1.2.3 Stereoscopic deflectometry 12

1.3 Profilometry 14

1.3.1 Principle of profilometry 14

1.3.2 Development of profilometry 16

1.3.3 Stereoscopic profilometry 24

1.4 Objective 26

1.5 Structure of the thesis 27

Chapter 2 Mathematical foundations of stereoscopic camera based structured light measurement systems 29

2.1 Geometric representations 29

2.2 Coordinate system transformation 31

2.3 Pinhole camera model 35

2.4 Beam reflection model 38

Chapter 3 Parameter calibration of stereoscopic camera based structured light measurement systems 41

3.1 Fundamentals of sinusoidal fringe pattern 43

3.2 Phase shifting method 45

3.3 Phase unwrapping method 47
3.3.1 Spatial phase unwrapping 48
3.3.2 Temporal phase unwrapping 49
3.4 Camera calibration 52
3.4.1 Camera parameter calibration 52
3.4.2 Stereoscopic camera calibration 55
3.4.3 Pinhole camera with lens distortion 56
3.5 Gamma calibration 60
3.6 Geometric calibration of the stereoscopic phase measuring deflectometry system 63
3.6.1 Geometric limitations 64
3.6.2 LCD screen position calibration 67
3.6.3 Laser tracker-assisted hand-eye calibration 73
3.7 Stereoscopic fringe projection profilometry system calibration 77
Chapter 4 Stereoscopic phase measuring deflectometry technique 79
4.1 Height-normal ambiguity elimination 79
4.2 Iterative algorithm for surface point determination 83
4.3 Sub-pixel interpolation 86
4.3.1 Bi-linear interpolation 87
4.3.2 Bi-cubic interpolation 91
4.4 2D Fourier integration based surface reconstruction 95
Chapter 5 Experimental measurement using the stereoscopic phase measuring deflectometry system 101
5.1 LCD gamma calibration 102
5.2 Stereoscopic camera calibration 104
5.3 Stereoscopic phase measuring deflectometry system calibration 106
5.4 Experimental measurements 111
5.4.1 Flat mirror measurement 111
5.4.2 Spherical mirror measurement 118

5.4.3 Discontinuous specular surface measurement 123

Chapter 6 Stereoscopic fringe projection profilometry 131

6.1 Mathematical principle of the stereoscopic fringe projection profilometry measurement 132

6.2 Experimental calibration of a stereoscopic phase measuring profilometry system 135

6.3 Experimental measurements using a stereoscopic fringe projection profilometry system 137

6.3.1 “Stair” structure object measurement 137

6.3.2 Spherical object measurement 142

6.3.3 Irregular surface object measurement 144

Chapter 7 Stereoscopic deflectometry-profilometry hybrid structured light measurement system 148

7.1 Principle of stereoscopic deflectometry-profilometry hybrid structured light measurement 149

7.2 Specular-diffuser hybrid surface reconstruction 152

7.3 Experimental measurements with a stereoscopic deflectometry-profilometry hybrid structured light system 153

7.3.1 Experimental set-up calibration 153

7.3.2 Separate projection measurement 154

7.3.3 Combined projection measurement 159

Chapter 8 Conclusions 167

8.1 Summary of contributions 167

8.2 Future prospects 170

Appendix 173

List of acronyms 183

Bibliography 185

Chapter 1 Introduction

Three-dimensional surface shape measurement finds many applications in various fields ranging from industrial inspection [1, 2], optical metrology [3], facial recognition [4], to medical diagnosis [5], among others. Different measurement techniques have been proposed to perform the surface shape measurement with respect to certain requirements. Among them, optical measurement techniques demonstrate great advantages as they provide a rapid measurement with high accuracy. What is more, they also guarantee non-contact measurement which is mandatory to measure some fragile, or easily scratched objects. The most commonly used optical based surface measurement techniques can be enlisted as photogrammetry, interferometry, laser scanning, etc. In this case, photogrammetry is mainly used to measure diffuser objects, interferometry is usually used to perform regular specular surface metrology, whereas laser scanning can be implemented to measure both specular and diffuser objects. Even though these above-mentioned systems are able to provide an accurate measurement within a relatively short time, they are either expensive or difficult to implement. Thus, a low cost, easy implemented, environmental variation insensitive optical measurement system is still highly demanded. Under this scenario, structured light measurement system is proposed as it demonstrates great flexibility to be implemented without a complicated optical scheme, and it also provides a high measurement accuracy.

This chapter provides an overview of the structured light measurement techniques, which are based on fringe pattern projection, to achieve three-dimensional surface shape measurement. In Section 1.1, a brief motivation of structured light measurement is discussed. In particular, it focuses on applications in both optical metrology and

industrial manufacturing inspection. Afterwards, Section 1.2 presents deflectometry technique, which is favored in specular surface measurement. Then, Section 1.3 discusses profilometry technique, which is used to measure the diffuser object surface shape. In Section 1.4, the objective of this thesis is presented. Finally, Section 1.5 summarizes the structure of this thesis.

1.1 Motivation

Three-dimensional surface shape measurement is mandatory in many industrial applications. For instance, the surface shape of a mechanical element directly determines the whole mechanical system performance and thus, it has to be precisely inspected during manufacturing. For facial recognition, accuracy heavily depends on the three-dimensional facial profile reconstruction. Moreover, in numerous optical imaging systems, reflective mirrors are implemented to perform either light steering or focusing. Thus, the surface shapes of these optical mirrors are crucial as they directly determine the imaging quality. In this section, we demonstrate the motivation of structured light measurement techniques using two examples: optical metrology and manufacturing inspection.

1.1.1 Optical metrology

Optical mirrors play an extremely important role throughout the whole optical development history. In the 17th century, Isaac Newton implemented the first reflective telescope with a spherical mirror, from which he had successfully accomplished the observation of Jupiter and Venus. Nowadays, the reflective scheme telescopes are still the most promising scientific instruments to perform astronomy observation, such as the 2.4 m aperture Hubble Space Telescope [6, 7], or the ~ 6.5 m aperture James Webb Space Telescope [8]. In these telescopes, the shapes of the reflective mirrors greatly influence the telescope performance. For Hubble Space Telescope, its primary mirror contains a 2.2 μm grinding error at the mirror perimeter, and thus, the imaging quality is greatly deteriorated and a Corrective Optical Space Telescope Axial Replacement (COSTAR) was needed to be installed to correct the spherical aberration. Apart from the telescopes, optical mirrors also work as key elements in numerous scientific detection instruments, such as the Laser Interferometer Gravitational-Wave Observatory (LIGO) for cosmic gravitational wave

detection. In LIGO, the optical interferometer is the most crucial section as it is used to detect the passing gravitational wave. Within LIGO optical interferometer, four 250 mm diameter fused-silica mirrors with multilayer dielectric coatings are introduced to act as the two detecting arms of a Michelson interferometer [9, 10].

The mirrors used in the above-mentioned telescopes or LIGO should be measured with high accuracy, and thus, interferometry is used to perform the surface measurement. Interferometers are accurate optical metrology instruments with accuracy that can reach nanometer scale. The principle of interferometry metrology is based on optical path difference detection between a reference wavefront and another wavefront modulated by the tested surface [3]. Specifically, the interference pattern generated by these two wavefronts reveals the surface shape deviation between the tested surface and the reference surface. However, the measurement dynamic range of a typical interferometer is not wide (i.e., several wavelengths), and this leads to the difficulties in measuring steep slope surfaces (i.e., large curvature mirrors or freeform mirrors). Hence, the most commonly used method to perform large curvature surface measurement with an interferometer is to implement specially designed reference mirrors. Nevertheless, such reference mirrors are expensive and difficult to be fabricated. Moreover, they still cannot provide a wide slope range measurement, and thus, optical stitching is usually unavoidable in large aperture surface measurement.

Under this scenario, structured light systems are proposed to measure high dynamic range specular surfaces, and this technique is referred as deflectometry. In a deflectometry system, a structured light pattern is generated on a digital screen and then this pattern is reflected by the measured surface and finally being captured by a camera. At this moment, by analyzing the reflected pattern in the camera and by comparing it with the original structured light pattern on the digital screen, both surface normal and height information can be calculated. Compared to interferometry, deflectometry promises a low cost, easy implemented system and it could also provide high measurement accuracy. In particular, deflectometry is testified available to measure various reflective mirrors. For instance, the Software Configurable Optical Test System (SCOTS) [11, 12], which is based on structured light projection, is proposed by the University of Arizona to measure the 8.4 m aperture aspherical primary mirror aligned in the Giant Magellan Telescope. In this case, the measurement result is comparable to the interferometric data obtained by using a phase shifting interferometer. What is more, SCOTS demonstrates its advantage in retrieving accurate surface data at the mirror edge, while such section may not be precisely measured by an interferometer giving its steep slopes [11]. Apart from the steep slope

aspherical mirror, SCOTS is also used to measure an aspherical X-ray mirror with a large radius (i.e., mirror radius of 54.29 m, mirror size of 100×30×40 mm). In particular, Burge used SCOTS to measure its slope error with precision and accuracy better than 100 $nrad$ (RMS) and ~200 $nrad$ (RMS), respectively [12].

Deflectometry systems are not only suitable to measure the surface shapes of reflective mirrors used for optical imaging, but they also find broad applications in industrial field such as solar concentrator inspection [13, 14]. Here, solar concentrators are reflective paraboloidal dishes. They are not applied to perform optical imaging, but they rather concentrate the sunlight to a small area. Later, the concentrated energy is converted to solar thermal energy, from which electricity is generated. Under this scenario, the surface shape of a solar concentrator directly determines the concentration efficiency, and thus, its surface shape has to be measured. Considering the specular characteristic of a solar concentrator, deflectometry is implemented to obtain the specular surface shape, such as deformable mirrors implemented in heliostat plants [15], or parabolic dish heliostats [16, 17].

1.1.2 Manufacturing inspection

The 3D geometric information of a mechanical workpiece is critical as it determines the performance of the manufactured element. Thus, the surface shape of this workpiece has to be inspected during the mechanical manufacturing, or we have to perform the surface shape measurement after fabrication, so that we can determine if the manufactured workpiece meets the accuracy requirement. In automobile processing industry, the shapes of different automobile body sections have to be inspected during the workpiece fabrication or installation [18, 19]. In 3D printing, surface defects are introduced during fabrication, and thus, dynamic surface inspection has to be implemented to monitor the printed element, from which we can introduce a dynamic correction to avoid the fabrication defects [20]. In aerospace industry, the surface shape of an aluminum sheet used as the aerospace component also has to be inspected, as machining will inevitably introduce surface shape deviation [21]. To perform an accurate surface inspection, Coordinate Measuring Machine (CMM) [22, 23] is broadly used. In a CMM system, a probe is positioned properly so it can contact the surface, and then the surface shape measurement is performed by scanning the whole measured workpiece with the probe. However, CMM is a contact measuring system, and thus, it is not feasible for numerous manufacturing inspections because it would damage the measured components during fabrication. Another technique

referred as laser tracking is also well studied to perform surface shape measurement [24, 25]. In this case, we put the retroreflectors, which are also known as fiducials, on the object to be measured. Later, we use a laser to point at these fiducials, so we obtain both the positions and the distances from the fiducials to the laser head. At this moment, the 3D surface map of the measured object can be reconstructed using the fiducial position and distance data. Laser tracking provides a non-contact surface shape measurement, but the fiducials still have to be positioned on the inspecting workpiece. Moreover, a laser tracker only guarantees point scanning, which makes large size workpiece measurement time-consuming [24, 25]. Finally, this method cannot provide a high measurement accuracy, because the laser tracking accuracy is about 10 μm at best.

Under this scenario, structured light measurement is proposed to perform the manufacturing inspection. For specular workpiece inspection, we simply introduce a deflectometry system. Nevertheless, numerous mechanical workpieces are roughly polished and are partially reflective, and this makes deflectometry not feasible to measure their surface shapes. Under this scenario, another structured light measurement technique, referred as profilometry, is proposed. In a profilometry system, the structured light pattern is projected to the surface under inspection by a digital video projector. On the other side, a camera is employed to capture the fringe pattern distorted by the inspected object. Finally, the surface shape of the object can be retrieved by performing surface height calculation between the video projector and the camera with the help of the fringe patterns. Compared to CMM or laser tracking, profilometry demonstrates two advantages as: (*i*) it guarantees a non-contact measurement, and (*ii*) it is feasible to perform multi-point measurement.

In particular, profilometry is favored in automobile field to accomplish 3D automobile body inspection. Once a complete 3D automobile surface structure is obtained by using profilometry measurement, a scaled body replica can be easily obtained through rapid prototyping (RP) [26]. Moreover, the measured surface shape also ensures 3D CAD-assisted modeling, from which we can further optimize the automobile design through reverse engineering [26]. Apart from the complete automobile body inspection, profilometry also finds its place in single automobile body section inspection where high accuracy is required into these geometric complex workpieces such as windshield [27] or automobile door [28]. Finally, profilometry not only demonstrates its ability in automobile processing industry, it is also feasible to measure more mechanical workpieces such as railway truck adapters with a large surface reflectivity variation [29], or aluminum alloy workpieces [30].

1.2 Deflectometry

In the previous section, both deflectometry and profilometry are presented as structured light systems to measure the surface shapes. Deflectometry is used for the surface shape measurement of specular objects, whereas profilometry is widely used to measure the surface shapes of diffuser objects. Here, Section 1.2.1 firstly describes the working principle of deflectometry, and Section 1.2.2 analyzes different deflectometry systems. Finally, Section 1.2.3 briefly discusses the stereoscopic deflectometry system and its advantages against the single camera based deflectometry system for surface shape measurement.

1.2.1 Principle of deflectometry

Deflectometry is a structured light-based specular surface shape measurement technique. The principle of deflectometry relies on the most fundamental Reflection Law. The basic deflectometry experimental setup is presented in Figure 1-1. In a deflectometry scheme, the screen which provides the structured light pattern is commonly a liquid crystal display (LCD) controlled by a computer. Here, structured light is an active illumination with specifically designed 2D intensity pattern, which allows us to establish the correspondence between the illumination source and the imaging sensor [31]. In particular, sinusoidal fringe pattern is one of the most commonly used structured light pattern implemented in deflectometry systems. Afterwards, we place the specular object to be measured at a certain position where the sinusoidal fringe pattern on the LCD screen can be properly reflected. On the other side, a commercial camera is appropriately located so that it can capture the reflected fringe pattern. In this case, as the curvature of the specular surface will distort the fringe pattern, the fringe pattern in the camera is different from the fringe pattern in the LCD. At this moment, we assume that a light projected from one LCD pixel is reflected by the specular surface for only one time, then this light is registered in a certain camera pixel. Moreover, this reflected light also passes through the optical center of the camera. Then, we can uniquely distinguish these two corresponding pixels on both the LCD and the camera image plane thanks to the characteristic of structured light. Now, by performing the reverse ray tracing with these two corresponding pixels from the camera to the LCD, the coordinate of the surface point can be determined. More importantly, as reverse ray tracing obeys Reflection Law, we can also calculate the surface normal at this surface point. Finally, by introducing

different integration methods with the calculated surface normal data, we can obtain the continuous surface map of the measured object (this is discussed in Chapter 4).

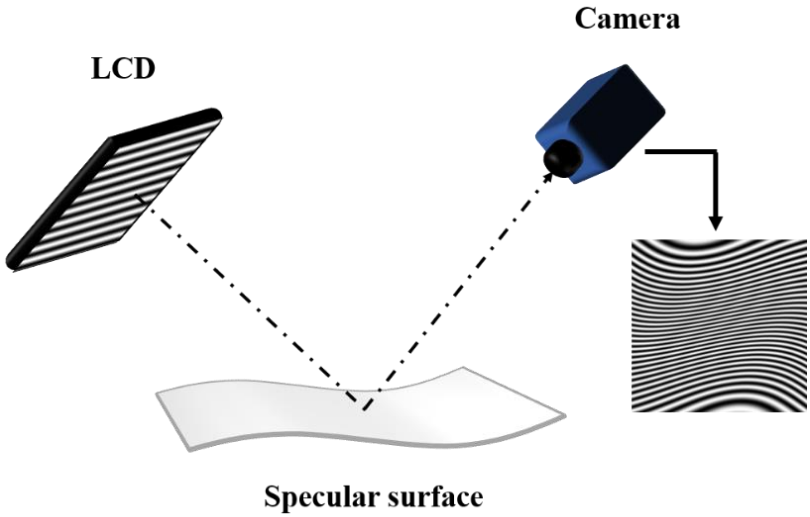

Figure 1-1. Schematic set-up of a structured light based deflectometry system.

Here, to perform reverse ray tracing, we have to scheme the deflectometry system (i.e., Figure 1-1). We regard the LCD as a flat plate presenting structured light patterns, whereas the camera is regarded as the combination of a flat image plane and a focusing lens. The flat image plane of the camera in fact is the charge-coupled device (CCD) plane. In a deflectometry system, the spatial position of the camera corresponding to the world coordinate is known through calibration, so the coordinates of any image plane pixel as well as the focusing lens center can be determined. Therefore, we select a pixel $\boldsymbol{A}$ on the image plane and then connect it to the camera optical center $\boldsymbol{O}$ to forge a primary reflection vector $\boldsymbol{V}$ (see red solid line in Figure 1-2). Here, vector $\boldsymbol{V}$ encounters the specular surface at point $\boldsymbol{P}$. On the other side, the LCD position corresponding to the world coordinate as well can be determined through LCD screen calibration, and thus, we can construct a secondary reflection vector $\boldsymbol{R}$ by connecting $\boldsymbol{A}$**'** with surface point $\boldsymbol{P}$ (see the red solid line in Figure 1-2). Here, we want to emphasize again that point $\boldsymbol{A}$**'** on the LCD is corresponding to point $\boldsymbol{A}$ on the image plane thank to the introduction of the structured light. At this moment, we can calculate both the coordinate and the surface normal of surface point $\boldsymbol{P}$ using the geometric information of the camera and the LCD. Finally, by implementing such reverse ray tracing within all pixels on the CCD, the whole surface normal distribution is obtained.

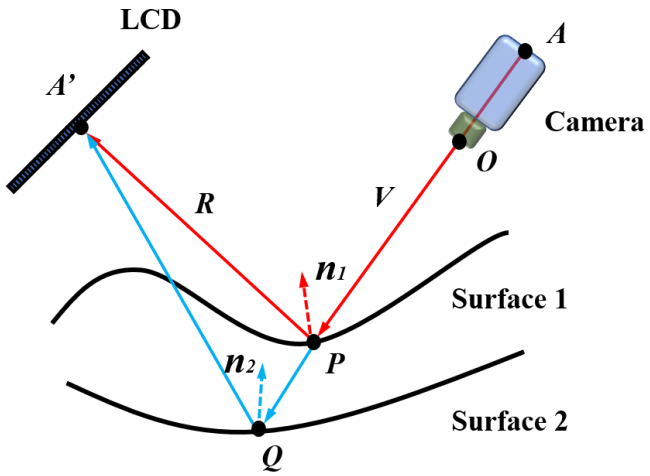

Figure 1-2. Principle diagram of height-normal ambiguity in a structured light based deflectometry system.

However, such reverse ray tracing method fails to give us a unique real surface point, but it rather gives infinite ambiguity points along vector $\boldsymbol{V}$. For instance, in the deflectometry system scheme (see Figure 1-2), we can decide the surface point at $\boldsymbol{P}$, where it provides a correct reflection relation between $\boldsymbol{A}$ and $\boldsymbol{A}$'. Nevertheless, we can also extend vector $\boldsymbol{V}$ to point $\boldsymbol{Q}$, where this point is located at another surface (i.e., see Surface 2 in Figure 1-2). Under this scenario, we then regard point $\boldsymbol{Q}$ as the surface point, we can construct a secondary reflection relation by connecting $\boldsymbol{A}$' and $\boldsymbol{Q}$. At this moment, the coordinate and the normal of $\boldsymbol{Q}$ is calculable and point $\boldsymbol{Q}$ can also be referred as the real surface point. Note that both $\boldsymbol{P}$ and $\boldsymbol{Q}$ show the correct reflection relation between the LCD and the camera, but these two points definitely represent two different surface shapes. Thus, the surface point coordinate and its normal cannot be uniquely determined within a deflectometry system, and this ambiguity is referred as height-normal ambiguity. We will further discuss the height-normal ambiguity elimination method for unique surface determination in Chapter 4.

1.2.2 Development of deflectometry

As height-normal ambiguity is inevitable in any deflectometry system for specular surface shape measurement, different deflectometry systems had been developed to solve this problem. Specifically, Knauer firstly proposed a phase measuring deflectometry (PMD) system [32] to eliminate the height-normal ambiguity and then performed the surface shape measurement. In their scheme, the height of a single

surface point should be initially obtained. Afterwards, the normal of this chosen point is determined. Finally, considering that the surface is continuously differentiable, other surface points can be calculated through numerical integration [33] with the help of this first point. This method is able to solve the height-normal ambiguity, but it is in fact difficult to be accomplished in the real implementation, because the height information of even a single surface point is not easy to be obtained.

Another feasible method to eliminate the height-normal ambiguity is to move the LCD along the normal of the LCD screen [34–36], so that a unambiguous reflection relation can be determined between the LCD and the camera. For instance, we first locate the LCD at position H in the deflectometry system in Figure 1-3. In this case, the corresponding point $\boldsymbol{A}$ and $\boldsymbol{A}$**'** cannot determine the surface point because of the height-normal ambiguity previously shown in Figure 1-2. However, we then introduce the LCD movement by shifting the LCD of a distance d to the second position H', and the correspondent point can be found on the LCD at $\boldsymbol{A}$**''** now. Finally, by intersecting $\boldsymbol{A}$**'** and $\boldsymbol{A}$**''**, a unique reflection vector $\boldsymbol{R}$ can be determined, and the real surface point is obtained from this reflection vector. Unfortunately, even though this LCD location shifting method is available to obtain the real surface point, such LCD shifting will inevitably introduce mechanical displacement error, which will deteriorate the measurement accuracy.

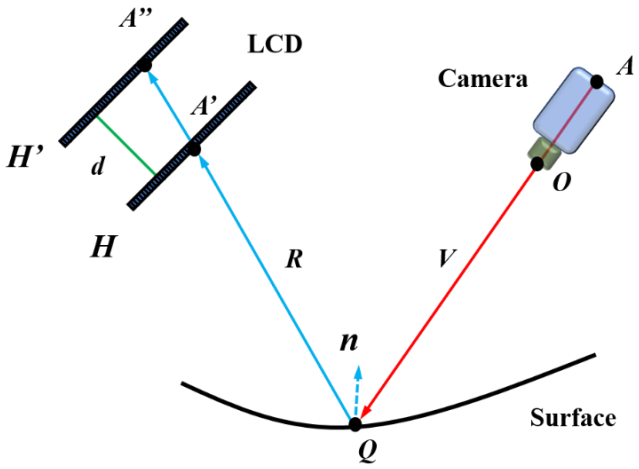

Figure 1-3. The deflectometry scheme to eliminate the height-normal ambiguity by introducing LCD displacement.

To avoid LCD displacement, one can always introduce one more LCD screen into a deflectometry system. Here, by locating a second LCD parallel to the first LCD, we can get the unambiguous reflection (i.e., vector $\boldsymbol{R}$ in Figure 1-3). However, even

though we can align the two LCDs strictly parallel, it is still impossible to perform the surface measurement with a deflectometry system containing two LCDs, because the LCD located closer to the specular surface will block the light projected by the farther LCD. Under this scenario, a beam splitter (BS) can be introduced into a two LCDs deflectometry system [37, 38], and this scheme is presented in Figure 1-4. In particular, the BS is located in a proper location where it can image the fringe patterns on the second LCD (i.e., LCD_2 in Figure 1-4) to a virtual plane (plane H) parallel to the primary LCD (i.e., LCD_1 in Figure 1-4). In this case, both the primary LCD at H' and the virtual second LCD at H ensures a virtual LCD displacement of d and thus, the unambiguous reflection vector is uniquely determined. Apart from using a beam splitter to provide the virtual LCD displacement, a more direct method to obtain a virtual LCD displacement is to put a transparent panel above the LCD screen, from which a biplanar fringe pattern projection is constructed [39]. This biplanar deflectometry system can easily solve the height-normal ambiguity by avoiding the physical movement of any system component. However, it is extremely difficult to find a flat beam splitter with the size of an LCD screen, and it is also unlikely to get a flat transparent panel with a great size. Thus, the measurement accuracy will be inevitably deteriorated by the surface inhomogeneity of the beam splitter or the transparent panel.

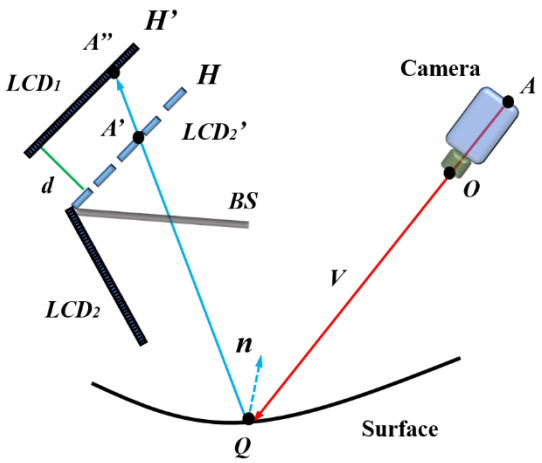

Figure 1-4. Measurement scheme of the deflectometry system with two LCDs and a beam splitter.

Now, to guarantee an accurate measurement without implementing more elements or introducing any component displacement, the classic Software Configurable Optical Test System (SCOTS) was proposed by Burge [11, 12]. In this case, SCOTS is regarded as a reverse Hartmann test model [3], from which the surface normal can be

calculated. The Hartmann test scheme is given in Figure 1-5 (a). In the Hartmann test, a point source is placed close to the curvature center of the tested mirror. Later, the Hartmann screen is positioned before the measured mirror, and it only allows the light entering the Hartmann screen holes to be reflected. At last, the detector is aligned close to the mirror focusing point to record the reflected pattern. In SCOTS, which is regarded as a reverse Hartmann test, the LCD presenting the structured light is reversely regarded as the detector (see Figure 1-5 (b)). Moreover, the point source is provided by the camera lens center, which is placed near the curvature center of the tested mirror. Here, the combination of the camera lens center and the camera pixels works as the Hartmann screen. Finally, the surface normal can be uniquely determined if we know the LCD pixel position, the camera lens center position and the mirror reflection region [40]. Even though SCOTS provides a feasible way to measure the mirror surface shape, the system alignment is rigorous as the geometric position of any component has to be precisely calibrated [40]. Moreover, SCOTS is only verified feasible to measure the aspherical or nearly flat mirrors, but the measurement of either a freeform mirror or a discontinuous mirror with SCOTS is still not demonstrated yet.

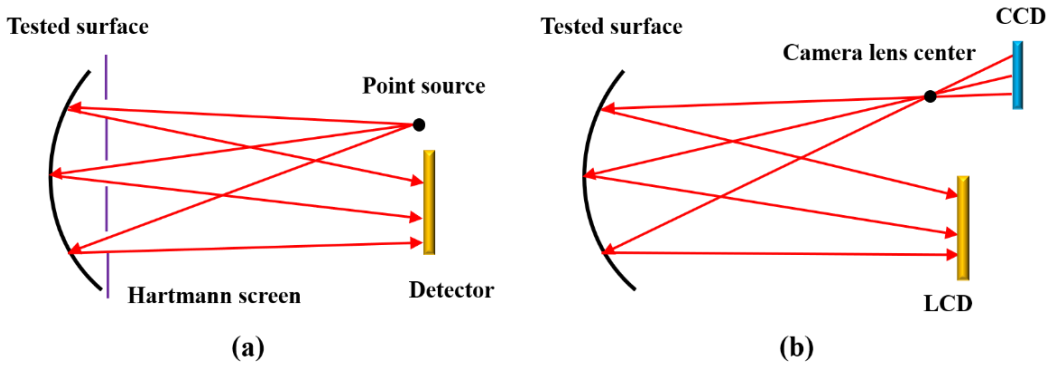

Figure 1-5. Surface shape measurement scheme: (a) the Hartmann test scheme, and (b) the SCOTS scheme (the reverse Hartmann test).

Apart from the above-discussed deflectometry system, modal phase measuring deflectometry (PMD) [41] was as well proposed for specular surface shape measurement. In this scheme, instead of using an initial height information of the studied surface, modal phase measuring deflectometry uses an already established mathematical model to express the entire measured surface shape [42]. Specifically, such mathematical model contains the known surface derivatives which can be modulated by derivative optimization coefficients. Here, the surface derivative can be represented by Chebyshev, B-splines or Zernike polynomials [43, 44]. Later, by modulating the optimization coefficients, the difference between the ray tracing

reprojection and the real captured reprojection on the LCD is minimized and the surface shape is then determined by such optimized coefficients. Even though modal deflectometry system fulfills the surface shape measurement, it finds limitation to accomplish freeform surface measurement because the discussed polynomials may not precisely describe the freeform surfaces.

1.2.3 Stereoscopic deflectometry

In the previous section, different deflectometry systems are discussed to solve the height-normal ambiguity. However, all above-mentioned deflectometry systems use only one camera. Indeed, these single camera contained deflectometry systems are able to perform an accurate specular surface shape measurement, but they either have the limitation in measuring various different surface types (i.e., SCOTS [11, 12] or Modal PMD [41]), or the measurement accuracy is greatly influenced by the system component performance (i.e., biplanar deflectometry systems [37–39]). Under this scenario, stereoscopic deflectometry is proposed, as it is feasible to measure different surface shapes such as plane, curved, or even freeform surfaces. Moreover, compared to single camera deflectometry systems, stereoscopic deflectometry only requires two cameras, so we can totally avoid the component displacement.

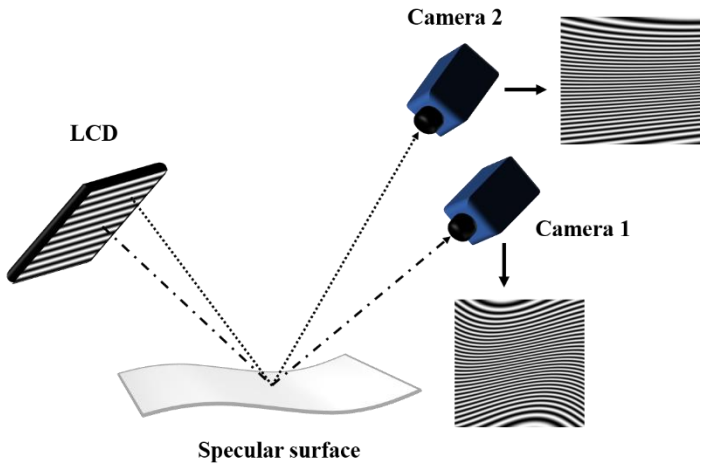

Figure 1-6. Scheme of a stereoscopic phase measuring deflectometry system.

The basic set-up of a stereoscopic deflectometry system contains an LCD screen, two cameras and the specular surface to be measured. The scheme of a stereoscopic deflectometry system is presented in Figure 1-6. Similar to single camera based deflectometry systems, the LCD introduced in the stereoscopic scheme provides

structured light patterns, and then they are reflected by the specular surface and imaged into both cameras at the same time. Moreover, as both cameras are located at different positions, they are inspecting the specular surface from different perspectives. Hence, the fringe patterns reflected into these two cameras are different, as each camera captures a distinct corresponding reflected section of the LCD screen.

Once the stereoscopic deflectometry system scheme is given, the height-normal ambiguity elimination method has to be discussed. The fundamental principle to solve the height-normal ambiguity within a stereoscopic system was firstly suggested by Knauer [32], which is based on a surface normal iteration calculation. Specifically, one pixel (i.e., pixel $\boldsymbol{A}$ in Figure 1-7) in the first camera is primarily selected and its reverse ray tracing relation is established between the LCD and this first camera considering the structured light correspondence. This primary reverse relation is represented in Figure 1-7 by the red solid lines. Here, we want to note that such reflection relation shares exactly the same sketch in Figure 1-2 where the height-normal ambiguity appears. Hence, we can tell that the real surface point is located at a certain point along vector $\boldsymbol{V}$. Then, we select one surface point $\boldsymbol{P}$ along vector $\boldsymbol{V}$ and assume this point as the real surface point. Moreover, the normal to this assumed surface point $\boldsymbol{P}$ (i.e., $\boldsymbol{n_1}$ in Figure 1-7) is calculated with inverse ray tracing between the LCD and the first camera. Afterwards, by connecting point $\boldsymbol{P}$ with the second camera lens center $\boldsymbol{O_2}$, we can obtain a secondary reflection vector (i.e., blue line $\boldsymbol{U}$ in Figure 1-7) and an intersection point $\boldsymbol{B}$ on the second camera image plane. Finally, by considering the structured light correspondence between the second camera and the LCD, the correspondent point $\boldsymbol{B'}$ on the LCD with respect to point $\boldsymbol{B}$ is determined, and thus, a secondary surface normal $\boldsymbol{n_2}$ can be obtained through $\boldsymbol{B}$ and $\boldsymbol{B'}$. Now, if point $\boldsymbol{P}$ which we selected is the real surface point, then surface normal $\boldsymbol{n_1}$ and $\boldsymbol{n_2}$ should coincide, as point $\boldsymbol{P}$ indeed provides the true reflection between the stereoscopic cameras and the LCD. However, if the selected point $\boldsymbol{P}$ is not the real surface point, then these two normal as $\boldsymbol{n_1}$ and $\boldsymbol{n_2}$ cannot coincide, but they are rather staggered or separated.

Now, in the stereoscopic deflectometry system discussed in Figure 1-7, the complicated height-normal ambiguity elimination can be easily transferred into finding a particular point along vector $\boldsymbol{V}$, from which the two calculated normal coincide. In particular, to search for this point, we can introduce iteration methods [32]. Once this point is acquired, we directly regard this point as the surface point, and the surface normal is as well obtained. This stereoscopic scheme definitely demonstrates its great ability to solve the height-normal ambiguity, but it may not be suitable to measure

all types of surface [32]. Moreover, as the surface normal is a three-dimensional vector, surface normal coincidence is difficult to be determined analytically, and this will complex the surface point determination.

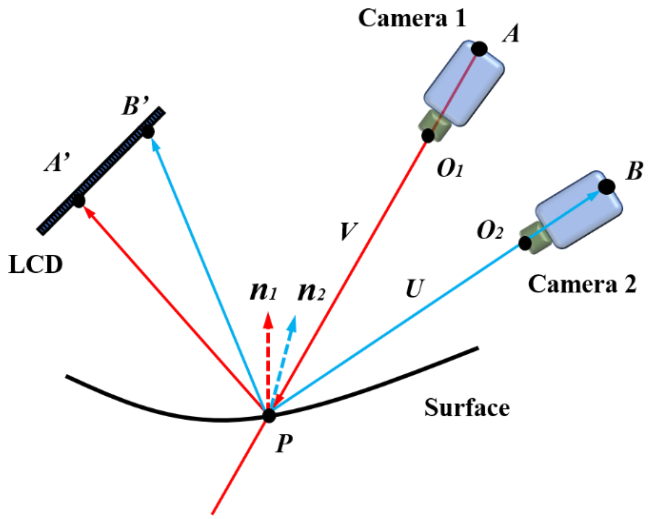

Figure 1-7. The principle scheme to solve the height-normal ambiguity within a stereoscopic deflectometry system.

1.3 Profilometry

In the previous section, deflectometry is systematically discussed to accomplish the specular surface shape measurement. In this section, we introduce profilometry technique, which is proposed to measure the three-dimensional surface shape of diffuser objects. Specifically, we primarily provide the working principle of a profilometry system. Afterwards, we further discuss the development of profilometry by introducing different profilometry techniques. Finally, stereoscopic profilometry is shown, and the advantages of a stereoscopic profilometry system compared to single camera profilometry systems are briefly discussed.

1.3.1 Principle of profilometry

Profilometry system is a structured light system used to measure the 3D surface shape of diffuser objects. The basic principle of profilometry relies on surface diffuser reflection. Compared to specular reflection, diffuser object reflects the incident light

into many different directions rather than directly reflects the incident light into one single direction. The difference between diffuser surface reflection and specular surface reflection is given in Figure 1-8.

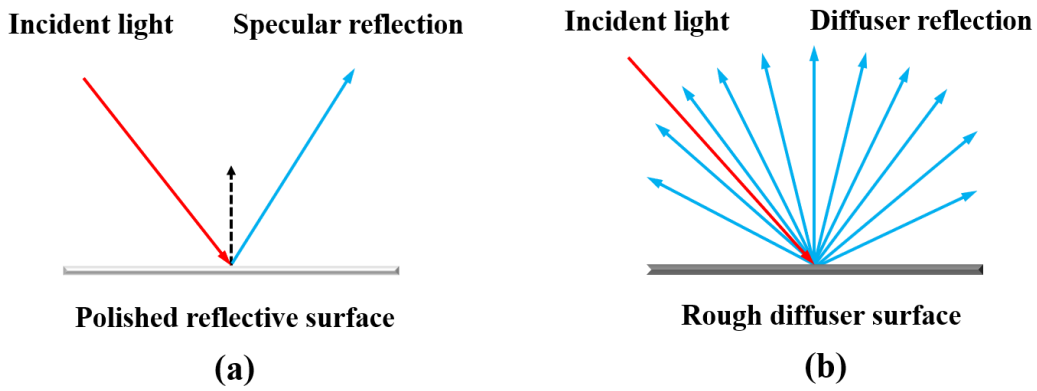

Figure 1-8. The reflection schemes: (a) the surface reflection at the specular surface, and (b) the surface reflection at the diffuser surface.

Now, by considering the diffuser characteristic of the measured surface, we directly project the structured light pattern to the object and then we capture the intensity pattern on the object with an image receiver. In this case, the LCD screen is not appropriate to provide the structured light projection, because the structured light pattern on the LCD is only observable if the measured surface is specular. Hence, the structured light in a profilometry system is normally provided by a video projector and the basic profilometry scheme is shown in Figure 1-9 (a). In a profilometry system, the video projector contains an illumination source, a spatial light modulator (i.e., normally as an LCD chip or a digital micromirror device (DMD)), and a focusing lens. The spatial light modulator in the video projector is used to generate the structured light pattern. On the other hand, the camera shares the same scheme of that used in the deflectometry system, as it has a CCD working as the image plane and a focusing lens. Here, we want to note that one of the most commonly used structured light pattern in profilometry systems is sinusoidal fringe pattern. Once the system scheme is determined, we use the video projector to project sinusoidal fringe patterns and then we use the camera to capture the distorted fringe patterns on the object. Such fringe pattern distortion is introduced by the surface shape variation. Finally, the surface point of the diffuser object is determined by calculating the surface height (see Figure 1-9 (b)) using fringe pattern correspondence between the video projector and the camera.

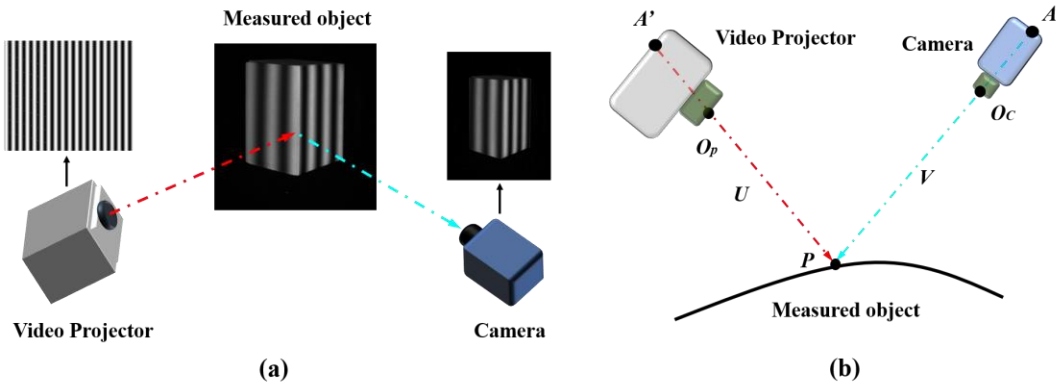

Figure 1-9. Schemes of the profilometry system: (a) the typical experimental set-up of a profilometry system, and (b) the surface height determination using a projector and a camera.

The most commonly used method to determine the surface point is to perform geometric triangulation between the video projector and the camera. In the video projector, the focusing lens is simplified to an optical pinhole ($\boldsymbol{O_P}$ in Figure 1-9 (b)), and the spatial light modulator (i.e., DMD or LCD chip) is regarded as the reverse image plane. Hence, the fringe pattern is generated in this reverse image plane. On the other hand, the camera is regarded as the combination of an optical center (i.e., $\boldsymbol{O_C}$ in Figure 1-9 (b)) and an image plane (i.e., CCD panel). In this case, the camera optical center is the geometric center of the camera focusing lens that allows all light to pass through. Later, we pick point $\boldsymbol{A}$ in the camera image plane and then we connect it with the camera optical center $\boldsymbol{O_C}$ to forge a projection vector $\boldsymbol{V}$. Then, we use the structured light patterns to find the correspondent point of $\boldsymbol{A}$ on the video projector image plane and we name it $\boldsymbol{A'}$. Afterwards, we connect $\boldsymbol{A'}$ to the video projector optical center $\boldsymbol{O_P}$ to build another vector $\boldsymbol{U}$. At this moment, once we know the spatial position relation between the video projector and the camera, we perform the geometric triangulation between vector $\boldsymbol{V}$ and vector $\boldsymbol{U}$, and their intersection point $\boldsymbol{P}$ is the final measured surface point. At last, if we perform such geometric triangulation within all pixels in the camera image plane, we get all surface points and the surface shape is finally obtained.

1.3.2 Development of profilometry

The development of profilometry can be dated back to 1980s when one classic structured light profilometry system was proposed by Srinivasan [45]. Such system is

referred as phase shifting profilometry (PSP). In this system, the structured light is presented as sinusoidal fringe patterns, which are generated through a laser interferometer. Afterwards, the sinusoidal fringe patterns are collimated by a collimating lens. As phase shifting technique is introduced into their system, the projection also contains a quarter-waveplate and a rotate polarizer to provide phase modulation. Once the fringe patterns are projected to the measured object, an image sensing array camera is implemented to capture the fringe patterns on the object. The scheme of Srinivasan profilometry system is given in Figure 1-10 (a). What is more, a geometric model of this profilometry system is sketched in Figure 1-10 (b), as it is used to perform the surface height calculation.

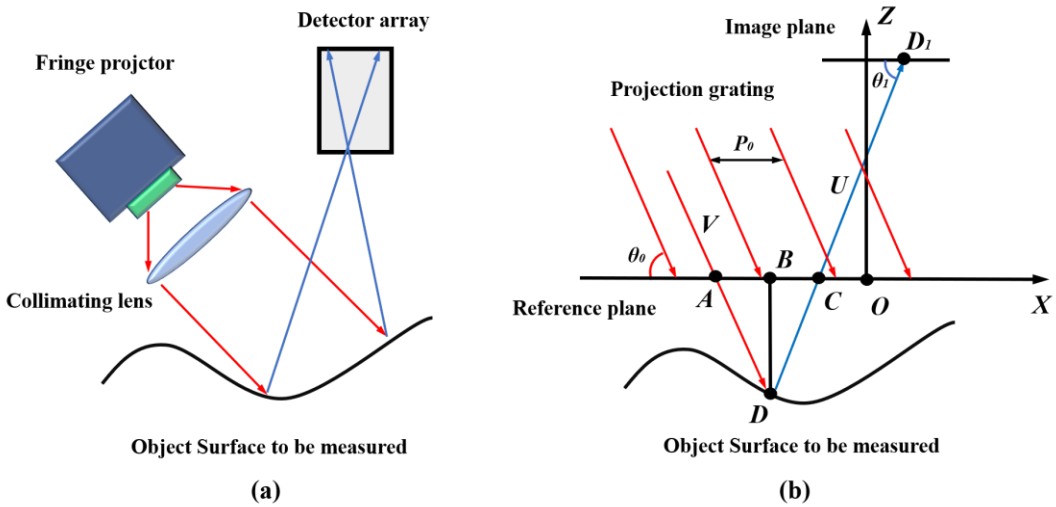

Figure 1-10. (a) Scheme of the Srinivasan profilometry system, and (b) the geometric model of this system for surface point calculation.

In Figure 1-10 (b), Z axis of the PSP system is defined as perpendicular to the camera image plane. Moreover, a reference plane perpendicular to Z axis is introduced to assist the surface height measurement. Firstly, we consider a point $\boldsymbol{C}$ on the reference plane. By introducing the image plane (see Figure 1-10 (b)), we record the intensities of point $\boldsymbol{C}$ at $\boldsymbol{D_1}$. Later, by performing phase shifting and phase unwrapping (this will be discussed in Chapter 3) to point $\boldsymbol{C}$, we can obtain the phase value of $\boldsymbol{C}$ as Φ_C. Now, by assuming the phase value at the system origin $\boldsymbol{O}$ is 0, Φ_C can be denoted as:

$$\Phi_C = 2\pi OC \big/ P_0 \,, \tag{1.1}$$

where OC denotes the geometric distance from point $\boldsymbol{O}$ to point $\boldsymbol{C}$, and P_0 is the period of the sinusoidal fringe pattern.

Secondly, by connecting point $\boldsymbol{D_1}$ with point $\boldsymbol{C}$ and extend this vector (i.e., vector $\boldsymbol{U}$) to the further space, we find that it intersects with the measured surface at point $\boldsymbol{D}$. At this time, let us assume that the reference plane is removed, and the image receiver directly captures the intensities of point $\boldsymbol{D}$. Thus, by introducing phase shifting and phase unwrapping to point $\boldsymbol{D}$, its phase value can be calculated as Φ_D.

Finally, we examine the projection vector $\boldsymbol{V}$ which passes through both point $\boldsymbol{A}$ on the reference plane and point $\boldsymbol{D}$ on the object surface. By simply analogizing to Eq. (1.1), the phase value at point $\boldsymbol{A}$ can be obtained as:

$$\Phi_A = 2\pi OA \big/ P_0 \,, \tag{1.2}$$

where OA denotes the geometric distance from point $\boldsymbol{O}$ to point $\boldsymbol{A}$.

However, in the real implementation, we are not projecting point $\boldsymbol{A}$ directly to the image plane and thus Φ_A seems not obtainable. Nevertheless, because both point $\boldsymbol{A}$ and point $\boldsymbol{D}$ are located along the same projection vector $\boldsymbol{V}$, and the reflection at $\boldsymbol{D}$ only changes the intensity but not the phase value, so the phase value at point $\boldsymbol{D}$ is equal to the phase value at point $\boldsymbol{A}$ (i.e., $\Phi_D = \Phi_A$). Now, note that we have relation $\Phi_D = \Phi_A$, and we also obtain the phase values at point $\boldsymbol{A}$ and point $\boldsymbol{C}$, the geometric distance between $\boldsymbol{A}$ and $\boldsymbol{C}$ can be calculated by considering the phase values at these two points as:

$$AC = (P_0 \big/ 2\pi)\Delta\Phi_{DC} \,, \tag{1.3}$$

where $\Delta\Phi_{DC}$ is the phase difference between Φ_D and Φ_C.

Then, the surface height of point $\boldsymbol{D}$ with respect to the reference plane is geometrically determined as:

$$BD = AC \cdot \tan\theta_0 \big/ [1 + \tan\theta_0 \big/ (AC \cdot \tan\theta_1)] \,, \tag{1.4}$$

where θ_0 and θ_1 are the angles of the intersection vectors.

Finally, once the surface height is calculated by Eq. (1.4), we can further acquire both the x and y coordinates of the surface point $\boldsymbol{D}$, and thus the complete geometric information of this surface point is known.

Apart from the Srinivasan system, other phase shifting profilometry methods are also proposed. For instance, Toyooka [46] suggested a phase shifting profilometry system using a slide projector to project the sinusoidal pattern, and thus the collimating lens is not necessary. Huang [47–49] simplified the phase shifting profilometry by introducing less system configuration constrains, at the expense of demanding a more accurate system calibration.

Phase-shifting profilometry provides an accurate surface shape measurement with an easy implementation. However, a reference plane is always required to determine the final surface height and thus, the surface shape of the reference plane affects the final measurement result. Moreover, as a reference plane is not allowed in some surface measurements, the introduction of such plane also constrains the further profilometry application.

Another structured light profilometry system is Moiré profilometry [50-52]. The basic process to perform Moiré profilometry measurement can be generalized as three steps. First of all, a fringe pattern is projected to the measured object and then we use a camera to capture this fringe pattern. This fringe pattern can be generated through a grating or a digital video projector. Afterwards, we superimpose another synthetic fringe pattern, which has the same frequency as the fringe pattern provided by the video projector, to construct a Moiré contour. The superimposition is performed by putting another grating in front of the image plane or directly adding digital fringe patterns to the captured image. Finally, by removing the high-frequency grid which contaminates the pure Moiré pattern, we can finally extract the surface shape of the measured object by further analysis. Here, as fringe patterns are more flexible to be generated through a video projector compared to a complex grating, we will only discuss digital Moiré profilometry.

The scheme of a digital Moiré profilometry system is similar to that in Figure 1-9 (b). The video projector is projecting the binary fringe pattern rather than the sinusoidal fringe pattern to the object. On the other side, once the image is captured by the camera, not only one single digital fringe pattern, but rather we introduce numerous digital fringe patterns, which have the same period as the fringe pattern from the video projector, to perform phase shifting. However, in these phase-shifted images, not only the Moiré contour map is obtained, but also the undesired high-frequency fringe pattern is mixed. Thus, different methods are proposed to eliminate such high-frequency noise, such as Fourier transform [53], wavelet transform [54], or the combination of wavelet and Fourier transform [55]. Once we eliminate the high-

frequency noise, phase unwrapping is performed (this will be discussed in Chapter 3) and the unwrapped phase map of the object is acquired. From the unwrapped phase map, we can easily determine the surface height as [56]:

$$h(x,y) = \frac{\lambda}{2\pi}\Phi(x,y)\,, \tag{1.5}$$

where λ in Eq. (1.5) means the Moiré wavelength, which is referred as the distance between the two continuous bright or dark grid on a flat calibration board, $\Phi(x,y)$ is the unwrapped phase of any pixel, and $h(x,y)$ is the surface height. At this moment, we can tell from Eq. (1.5) that the Moiré wavelength has to be known and this is normally obtained by system calibration using a flat plate [57]. Therefore, a flat reference is also used in Moiré profilometry.

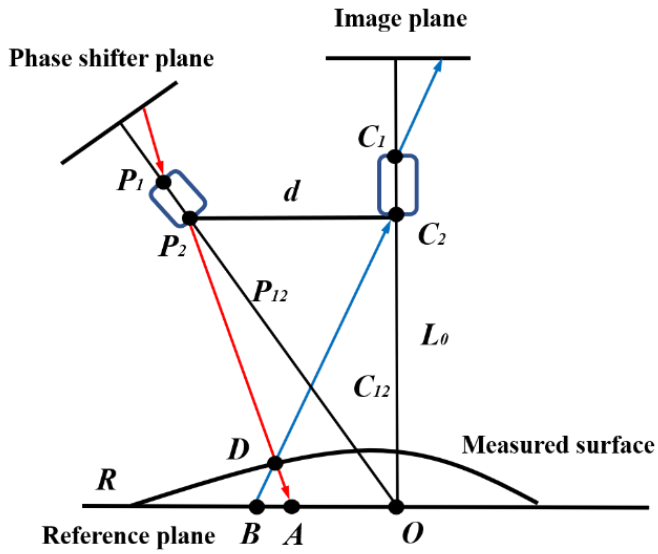

Figure 1-11. Geometric scheme of Fourier transform profilometry (FTP) system.

Apart from phase measuring profilometry and Moiré profilometry, Fourier transform profilometry (FTP) [58] is also a popular structured light system to measure the diffuser object surface shape as it only requires one or two frames. In FTP, we as well project SFPs to the measured object, and such sinusoidal fringe patterns (SFPs) are distorted by the object. Now, the surface height information is encoded into these distorted fringe patterns. Afterwards, we extract the surface shape by sequentially performing Fourier transform, spatial domain filtering and inverse Fourier transform. The basic geometry FTP scheme is given in Figure 1-11. The optical axis of the video projector lens is defined by vector $\boldsymbol{P_{12}}$ passing through points $\boldsymbol{P_1}$ and $\boldsymbol{P_2}$, and the

optical axis of the camera is defined by vector $\boldsymbol{C_{12}}$ passing through $\boldsymbol{C_1}$ and $\boldsymbol{C_2}$. Vector $\boldsymbol{P_{12}}$ and vector $\boldsymbol{C_{12}}$ intersect at $\boldsymbol{O}$ located on the reference plane R. Here, plane R is introduced to assist us to decide the surface height. Now, $\boldsymbol{D}$ is referred as the surface point, so we forge a third vector passing through $\boldsymbol{D}$ and $\boldsymbol{C_2}$ and it interests with plane R at point $\boldsymbol{B}$. Also, by forging a fourth vector passing through $\boldsymbol{D}$ and $\boldsymbol{P_2}$, we obtain its intersection point with plane R at point $\boldsymbol{A}$. The distance between $\boldsymbol{C_2}$ and $\boldsymbol{P_2}$ is named as d and the distance between $\boldsymbol{C_2}$ and $\boldsymbol{O}$ is defined as L_0.

Now, considering we mount the measured object on the reference plane R, the deformed fringe pattern obtained by the image receiver is represented as:

$$g(x,y) = r(x,y) \sum_{n=-\infty}^{\infty} A_n \exp(i(2\pi n f_0 x + n\Phi(x,y))) \,, \tag{1.6}$$

where $r(x,y)$ is the nonuniform distribution of the measured surface reflectivity. A_n is the Fourier series weighting factor, f_0 is the fundamental frequency of the obtained fringe pattern image. $\Phi(x,y)$ is the phase modulation introduced by the measured object.

Later, let us imagine that the fringe pattern is directly distorted by the reference plane, then the deformed fringe pattern is written as:

$$g_0(x,y) = r_0(x,y) \sum_{n=-\infty}^{\infty} A_n \exp(i(2\pi n f_0 x + n\Phi_0(x,y))) \,, \tag{1.7}$$

where $r_0(x,y)$ is the nonuniform distribution of the reference plane reflectivity. $\Phi_0(x,y)$ is the phase modulation introduced by the reference plane.

At this moment, we perform Fourier transform to Eq. (1.6) and then introduce the bandpass filter to only remain the fundamental component. Afterwards, we introduce inverse Fourier transform to the remained fundamental component and the complex signals are represented as:

$$\hat{g}(x,y) = A_1 r(x,y) \exp(i2\pi f_0 x + \Phi(x,y)) \,, \tag{1.8}$$

$$\hat{g}_0(x,y) = A_1 r_0(x,y) \exp(i2\pi f_0 x + \Phi_0(x,y)) \,, \tag{1.9}$$

where Eq. (1.8) corresponds to Eq. (1.6), and Eq. (1.9) corresponds to Eq. (1.7). Thus, by combining Eq. (1.8) and Eq. (1.9), and later compute the logarithm, we can obtain a following equation as:

$$\log[\hat{g}(x,y)\cdot\hat{g}_0(x,y)] = \log[|A_1|^2 r(x,y)] + i\Delta\Phi(x,y)\,. \tag{1.10}$$

Finally, by only extract the imaginary value within Eq. (1.10), a continuous phase difference is determined. Once we obtain this phase difference value, we can calculate the surface height as:

$$h(x,y) = \frac{L_0\Delta\Phi(x,y)}{\Delta\Phi(x,y) - 2\pi f_0 d}\,. \tag{1.11}$$

Based on this basic FTP principle, several improved schemes have also been proposed. For instance, quasi-sine projection and π phase shifting techniques are applied into the FTP system to extend the low frequency of the fundamental component to zero, whereas the high frequency can be extended to $2f_0$ without overlaps [59, 60]. For coarse object measurement, 2D FTP is discussed as it is more feasible to tackle the surface discontinuity [61]. Moreover, to efficiently obtain the phase information, windowed Fourier transform (WFT) [62, 63] and wavelet transform (WT) [64–67] are also introduced.

Recently, fringe projection profilometry (FPP) [68] has been proposed as another promising structured light system to measure the diffuser object surface. The basic principle of FPP also relies on sinusoidal fringe pattern projection and phase unwrapping. Nevertheless, it adopts a more intuitive geometric triangulation to directly obtain the surface point, and thus the complicated Fourier transform, or phase measuring process can be avoided. In FPP, we use the video projector to project a series of sinusoidal fringe patterns to the object, these fringe patterns are encoded by certain phase distributions. The FPP scheme is given in Figure 1-12, from which we show the phase distribution on the spatial light modulator plane of the video projector. Later, a camera is introduced to capture the fringe patterns on the object, and we can obtain the phase distribution on the object using phase shifting combined with phase unwrapping (see Chapter 3). Now, as diffuser surface reflection only changes the intensity but not the phase value, the phase range in the camera is the same as that provided by the spatial light modulator plane of the video projector, but the spatial phase distributions between the camera image plane and the video projector plane are geometrically distorted by the measured object. Finally, by picking the phase value of one point on the camera image plane and finding the same phase point on the spatial light modulator plane of the video projector, we can determine the surface point through triangulation once we calibrate the video projector, the camera and the geometric relation between these two devices [69]. Here, to perform geometric

triangulation, we select one point ***A*** and connect it with the video projector optical center to forge a projection vector ***V***. On the other hand, we connect point ***A'***, which contains the same phase value as it of ***A***, to the camera optical center to forge the receiving vector ***U***. Now, by extending these two vectors, we can determine their intersection point ***P*** as the surface point on the object.

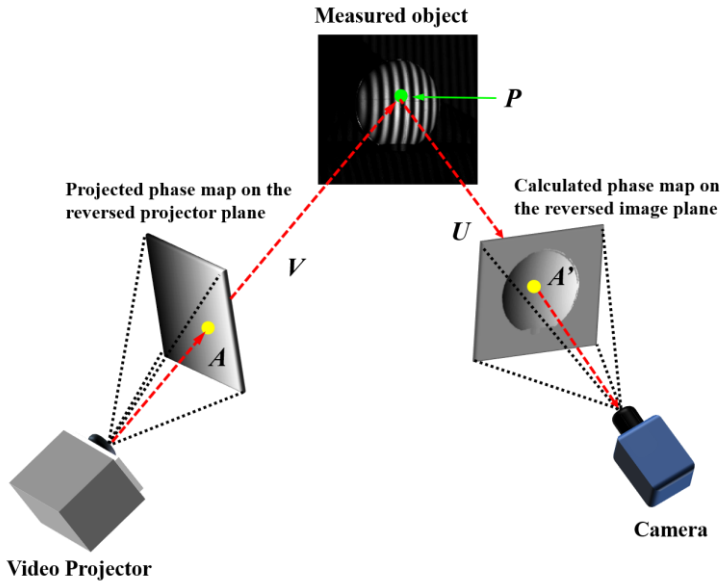

Figure 1-12. Principle scheme of the fringe projection profilometry (FPP) system.

However, as we are using sinusoidal fringe patterns, it is obvious that the phase value within either the horizontal or vertical direction is always the same. For instance, in Figure 1-12, the phase value on the video projector plane within a column is always equivalent. Under this scenario, geometric triangulation is not performable as even though one can select a unique point on the camera image plane, this point rather finds numerous points with the same phase value in the video projector plane. Thus, orthogonal fringe patterns are used to find the unique corresponding phase points between the image plane and the video projector plane. To avoid the orthogonal fringe pattern projection, another triangulation method is proposed by introducing a baseline, which is forged by the optical centers between the video projector and the camera [70–72].

Fringe projection profilometry provides a very robust surface point measurement compared to Fourier transform profilometry or phase shifting profilometry as it can be used to even measure discontinuous objects. However, FPP calibration is complex, because apart from the geometric calibrations of the camera and the video projector

[69], we also have to calibrate the gamma nonlinearity of the video projector [73, 74]. Here, gamma nonlinearity is referred as the output intensity and the input gray level in a projection component does not follow a linear tendency.

1.3.3 Stereoscopic profilometry

In Section 1.3.2, we have shown different profilometry systems with one camera, but these systems may find difficulties in measuring discontinuous objects (i.e. phase shifting profilometry or Fourier transform profilometry), or the system calibration is challenging (i.e., fringe projection profilometry). Thus, in this subsection, we discuss a stereoscopic fringe projection profilometry (SFPP) system [75–78]. We also briefly demonstrate its advantages against the single camera profilometry systems in performing surface shape measurement.

The core component of a stereoscopic profilometry system are two cameras located at different positions to capture the same measured object from different perspectives [79]. In this case, one can reconstruct the object surface information through the correspondence between the scenes of these two cameras [80]. To establish the correspondence between both cameras, various algorithms are proposed such as area-based algorithm [80], window adaptive algorithm [81] or multi-view algorithm [82] etc., and these algorithms are all based on the intensity registered into both cameras. The intensity-based technique seems promising, but it requires a complicated algorithm to establish the correspondence. Under this scenario, structured light projection based stereoscopic profilometry system is proposed, from which the correspondence is easily established through analytical phase values rather than the intensity information. Similar to a single camera profilometry system, the structured light used in a stereoscopic fringe projection profilometry are also presented as sinusoidal fringe patterns. Later, we sequentially project these patterns to the measured object, so the unwrapped phase map on the measured object in each camera can be obtained through phase shifting and phase unwrapping (see Chapter 3). Here, as both cameras capture a same object, the phase maps of both cameras have the same distribution. Finally, as the phase maps within the two cameras are obtained, we perform geometric triangulation by searching the correspondent points between both phase maps, and the surface point is determined. The basic system setup of a SFPP system is given in Figure 1-13.

In Figure 1-13, the video projector projects the fringe patterns to the object, each camera captures the fringe patterns on the object, so the unwrapped phase maps are

calculated (i.e., Phase map 1 and Phase map 2). Now, we select one phase point at $\boldsymbol{A}$ in the first phase map and we obtain its phase value as Φ_A. On the other hand, we look for the same phase value point in the second camera phase map, and this point is located at $\boldsymbol{A'}$. As we obtain the optical centers of both cameras through camera calibration, we simply connect $\boldsymbol{A}$ with $\boldsymbol{O_1}$, and $\boldsymbol{B}$ with $\boldsymbol{O_2}$ to trace two vectors $\boldsymbol{V}$ and $\boldsymbol{U}$. Finally, by extending $\boldsymbol{V}$ and $\boldsymbol{U}$, they intersect at point $\boldsymbol{P}$ and we regard this point as the surface point on the object.

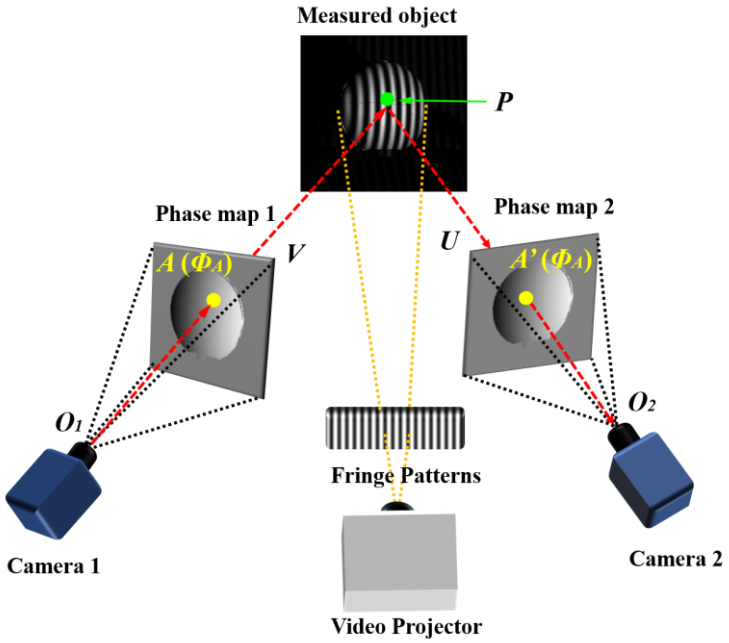

Figure 1-13. System setup of a stereoscopic fringe projection profilometry (SFPP) system.

Compared to single camera fringe projection profilometry systems, stereoscopic fringe projection profilometry (SFPP) system shows great system flexibility. First of all, it is not necessary to calibrate the non-linear gray level-intensity response of the video projector (i.e., gamma effect) in SFPP. This is because the phase point correspondence in SFPP is directly established between the two cameras. Hence, even though a phase shifting error is introduced by the video projector gamma effect, such phase shifting error is equivalently introduced in both cameras. Therefore, as we are only searching for the same phase value in both cameras, such equivalent phase error does not affect the correct phase point correspondence. On the other hand, as geometric triangulation is only performed within the cameras in an SFPP system, the spatial position of the video projector to the cameras is not critical. Hence, the position

of the video projector does not have to be calibrated, and we can flexibly modify it to provide proper illuminations for different measured objects.

1.4 Objective

The major goals of this thesis are listed in the following:

- **Develop a stereoscopic phase measuring deflectometry system:** In this thesis, we will develop a stereoscopic phase measuring deflectometry system to measure the surface shapes of different specular objects. In particular, we aim at developing a robust method to perform specular surface measurement. Here, specular surface measurement requires: (*i*) a method to eliminate the height-normal ambiguity in a stereoscopic deflectometry system; (*ii*) an accurate algorithm to calculate the surface derivatives; (*iii*) a fast and robust method to reconstruct the surface from the surface derivatives. Once we have proposed the measurement principle, we will calibrate a stereoscopic phase measuring deflectometry system and use it to measure various specular surfaces to verify the feasibility of our proposed system. The detail of this research will be introduced in Chapters 4 and 5.
- **Develop a stereoscopic fringe projection profilometry system:** As deflectometry only allows us to measure specular surface shapes, we will also develop a stereoscopic fringe projection profilometry system to measure the surface shapes of diffuser objects. In this stereoscopic profilometry system, we would like to: (*i*) use the same stereoscopic camera as in the previous deflectometry system to implement a stereoscopic profilometry system, so that we can obtain a flexible system calibration; (*ii*) develop a numerical method to perform an accurate geometric triangulation, so that we can enhance the surface reconstruction accuracy. Once the measurement principle of this stereoscopic profilometry system is determined, we will calibrate a stereoscopic fringe projection profilometry system, and then we will experimentally measure different diffuser objects to verify the performance of our proposed system. The detail of this research will be introduced in Chapter 6.
- **Develop a stereoscopic deflectometry-profilometry hybrid system:** We use deflectometry to measure a specular surface, and we also use

profilometry to measure a diffuser surface. However, it is surprising that hardly any structured light system had been proposed to measure a specular-diffuser hybrid object, which is also vastly used in industrial applications. Therefore, we combine stereoscopic deflectometry with stereoscopic profilometry to develop a stereoscopic deflectometry-profilometry hybrid system to measure the surface shape of a specular-diffuser object. In this stereoscopic deflectometry-profilometry hybrid system, we will: (*i*) combine stereoscopic profilometry with stereoscopic deflectometry, so that we can obtain a flexible system calibration; (*ii*) develop a specular-diffuser surface reconstruction method to finally extract the complete surface shape of the specular-diffuser hybrid object. After we determine the measurement principle of this system, we will calibrate a stereoscopic deflectometry-profilometry system to measure a specular-diffuser hybrid object to verify the performance of this system. The detail of this research will be explained in Chapter 7.

1.5 Structure of the thesis

The outline of this thesis is as follows:

In Chapter 2, the mathematical foundations which are necessary to perform deflectometry or profilometry measurement are provided. In particular, we firstly show the mathematical descriptions of the basic geometric elements, such as point, vector, line and plane. Later, we mathematically discuss the representation of coordinate system transformation in three-dimensional space. What is more, we also introduce the pinhole camera model. Finally, the light reflection model, which is used in deflectometry measurement, is mathematically presented.

In Chapter 3, we discuss the parameter calibration in stereoscopic camera based structured light measurement systems. We firstly explain phase shifting and phase unwrapping techniques with using sinusoidal fringe patterns, from which we can obtain an unwrapped phase map. Later, we explain the system parameter calibration in stereoscopic structured light measuring systems, such as gamma calibration, camera intrinsic and extrinsic parameter calibration, and stereoscopic camera calibration. Finally, we present the whole system geometric scheme calibration.

In Chapter 4, we explain the complete method to perform the specular surface measurement with a stereoscopic phase measuring deflectometry (SPMD) system. We

firstly present a phase minimization method combined with a polynomial fitting algorithm to accomplish the surface derivative calculation. Later, by introducing sub-pixel interpolation, we further enhance the phase pair correspondence. Finally, we propose 2D Fourier integration for specular surface reconstruction.

In Chapter 5, we experimentally measure the specular surfaces with a stereoscopic phase measuring deflectometry (SPMD) system. In particular, we present the complete SPMD system calibration. Later, three representative specular surfaces, such as a flat mirror, a spherical mirror and a discontinuous specular disk, are experimentally measured.

In Chapter 6, we describe the diffuser surface measurement with a stereoscopic fringe projection profilometry (SFPP) system. First of all, we mathematically describe a geometric triangulation method to obtain the surface point. Then, we provide the experimental calibration of a SFPP system. Finally, the feasibility of this system is experimentally verified by measuring three diffuser objects with different surface structures.

In Chapter 7, we combine stereoscopic deflectometry with stereoscopic profilometry to perform the specular-diffuser hybrid object measurement. We describe this hybrid measurement system and the diffuser-specular surface reconstruction method. Finally, we measure a specular-diffuser hybrid object using both separate projection method and combined projection method.

Finally, the conclusions of this work are summarized and a proposal for the future research is presented in Chapter 8.

Chapter 2 Mathematical foundations of stereoscopic camera based structured light measurement systems

This chapter shows the basic mathematical foundations used in this thesis to perform the surface shape measurement. We firstly present the mathematical descriptions of the basic geometric elements, such as point, vector, line and plane. Secondly, we mathematically show the representation of geometric rotation and shifting in three-dimensional space, and then we discuss the coordinate system transformation because we need to work in different coordinate systems in both the stereoscopic phase measuring deflectometry (SPMD) system and the stereoscopic fringe projection profilometry (SFPP) system. Thirdly, we introduce the geometric representation of a pinhole camera and the light projection model in this pinhole camera. In the last section, the light reflection model is mathematically presented, as it is required in SPMD surface normal calculation.

2.1 Geometric representations

In both the stereoscopic phase measuring deflectometry system and the stereoscopic fringe projection profilometry system, the geometric representations are the foundations to perform surface measurement.

The most basic geometric representation is point, that a point represents a location in the space. Specifically, in Euclidean geometry, a point does not have any length,

area, volume or other dimensional characteristics. Moreover, a three-dimensional point is defined with respect to a three-dimensional coordinate system and it can be represented by three tuples in a vector notation as $\boldsymbol{P}=(x,y,z)$. Note that the mathematically representation of a point is defined in a certain coordinate system, so once we use another coordinate system to describe this same point, the three tuples in the vector notation will be changed with respect to the new coordinate system.

Now, let us imagine if we have point $\boldsymbol{A}=(x_A,y_A,z_A)$ and point $\boldsymbol{B}=(x_B,y_B,z_B)$ in the same Cartesian coordinate system $(O\text{-}X,Y,Z)$, we can connect these two points to define a vector. This vector has its direction and magnitude, as the direction of the vector is defined by the connection order between these two points, and its magnitude is the length between these two points in the $(O\text{-}X,Y,Z)$ coordinate system. For instance, by connecting from point $\boldsymbol{A}$ to point $\boldsymbol{B}$ in Figure 2-1, we obtain vector $\boldsymbol{v}$ and it can be mathematically written as:

$$\boldsymbol{v} = \left[x_B - x_A, y_B - y_A, z_B - z_A\right]. \tag{2.1}$$

The magnitude of $\boldsymbol{v}$ is then calculated as:

$$\left\|\boldsymbol{v}\right\| = \sqrt{(x_B - x_A)^2 + (y_B - y_A)^2 + (z_B - z_A)^2}\,. \tag{2.2}$$

From Eqs. (2.1) and (2.2), we can further calculate the unit vector of $\boldsymbol{v}$ as:

$$\boldsymbol{V} = \frac{\boldsymbol{v}}{\left\|\boldsymbol{v}\right\|}, \tag{2.3}$$

where the magnitude of this unit vector $\boldsymbol{V}$ is 1.

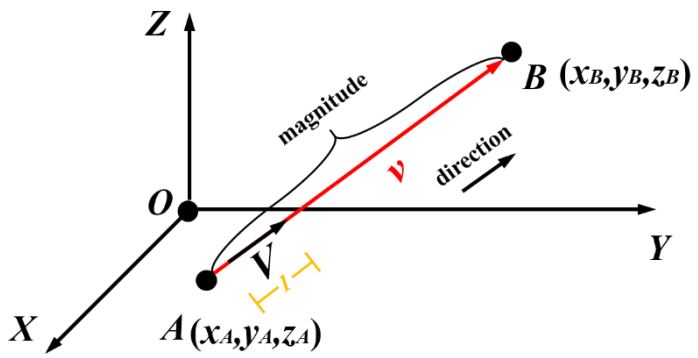

Figure 2-1. Vector $\boldsymbol{v}$ forged by connecting from point $\boldsymbol{A}$ to point $\boldsymbol{B}$ in the coordinate system $(O\text{-}X,Y,Z)$, and the unit vector $\boldsymbol{V}$ is calculated from $\boldsymbol{v}$.

Now, if we inversely connect from point $\boldsymbol{B}$ to point $\boldsymbol{A}$ to define a new vector, it can be written as -$\boldsymbol{v}$, and this inverse vector provides an opposite direction to that of vector $\boldsymbol{v}$.

As a vector is mathematically determined, we further discuss the mathematical representation of a straight line. A straight line is either represented by two points in the space through which they pass, or it is defined through a point and a vector in the three-dimensional space. Here we need to note that a line has no direction, as it only demonstrates infinite points along this line in the space. The mathematical definition of a line, which passed through point $\boldsymbol{A}$=(x_A,y_A,z_A) in (O-X,Y,Z) coordinate system, can be defined as bellow:

$$P_{\boldsymbol{A}} = \boldsymbol{V} \cdot t + \boldsymbol{A}\,, \tag{2.4}$$

where $P_{\boldsymbol{A}}$ is the three-dimensional coordinate of any point along this line, $\boldsymbol{V}$ is the normalized vector of this line, and t is an arbitrary real number.

As now we are equipped with the knowledge of point, vector and line, we finally discuss the plane. A plane is a flat, two-dimensional surface that infinitely extend in the three-dimensional space. The common way to describe a plane is to define it through a point and a surface normal. As the plane is flat, it must be perpendicular to a certain nonzero vector $\boldsymbol{n}$, and we define $\boldsymbol{n}$=[n_x,n_y,n_z] as the normal of the plane. Moreover, this plane passes through a three-dimensional point at $\boldsymbol{P_0}$=(x_0,y_0,z_0). Then, we connect any point $\boldsymbol{P}$=(x,y,z) on this plane to $\boldsymbol{P_0}$ to forge a line, and this line must be perpendicular to normal $\boldsymbol{n}$. In this case, we can obtain the following equation as:

$$n_x(x - x_0) + n_y(y - y_0) + n_z(z - z_0) = 0\,, \tag{2.5}$$

where Eq. (2.5) is the mathematical representation of a flat plane. Moreover, by further expand Eq. (2.5), we can write this plane function as:

$$n_x x + n_y y + n_z z + d = 0\,, \tag{2.6}$$

where d is a constant.

2.2 Coordinate system transformation

Stereoscopic phase measuring deflectometry (SPMD) system contains two cameras and an LCD screen; whereas stereoscopic fringe projection profilometry (SFPP)

system contains two cameras and a video projector. Both systems have different components located at different positions, and these components have their own coordinate systems. To perform surface reconstruction with either the SPMD system or the SFPP system, it is necessary to perform all the operations in only one coordinate system. Under this scenario, coordinate system transformation is mandatory.

Coordinate system transformation is used to represent the geometric relation between different coordinate systems through rotation and shifting. We firstly discuss the coordinate system rotation. For instance, we have two Cartesian coordinate systems shown in Figure 2-2, and the second coordinate system (O_2-X_2, Y_2, Z_2) (i.e., the blue label coordinate system) is obtained from the first coordinate system (O_1-X_1, Y_1, Z_1) (i.e., the black label coordinate system) by rotating an angle of φ around Z axis. Then, the relations between the two coordinate systems are given as:

$$\begin{pmatrix} x_2 \\ y_2 \\ z_2 \end{pmatrix} = \begin{pmatrix} \cos\varphi & \sin\varphi & 0 \\ -\sin\varphi & \cos\varphi & 0 \\ 0 & 0 & 1 \end{pmatrix} \begin{pmatrix} x_1 \\ y_1 \\ z_1 \end{pmatrix}, \tag{2.7}$$

$$\begin{pmatrix} x_1 \\ y_1 \\ z_1 \end{pmatrix} = \begin{pmatrix} \cos\varphi & -\sin\varphi & 0 \\ \sin\varphi & \cos\varphi & 0 \\ 0 & 0 & 1 \end{pmatrix} \begin{pmatrix} x_2 \\ y_2 \\ z_2 \end{pmatrix}. \tag{2.8}$$

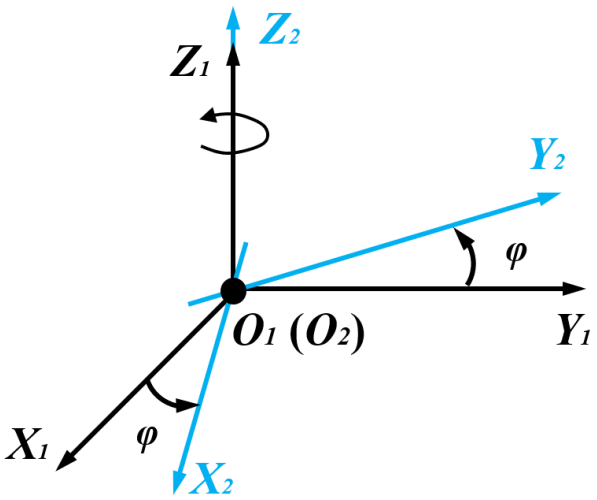

Figure 2-2. The second coordinate system (O_2-X_2, Y_2, Z_2) is obtained from the first coordinate system (O_1-X_1, Y_1, Z_1) by rotating an angle of φ around Z axis.

In Eq. (2.7), (x_2,y_2,z_2) is the coordinate of a point in the second coordinate system, whereas (x_1,y_1,z_1) is the coordinate of this same point but described in the first coordinate system.

If the rotation between two Cartesian coordinate systems (i.e., from (O_1-X_1, Y_1, Z_1) to (O_2-X_2, Y_2, Z_2)) is introduced only through Y axis for β degree (counterclockwise direction), then the relation between the two Cartesian coordinate systems can be written as:

$$\begin{pmatrix} x_2 \\ y_2 \\ z_2 \end{pmatrix} = \begin{pmatrix} \cos\beta & 0 & -\sin\beta \\ 0 & 1 & 0 \\ \sin\beta & 0 & \cos\beta \end{pmatrix} \begin{pmatrix} x_1 \\ y_1 \\ z_1 \end{pmatrix}. \tag{2.9}$$

Finally, when the geometric relation from the second coordinate system to the first coordinate system is the rotation around X axis for α degree (counterclockwise direction), then the relation between the two Cartesian coordinate systems can be written as:

$$\begin{pmatrix} x_2 \\ y_2 \\ z_2 \end{pmatrix} = \begin{pmatrix} 1 & 0 & 0 \\ 0 & \cos\alpha & \sin\alpha \\ 0 & -\sin\alpha & \cos\alpha \end{pmatrix} \begin{pmatrix} x_1 \\ y_1 \\ z_1 \end{pmatrix}. \tag{2.10}$$

Now, let us consider the coordinate system (O_1-X_1, Y_1, Z_1) is sequentially rotated to (O_2-X_2, Y_2, Z_2) by φ degree around Z axis, then β degree around Y axis, and finally α degree around X axis (these three rotations are all performed in a counterclockwise direction), we can establish the geometric relation between the two Cartesian coordinate systems as:

$$(x_2, y_2, z_2)^T = \boldsymbol{R} \cdot (x_1, y_1, z_1)^T, \tag{2.11}$$

where $\boldsymbol{R}$ is calculated as:

$$\boldsymbol{R} = \begin{pmatrix} \cos\beta\cos\varphi & \cos\beta\sin\varphi & -\sin\beta \\ -\cos\alpha\sin\varphi + \sin\alpha\sin\beta\cos\varphi & \cos\alpha\sin\varphi + \sin\alpha\sin\beta\cos\varphi & \sin\alpha\cos\beta \\ \sin\alpha\sin\varphi + \cos\alpha\sin\beta\cos\varphi & -\sin\alpha\cos\varphi + \cos\alpha\sin\beta\sin\varphi & \cos\alpha\cos\beta \end{pmatrix}. \tag{2.12}$$

The above relation reveals the coordinate system rotation between two different Cartesian coordinate systems. Nevertheless, apart from rotation, the coordinate system may also be shifted between different coordinate systems. The coordinate system shifting is shown by Figure 2-3, as we shift the first Cartesian coordinate

system (O_1-X_1, Y_1, Z_1) to the second Cartesian coordinate system (O_2-X_2, Y_2, Z_2) by vector $\boldsymbol{T}$=[t_x, t_y, t_z].

Then, the relation between the two Cartesian coordinate systems through vector $\boldsymbol{T}$ is given as:

$$(x_2, y_2, z_2) = (x_1 + t_x, y_1 + t_y, z_1 + t_z), \tag{2.13}$$

where (x_2,y_2,z_2) is the coordinate of a point in the second coordinate system, and (x_1,y_1,z_1) is the coordinate of this same point in the first coordinate system.

At last, if both rotation and shifting appear in coordinate system transformation, the transformation relation can be described by using a 4×4 matrix as:

$$\begin{pmatrix} x_2 \\ y_2 \\ z_2 \\ 1 \end{pmatrix} = \begin{pmatrix} \boldsymbol{R_{11}} & \boldsymbol{R_{12}} & \boldsymbol{R_{13}} & \boldsymbol{T_1} \\ \boldsymbol{R_{21}} & \boldsymbol{R_{22}} & \boldsymbol{R_{23}} & \boldsymbol{T_2} \\ \boldsymbol{R_{31}} & \boldsymbol{R_{32}} & \boldsymbol{R_{33}} & \boldsymbol{T_3} \\ 0 & 0 & 0 & 1 \end{pmatrix} \cdot \begin{pmatrix} x_1 \\ y_1 \\ z_1 \\ 1 \end{pmatrix}, \tag{2.14}$$

where terms $\boldsymbol{R_{ij}}$ (i=1,2,3; j=1,2,3) is equal to $\boldsymbol{R}$ in Eq. (2.12), and terms $\boldsymbol{T_m}$ is equal to vector $\boldsymbol{T}$. We entitle the whole coordinate system transformation matrix in Eq. (2.14) as $\boldsymbol{RT}$.

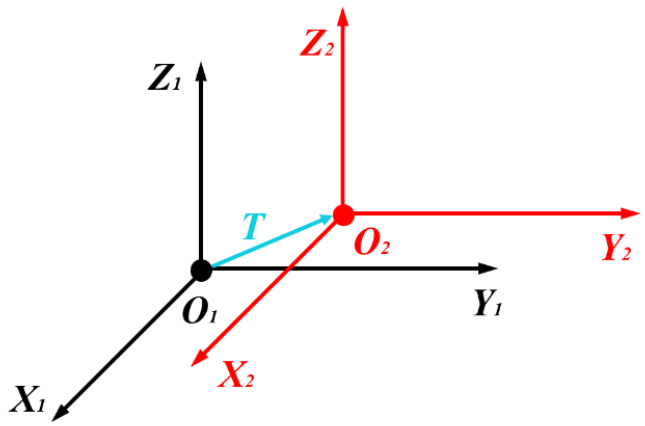

Figure 2-3. The second coordinate system (O_2-X_2, Y_2, Z_2) is obtained from the first coordinate system (O_1-X_1, Y_1, Z_1) by shifting with vector $\boldsymbol{T}$.

Note that the above-discussed coordinate transformation is performed from the first coordinate system (O_1-X_1, Y_1, Z_1) to the second coordinate system (O_2-X_2, Y_2, Z_2). Nevertheless, we also have to tackle with the inverse coordinate system transformation, because we need to transform from the second coordinate system (O_2-

X_2, Y_2, Z_2) to the first coordinate system (O_1-X_1, Y_1, Z_1). In this case, the inverse Cartesian coordinate system transformation can be performed by the following relation as:

$$\begin{pmatrix} x_1 \\ y_1 \\ z_1 \\ 1 \end{pmatrix} = \begin{pmatrix} \boldsymbol{R_{11}} & \boldsymbol{R_{12}} & \boldsymbol{R_{13}} & \boldsymbol{T_1} \\ \boldsymbol{R_{21}} & \boldsymbol{R_{22}} & \boldsymbol{R_{23}} & \boldsymbol{T_2} \\ \boldsymbol{R_{31}} & \boldsymbol{R_{32}} & \boldsymbol{R_{33}} & \boldsymbol{T_3} \\ 0 & 0 & 0 & 1 \end{pmatrix}^{-1} \cdot \begin{pmatrix} x_2 \\ y_2 \\ z_2 \\ 1 \end{pmatrix}, \tag{2.15}$$

where we simply use the inverse transformation matrix of $\boldsymbol{RT}^{-1}$. Here, as $\boldsymbol{RT}$ is a square matrix obtained from the real experimental measurement, the determinant of this matrix will almost never be zero, so we can always get the inverse matrix $\boldsymbol{RT}^{-1}$.

The above-discussed coordinate transformation is performed only between two coordinate systems. Nevertheless, in the real implementation, we may need to introduce several coordinate system transformations, and thus, we still need to investigate the coordinate system transformation among more coordinate systems. Such multi-coordinate system transformation is performed by sequentially transforming from the primary coordinate system to the final coordinate system using the coordinate system transformation matrix $\boldsymbol{RT}$. This process can be expressed by the following equation as:

$$\begin{pmatrix} x_n \\ y_n \\ z_n \\ 1 \end{pmatrix} = \boldsymbol{RT_n} \cdot \boldsymbol{RT_{n-1}} \cdot \ldots \cdot \boldsymbol{RT_2} \cdot \boldsymbol{RT}_1 \cdot \begin{pmatrix} x_1 \\ y_1 \\ z_1 \\ 1 \end{pmatrix}, \tag{2.16}$$

where term n means we transform the coordinate systems from the first coordinate system to the last coordinate system with n steps, and term $\boldsymbol{RT_n}$ is the transformation matrix corresponding to any transformation step.

2.3 Pinhole camera model

In structured light measurement systems, we use two cameras to capture the image and then perform inverse ray tracing or triangulation. Hence, we need to establish the mathematically model of the camera and describe the relation between the three-dimensional scene and the two-dimensional captured image. To mathematically define a camera, we express the camera with a pinhole camera model, which describes the

image formation as perspective projection from the three-dimensional space to the two-dimensional image plane.

For a digital camera, it contains an image receiver (i.e., charged-coupled device) and an objective lens. Here, the objective lens collects the light and then registers the intensity to the image receiving plane. However, the objective lens distortion will distort the received two-dimensional image and such distortion complicates the mathematical representation of the light projection. Therefore, we use a pinhole camera model, in which we regard the objective lens as a simple pinhole and no lenses are used to focus the light. In this case, the geometric lens distortion is totally avoided, and the light in the object space can only pass through this pinhole and finally reaches the image receiving plane. A simple diagram of a pinhole camera system is given below in Figure 2-4.

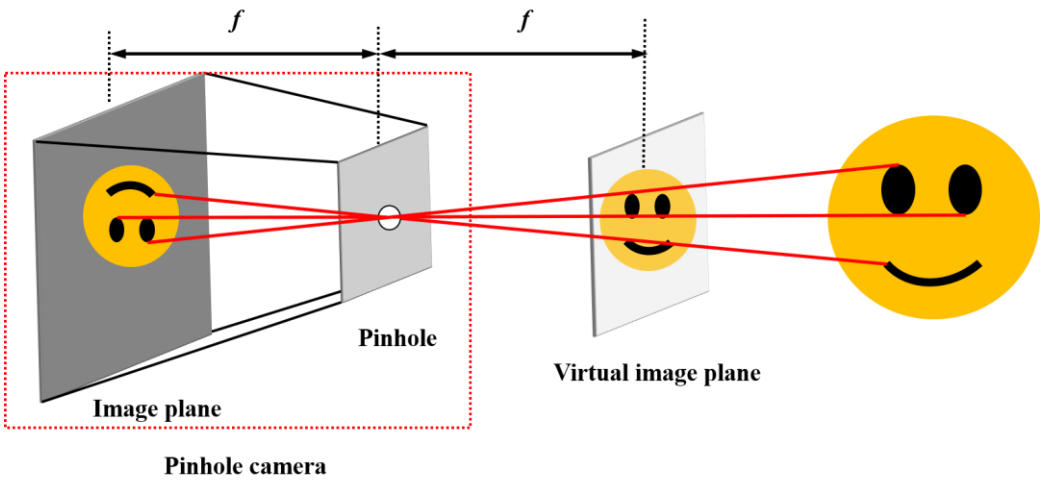

Figure 2-4. The diagram of a pinhole camera and the perspective projection.

In a pinhole camera (see Figure 2-4), the focal length f of this pinhole camera is defined as the focal length of the objective lens, and it is the distance from the image plane to the pinhole. The object is projected through this pinhole and then reaches the image receiving plane to forge an inverse image. Moreover, we also define another virtual image plane, which is parallel to the image receiving plane, to get the upright virtual image. This virtual image plane is located in front of the pinhole with a distance as f. Under this scenario, the sizes of the images in the image receiving plane and the virtual image plane are equal.

Once the pinhole camera scheme is fully described, we are also interested in mathematically defining the light projection model in a pinhole camera. To do so, let

us firstly define the camera pinhole as the coordinate system origin $\boldsymbol{O}$, the vector passing through the pinhole and being perpendicular to the image receiving plane is defined as Z axis (this is also referred as the optical axis), and this coordinate system follows a right hand distribution. Afterwards, we project the pinhole vertically to the image plane and this intersection point $\boldsymbol{R}$ (see Figure 2-5) is defined as the principle point.

Now, let us define one point $\boldsymbol{P}=(x,y,z)$ as the real object point in the pinhole camera coordinate in Figure 2-5. We project this point $\boldsymbol{P}$ from the object space through the pinhole to the image plane at $\boldsymbol{Q}=(x',y',z')$. Then, the geometric relation between point $\boldsymbol{P}$ and point $\boldsymbol{Q}$ can be mathematically calculated through similar triangles as:

$$x' = -f\frac{x}{z}, \tag{2.17}$$

$$y' = -f\frac{y}{z}. \tag{2.18}$$

From Eqs. (2.17) and (2.18), we can project one object point from the object space to the image receiving plane. Nevertheless, the inverse projection from the image receiving plane to the object space cannot give us the intersection point, because the distance in Z direction (i.e., term z in Eq. (2.17) or (2.18)) cannot be uniquely decided.

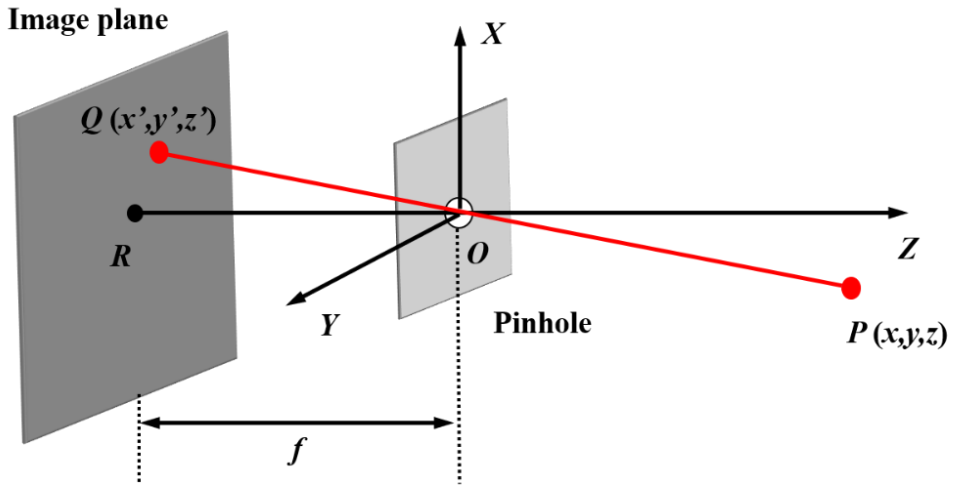

Figure 2-5. The geometry scheme of the pinhole camera and the perspective projection model.

The pinhole camera model and the light projection model are above-discussed. Nevertheless, the pinhole camera model cannot accurately describe the light projection in the real implementation, because lens distortion has not been considered. Therefore,

we have to introduce camera calibration to determine the lens distortion, and then we should introduce such distortion into the pinhole camera for a more comprehensive camera model. The camera calibration will be systematically discussed in Section 3.4.

2.4 Beam reflection model

The fundamental measurement principle of a stereoscopic phase measuring deflectometry system is the light reflection at the specular surface. Specifically, the light being projected to the specular surface is reflected to another direction, that the incident angel and the exit angel follow Reflection Law. Here, to mathematically describe the surface reflection, we establish a beam reflection model.

We initially establish a light-plane reflection model, that we assume the light is projected to a specular flat surface and later is reflected to another direction. The light in this case can be described by a line function as:

$$P_{\boldsymbol{A}} = \boldsymbol{V} \cdot t + \boldsymbol{A}\,, \tag{2.19}$$

where $\boldsymbol{V}$ is the normalized vector of this ray in a given coordinate system, $\boldsymbol{A}$ is a three-dimensional point along this ray in the same coordinate system, and t is an arbitrary real number.

On the other side, the specular plane surface can be presented as a set of point $\boldsymbol{P}$ from which,

$$(\boldsymbol{P} - \boldsymbol{P_0}) \cdot \boldsymbol{n} = 0\,, \tag{2.20}$$

where $\boldsymbol{n}$ is the normal of this plane surface, $\boldsymbol{P_0}$ is a point on this specular plane.

If the light ray and the specular surface are not parallel, then the intersection point $\boldsymbol{S}$ of the light and the plane can be calculated as:

$$\boldsymbol{S} = \boldsymbol{V}\frac{(\boldsymbol{P_0} - \boldsymbol{A}) \cdot \boldsymbol{n}}{\boldsymbol{V} \cdot \boldsymbol{n}} + \boldsymbol{A}\,. \tag{2.21}$$

By solving Eq. (2.21), we get the intersection point $\boldsymbol{S}$ between the incident light and the plane specular surface.

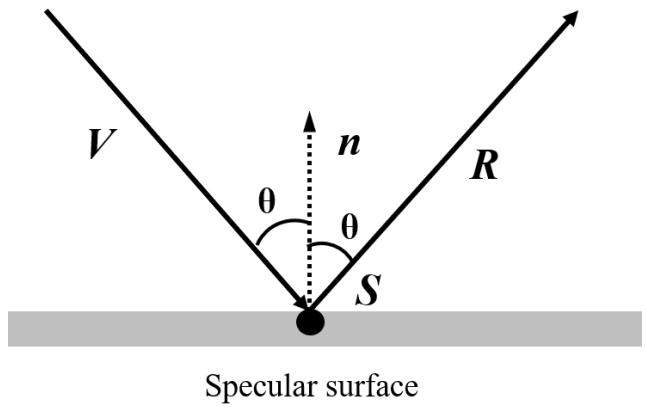

Figure 2-6. Geometric diagram of light reflection at the specular surface.

In the light reflection scheme, the vector of the reflected light is also necessary, so we calculate the vector of the reflection beam using the scheme described in Figure 2-6. Note that in Figure 2-6, the surface normal to the specular plane is $\boldsymbol{n}$, and the vector of the incident light is $\boldsymbol{V}$. Then, the reflected vector $\boldsymbol{R}$ can be calculated as:

$$\boldsymbol{R} = \boldsymbol{V} - 2(\boldsymbol{V} \cdot \boldsymbol{n})\boldsymbol{n} \,, \tag{2.22}$$

where $\boldsymbol{n}$ must be normalized.

The above-discussed reflection case enables us to calculate the reflected light by knowing the normal of the specular surface and the vector of the incident light. However, in the real deflectometry measurement, the surface normal is not given, but we have to use the incident light and the exit light to calculate this surface normal. Here, the normalized vector of the incident light is $\boldsymbol{V}$, and the normalized vector of the exit light is $\boldsymbol{R}$. Then, we have the surface normal calculated as:

$$\boldsymbol{N} = \boldsymbol{R} - \boldsymbol{V} \,. \tag{2.23}$$

Finally, by normalizing surface normal $\boldsymbol{N}$ in Eq. (2.23), we obtain the normalized surface normal as $\boldsymbol{n}$.

Chapter 3 Parameter calibration of stereoscopic camera based structured light measurement systems

This chapter describes the methods to calibrate all parameters that appear in the stereoscopic camera based structured light measurement systems. The structured light measurement systems studied in this thesis contain a stereoscopic phase measuring deflectometry (SPMD) system, a stereoscopic fringe projection profilometry (SFPP) system, and a stereoscopic deflectometry-profilometry hybrid (SDPH) system. Note that as SDPH is the combination of SPMD and SFPP, and it shares the same system parameters as the other two systems, so we will not discuss the parameter calibration of an SDPH system here.

In an SPMD system, it has an LCD screen to project the structured light patterns (i.e., sinusoidal fringe patterns), and two cameras to capture these sinusoidal fringe patterns (SFPs) reflected by the measured specular surface. The surface measurement is then performed by the inverse ray tracing between the stereoscopic camera and the LCD using phase map correspondence (this is to be discussed comprehensively in Chapter 4). Here, the phase maps in both cameras are obtained through phase shifting and phase unwrapping.

On the other hand, an SFPP system has a video projector and two cameras. The video projector provides the structured light patterns (i.e., SFPs) and the cameras are

used to capture the SFPs projected on the measured diffuser object. The surface reconstruction then is accomplished through geometric triangulation using the phase maps into both cameras. Again, the phase maps in an SFPP system are also obtained through phase shifting and phase unwrapping.

As sinusoidal fringe patterns (SFPs) are used in both stereoscopic phase measuring deflectometry and stereoscopic fringe projection profilometry, we firstly discuss in this chapter the sinusoidal fringe patterns, which are adopted into our system as structured light patterns. Next, a phase shifting method is discussed as it allows the acquisition of the phase map from the captured SFPs. However, the phase map obtained from phase shifting presents wrapped characteristic, and thus we introduce phase unwrapping techniques to further obtain the unwrapped phase map. In this case, both spatial phase unwrapping and temporal phase unwrapping are discussed, and temporal phase unwrapping is finally chosen to perform phase unwrapping.

Once the continuous unwrapped phase map is obtained, we then focus on system component calibration. For system component calibration, we preliminary explain camera calibration and we obtain camera intrinsic parameters, camera extrinsic parameters and the geometric relation between the stereoscopic camera. Afterwards, we discuss the projection components calibration, such as LCD screen calibration in the SPMD system and video projector calibration in the SFPP system. Here, both elements show projection intensity nonlinearity which is referred as gamma effect. We then construct an inverse look up table (LUT) to compensate the gamma error.

Finally, the geometric calibrations of both the SPMD system and the SFPP system are presented. Here, SFPP system calibration is more flexible, as we only have to obtain the geometric relation between the stereoscopic camera. Nevertheless, SPMD system calibration is more complicated. In particular, we discuss the system geometric positioning limitation, so that we can define the separation distance between the stereoscopic camera. What is more, we also calibrate the geometric position relation between the LCD screen and the stereoscopic camera. To do so, we combine an “inverse” camera calibration with a laser tracker-assisted hand-eye calibration.

3.1 Fundamentals of sinusoidal fringe pattern

In order to perform surface shape measurement, the correspondence between the image receiver (i.e., the stereoscopic camera) and the projection component (i.e., the LCD or the video projector) has to be established. For instance, in a stereoscopic fringe projection profilometry system, the point correspondence between the stereoscopic camera (that we know one point in the first camera image plane and its correspondent point in the second camera image plane) has to be determined, so that we can perform geometric triangulation for surface point determination. In a stereoscopic phase measuring deflectometry system, we construct the point correspondence between the LCD and the cameras, so that we can accomplish the inverse ray tracing for surface normal calculation. To establish such correspondence in either an SFPP system or an SPMD system, structured light patterns are generated on the projection components and later being captured by the cameras. The most commonly used structured light patterns are binary pattern and sinusoidal fringe pattern.

Binary pattern is a straightforward approach to establish the point correspondence. Particularly, binary values (i.e., intensities as 0 and 1) are encoded into each stripe in the projection patterns. These stripes are presented horizontally or vertically in each pattern. Afterwards, by implementing a binary coding strategy [83], the correspondence is established through a sequential projection. For instance, one can distinguish one unique pixel among a total of 1024 pixels with 10 binary projections (i.e., $1024 = 2^{10}$). To reduce the total number of the binary projection, gray coding pattern [84] is suggested by using the same binary pattern principle. In this case, instead of implementing only a binary bit as either 0 or 1, we can introduce M distinct levels to expand the coding flexibility. For instance, if we select the distinct level M as 4, we can distinguish a unique point from a total of 1024 pixels with only 5 projections (i.e., $1024 = 4^5$). Compared to binary pattern, gray coded pattern demonstrates the advantage in reducing the projection pattern number, so it guarantees a greater robustness and a higher efficiency. Nevertheless, both binary pattern and gray pattern are not favored by structured light systems as they fail to give a high spatial resolution. Moreover, binary pattern cannot be used to perform sub-pixel matching (this is to be discussed in Section 4.3), which is critical in enhancing the surface measurement accuracy.

Under this scenario, the more appropriate sinusoidal fringe pattern (SFP) is proposed to overcome the limitation of the binary pattern. The major difference

between the SFP and the binary coding pattern is that SFP is coded by the phase value rather than the binary intensity. Hence, the intensity at each pixel in an SFP pattern is represented by Eq. (3.1),

$$I_n(x,y) = \frac{I_{\max}}{2}\left(1 + \sin\left(\Phi(x,y) + \frac{2\pi(n-1)}{N}\right)\right), \quad n = 1, \ldots, N, \tag{3.1}$$

where $I_n(x,y)$ is the intensity of a pixel in the sinusoidal fringe pattern, and I_{max} is the maximum intensity in the bitmaps. $\Phi(x,y)$ is the absolute unwrapped phase value at a projecting pixel, and N is the total phase shifting step number. Here, the phase map can be calculated by phase shifting the sinusoidal fringe patterns by N steps (this is to be discussed in Section 3.2).

Now, we project this SFP on the measured object, the sinusoidal intensity distribution is distorted by the tested object and we can write this distorted sinusoidal fringe pattern captured by the camera as:

$$I_n(i,j) = A(i,j) + B(i,j)\sin\left(\Phi(i,j) + \frac{2\pi(n-1)}{N}\right), \quad n = 1, \ldots, N, \tag{3.2}$$

where (i,j) is the pixel coordinate into the camera image plane, and $I_n(i,j)$ is the intensity of a pixel on the camera image plane. $A(i,j)$ is the average intensity determined by the background illumination, $B(i,j)$ is the intensity modulation related to the surface reflectivity and pattern contrast. Here, both $A(i,j)$ and $B(i,j)$ do not depend on the phase shifting term N.

Moreover, in a stereoscopic phase measuring deflectometry system, the camera is focused at the measured specular surface rather than the LCD screen for a better spatial resolution. Thus, the SFP on the LCD screen is defocused and blurred in the camera, and such defocusing is equivalent to a low pass filter. Nevertheless, as the SFP only has one single frequency (i.e., Eq. (3.2)), it is free of any information transmission reduction even though it passes through a low pass filter. In other words, camera defocusing (i.e., the low pass filtering) only reduces the amplitude of the SFP, but it cannot change the phase value coded into the SFP. Hence, this characteristic is favored by structured light measurement systems, as it will provide an accurate phase pair correspondence regardless of defocusing.

3.2 Phase shifting method

In the previous section, we demonstrate the benefit of using sinusoidal fringe patterns (SFPs) as they maintain the correct phase information even though the SFPs are defocused in the camera. In this section, we will discuss phase shifting to obtain the phase information on the measured object from the captured SFPs.

To perform phase shifting, a series of SFPs with the same frequency are sequentially projected to the measured surface and the captured SFPs on the surface can be represented by Eq. (3.2). Now, let us assume we project four different SFPs and the phase value shifted within each adjoining fringe pattern is $\pi/2$ (i.e., $N = 4$ in Eq. (3.2)), then these four fringe patterns are given as:

$$I_1(i,j) = A(i,j) + B(i,j)\sin(\Phi(i,j)), \tag{3.3}$$

$$I_2(i,j) = A(i,j) + B(i,j)\cos(\Phi(i,j)), \tag{3.4}$$

$$I_3(i,j) = A(i,j) - B(i,j)\sin(\Phi(i,j)), \tag{3.5}$$

$$I_4(i,j) = A(i,j) - B(i,j)\cos(\Phi(i,j)). \tag{3.6}$$

By processing these four SFPs, we can calculate the wrapped phase as:

$$\varphi(i,j) = \arctan\left(\frac{I_1(i,j) - I_3(i,j)}{I_2(i,j) - I_4(i,j)}\right), \tag{3.7}$$

where the arctangent function is defined below as:

$$\arctan\left(\frac{p}{q}\right) = \begin{cases} \arctan\left(\dfrac{p}{q}\right), & \text{if } q \geq 0 \\ \arctan\left(-\left|\dfrac{p}{q}\right|\right) + \pi, & \text{if } q < 0 \text{ and } p \geq 0 \\ \arctan\left(\left|\dfrac{p}{q}\right|\right) - \pi, & \text{if } q < 0 \text{ and } p < 0 \end{cases}. \tag{3.8}$$

At this moment, we need to emphasize that such calculated phase term $\varphi(i,j)$ is different from the real phase value $\Phi(i,j)$ in the sinusoidal fringe patterns. In Eq. (3.2), the phase value $\Phi(i,j)$ is a continuous real phase that its range is not limited to [-π,π]. However, in Eq. (3.8), the phase value $\varphi(i,j)$ is determined through an arctangent function, from which its range is limited to [-π,π]. Thus, the relation between the wrapped phase $\varphi(i,j)$ and the unwrapped phase $\Phi(i,j)$ is defined by the following equation:

$$\varphi(i,j) = \mathrm{mod}(\Phi(i,j), 2\pi)\,, \tag{3.9}$$

where term "*mod*" means the phase modulation of 2π. The phase unwrapping methods will be further reviewed in the next section.

Apart from four-step phase shifting, other phase shifting methods are also discussed such as three-step phase shifting [85, 86] or five-step phase shifting [87]. Even though they adopt different steps, they use a same universal phase shifting principle, and thus, the wrapped phase map can be calculated through:

$$\varphi(i,j) = \arctan\left(\frac{\sum_{n=1}^{N}\left[I_n(i,j)\cos(2\pi\,\frac{n-1}{N})\right]}{\sum_{n=1}^{N}\left[I_n(i,j)\sin(2\pi\,\frac{n-1}{N})\right]}\right). \tag{3.10}$$

To perform phase shifting, we have to introduce at least three SFP steps (i.e., $N = 3$). However, three-step phase shifting is susceptible to noise, so phase shifting with more steps is desired. On the other hand, more phase shifting steps will extend the measurement time, and thus reduce the measurement efficiency. Under this scenario, the trade-off between phase shifting accuracy and efficiency has to be considered before the measurement. In this work, we use four steps to perform phase shifting.

Phase shifting can be accomplished by projecting the sinusoidal fringe pattern series and then performing the calculation through Eq. (3.10). However, in the real implementation, gamma nonlinearity, pixel quantization, and temporal fluctuation of the projection components restrict us from obtaining ideal SFPs. Thus, phase shifting error could be introduced by such imperfect SFPs. Under this scenario, the imperfection of the SFPs has to be eliminated to minimize the phase shifting error. The SFP error elimination with respect to the above-mentioned three aspects are discussed below.

To eliminate the SFP error originated from gamma nonlinearity, we have to firstly introduce the gamma effect. Gamma nonlinearity is described as the output intensity is not following a linear relation with the input gray level in a projection component. Such characteristic is broadly applied into the projection components such as televisions or video projectors to fit the human vision perception, but it introduces luminance error if we receive these images with a digital receiver such as a CCD. Thus, gamma nonlinearity has to be corrected if we want to get a correct phase shifted pattern. In this case, we can either adopt an analytical compensation during phase shifting [88], or we can directly introduce gamma calibration to the projection

components. In this work, we select direct gamma calibration rather than analytical compensation, because direct gamma calibration is more universal, and this method is later presented in Section 3.5. Once we have performed the gamma calibration, the projection component can be used to correctly present any sinusoidal fringe pattern.

Pixel quantization is another problem that occurs during phase shifting. For instance, we can calculate a precise intensity distribution from Eq. (3.1), but in the real implementation, the video projector or the LCD rather gives us the quantified intensity as any intensity are quantified to a positive integer (i.e., intensity as 14.56 is quantified to intensity as 15). To compensate this quantization error, a characteristic polynomial method [89, 90] can be used. Nevertheless, if the input signal covers the complete gray level range (i.e., 8 bits, 0 to 255), the quantization effect can be greatly reduced [89, 90]. Moreover, as we will perform sub-pixel interpolation (see Section 4.3) during the measurement, quantization error can be neglected.

Temporal fluctuation effect in the projection components is always neglected during phase shifting. Indeed, by modeling the projecting frequency of the projection component equal to the receiving frequency of the image receiver, we can reduce the pattern fluctuations and obtain an accurate phase shifting. However, fluctuations still exist especially when we use the liquid crystal (LC) molecule based phase modulation projections (i.e., LCD screen or LCD chip-based video projector) [91]. To eliminate the fluctuations introduced by LC molecular flicker, we can average numerous frames. However, this is definitely extending the measurement time, and thus, the trade-off between the measurement accuracy and efficiency has to be considered. In this work, as we focus on the measurement accuracy, we adopt a fringe averaging method during the measurement.

3.3 Phase unwrapping method

In Section 3.2, we discuss the phase shifting method to obtain the phase map from sinusoidal fringe patterns. Unfortunately, as phase shifting only provides the phase value ranging from [-π, π], the real phase value cannot be obtained but it is rather shown as a discontinuous wrapped phase map. In this case, such discontinuous phase map shows the “phase jump” at any discontinuous boundary such as the example provided in Figure 3-1. Figure 3-1 shows the phase maps on a flat mirror we later obtained through phase shifting from the experimental measurement. In Figure 3-1 (a), we can easily find the phase jump, and the phase value is only ranging within [-

π, π]. In Figure 3-1 (b), we give the unwrapped phase map of Figure 3-1 (a), and it shows a continuous phase map after phase unwrapping. To perform phase unwrapping and obtain the continuous phase map, two different methods as spatial phase unwrapping and temporal phase unwrapping are discussed.

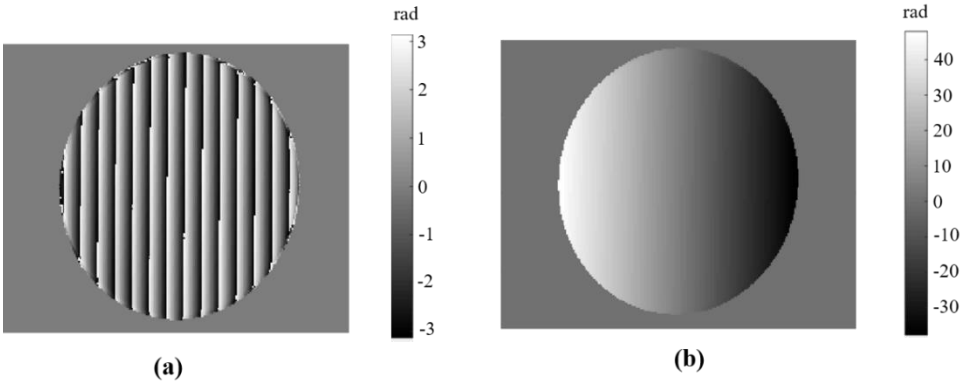

Figure 3-1. The phase maps on a flat mirror: (a) the wrapped phase map, and (b) the unwrapped continuous phase map.

3.3.1 Spatial phase unwrapping

Spatial phase unwrapping is a direct phase unwrapping method based on spatial phase jump distribution [92]. To perform spatial phase unwrapping, we firstly get the wrapped phase map using phase shifting technique. Later, the phase discontinuity is examined through the whole wrapped phase map, so we acquire all phase jump points. From these phase jump points, we can further regulate the whole wrapped phase map to numerous phase sections where any adjacent section shares a phase modulation as 2π. Later, we add an integer multiple of 2π to these phase sections so that we can finally get a continuous phase map. Note that this compensated phase map in fact still cannot represent the real phase map, as there appears a constant phase difference between the real phase map and this unwrapped phase map. Therefore, to obtain the real phase map, a reference point with its phase value known is mandatory. To perform spatial phase unwrapping with higher precision, different algorithms are proposed such as quality-guided algorithm [93], minimum weight discontinuity algorithm [94], and minimum L^P-norm algorithm [95].

However, all spatial phase unwrapping methods face a great limitation as they find difficulty in unwrapping discontinuous objects. For instance, a discontinuous object can be assumed as several isolated sub-sections, and we can obtain the wrapped phase

maps corresponding to each sub-section by phase shifting. Later, by using spatial phase unwrapping, the absolute unwrapped phase map of any sub-section can be calculated. Unfortunately, as the internal phase relation between each isolated sub-section is not obtainable, we cannot obtain the correct phase relation between each sub-section. Therefore, the accurate phase map for the whole discontinuous object cannot be obtained. In particular, as we will measure a specular-diffuser hybrid object in this work (see Chapter 7) and it introduces discontinuous sections, we will not use spatial phase unwrapping in this thesis.

3.3.2 Temporal phase unwrapping

Temporal phase unwrapping is another phase unwrapping technique which is accomplished by sequentially projecting sinusoidal fringe patterns with different frequencies [96, 97]. In temporal phase unwrapping, the knowledge between each adjacent phase jump point is not mandatory, and thus, phase unwrapping for a discontinuous object can be performed. What is more, temporal phase unwrapping directly gives us the absolute phase value, so we no longer need a reference phase point to determine the constant phase difference between the real phase map and the unwrapped phase map.

The main principle of temporal phase unwrapping is to project more than one series of sinusoidal fringe patterns to the measured object. Specifically, these different SFP series are distinguished by implementing distinct fringe frequencies. In these series, the lowest frequency SFP series should demonstrate no phase jump once we perform phase shifting. Later, we use this lowest frequency phase map to gradually unwrap the other phase maps with different frequencies. In this case, we sequentially unwrap from low frequency to high frequency. For instance, assume that we have three SFP series, and their frequencies are f_L, f_M, f_H, respectively. Here, f_L refers to the lowest frequency (i.e., the wrapped phase map of this series does not show phase jumps), f_M represents the middle frequency and f_H represents the highest frequency. Moreover, the fringe wavelengths of the sinusoidal fringe patterns corresponding to these three frequencies are given as λ_L, λ_M, λ_H; and their absolute unwrapped phase maps are $\Phi_L(i,j)$, $\Phi_M(i,j)$, $\Phi_H(i,j)$. Here, (i,j) denotes the pixel coordinate in the camera image plane. Giving the characteristic of the sinusoidal fringe pattern, we can easily deduce that the unwrapped phase maps between the lowest frequency fringe patterns and the middle frequency fringe patterns obey the following relationship:

$$\Phi_M(i,j) = (\lambda_L / \lambda_M)\Phi_L(i,j)\,, \tag{3.11}$$

where $\Phi_L(i,j)$ ranges within $[-\pi,\pi]$.

Now, let us focus only on the lowest frequency SFP series and the middle frequency SFP series. Considering that the phase jump is 2π, we can establish the relation between the unwrapped phase and the wrapped phase within the lowest frequency fringe patterns and the middle frequency fringe patterns as below:

$$\begin{cases} \Phi_M(i,j) = \varphi_M(i,j) + 2\pi K_M(i,j) \\ \Phi_L(i,j) = \varphi_L(i,j) + 2\pi K_L(i,j) \end{cases}, \tag{3.12}$$

where $\varphi_M(i,j)$ and $\varphi_L(i,j)$ represent the wrapped phase maps corresponding to the lowest frequency and the middle frequency, $K_M(i,j)$ and $K_L(i,j)$ are integers. In particular, as we have mentioned that the lowest phase map is free of phase jump, so in fact $K_L(i,j)$ is 0. Now, we combine Eq. (3.11) and Eq. (3.12) together, we can calculate the integer K_M as:

$$K_M(i,j) = Round\left[\frac{(\lambda_L / \lambda_M)\varphi_L(i,j) - \varphi_M(i,j)}{2\pi}\right], \tag{3.13}$$

where "*Round*" means we take the closest integer. Finally, as we obtain the integers $K_M(i,j)$ to all pixels in the middle frequency phase map, we can then calculate the unwrapped phase map with respect to the middle frequency sinusoidal fringe patterns with Eq. (3.12).

Once we get the unwrapped phase map that corresponds to the middle frequency SFP series, we can then use this middle frequency phase map to unwrap the highest frequency phase map of $\Phi_H(i,j)$. Similar to Eq. (3.11), we can write the unwrapped phase relationship between the middle frequency fringe patterns and the highest frequency fringe patterns as:

$$\Phi_H(i,j) = (\lambda_M / \lambda_H)\Phi_M(i,j)\,. \tag{3.14}$$

We can also give the relation between the unwrapped phase map and the wrapped phase map that corresponds to the highest frequency fringe patterns as:

$$\Phi_H(i,j) = \varphi_H(i,j) + 2\pi K_H(i,j)\,, \tag{3.15}$$

where $\varphi_H(i,j)$ denotes the wrapped phase maps of the highest frequency fringe patterns, and $K_H(i,j)$ is an integer. At this moment, note that the unwrapped phase

map $\Phi_M(i,j)$ is already calculated by Eq. (3.12), we can then directly combine Eq. (3.14) and Eq. (3.15) together to get the integer $K_H(i,j)$ as:

$$K_H(i,j) = Round\left[\frac{(\lambda_M/\lambda_H)\Phi_M(i,j) - \varphi_H(i,j)}{2\pi}\right]. \tag{3.16}$$

Once $K_H(i,j)$ is calculated, the phase map of the sinusoidal fringe patterns with respect to the highest frequency is determined.

The above-discussed temporal phase unwrapping method can be implemented by introducing more frequencies, and this is the Huntley method [96, 97]. By increasing the number of the frequency of SFPs, we can further enhance the phase unwrapping robustness. However, by projecting more SFPs, we need longer measurement time, and thus the measurement efficiency is decreased. On the other hand, we can also decrease the number of the frequency by only using two frequencies for phase unwrapping [98, 99]. This two frequencies method provides a high measurement efficiency as less patterns have to be projected. However, it may bring potential problems in the real implementation. For instance, if the frequencies between the lowest frequency SFPs and the high frequency SFPs vary greatly, the phase unwrapping accuracy is easily deteriorated by the intensity noise coming from the camera sensor or projection components (i.e., the LCD screen or the video projector).

Apart from multi-frequency temporal phase unwrapping, multi-wavelength method [99, 100] or binary coding method [101, 102] are also suggested to perform temporal phase unwrapping. Nevertheless, multi-wavelength unwrapping presents a weaker phase unwrapping reliability compared to multi-frequency unwrapping [103]. Binary coding method is a well-studied phase unwrapping method, but it obviously cannot provide a better resolution than sinusoidal fringe patterns [104]. What is more, optical defocusing introduces blur to the binary patterns, and this will unavoidable introduce phase unwrapping error [105].

At this time, a complete procedure to obtain the unwrapped phase map by temporal phase unwrapping is demonstrated. First of all, we project three series of sinusoidal fringe patterns with different frequencies to the measured surface. Next, we use both cameras to capture these SFPs on the measured object. Afterwards, we use four-step phase shifting method to calculate the wrapped phase maps with respect to these three different frequencies. Finally, as we get these three different wrapped phase maps with respect to all sinusoidal fringe pattern series, we implement temporal phase

unwrapping to unwrap the phase maps from the lowest frequency to the highest frequency until we acquire the unwrapped phase map.

3.4 Camera calibration

In the previous three sections, we discuss the methods to obtain the absolute unwrapped phase map. Therefore, we can establish the phase correspondence between the camera and the projection components. However, by only getting unwrapped phase maps is not sufficient to perform the surface point determination, because we also have to know the geometric scheme of the structured light measurement systems. Under this scenario, a system calibration has to be introduced. Specifically, to perform a complete system calibration, we need to calibrate the cameras, the projection components (i.e., the LCD or the video projector), and the geometric relation between the cameras and the projection components, respectively. In this section, we will focus on camera parameter calibration.

3.4.1 Camera parameter calibration

The cameras implemented in the structured light measurement systems are used to capture the distorted sinusoidal fringe patterns. In this case, the light reflected by the surface enters the camera from its optical lens system. To simplify the light projection, we assumed a pinhole camera (see Chapter 2), from which the camera optical center is regarded as a small pinhole and the light projecting through this pinhole follows the collinearity principle. The pinhole camera gives us the specific camera parameters, such as the focal length of the pinhole camera, and the image center. However, a pinhole camera cannot precisely describe the camera used in the real implementation, as optical distortion introduced by the optical lens system is not known. Thus, to obtain the parameters of a real camera, these above-mentioned parameters (i.e., optical distortion, focal length, principle point) should be calibrated and they are entitled as intrinsic parameters. Apart from these camera intrinsic parameters which demonstrate the camera characteristics, we also have to determine the 3D spatial position and orientation of the camera to the calibration target coordinate system (i.e., in camera calibration, the calibration target is a checkerboard). The geometric relation between the camera coordinate system and the calibration target coordinate system is referred as extrinsic parameters. In this case,

extrinsic parameters consist of two parameters as camera rotation and camera shifting between the camera coordinate system and the calibration target coordinate system.

To acquire the intrinsic and the extrinsic parameters of a camera through camera calibration, we apply the already well-established camera model and its corresponding camera calibration procedure [106, 107]. The experimental calibration is accomplished by directly using Camera Calibration Toolbox developed by Jean-Yves Bouguet [108]. Here, we select the binary square checkerboard pattern as the calibration target to perform camera calibration. In particular, we firstly place the camera at a fixed position where it can capture the checkerboard. Secondly, we change the checkerboard to different positions by implementing both spatial shifting and rotation. Now, within each changed position, we use the camera to capture a corresponding checkerboard image. Here, we want to note that a great number of checkerboard movement is required to guarantee the calibration accuracy (i.e., normally greater than 20 images). Thirdly, once we register all checkerboard images with respect to each spatial position, we extract all grid corners on the checkerboard pattern within each frame and store these grid patterns for further analysis. Finally, nonlinear estimation is used to extract both the intrinsic and the extrinsic parameters [106] using the previously stored grid corner information.

After we perform the camera calibration, three intrinsic parameters are obtained. The principle point (u_0, v_0) is defined with the unit of CCD pixel size, and it represents the intersection of the camera optical axis and the camera image plane (i.e., CCD panel). The focal lengths of the camera lens are given in both X and Y directions of the camera coordinate system, and they are represented with the unit of pixel size as f_x and f_y, respectively. The camera distortion is presented by a vector as $[k_1, k_2, k_3, k_4, k_5]$ [109], from which k_1, k_2, k_3 are used to express radial distortion, and k_4, k_5 for tangential distortion. Hence, we can write the relation between a distorted projection point and its corresponding ideal projection point on the camera image plane as:

$$\begin{pmatrix} x_d \\ y_d \end{pmatrix} = (1 + k_1 r^2 + k_2 r^4 + k_3 r^6) \cdot \begin{pmatrix} x_o \\ y_o \end{pmatrix} + \begin{pmatrix} 2k_4 x_o y_o + k_5 (r^2 + 2{x_o}^2) \\ k_4 (r^2 + 2{y_o}^2) + 2k_5 x_o y_o \end{pmatrix}, \tag{3.17}$$

where (x_o, y_o) is the undistorted position of a point in the image plane, whereas (x_d, y_d) is the distorted position of this point in the image plane. Here, we would like to note that point (x_o, y_o) is normalized by Eqs. (3.18) and (3.19), as (x, y, z) represents this same undistorted point but it is depicted in the camera coordinate system by:

$$x_o = \frac{x}{z}, \tag{3.18}$$

$$y_o = \frac{y}{z}. \tag{3.19}$$

Finally, term r in Eq. (3.17) is calculated as:

$$r^2 = {x_o}^2 + {y_o}^2 . \tag{3.20}$$

We also want to mention that another normally discussed intrinsic parameter as skew factor is ignored in our calibration. This is because the deviation between X and Y axes is almost 90 degree in our camera, which leads to the skewness extremely close to zero.

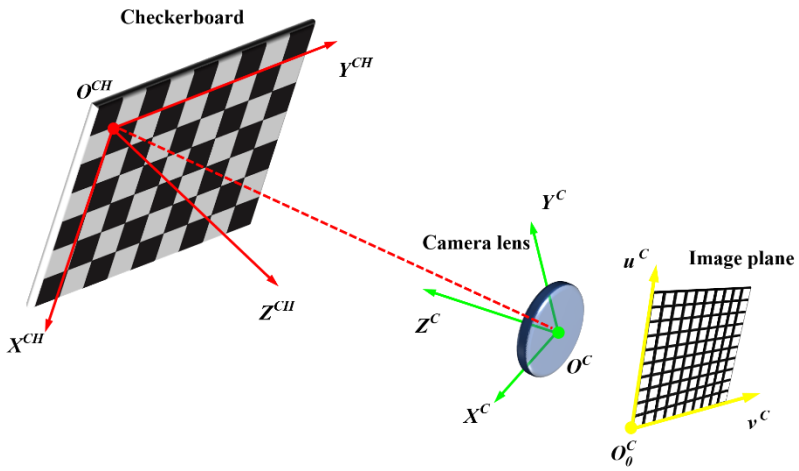

Figure 3-2. The coordinate transformation scheme between the checkerboard coordinate system and the camera coordinate system.

At this moment, all intrinsic parameters are obtained through camera calibration. We then discuss the extrinsic parameter calibration. As it is previously discussed, extrinsic parameters are given as a rotation matrix and a shifting vector between the camera coordinate system and the checkerboard coordinate system. For the checkerboard used in the camera calibration, the checkerboard coordinate origin is defined at the upper left corner grid intersection of the checkerboard pattern, and its X-Y plane is parallel to the checkerboard plane. We present the coordinate system transformation between the checkerboard coordinate system and the camera coordinate system in Figure 3-2, from which the checkerboard coordinate system is denoted as (O^{CH}-X^{CH}, Y^{CH},Z^{CH}), the camera coordinate system is denoted as (O^C-X^C, Y^C,Z^C), and the image plane coordinate system is ($O_0{}^C$-u^C,v^C).

By using the same Bouguet Calibration Toolbox [108], we obtain a 3×3 matrix $\boldsymbol{R_{CHtC}}$ and a 1×3 vector $\boldsymbol{T_{CHtC}}$, from which $\boldsymbol{R_{CHtC}}$ describes the rotation from the checkerboard coordinate system to the camera coordinate system, and $\boldsymbol{T_{CHtC}}$ determines the shifting in the same direction. Note that as we use numerous frames to perform the camera calibration and we move the checkerboard to different positions, we obtain distinct $\boldsymbol{R_{CHtC}}$ and $\boldsymbol{T_{CHtC}}$ with respect to each checkerboard location. In a given checkerboard frame, we assume one point in the checkerboard coordinate system as (x^{CH},y^{CH},z^{CH}) and this point in the camera coordinate system as (x^{C},y^{C},z^{C}), then we can transform this point from the checkerboard coordinate system to the camera coordinate system by:

$$(x^{C},y^{C},z^{C})^{T} = \boldsymbol{R_{CHtC}} \cdot (x^{CH},y^{CH},z^{CH})^{T} + \boldsymbol{T_{CHtC}}\,, \tag{3.21}$$

where $\boldsymbol{R_{CHtC}}$ and $\boldsymbol{T_{CHtC}}$ are the rotation matrix and the shifting vector, respectively.

3.4.2 Stereoscopic camera calibration

From camera calibration, we can obtain both intrinsic and extrinsic parameters of a single camera. However, into our structured light measurement systems, we introduce stereoscopic camera to perform the measurement, and thus, the geometric relation between these two cameras also has to be acquired. Here, such geometric relation denotes the three-dimensional shifting and rotation of any point from the second camera coordinate system to the first camera coordinate system. Such transformation can be mathematically represented below as:

$$\boldsymbol{P_1} = \boldsymbol{R_{C2tC1}} \cdot \boldsymbol{P}_2 + \boldsymbol{T_{C2tC1}}\,, \tag{3.22}$$

where $\boldsymbol{R_{C2tC1}}$ is the 3×3 rotation matrix from the second camera coordinate system to the first camera coordinate system, and $\boldsymbol{T_{C2tC1}}$ is the corresponding 1×3 shifting vector. $\boldsymbol{P_2}$ is the coordinate of point $\boldsymbol{P}$ defined in the second camera coordinate system. $\boldsymbol{P_1}$, on the other hand, is the coordinate of the same point $\boldsymbol{P}$ but is represented in the first camera coordinate system. Finally, to obtain both $\boldsymbol{R_{C2tC1}}$ and $\boldsymbol{T_{C2tC1}}$, we also use the already well-established Camera Calibration Toolbox [108].

To perform stereoscopic camera calibration, we place both cameras properly so that they can inspect the checkerboard from their own perspectives. The stereoscopic camera calibration scheme is given in Figure 3-3, where $\boldsymbol{P}$ is a point in the object space. What is more, the checkerboard coordinate system is denoted as (O^{CH}-

X^{CH}, Y^{CH}, Z^{CH}), the first camera coordinate system is denoted as (O_1^C-X_1^C, Y_1^C, Z_1^C) and the second camera coordinate system is (O_2^C-X_2^C, Y_2^C, Z_2^C).

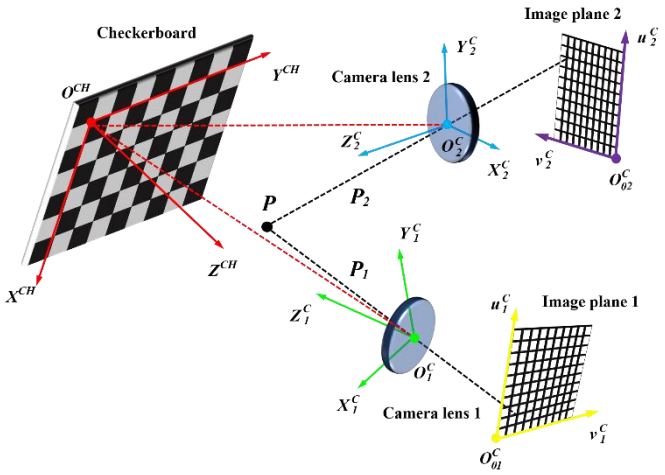

Figure 3-3. The stereoscopic camera calibration scheme using a checkerboard pattern.

In this case, both cameras inspect the checkerboard but from different perspectives, so the checkerboard images captured by these two cameras are distinct. Later, we change the spatial position of the checkerboard, so we capture a series of checkerboard images within each camera. Afterwards, the checkerboard grid intersection pattern of each frame are extracted within both cameras. Finally, by adopting a generalized least-squares algorithm [110], we can determine the stereoscopic camera calibration parameters (i.e., $\boldsymbol{R}_{C2tC1}$ and $\boldsymbol{T}_{C2tC1}$) using all checkerboard grid patterns in these two cameras.

3.4.3 Pinhole camera with lens distortion

To calibrate a camera, we assumed a pinhole camera model with lens distortion, and such pinhole camera model can accurately describe the cameras used in the real implementation. In this sub-section, we thoroughly discuss the light projection in such lens distortion contained pinhole camera. To be more specific, we mathematically establish a light projection model, from which it shows how a given point in the object space is finally imaged to the camera image plane (i.e., CCD panel). Moreover, as the real implementation rather requires the inverse light projection (that we know the pixel location on the CCD panel and we want to know its inverse projection vector to the object space), we also depict the inverse light projection in a pinhole camera.

To describe the light projection in a pinhole camera, we assume that the intrinsic and the extrinsic parameters of this pinhole camera are already obtained. Under this scenario, we generalize light projection into four sequential steps and the light projection scheme is depicted in Figure 3-4. Firstly, we transform the studied point $\boldsymbol{M}$ from the world coordinate system (i.e., object space) to the camera coordinate system. Here, to ease the computational complexity, we directly regard the checkerboard as the world coordinate system (i.e., see (O^W-X^W,Y^W,Z^W) in Figure 3-4), and the world coordinate system origin coincides with the checkerboard coordinate system origin. Then, the transformation of point $\boldsymbol{M}$ from the world coordinate system to the camera coordinate system (see (O^C-X^C,Y^C,Z^C) in Figure 3-4) can be expressed as:

$$({x_M}^C, {y_M}^C, {z_M}^C)^T = \boldsymbol{R_{WtC}} \cdot ({x_M}^W, {y_M}^W, {z_M}^W)^T + \boldsymbol{T_{WtC}}, \tag{3.23}$$

where $({x_M}^W, {y_M}^W, {z_M}^W)$ and $({x_M}^C, {y_M}^C, {z_M}^C)$ are the coordinates of point $\boldsymbol{M}$ in the world coordinate system and the camera coordinate system, respectively. $\boldsymbol{R_{WtC}}$ and $\boldsymbol{T_{WtC}}$ are the rotation matrix and the shifting vector that we can obtain from camera extrinsic calibration (by using the checkerboard shown in Figure 3-4).

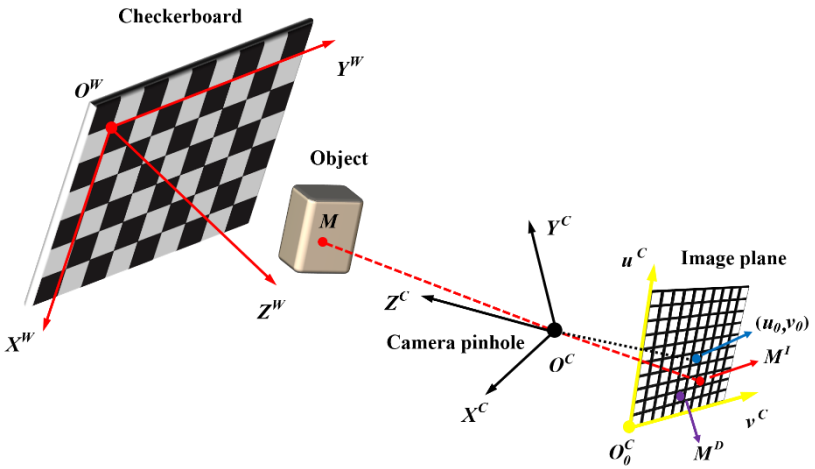

Figure 3-4. Light projection scheme using a pinhole camera model. $\boldsymbol{M}$ is the studied point in the object space, (O^W-X^W,Y^W,Z^W) is the world coordinate system, $\boldsymbol{O_C}$ is the camera pinhole, (O^C-X^C,Y^C,Z^C) is the camera coordinate system, and ($O_0{}^C$-u^C,v^C) is the CCD pixel coordinate system.

The second step during light projection is to project point $\boldsymbol{M}$ to the image plane by using perspective projection. Here, the image plane is perpendicular to Z^C axis of the camera coordinate system, and we assume that the image plane intersects with Z^C

axis at Z^C=-1. If $\boldsymbol{M}^{\boldsymbol{I}}$ is the projection point of $\boldsymbol{M}$ on the image plane, then its coordinate in the camera coordinate system (O^C-X^C, Y^C,Z^C) can be given as:

$$({x_M}^I, {y_M}^I, -1) = (\frac{{x_M}^C}{-{z_M}^C}, \frac{{y_M}^C}{-{z_M}^C}, \frac{{z_M}^C}{-{z_M}^C}) \,. \tag{3.24}$$

At this moment, we obtain the projection of point $\boldsymbol{M}$ on the image plane. However, the real projection point on the image plane cannot be directly decided by Eq. (3.24), because lens distortion will shift the ideal point $\boldsymbol{M}^{\boldsymbol{I}}$=($x_M^I$,$y_M^I$,-1) to the distorted point $\boldsymbol{M}^{\boldsymbol{D}}$=($x_M^D$,$y_M^D$,-1) on the image plane, and the coordinate of the distorted point can be obtained by using the distortion coefficients (see Eq. (3.17)) as:

$$\begin{pmatrix} {x_M}^D \\ {y_M}^D \end{pmatrix} = (1 + k_1 r^2 + k_2 r^4 + k_3 r^6) \cdot \begin{pmatrix} {x_M}^I \\ {y_M}^I \end{pmatrix} + \begin{pmatrix} 2k_4 {x_M}^I {y_M}^I + k_5 (r^2 + 2({x_M}^I)^2) \\ k_4 (r^2 + 2({y_M}^I)^2) + 2k_5 {x_M}^I {y_M}^I \end{pmatrix}, \tag{3.25}$$

where the coefficient series k is acquired by camera intrinsic calibration, and term r in Eq. (3.25) is given as:

$$r^2 = ({x_M}^I)^2 + ({y_M}^I)^2 \,. \tag{3.26}$$

As lens distortion has been considered (i.e., Step 3, see Eq. (3.25)), we obtain the distorted projection coordinate of $\boldsymbol{M}$ on the image plane as $\boldsymbol{M}^{\boldsymbol{D}}$=($x_M^D$,$y_M^D$,1). However, in a real digital camera, this point is rather presented in the unit of CCD pixel, so $\boldsymbol{M}^{\boldsymbol{D}}$ should be transferred to the CCD pixel coordinate system (O_0^C-u^C,v^C) as $\boldsymbol{M}^{\boldsymbol{P}}$. To do so, we introduce the camera intrinsic matrix, and the pixelized coordinate of $\boldsymbol{M}^{\boldsymbol{P}}$ is given as:

$$({x_M}^P, {y_M}^P, 1)^T = A \cdot ({x_M}^D, {y_M}^D, 1)^T \,, \tag{3.27}$$

where (x_M^P,y_M^P) is the pixelized coordinate of point $\boldsymbol{M}^{\boldsymbol{D}}$ in (O_0^C-u^C,v^C) coordinate system, A is the intrinsic matrix of the camera represented as Eq. (3.28),

$$A = \begin{pmatrix} f_x & 0 & u_0 \\ 0 & f_y & v_0 \\ 0 & 0 & 1 \end{pmatrix}. \tag{3.28}$$

Here, f_x and f_y are the camera focal lengths along μ and υ axes (with the unit of CCD pixel side length), and (u_0,v_0) is the principle point of the camera.

The above-discussed four-steps method enables us to project one point from the world coordinate system (which is also the checkerboard coordinate system) to the

CCD pixel coordinate system in a distortion considered pinhole camera model. However, in the real implementation, we rather have the studied point in the CCD pixel coordinate system as $\boldsymbol{M^P}$ and we prefer to inversely project it to the world coordinate system. Thus, we need to implement the inverse light projection.

The first step to perform the inverse projection is to transfer point $\boldsymbol{M^P}$ from the CCD pixel coordinate system ($O_0{}^C$-u^C,v^C) to the camera image plane. Hence, we simply use the inverse camera intrinsic matrix and we get the following relation as:

$$({x_M}^D, {y_M}^D, 1)^T = A^{-1} \cdot ({x_M}^P, {y_M}^P, 1)^T , \tag{3.29}$$

where matrix A is given in Eq. (3.28), $({x_M}^P, {y_M}^P)$ is the coordinate of pixel $\boldsymbol{M^P}$ in the CCD pixel coordinate system, and $({x_M}^D, {y_M}^D)$ is the x and y components of this point in the camera coordinate system (O^C-X^C, Y^C, Z^C). Here, we need to note that the camera lens distortion is not compensated within this step.

In the second step, we introduce the inverse camera distortion correction to extract the ideal projection point $\boldsymbol{M^I}$ from the distortion contained point $\boldsymbol{M^D}$. Under this scenario, we need to inversely perform the calculation of Eq. (3.25), from which we will get the ideal point $({x_M}^I, {y_M}^I)$ from the distorted point $({x_M}^D, {y_M}^D)$ in the camera coordinate system. Nevertheless, we want to note that the inverse calculation of Eq. (3.25) is not analytically obtainable, so we use a least squared technique based iteration to obtain the undistorted point [106]. As such distortion correction is already provided in the well-developed Bouguet Camera Calibration Toolbox [108], we directly use Camera Calibration Toolbox rather than further discussing the iteration algorithm here.

The third step is the inverse perspective projection. In particular, we are interested in knowing how one point in the CCD panel is inversely passing through the camera optical center (i.e., the pinhole) and goes into the object space (where the measured object is located). To do so, we intersect point $\boldsymbol{M^I}$=$({x_M}^I, {y_M}^I, {z_M}^I)$ on the CCD plane with the camera optical center $\boldsymbol{O_C}$=(x_{OC}, y_{OC}, z_{OC}) to establish an inverse projection vector $\boldsymbol{V_{OM}}^C$ in the camera coordinate system, this vector can be described as:

$$\boldsymbol{V_{OM}}^{\boldsymbol{C}} = \left[x_{OC} - {x_M}^I, y_{OC} - {y_M}^I, z_{OC} - {z_M}^I \right], \tag{3.30}$$

where (x_{OC}, y_{OC}, z_{OC}) is the coordinate of the camera pinhole $\boldsymbol{O_C}$ in (O^C-X^C, Y^C, Z^C) coordinate system. Here, term ${z_M}^I$ is the focal length of the camera which can be obtained from camera intrinsic parameter calibration.

Vector $\boldsymbol{V_{OM}}^{C}$ defines the projection ray in the camera coordinate system, so the studied point is located somewhere along this vector. Here, we want to emphasize that within our structured light measurement systems, by only knowing this inverse vector is already enough to perform the geometric triangulation (for SFPP measurement) or the inverse ray tracing (for SPMD measurement). The inverse ray tracing for SPMD measurement will be systematically described in Chapter 4, and the geometric triangulation for SFPP measurement will be comprehensively discussed in Chapter 6, respectively.

Note that vector $\boldsymbol{V_{OM}}^{C}$ at this moment is defined in the camera coordinate system. To perform any further calculation, we need to transform this vector from the camera coordinate system to the world coordinate system (i.e., the world coordinate system coincides with the checkerboard coordinate system), and this is the fourth step in inverse light projection. As the extrinsic parameters of the camera are already determined through camera calibration, we can easily transfer vector $\boldsymbol{V_{OM}}^{C}$ from the camera coordinate system to the world coordinate system as:

$$\boldsymbol{V_{OM}}^{W} = \boldsymbol{R_{WtC}}^{-1} \cdot \boldsymbol{V_{OM}}^{C}, \tag{3.31}$$

where $\boldsymbol{R_{WtC}}$ is the rotation matrix from the world coordinate system to the camera coordinate system.

3.5 Gamma calibration

In the previous section, we systematically present the camera calibration. Nevertheless, in a structured light measurement system, the projection component (i.e., LCD screen or video projector) is another crucial element as it provides sinusoidal fringe patterns. For instance, in a stereoscopic fringe projection profilometry system, we use a video projector to provide the sinusoidal fringe patterns; whereas in a stereoscopic phase measuring deflectometry system, we use an LCD to generate the sinusoidal fringe patterns. Thus, the accuracy of the SFP generation through these projection components is critical, as it directly decides the accuracy of phase shifting and phase unwrapping. Unfortunately, the projection components all present gamma effect, and as a consequence, the generated projection intensity responds nonlinearly to the gray level sent to the projection components. Such nonlinearity is purposely introduced to fit the human vision perception, but it deteriorates the ideal SFPs, and thus, it degenerates the accuracy to obtain the unwrapped phase maps.

The most common gamma nonlinearity can be seen in Figure 3-5 (a), which is an experimentally measured gray level-intensity response of the LCD panel used in our deflectometry system (see the red dots). Here, we can easily tell from Figure 3-5 (a) that the gray level is not linearly corresponding to the intensity. Hence, it has to be compensated until it shows a linear response. To perform gamma nonlinearity correction, we select the most robust solution, which is based on the inverse look up table (LUT) establishment [68, 73]. To perform the inverse LUT compensation, we sequentially send increasing gray levels to the LCD screen and we directly use a camera to capture the images on the LCD screen. Afterwards, we select a small central section in each intensity pattern captured by the camera and get the average intensity in this small section. Now, by using the averaged intensities and their corresponding gray levels within all frames, we can fit a gray level-intensity curve and this curve can be fitted with a high order polynomial function. This polynomial function is modeled into the following form as:

$$I(g) = c_0 + \sum_{i=1}^{N} c_i g^i \ , \tag{3.32}$$

where $I(g)$ is the output intensity, g is the gray level sent to the LCD screen, c_0 and c_i are constants, and N is the coefficient order.

In different projection components, the highest coefficient order ranges distinctly. For instance, Zhang used a seventh order polynomial to establish the gamma response [73], whereas the lowest polynomial order ever reported is two [111]. In our scheme, we find out that a third order polynomial is sufficient to precisely obtain a well fitted gray level-intensity curve, as it is shown in Figure 3-5 (a) (see the blue continuous curve).

Once this polynomial function (i.e., gray level versus intensity) is obtained, we build its corresponding inverse function (i.e., normalized intensity versus gray level), and this inverse function is the inverse look up table (LUT) (see Figure 3-5 (b)). Finally, we use this inverse LUT to re-calibrate the gray level-intensity response, and the new calibrated response is shown in Figure 3-6 by the red dots. By comparing the calibrated gray level-intensity response (red dots in Figure 3-6) to an ideal linear response (i.e., the blue line in Figure 3-6), we find out that the gamma nonlinearity is corrected, as the red dots accurately coincide with the blue line. In Figure 3-6, one may notice that the gray level is not strictly following the range between 0 to 255. Nevertheless, the limited range will not influence the gamma correction, because we do not use the full intensity range in the real implementation [74].

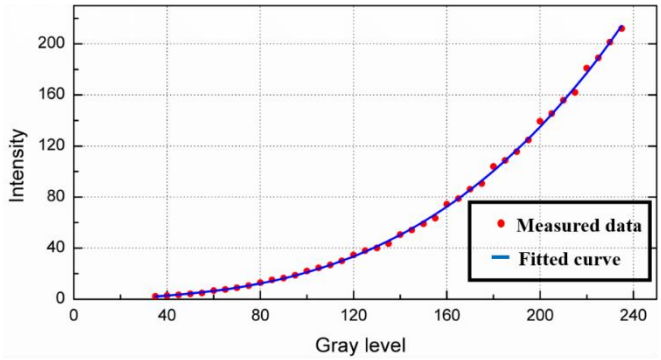

(a)

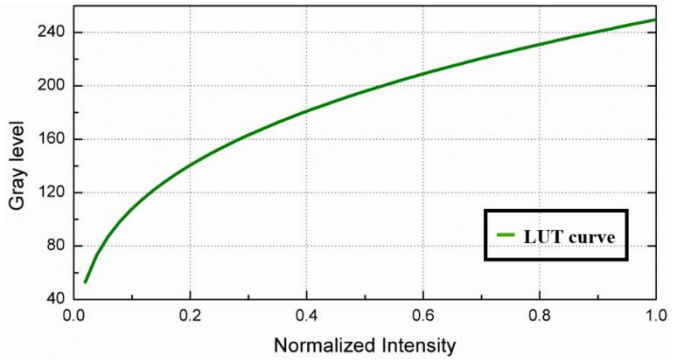

(b)

Figure 3-5. Gamma nonlinearity calibration of the LCD panel used in the stereoscopic phase measuring deflectometry system: (a) The experimentally measured gray level-intensity response (the red dots), and the fitted third order polynomial gray level-intensity curve (the blue continuous curve); and (b) the inverse look up table of the third order polynomial function (the green continuous curve).

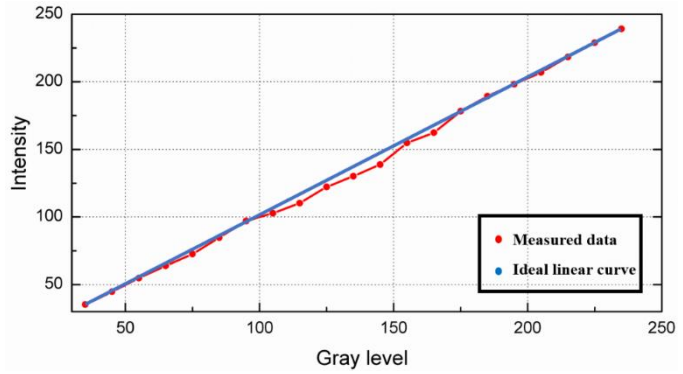

Figure 3-6. The experimentally measured gray level-intensity response after gamma correction.

3.6 Geometric calibration of the stereoscopic phase measuring deflectometry system

At this moment, we are equipped with both the camera calibration parameters and the gamma correction. Hence, we discuss the geometric calibration of the stereoscopic phase measuring deflectometry (SPMD) system, from which we can get the internal geometric relation between the system components. The SPMD system contains an LCD screen, two cameras (i.e., the stereoscopic camera) and the measured specular object. The principle scheme for SPMD system calibration is given in Figure 3-7.

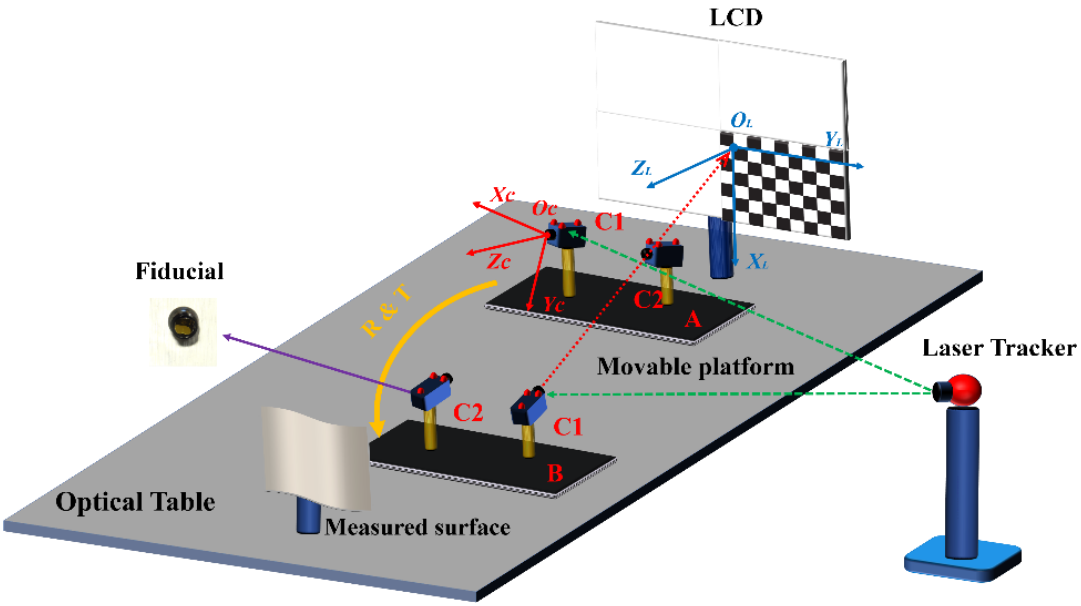

Figure 3-7. Basic calibration scheme of the stereoscopic phase measuring deflectometry (SPMD) system.

For SPMD system calibration, the LCD screen is fixed at a given position to provide either sinusoidal fringe patterns (for surface measurement) or a digital checkerboard pattern (for LCD screen position calibration). On the other hand, two cameras are fixed on a movable iron platform. Once we want to change the camera positions, we only move the whole iron platform, but we never change the internal geometric relation between the two cameras. Here, we want to note that the stereoscopic camera movement is introduced to perform the LCD screen position calibration (we will discuss this in Section 3.6.2 with more details). Finally, the specular object to be measured is placed to the other end of the system, and we let its reflective side face the LCD screen. Thus, the measured surface can reflect the SFPs on the LCD screen to the stereoscopic camera. Moreover, we can find in Figure 3-7

that a laser tracker is introduced. Here, the laser tracker records the camera positions with the help of fiducial markers, so we can perform the laser tracker-assisted hand-eye calibration (we will discuss this in Section 3.6.3).

3.6.1 Geometric limitations

To perform the specular surface measurement with a stereoscopic phase measuring deflectometry system, we have to guarantee that both cameras can capture the sinusoidal fringe patterns reflected by the whole measured surface within their field of views. Only under this scenario, the phase correspondence between the LCD screen and the cameras can be established. Therefore, the separation limitation between the two cameras needs to be decided. Moreover, we also have to investigate the distance from the cameras to the measured surface as well as the distance from the cameras to the screen.

To calculate the geometric limitation of a stereoscopic phase measuring deflectometry system, we assume a flat mirror as the measured surface placed parallel to the LCD screen surface (the LCD screen is regarded as flat) at a distance of d. What is more, the mirror central point $\boldsymbol{O_m}$ and the screen central point $\boldsymbol{O_s}$ are both located on the same line perpendicular to both devices. Under this scenario, the vector forged by intersecting $\boldsymbol{O_m}$ and $\boldsymbol{O_s}$ is regarded as the optical axis. To better visualize this scheme, we depict this system in Figure 3-8.

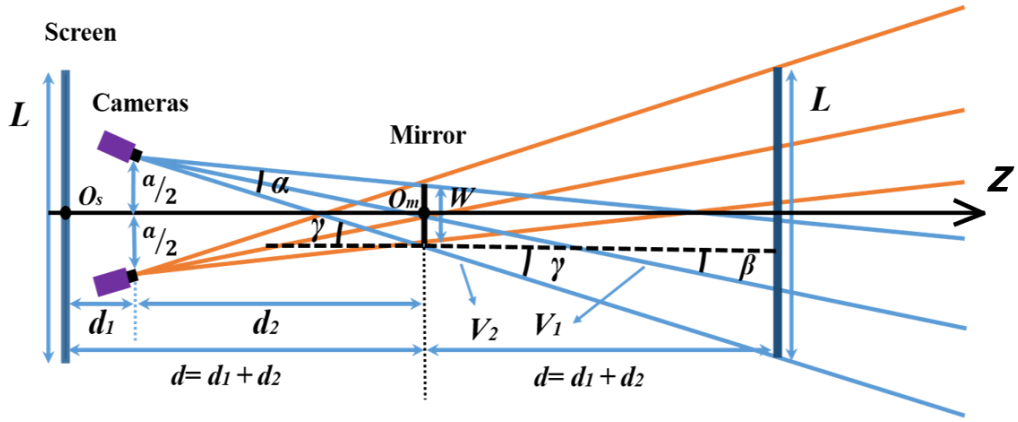

Figure 3-8. Principle scheme of the SPMD system by placing both cameras and the LCD screen facing the measured flat mirror.

Then, considering that the LCD screen is reflected by the flat mirror, the image of the LCD screen via the mirror is obtained at the back side of the mirror with a same

distance of d. The size of the mirror is W and the size of the screen is L. Therefore, the screen image obtained by the mirror reflection also has a size of L. On the other hand, both cameras are located in front of the screen facing the measured mirror, and the distance from both cameras to the screen is set as d_1. In other words, this means that both cameras are placed at the same distance to the screen in Z direction, and the connection vector between the two camera optical centers is parallel to the LCD screen. In this case, the connection vector between the two cameras is also parallel to the mirror surface, and the separation distance from the cameras to the mirror is defined as d_2. Moreover, the separation distance between the two cameras is assumed to be a. To simplify the system scheme, both cameras are placed at the same distance $a/2$ away from Z axis.

Note that as the camera has a limited field of view (FOV), the mirror inspection size is restricted by both the camera FOV and the distance from the camera to the mirror (d_2). Considering our SPMD system, the camera FOV is already fixed so that the only parameter determining the mirror inspection size is the distance from the camera to the mirror (d_2). By considering a simple geometric relation, the minimum inspection size of a mirror is obtained when the camera is inspecting vertically to the mirror and their geometric centers are both located in Z direction as it is demonstrated in Figure 3-9 (i.e., the red line case).

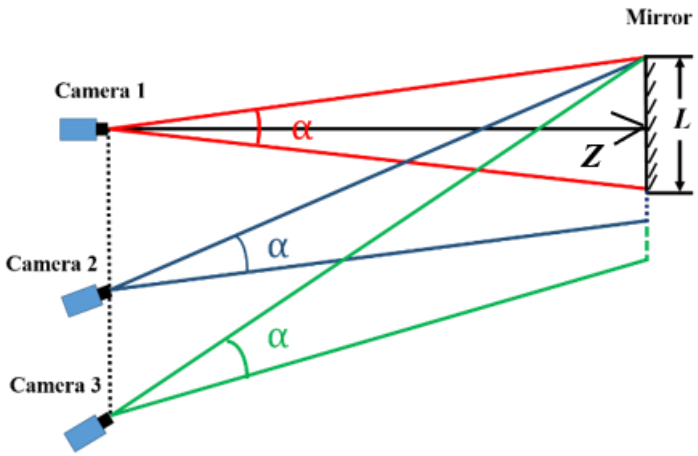

Figure 3-9. The camera inspection schemes: (a) The red line case: the camera is inspecting the mirror vertically. (b) The blue line case: the camera is inspecting the mirror with a tilted angel. (c) The green line case: the camera is inspecting the mirror with a greater tilted angel.

Then, the minimum distance from the camera to the mirror in Figure 3-9 (the red line case) can be represented as:

$$d_{2\min} = \frac{L}{2 \cdot \tan(\alpha/2)}, \tag{3.33}$$

where L is the size of the mirror and α is the FOV angle of the camera.

To guarantee that the mirror with the size of L can be totally examined, we have to place the mirror in a particular position where the distance from the camera to the mirror is greater than d_{2min}, therefore the mirror can be totally observed regardless of the spatial position of the camera to the mirror. For instance, if the size of the measured mirror is 160 *mm*, and the camera FOV angle is 11°, then the distance from any camera in the SPMD system to the mirror should be greater than 830.8 *mm*.

Once the mirror is deployed, the geometric alignment of the cameras as well as the LCD screen should be implemented. In Figure 3-8, apart from the FOV angel α, two more angles have to be defined. First, we connect the center of the mirror $\boldsymbol{O_m}$ to the first camera center to forge an input vector $\boldsymbol{V_1}$, then the angle between $\boldsymbol{V_1}$ and Z axis is defined as β. Afterwards, a second vector $\boldsymbol{V_2}$ is generated by connecting the edge of the mirror to the first camera center. At this moment, this third angle, represented as the intersection angle between $\boldsymbol{V_2}$ and Z direction, is entitled as γ. Therefore, two geometric relations can be obtained as:

$$\gamma \leq \beta + \frac{\alpha}{2}, \tag{3.34}$$

$$\tan\gamma \leq \frac{a+W}{2d_2}. \tag{3.35}$$

Subsequently, to ensure that each camera can capture the sinusoidal fringe patterns reflected by the whole mirror (so that we can measure the whole mirror), the LCD screen should provide a larger illumination area than the whole field of view of any camera, so that the mirror can be fully projected. By taking this condition into consideration, we can obtain a third geometric relation associating the objective space with the image space, and this relation is shown as:

$$\tan\gamma \cdot d + \frac{W}{2} \leq \frac{L}{2}. \tag{3.36}$$

Finally, as d_2 (distance from the camera to the mirror) is generally much greater than W (i.e., W is the size of the mirror), a geometric approximation can be obtained by focusing on the triangle forged by the two sides of angle α and the mirror. Such approximation is presented below as:

$$\tan\alpha \approx \frac{W}{d_2}. \tag{3.37}$$

By merging Eqs. (3.35), (3.36) and (3.37) with the condition $d{=}d_1{+}d_2$, the distance between the two cameras can be finally determined as follow:

$$a\left(1+\frac{d_1\cdot\tan\alpha}{W}\right)\leq L-2W-d_1\cdot\tan\alpha\,. \tag{3.38}$$

Here, we want to note that in the real implementation, the FOV angle of the camera (i.e., α) is normally small, and the camera is generally placed near the screen to provide a compact system. Therefore, Eq. (3.38) can be simplified by ignoring the d_1 and α containing terms and finally the distance between the two cameras is represented as Eq. (3.39), as the camera separation distance a is determined by the sizes of the screen and the mirror,

$$a\leq L-2W\,. \tag{3.39}$$

At this moment, the complete system geometric scheme is depicted. In order to perform the stereoscopic phase measuring deflectometry measurement, the measured specular surface has to be placed away from the cameras with a distance greater than d_{2min} calculated by Eq. (3.33). On the other hand, these two cameras are arranged in a manner that their separation should satisfy the condition as Eq. (3.39). In fact, this demonstrates that a bigger screen is favored, and mirror with its size greater than half of the screen cannot be directly measured within just one measurement. Moreover, the cameras and the screen should be closely aligned (d_1 is a small value), so that we can obtain a compact system. At last, we should arrange a large camera separation a, because a great camera separation favors both the geometric triangulation (for SFPP measurement) and the inverse ray tracing (for SPMD measurement).

3.6.2 LCD screen position calibration

From Section 3.6.1, we can determine the stereoscopic phase measuring deflectometry system scheme, such as where to locate the LCD screen and the

stereoscopic camera. Now, to perform the inverse ray tracing for specular surface normal calculation, we should determine the position of the LCD screen with respect to the stereoscopic camera. In other words, we need to perform the coordinate system transformation from the LCD screen coordinate system to the camera coordinate system. To describe such coordinate system transformation, we present all the coordinate systems in an SPMD system in Figure 3-10.

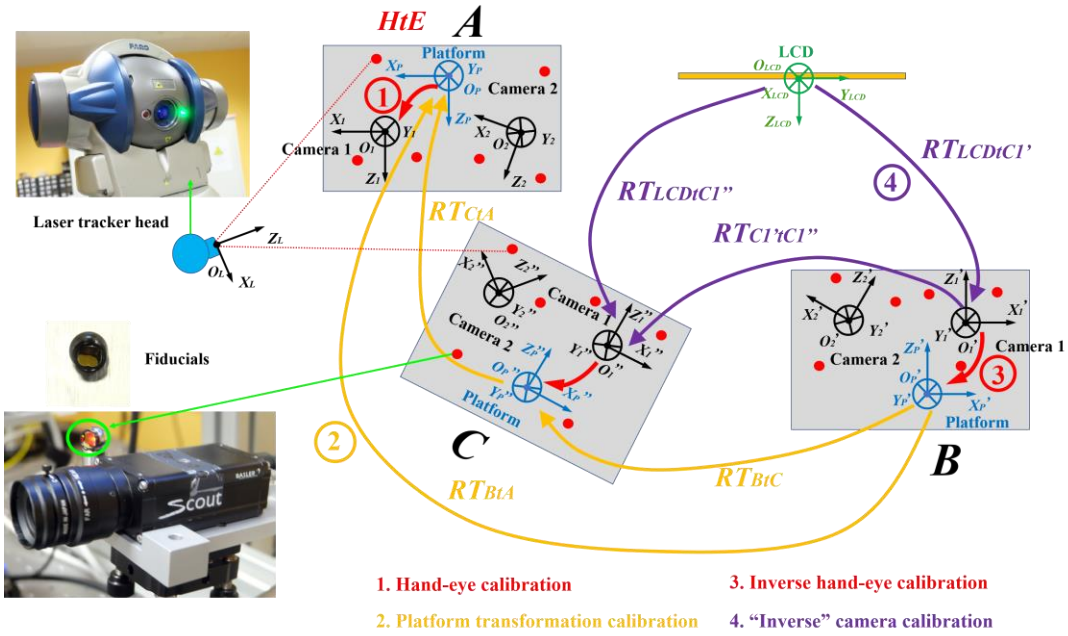

Figure 3-10. The LCD screen position calibration scheme: (a) Step 1, hand-eye calibration from which we can transform between the first camera coordinate system and the iron platform coordinate system. The coordinate system of the first camera at position A (O_1-X_1,Y_1,Z_1) is regarded as the world coordinate system. (b) Step 2, the platform transformation between position A and position B. This transformation is implemented to guarantee that the cameras can inspect the LCD screen. (c) Step 3, the inverse hand-eye calibration that we transform between the platform coordinate system and the first camera coordinate system at position B. (d) Step 4, the "inverse" camera calibration to determine the transformation between the LCD screen and the first camera at position B.

In Figure 3-10, the stereoscopic camera is fixed on an iron movable platform and this platform is initially located at position A. The LCD screen is placed on the other side and its projection direction is the same as the camera inspecting direction. The coordinate system of the first camera at position A is entitled as (O_1-X_1,Y_1,Z_1), the

coordinate system of the second camera at position A is defined as (O_2-X_2, Y_2,Z_2), the geometric relation between (O_2-X_2, Y_2,Z_2) and (O_1-X_1, Y_1,Z_1) can be obtained through stereoscopic camera calibration. Afterwards, we also define the coordinate system of the iron movable platform at position A as (O_P-X_P, Y_P,Z_P), and the coordinate system of the LCD screen as (O_{LCD}-X_{LCD}, Y_{LCD},Z_{LCD}). In this section, we focus on the coordinate system transformation from the LCD screen to the first camera, and such transformation is described as from (O_{LCD}-X_{LCD}, Y_{LCD},Z_{LCD}) to (O_1-X_1, Y_1,Z_1).

To perform the coordinate system transformation from (O_{LCD}-X_{LCD}, Y_{LCD},Z_{LCD}) to (O_1-X_1, Y_1,Z_1), we need to define the world coordinate system of the whole SPMD system at the very beginning. In this case, we define the coordinate system of the first camera at position A (O_1-X_1, Y_1,Z_1) as the world coordinate system. The optical center of this camera is the world coordinate origin, the optical axis of the first camera is Z axis of the world coordinate system, and it is a right hand coordinate system.

Once the world coordinate system is defined, we present the LCD screen position calibration process. This calibration can be sequentially performed in four steps as: (*i*) the hand-eye calibration, (*ii*) the platform transformation calibration, (*iii*) the inverse hand-eye calibration, and (*iv*) the "inverse" camera calibration. These four steps can be seen in Figure 3-10.

The first step in LCD screen position calibration is the hand-eye calibration. Now, as both cameras are fixed on the movable platform, we regard the movable iron platform as the "robot hand" which provides the camera location transformation, and we also regard the cameras as the "eye" to inspect the measured surface. The coordinate system transformation from "hand" to "eye" is presented as the transformation from (O_P-X_P, Y_P,Z_P) to (O_1-X_1, Y_1,Z_1), and such coordinate system transformation is entitled as the hand-eye calibration. This hand-eye calibration is mathematically presented by matrix ***HtE***. As hand-eye calibration is complex, it is later comprehensively discussed with a whole sub-section (Section 3.6.3).

The second step is the platform transformation calibration. Now, as both cameras are still positioned at A to inspect the measured surface, they cannot inspect the LCD screen. Thus, to calibrate the transformation from the LCD screen coordinate system to the world coordinate system, we move the whole iron platform from position A to position B, so that the cameras can inspect the LCD screen now. The coordinate system of the movable platform as position B is entitled as (O_P'-X_P', Y_P',Z_P'), and the coordinate system of the first camera at position B is (O_1'-X_1', Y_1',Z_1'). The platform coordinate system transformation from position B to position A is mathematically

described as matrix $\boldsymbol{RT_{BtA}}$ (i.e., from (O_P'-X_P', Y_P', Z_P') to (O_P-X_P, Y_P, Z_P)). Here, to obtain matrix $\boldsymbol{RT_{BtA}}$, we introduce the laser tracker. In particular, we put six fiducial markers above both cameras at position A, and we use a laser tracker to record the positions of these six fiducials at position A with respect to the laser tracker head (see the sub-figure at the left side in Figure 3-10). Afterwards, we move the movable platform to position B, and we perform laser tracking again to get the six fiducial locations at position B. Now, with the six fiducial positions in both position A and position B, we can calculate the platform transformation matrix $\boldsymbol{RT_{BtA}}$ from (O_P'-X_P', Y_P', Z_P') to (O_P-X_P, Y_P, Z_P). Specifically, the calculation can be described by the following equation:

$$\begin{pmatrix} x_1 & x_2 & x_3 & x_4 & x_5 & x_6 \\ y_1 & y_2 & y_3 & y_4 & y_5 & y_6 \\ z_1 & z_2 & z_3 & z_4 & z_5 & z_6 \\ 1 & 1 & 1 & 1 & 1 & 1 \end{pmatrix} = \boldsymbol{RT_{BtA}} \cdot \begin{pmatrix} x_1' & x_2' & x_3' & x_4' & x_5' & x_6' \\ y_1' & y_2' & y_3' & y_4' & y_5' & y_6' \\ z_1' & z_2' & z_3' & z_4' & z_5' & z_6' \\ 1 & 1 & 1 & 1 & 1 & 1 \end{pmatrix}, \tag{3.40}$$

where term (x_i,y_i,z_i) on the left side of the equation means the six fiducial marker positions measured by the laser tracker at position A, term (x_i', y_i', z_i') on the right side of the equation means the six fiducial marker positions measured by the laser tracker at position B, and term $\boldsymbol{RT_{BtA}}$ is a 4×4 matrix representing the platform transformation from position B to position A. Here, as we use six fiducials, the number of i is six.

The third step is the inverse hand-eye calibration. Nevertheless, as the inverse hand-eye calibration is simply the inverse calculation of the first step, it is not discussed here.

The fourth step is the "inverse" camera calibration. For this step, we use the first camera at position B to perform the "inverse" camera calibration to decide the coordinate system transformation from (O_{LCD}-X_{LCD}, Y_{LCD}, Z_{LCD}) to (O_1'-X_1', Y_1', Z_1'). In particular, we generate a digital checkerboard on the LCD screen, and we let the digital checkerboard coordinate system origin coincide with the LCD screen center. Therefore, the LCD coordinate system coincides with this digital checkerboard coordinate system. Now, by using the first camera at position B to inspect the digital checkerboard on the LCD screen, we can perform the "inverse" camera calibration with Camera Calibration Toolbox to get the coordinate system transformation matrix from (O_{LCD}-X_{LCD}, Y_{LCD}, Z_{LCD}) to (O_1'-X_1', Y_1', Z_1'). This transformation matrix is in fact the extrinsic camera calibration parameter. Nevertheless, with only one frame, we cannot perform the "inverse" camera calibration, but more frames are required to

guarantee the "inverse" camera calibration accuracy. Therefore, we shift the movable platform from position B to more positions (i.e., such as position C in Figure 3-10), where the first camera can still inspect the digital checkerboard to accomplish the "inverse" camera calibration. Based on this principle, we shift the iron platform to 40 different positions. Once we accomplish the "inverse" camera calibration with placing the camera at 40 different positions, we then select the particular coordinate system transformation relation from (O_{LCD}-X_{LCD}, Y_{LCD}, Z_{LCD}) to (O_1'-X_1', Y_1', Z_1'), and it is presented as matrix $\boldsymbol{RT_{LCDtC1'}}$ as the fourth step in Figure 3-10.

Once we get all the coordinate system transformation matrices of all four steps in Figure 3-10 (i.e., matrix $\boldsymbol{RT_{LCDtC1'}}$ for Step 4, matrix $\boldsymbol{HtE^{-1}}$ for Step 3, matrix $\boldsymbol{RT_{BtA}}$ for Step 2, and matrix $\boldsymbol{HtE}$ for Step 1), we move the movable platform back to the initial position A, so that the stereoscopic camera can inspect the measured specular surface again.

At this moment, we can establish the coordinate system transformation from (O_{LCD}-X_{LCD}, Y_{LCD}, Z_{LCD}) to (O_1-X_1, Y_1, Z_1) sequentially by four steps as: (*i*) the "inverse" camera calibration from (O_{LCD}-X_{LCD}, Y_{LCD}, Z_{LCD}) to (O_1'-X_1', Y_1', Z_1') (i.e., Step 4 in Figure 3-10, $\boldsymbol{RT_{LCDtC1'}}$); (*ii*) the inverse hand-eye calibration from (O_1'-X_1', Y_1', Z_1') to (O_P'-X_P', Y_P', Z_P') (i.e., Step 3 in Figure 3-10, $\boldsymbol{HtE^{-1}}$); (*iii*) the iron platform transformation from (O_P'-X_P', Y_P', Z_P') to (O_P-X_P, Y_P, Z_P) (i.e., Step 2 in Figure 3-10, $\boldsymbol{RT_{BtA}}$); and (*iv*) the hand-eye calibration from (O_P-X_P, Y_P, Z_P) to (O_1-X_1, Y_1, Z_1) (i.e., Step 1 in Figure 3-10, $\boldsymbol{HtE}$).

From the above discussion, we know the complete process to perform the LCD screen position calibration. Now, we mathematically describe the geometric transformation between the LCD screen and the first camera at position A. To do so, we select one point $\boldsymbol{S}$=(x_{LCD}, y_{LCD}, z_{LCD}) in the LCD coordinate system (O_{LCD}-X_{LCD}, Y_{LCD}, Z_{LCD}) to perform the analysis.

Firstly, we transform point $\boldsymbol{S}$ from (O_{LCD}-X_{LCD}, Y_{LCD}, Z_{LCD}) coordinate system to (O_1'-X_1', Y_1', Z_1') coordinate system, and point $\boldsymbol{S}$ can be obtained in (O_1'-X_1', Y_1', Z_1') (i.e., the coordinate system of the first camera at position B) as:

$$(x_C', y_C', z_C', 1)^T = \boldsymbol{RT_{LCDtC1'}} \cdot (x_{LCD}, y_{LCD}, z_{LCD}, 1)^T . \tag{3.41}$$

where (x_C', y_C', z_C') is the coordinate of point $\boldsymbol{S}$ in (O_1'-X_1', Y_1', Z_1') coordinate system.

Secondly, we sequentially transform point $\boldsymbol{S}$ from (O_1'-X_1', Y_1',Z_1') coordinate system to (O_P'-X_P', Y_P',Z_P') coordinate system through inverse hand-eye calibration as:

$$(x_P', y_P', z_P', 1)^T = \boldsymbol{HtE^{-1}} \cdot (x_C', y_C', z_C', 1)^T , \tag{3.42}$$

where $\boldsymbol{HtE^{-1}}$ is the inverse hand-eye calibration matrix, and (x_P',y_P',z_P') is the coordinate of point $\boldsymbol{S}$ in (O_P'-X_P', Y_P',Z_P') coordinate system.

Thirdly, point $\boldsymbol{S}$ is transformed from (O_P'-X_P', Y_P',Z_P') coordinate system to (O_P-X_P, Y_P,Z_P) coordinate system (see the platform at position A in Figure 3-10). Under this scenario, point $\boldsymbol{S}$ in (O_P-X_P, Y_P,Z_P) coordinate system is written as:

$$(x_P, y_P, z_P, 1)^T = \boldsymbol{RT_{BtA}} \cdot (x_P', y_P', z_P', 1)^T , \tag{3.43}$$

where $\boldsymbol{RT_{BtA}}$ is the platform transformation matrix from position B to position A.

Finally, we introduce the hand-eye calibration to transform point $\boldsymbol{S}$ from (O_P-X_P, Y_P,Z_P) to (O_1-X_1, Y_1,Z_1). Then, point $\boldsymbol{S}$ is finally transformed into the world coordinate system (i.e., the coordinate system of the first camera at position A) as:

$$(x_C, y_C, z_C, 1)^T = \boldsymbol{HtE} \cdot (x_P, y_P, z_P, 1)^T , \tag{3.44}$$

where $\boldsymbol{HtE}$ is the hand-eye calibration matrix.

From the above-discussed four steps, we can transform any point in the LCD screen coordinate system (O_{LCD}-X_{LCD}, Y_{LCD},Z_{LCD}) to the world coordinate system (O_1-X_1, Y_1,Z_1) through the platform B path by the following relation:

$$(x_C, y_C, z_C, 1)^T = \boldsymbol{HtE} \cdot \boldsymbol{RT_{BtA}} \cdot \boldsymbol{HtE^{-1}} \cdot \boldsymbol{RT_{LCDtC1'}} \cdot (x_{LCD}, y_{LCD}, z_{LCD}, 1)^T . \tag{3.45}$$

Here, we write the matrix production of the whole inner terms as $\boldsymbol{RT_{LCDtW}}$ to define the transformation from the LCD coordinate system to the world coordinate system. $\boldsymbol{RT_{LCDtW}}$ then is presented as:

$$\boldsymbol{RT_{LCDtW}} = \boldsymbol{HtE} \cdot \boldsymbol{RT_{BtA}} \cdot \boldsymbol{HtE^{-1}} \cdot \boldsymbol{RT_{LCDtC1'}} . \tag{3.46}$$

Here, we want to note that in the real experimental implementation, we not only transform the iron platform to just one position (i.e., position B), but we rather introduce 40 times the iron platform transformations (i.e., such as position C) to discriminate the "inverse" camera calibration error. Thus, we may encounter one issue as to define which transformation path among these 40 transformations should be used to perform the LCD screen coordinate system determination. Theoretically, any

path should yield a same result, because the absolute geometric position between the LCD screen and the initial iron platform (first camera at position A) is never changed. However, due to the laser tracking error and the LCD screen calibration error, the transformation relation between the LCD screen coordinate system (O_{LCD}-$X_{LCD}, Y_{LCD}, Z_{LCD}$) to the world coordinate system (the world coordinate system is also the coordinate system of the first camera at position A, (O_1-X_1, Y_1, Z_1)) may vary slightly within each transformation path. Thus, we obtain all $\boldsymbol{RT_{LCDtW}}$ terms corresponding to all 40 platform transformations and then we calculate an average transformation matrix from these 40 results. This averaged matrix is regarded as the real transformation matrix from the LCD screen coordinate system to the world coordinate system.

3.6.3 Laser tracker-assisted hand-eye calibration

As it is previously described, to perform the complete coordinate system transformation from (O_{LCD}-$X_{LCD}, Y_{LCD}, Z_{LCD}$) to ($O_1$-$X_1, Y_1, Z_1$), we need to obtain the coordinate system transformation from (O_P-X_P, Y_P, Z_P) to (O_1-X_1, Y_1, Z_1), and this is called the hand-eye calibration (i.e., matrix $\boldsymbol{HtE}$ in Section 3.6.2). To perform the hand-eye calibration, not only we need to move the iron platform to different places (such as position B or position C in Figure 3-10) to inspect the digital checkerboard on the LCD screen from different perspectives, but we also need to use a laser tracker to record the iron platform location corresponding to any movement position. Here, we again use the same SPMD scheme presented in Figure 3-10 to comprehensively describe the hand-eye calibration.

For hand-eye calibration, we preliminarily focus on the movable platform at position A. Here, the coordinate system of the first camera at position A (O_1-X_1, Y_1, Z_1) is the world coordinate system. Now, we put six fiducial markers above both cameras (see the example in the sub-figure at the left bottom corner in Figure 3-10, each camera supports three fiducial markers), and we regard these six fiducial markers be in the iron platform coordinate system (O_P-X_P, Y_P, Z_P). In particular, we need to note that once the fiducial markers are fixed, we never change their positions. Afterwards, we introduce a laser tracker to track the spatial positions of these fiducial markers (see the red dash lines in Figure 3-10), so we know the spatial positions of all six fiducial markers at position A with respect to the laser tracker head system (O_L-X_L, Y_L, Z_L).

Later, we move the movable platform to position B, where the six fiducial markers are located in the new iron platform coordinate system (O_P'-X_P', Y_P', Z_P'). Once it is moved to position B, we firstly use the laser tracker to again track the spatial positions of all fiducial markers. Here, as the movable platform transformation is a rigid body transformation, we use the positions of these six tracked fiducial in both (O_P-X_P, Y_P, Z_P) and (O_P'-X_P', Y_P', Z_P') to calculate the rigid body transformation matrix $\boldsymbol{RT_{BtA}}$ (see the orange curve $\boldsymbol{RT_{BtA}}$ in Figure 3-10). Here, $\boldsymbol{RT_{BtA}}$ implies the coordinate system transformation from (O_P'-X_P', Y_P', Z_P') to (O_P-X_P, Y_P, Z_P). On the other hand, we use the first camera at position B to inspect the LCD screen, where the LCD screen presents a checkerboard pattern. The first camera at position B then record the digital checkerboard pattern on the LCD screen, and this frame is later used for the "inverse" camera calibration. From such "inverse" camera calibration, we can determine the transformation matrix $\boldsymbol{RT_{LCDtC1'}}$ from (O_{LCD}-X_{LCD}, Y_{LCD}, Z_{LCD}) to (O_1'-X_1', Y_1', Z_1') (see the purple curve $\boldsymbol{RT_{LCDtC1'}}$ in Figure 3-10).

However, if we only capture one digital checkerboard pattern at position B, we cannot perform the "inverse" camera calibration because there is only one frame. Thus, we move the iron platform to another position C to repeat another calibration. Specifically, we track the six fiducial trackers when the platform is moved to position C, so we get the rigid body transformation matrix $\boldsymbol{RT_{CtA}}$ from (O_P''-X_P'', Y_P'', Z_P'') to (O_P-X_P, Y_P, Z_P) (see the orange curve $\boldsymbol{RT_{CtA}}$ in Figure 3-10). On the other side, we use the first camera at position C to capture the checkerboard pattern on the LCD screen, so we can also accomplish another "inverse" camera calibration to determine the transformation matrix $\boldsymbol{RT_{LCDtC1''}}$ from the LCD screen coordinate system (O_{LCD}-X_{LCD}, Y_{LCD}, Z_{LCD}) to the first camera coordinate system (O_1''-X_1'', Y_1'', Z_1'') (see the purple curve $\boldsymbol{RT_{LCDtC1''}}$ in Figure 3-10).

Finally, we repeat this above-demonstrated steps for in total 40 times in the real implementation (these 40 times include position A and position B). We move the platform to 40 different positions and use the first camera to capture the checkerboard pattern on the LCD screen from 40 different perspectives, so that the "inverse" camera calibration is performed with all these 40 different positions, and we obtain 40 different extrinsic camera calibration parameters. On the other hand, we also use the laser tracker to record the positions of the fiducial markers on the iron platform with respect to these 40 movements, and we get 40 rigid body transformation matrices. Then, the laser tracker-assisted hand-eye calibration can be obtained through these 40 movements. The procedure to mathematically obtain the hand-eye calibration matrix $\boldsymbol{HtE}$ is discussed below.

Here, we use the iron platform at both position B and position C as an example to demonstrate the matrix $\boldsymbol{HtE}$ calculation. We firstly move the iron platform from position A to position B, and we can use the laser tracker to experimentally measure $\boldsymbol{RT_{BtA}}$ (i.e., the platform transformation matrix from position B to position A). Afterwards, we move the iron platform from position B to position C, we can use the laser tracker to get $\boldsymbol{RT_{CtA}}$ (i.e., the platform transformation matrix from position C to position A). Now, $\boldsymbol{RT_{BtA}}$ and $\boldsymbol{RT_{CtA}}$ can be mathematically described as:

$$\boldsymbol{RT_{BtA}} = \begin{bmatrix} \boldsymbol{R_{BtA}} & \boldsymbol{T_{BtA}} \\ 0 & 1 \end{bmatrix}, \tag{3.47}$$

$$\boldsymbol{RT_{CtA}} = \begin{bmatrix} \boldsymbol{R_{CtA}} & \boldsymbol{T_{CtA}} \\ 0 & 1 \end{bmatrix}. \tag{3.48}$$

At this moment, we can determine the platform transformation from position B to position C as:

$$\boldsymbol{RT_{BtC}} = \boldsymbol{RT_{CtA}}^{-1} \cdot \boldsymbol{RT_{BtA}}. \tag{3.49}$$

On the other hand, we experimentally measure $\boldsymbol{RT_{LCDtC1'}}$ by "inverse" camera calibration. Here, $\boldsymbol{RT_{LCDtC1'}}$ is the coordinate transformation matrix from the LCD coordinate system (O_{LCD}-X_{LCD}, Y_{LCD}, Z_{LCD}) to the first camera coordinate system at position B (O_1'-X_1', Y_1', Z_1'). Moreover, we also get $\boldsymbol{RT_{LCDtC1''}}$ from the secondary "inverse" camera calibration. Here, $\boldsymbol{RT_{LCDtC1''}}$ is the transformation matrix from the LCD coordinate system (O_{LCD}-X_{LCD}, Y_{LCD}, Z_{LCD}) to the first camera coordinate system at position C (O_1''-X_1'', Y_1'', Z_1''). $\boldsymbol{RT_{LCDtC1'}}$ and $\boldsymbol{RT_{LCDtC1''}}$ are mathematically described as:

$$\boldsymbol{RT_{LCDtC1'}} = \begin{bmatrix} \boldsymbol{R_{LCDtC1'}} & \boldsymbol{T_{LCDtC1'}} \\ 0 & 1 \end{bmatrix}, \tag{3.50}$$

$$\boldsymbol{RT_{LCDtC1''}} = \begin{bmatrix} \boldsymbol{R_{LCDtC1''}} & \boldsymbol{T_{LCDtC1''}} \\ 0 & 1 \end{bmatrix}. \tag{3.51}$$

Thus, we describe the first camera coordinate system transformation from position B (O_1'-X_1', Y_1', Z_1') to position C (O_1''-X_1'', Y_1'', Z_1'') as:

$$\boldsymbol{RT_{C1'tC1''}} = \boldsymbol{RT_{LCDtC1''}} \cdot \boldsymbol{RT_{LCDtC1'}}^{-1}. \tag{3.52}$$

Once we obtain the relations in Eqs. (3.49) and (3.52), we can establish the unitary coordinate system transformation between position B and position C (see the closed inner loop constructed by the purple $\boldsymbol{RT}_{C1'tC1''}$ curve, the two red $\boldsymbol{HtE}$ curves, and the orange $\boldsymbol{RT}_{BtC}$ curve in Figure 3-10), and the internal transformation relation in this loop can be demonstrated as:

$$\boldsymbol{RT}_{BtC} = \boldsymbol{HtE} \cdot \boldsymbol{RT}_{C1'tC1''} \cdot \boldsymbol{HtE}^{-1}. \tag{3.53}$$

where $\boldsymbol{HtE}$ is the hand-eye calibration matrix which we want to obtain. Furthermore, Eq. (3.53) can be transformed into:

$$\boldsymbol{RT}_{BtC} \cdot \boldsymbol{HtE} = \boldsymbol{HtE} \cdot \boldsymbol{RT}_{C1'tC1''}. \tag{3.54}$$

Now, we want to calculate term $\boldsymbol{HtE}$ in Eq. (3.54). Therefore, we analogues Eq. (3.54) as the following equation:

$$\boldsymbol{A} \cdot \boldsymbol{X} = \boldsymbol{X} \cdot \boldsymbol{B}, \tag{3.55}$$

where $\boldsymbol{A}$ and $\boldsymbol{B}$ are experimentally measured, and we only have to calculate matrix $\boldsymbol{X}$.

To calculate matrix $\boldsymbol{X}$, we can introduce various algorithms that are well developed in the robotics community. The most classic methods are listed as: (*i*) the linear algebra method proposed by Tsai and Lenz [112], (*ii*) the simultaneously nonlinear minimization method (based on the rotation quaternation and the shifting vector) proposed by Horaud and Dornaika [113], (*iii*) the exact and least-squares solutions proposed by Park and Martin [114], and (*iv*) the unit dual quaternion method proposed by Daniilidis [115].

In our system, we select Tsai method to perform the hand-eye calibration as it yields a robust calibration. In particular, we use Matlab Toolbox developed by Christian Wengert [116], which is based on Tsai method, to accomplish the experimental hand-eye calibration. Moreover, Tsai has proved that by introducing more platform transformation, the hand-eye calibration error can be dramatically reduced [112]. Thus, in our experimental calibration, we transform the platform to 40 different positions to accomplish the hand-eye calibration.

3.7 Stereoscopic fringe projection profilometry system calibration

In a stereoscopic fringe projection profilometry (SFPP) system, we use the same stereoscopic camera to inspect the measured diffuser object, but we replace the LCD screen by a video projector, so that the projection intensity on the diffuser object is strong enough to be detected. Moreover, as surface point determination in an SFPP system is performed by the geometric triangulation between the stereoscopic camera (see Section 1.3.3), we no longer need the inverse ray tracing, and thus, the video projector position calibration is not mandatory. In fact, we only need to put the video projector at a proper position where it can illuminate the measured object homogeneously. Under this scenario, the SFPP system calibration is more straightforward, as we only need to determine the geometric relation between the two cameras.

Here, we directly use the same stereoscopic camera calibration discussed in Section 3.4.2 to determine the geometric relation between the two cameras. Note that as the stereoscopic camera system is used in both an SFPP and an SPMD system, we only calibrate the stereoscopic camera for one time and this stereoscopic camera system is universally used in both stereoscopic fringe projection profilometry and stereoscopic phase measuring deflectometry.

Apart from the stereoscopic camera calibration, we also need to adjust the image projecting frequency of the video projector and the image receiving frequency of the camera to be equal. The video projector in our SFPP system is an LCD chip-based video projector, and it has the ability to process limited patterns in a given time. For instance, if the video projector can process 60 images within 1 second, then its frequency is 60 Hz. On the other hand, the camera is able to capture limited images in a given time. For instance, if we use the camera to capture 60 images within 1 second, then the camera frequency is 60 Hz. Here, if we want to use the camera to capture the correctly corresponding frame provided by the video projector, we have to set the frequency of the camera equal to the frequency of the video projector. Otherwise, if the frequencies between the video projector and the camera are not equal, we will observe a “flicker effect” in the camera which will deteriorate the received image intensity distribution, and therefore, the accuracy of the unwrapped phase map will be degenerated.

Chapter 4 Stereoscopic phase measuring deflectometry technique

In this chapter, we present the stereoscopic phase measuring deflectometry (SPMD) technique to measure the shape of a specular surface. In Section 4.1, we propose a height-normal ambiguity elimination method, from which we can obtain both the surface normal and the absolute surface height of the measured object, simultaneously. In particular, the height-normal ambiguity elimination is accomplished by minimizing the difference between the phase distributions on the LCD and the stereoscopic camera. To accomplish this, we develop a polynomial fitting method in Section 4.2, and the surface normal is therefore determined. Moreover, to enhance the surface normal measurement accuracy, we also introduce sub-pixel interpolation to establish the correspondence between the phase maps on the LCD plane and the camera image plane. Specifically, two different methods described as bi-linear sub-pixel interpolation and bi-cubic sub-pixel interpolation are discussed in Section 4.3, respectively. Here, we select bi-cubic interpolation method to obtain a better performance. Finally, once we obtain the surface normal distribution of the complete measured surface, we use a 2D Fourier transform integration method to reconstruct the specular surface shape.

4.1 Height-normal ambiguity elimination

Stereoscopic phase measuring deflectometry (SPMD) is a specular surface shape measurement technique based on surface normal calculation. In this section, we

introduce the principle of SPMD measurement, and we use a phase difference minimization method to solve the height-normal ambiguity issue in the SPMD system.

Stereoscopic phase measuring deflectometry system consists of a flat LCD screen displaying sinusoidal fringe patterns (SFPs), two cameras capturing the reflected fringes, and the tested specular surface. In this case, the phase distribution on the LCD is recorded, and we use this phase distribution to generate the SFPs. Later, the fringe patterns are reflected by the specular surface and then being captured by both cameras. Now, we use the camera distortion coefficients, which are obtained from the camera intrinsic parameter calibration (see Section 3.4.1), to undistort the captured sinusoidal fringe pattern images. Once we have the undistorted sinusoidal fringe patterns captured by the cameras, we use phase shifting and phase unwrapping to calculate the unwrapped phase distributions into both cameras. At this moment, as we have the phase distribution on the LCD and the phase maps in both cameras, we use these phase maps to perform the inverse ray tracing to determine the surface normal.

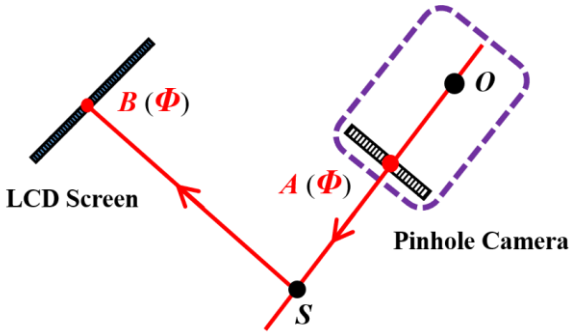

Figure 4-1. Scheme of the inverse ray tracing from the pinhole camera to the LCD screen.

Here, the inverse ray tracing is described in four sequential steps by using a pinhole camera model in Figure 4-1: (*i*) we select one point $\boldsymbol{A}$ on the camera image plane, then we record both the phase value and the spatial position of this point, (*ii*) we connect the camera pinhole $\boldsymbol{O}$ to this point to forge the primary vector, then we choose one point $\boldsymbol{S}$ along this vector as the reflection point, (*iii*) we find on the LCD screen another point $\boldsymbol{B}$ that it has the same phase value as it of the selected point $\boldsymbol{A}$, (*iv*) we record the position of point $\boldsymbol{B}$, and then we connect $\boldsymbol{S}$ with $\boldsymbol{B}$ to forge the second vector. From these two vectors, we can calculate the normal to the surface. The inverse ray tracing thus is described as the projection from the pinhole camera to the LCD screen.

Now, as the inverse ray tracing has been presented, we discuss the surface normal determination in a stereoscopic phase measuring deflectometry (SPMD) system with Figure 4-2.

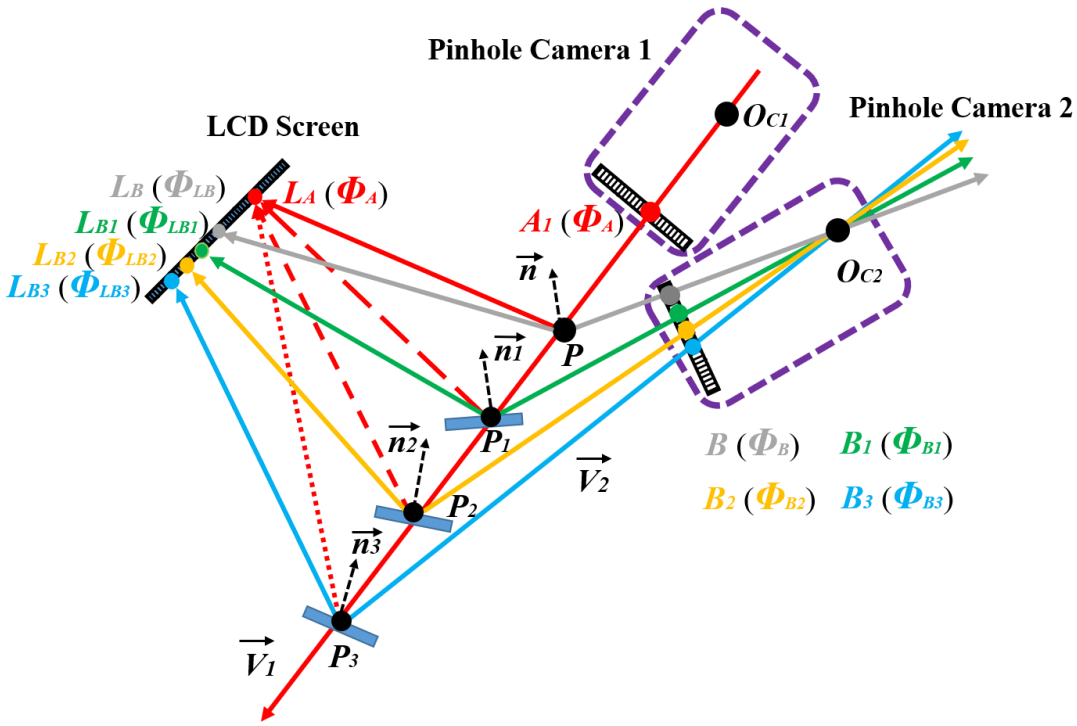

Figure 4-2. Scheme of the SPMD system for surface normal determination.

To perform the SPMD surface point determination, we firstly calculate the phase maps in both cameras using the captured fringe pattern images with phase shifting and phase unwrapping. Here, we need to emphasize that as we have already used camera distortion coefficients to correct the distortion of the fringe pattern images, these images are in fact presented without any optical distortion. Next, we select any given point $\boldsymbol{A_1}$ on the first camera image plane, and we build the basic vector $\boldsymbol{V_1}$ by connecting $\boldsymbol{A_1}$ with the camera pinhole $\boldsymbol{O_{C1}}$. Here, $\boldsymbol{V_1}=\boldsymbol{A_1}-\boldsymbol{O_{C1}}$. $\boldsymbol{V_1}$ is presented in Figure 4-2 as the red solid line, and the phase value of $\boldsymbol{A_1}$ is Φ_A. Then, we find on the LCD screen a certain point $\boldsymbol{L_A}$ which contains the same phase value as it of $\boldsymbol{A_1}$ by sub-pixel interpolation (this is to be discussed in Section 4.3). Here, the phase value of point $\boldsymbol{L_A}$ is as well Φ_A. Now, because the phase value is not changed through surface reflection, we can tell that the ray exits from $\boldsymbol{L_A}$ is reflected by the specular surface and then being projected to the pinhole of the first camera through $\boldsymbol{A_1}$. Thus, the actual surface point corresponding to $\boldsymbol{A_1}$ must be located at one point along vector $\boldsymbol{V_1}$, but the height-normal ambiguity restricts us from finding this real surface point.

Nevertheless, we can select any point $\boldsymbol{P}$ along $\boldsymbol{V_1}$, and we obtain the reflected ray as $\boldsymbol{PL_A}$ ($\boldsymbol{PL_A}=\boldsymbol{L_A}-\boldsymbol{P}$). Then, by using Reflection Law, the surface normal $\boldsymbol{n}$ at point $\boldsymbol{P}$ can be obtained ($\boldsymbol{n}=\boldsymbol{PL_A}-\boldsymbol{V_1}$). Here, we give three potential surface points (i.e., $\boldsymbol{P_1}$, $\boldsymbol{P_2}$ and $\boldsymbol{P_3}$ in Figure 4-2) along vector $\boldsymbol{V_1}$, and their corresponding normal are drawn in Figure 4-2. Within these three points, we assume that $\boldsymbol{P_1}$ is the real surface point, whereas $\boldsymbol{P_2}$ and $\boldsymbol{P_3}$ represent the fake surface points.

For the next step, we introduce the second camera to find the real surface point along $\boldsymbol{V_1}$. Here, with the help of the second pinhole camera, another inverse ray tracing relation is established. Let point $\boldsymbol{P}$ along $\boldsymbol{V_1}$ be the hypothetical surface point, then vector $\boldsymbol{V_2}$ joining point $\boldsymbol{P}$ with the second camera pinhole $\boldsymbol{O_{C2}}$ is computed ($\boldsymbol{V_2}=\boldsymbol{P}-\boldsymbol{O_{C2}}$). The intersection of $\boldsymbol{V_2}$ to the second camera image plane gives us point $\boldsymbol{B}$ (see the gray line case in Figure 4-2), and its phase value Φ_B is calculated through sub-pixel interpolation (this is to be discussed in Section 4.3). As it was previously described, the normal to the hypothesis surface point $\boldsymbol{P}$ (i.e., $\boldsymbol{n}$) was calculated from the first pinhole camera, so we use such normal $\boldsymbol{n}$ to determine the inverse reflection point $\boldsymbol{L_B}$ on the LCD plane corresponding to point $\boldsymbol{B}$. We also want to note that the phase value at point $\boldsymbol{L_B}$ is also calculated through sub-pixel interpolation as Φ_{LB} (this sub-pixel interpolation is also to be discussed in Section 4.3). Now, if the hypothetical point $\boldsymbol{P}$ we selected coincides with the real surface point $\boldsymbol{P_1}$, the phase values at $\boldsymbol{B_1}$ and $\boldsymbol{LB_1}$ (i.e., Φ_{B1} and Φ_{LB1}) should be equal, this is shown in Figure 4-2 as the green lines. However, if the hypothetical point $\boldsymbol{P}$ we picked is a fake surface point $\boldsymbol{P_2}$, then the corresponding points on both the LCD screen and the second camera image plane as $\boldsymbol{B_2}$ and $\boldsymbol{LB_2}$ have different phase values (yellow solid lines obtained from $\boldsymbol{n_2}$ in Figure 4-2). Thus, the phase difference between these two points is not zero. The reason to such phase difference is that in the real implementation, $\boldsymbol{LB_2}$ is reflected by another surface point rather than $\boldsymbol{P_2}$ and this leads to the real reflected point located somewhere else but not $\boldsymbol{B_2}$. Finally, we also pick a third fake point $\boldsymbol{P_3}$ as the hypothetical surface point. By comparing it to $\boldsymbol{P_2}$, point $\boldsymbol{P_3}$ is located farther to the real surface point $\boldsymbol{P_1}$ along vector $\boldsymbol{V_1}$ (see the blue solid line case in Figure 4-2). Thus, the phase difference between $\boldsymbol{P_3}$ and $\boldsymbol{LB_3}$ is greater than it of the $\boldsymbol{P_2}$ case.

From the above discussion, the surface point determination can be performed by minimizing the absolute phase difference with respect to point $\boldsymbol{P}$ along vector $\boldsymbol{V_1}$. We should highlight that the absolute phase difference along the inspecting vector (i.e. $\boldsymbol{V_1}$) is a smooth function presenting only one minimum, and this minimum point coincides with the real surface point. Under this scenario, the square of the phase difference corresponding to this real surface point should also be a minimum. Thus,

the surface point determination can be transferred into finding one point along vector $\boldsymbol{V_1}$ which allows the phase difference square value between the second camera and the LCD being the minimum. Then, the surface point determination is mathematically obtained by minimizing the phase difference square function. Finally, to numerically present the whole surface normal measurement process, we describe the complete mathematical phase minimization process in Appendix.

4.2 Iterative algorithm for surface point determination

By now, the surface point determination is analogous as finding one point along the inspecting vector $\boldsymbol{V_1}$ that makes its corresponding phase difference square value between the second camera and the LCD to be the minimum. Thus, to execute the surface point determination, we have the following mathematical expression as:

$$(\Phi_B - \Phi_{LB})^2 = \delta\,, \tag{4.1}$$

where δ is the square of the phase difference, Φ_B and Φ_{LB} are the correspondent phase values on the second camera image plane and the LCD panel with respect to the potential surface point along $\boldsymbol{V_1}$, respectively. In Eq. (4.1), we want to obtain the square of the phase difference equal as zero. However, the phase acquisition error (i.e., error from the camera pixel quantization) or the system calibration error in the real implementation leads the minimum phase difference square greater than zero. So, we set another tiny value ε, and it denotes an arbitrary small quantity with respect to the square of the phase difference. If phase difference square δ of a surface point along the inspecting vector $\boldsymbol{V_1}$ is smaller than this tiny value ε, we take this point and regard it as the real surface point. To perform the surface point determination process with Eq. (4.1), we have discussed a polynomial fitting phase minimization method.

In polynomial fitting phase minimization method, we preliminarily select a pixel on the first camera image plane and forge its inspecting vector $\boldsymbol{V_1}$. Afterwards, we pick several hypothesis surface points along $\boldsymbol{V_1}$. Once these hypothesis points are selected, we perform the inverse ray tracing between the second pinhole camera and the LCD to all these selected hypothesis surface points, from which the phase difference square values of these hypothesis points are all calculated. For instance, we select 6 hypothesis points as $\boldsymbol{P_1}$ to $\boldsymbol{P_6}$, and their corresponding phase difference square values are calculated as $\Delta\Phi_{P1}$ to $\Delta\Phi_{P6}$. Here, these six hypothesis points are depicted as the red dots in Figure 4-3. Moreover, $\boldsymbol{O}$ represents the real surface point, the

horizontal axis means the position of the hypothesis point to the real surface point. Now, we fit these phase difference square values to a second order polynomial function as the purple curve. Finally, as we get the mathematical description of this second order polynomial function, we look for its minimum. Then, we decide this minimum point in the polynomial function as the real surface point (i.e., purple dot $\boldsymbol{P}$).

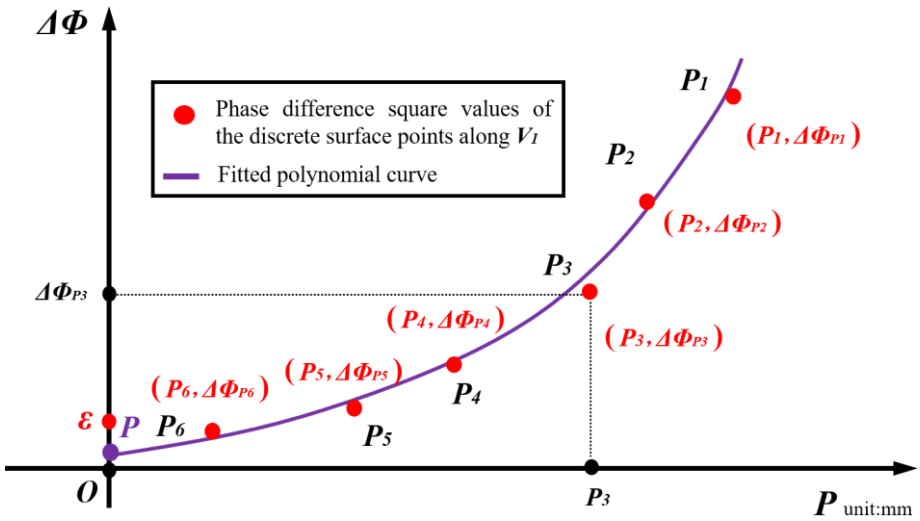

Figure 4-3. Schematic diagram to determine the real surface point by using a polynomial fitting method. The red dots are the hypothesis surface points along vector $\boldsymbol{V}_1$, and the purple curve is the polynomial function curve fitted by using the red dots.

To accomplish a robust phase minimization, it is better to locate the hypothesis surface points close to the real surface. However, the hypothesis points may not always be directly estimated close to the actual surface in the real implementation, and therefore, the surface point determination may not be directly accomplished by performing just one time the polynomial fitting minimization. Nevertheless, as polynomial fitting guarantees the phase difference square value being gradually modulated close to the minimum, we can then determine the final surface point accurately by simply introducing more iterations until the phase difference square value δ is smaller than ε (see Figure 4-3 and Eq. (4.1)). Hence, we give the flow chart in Figure 4-4 to present the phase minimization iteration.

In Figure 4-4, we firstly determine several hypothesis points along the inspecting vector $\boldsymbol{V}_1$ and calculate their corresponding phase difference square values between the second camera and the LCD. This is entitled as Step 1. In Step 2, we use these

obtained phase difference square values to fit a second order polynomial function. Thus, the particular surface point $\boldsymbol{P}$ corresponding to the minimum value of this polynomial function is obtained. In Step 3, once we obtain this surface point $\boldsymbol{P}$ through polynomial fitting, we again calculate its phase difference square value between the LCD and the second camera, and this value at point $\boldsymbol{P}$ is calculated as δ. In Step 4, we compare this phase difference square value δ at point $\boldsymbol{P}$ with ε. If this δ at point $\boldsymbol{P}$ is smaller than ε, we terminate the process and then we output this point $\boldsymbol{P}$ as the actual surface point. Otherwise, if this δ at point $\boldsymbol{P}$ is larger than ε, we trigger the subsequent polynomial fitting iteration until δ becomes smaller than ε (see Eq. (4.1)). Finally, we want to emphasize that the hypothesis surface points vary within each iteration loop, and they are gradually approaching the real surface point thanks to the smooth behavior of the phase difference square function.

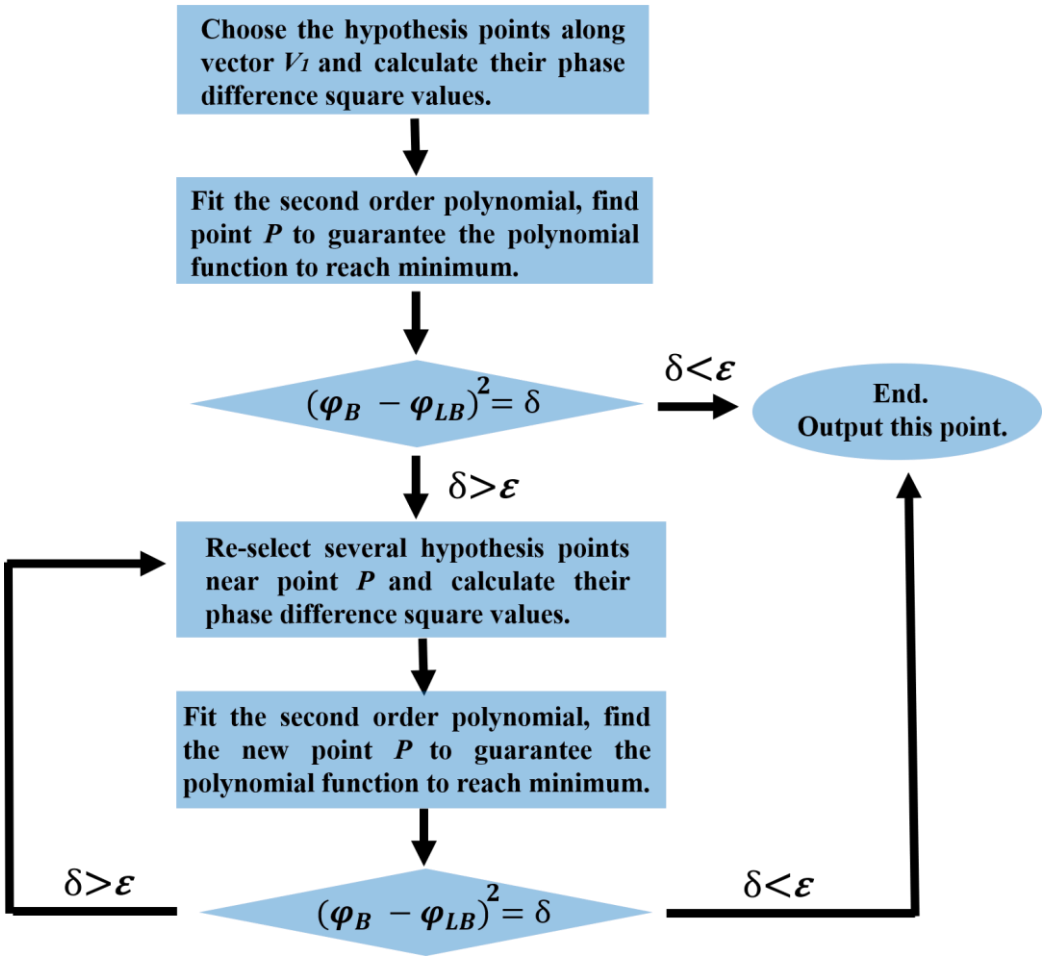

Figure 4-4. Flow chart of the surface point determination process using the second order polynomial fitting iteration method.

Finally, we want to note that in the real experimental implementation, polynomial fitting method is efficient as most surface points on the tested surface can be directly decided without any iteration calculation.

4.3 Sub-pixel interpolation

To obtain the surface normal from inverse ray tracing, we need to establish the phase pair correspondence between the camera image plane and the LCD plane. However, as it is discussed in Section 3.2, the LCD pixel or the CCD pixel introduces a quantization error to the phase function because of the finite size of the pixel [89], and thus, the phase pair correspondence is affected by such quantization error. To solve this error, sub-pixel interpolation [117–119] is proposed to achieve an accurate phase pair correspondence.

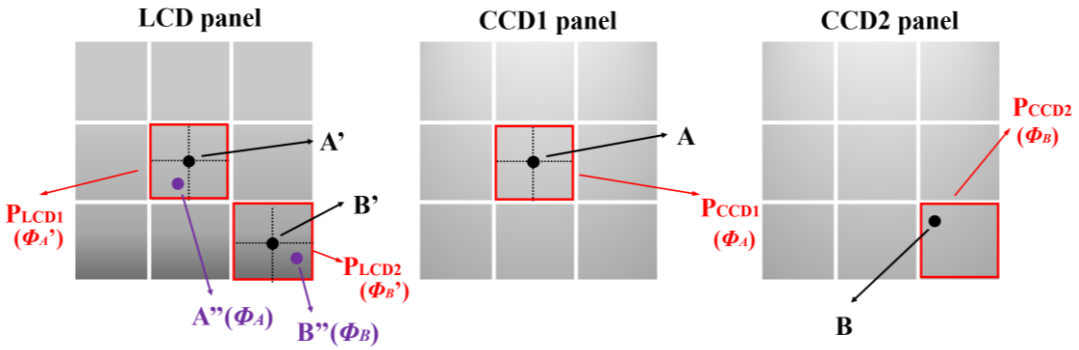

Figure 4-5. Scheme of sub-pixel interpolation between the LCD panel and the camera image planes. The LCD panel contains a 3×3 pixel region, the first camera image plane has a 3×3 pixel region, and the second camera image plane as well has a 3×3 pixel region.

For instance, we select pixel P_{CCD1} in the first CCD panel and we get its phase value as Φ_A (see the middle sub-figure in Figure 4-5). Here, point $\boldsymbol{A}$ is the geometric center of this CCD pixel. On the other side, we find its corresponding phase pair pixel P_{LCD1} on the LCD panel, that the phase value at P_{LCD1} is the closest to the phase value at pixel P_{CCD1}. In this case, we use the LCD pixel center (i.e., point $\boldsymbol{A'}$) to describe the geometric position of pixel P_{LCD1}. Nevertheless, even though we can determine the phase pair correspondence at the pixel level, the phase value at point $\boldsymbol{A'}$ in the LCD plane is not exactly equal to Φ_A due to the LCD pixel quantization error. In fact, the real phase value of point $\boldsymbol{A'}$ is Φ_A', from which $\Phi_A' = \Phi_A + \varepsilon_\Phi$, where ε_Φ is a tiny phase

offset introduced by the pixel quantization error. Under this scenario, to accurately perform the inverse ray tracing, we need to find a point that its phase value is exactly Φ_A rather than Φ_A' in this LCD pixel. To do so, we search point ***A''*** (i.e., phase value of ***A''*** is Φ_A) in the same LCD pixel P_{LCD1}, but this point is located in another geometric position rather than the center of pixel P_{LCD1}. Therefore, we have to introduce a sub-pixel interpolation method to decide the position of ***A''***, so that we can establish a refined correspondence between the LCD screen and the first camera image plane. To be more specific, we use a sub-pixel interpolation method to calculate the geometric position of point ***A''*** in the LCD pixel P_{LCD1}. Here, we introduce both bi-linear interpolation and bi-cubic interpolation, and they are later discussed.

After we have established the phase point correspondence between the first camera and the LCD by using sub-pixel interpolation, we also need to perform a secondary sub-pixel interpolation between the second CCD plane and the LCD plane. In particular, we perform the inverse ray tracing between the LCD and the second camera, so we obtain two corresponding points as ***B*** on the second CCD plane (see the right sub-figure in Figure 4-5) and ***B''*** on the LCD panel. Here, point ***B''*** is located in pixel P_{LCD2}, and point ***B*** is located in pixel P_{CCD2}. Nevertheless, both ***B''*** and ***B*** are not located at their pixel centers. Thus, the phase values at point ***B''*** and ***B*** cannot be directly given, but we also need to calculate their phase values again by using sub-pixel interpolation.

4.3.1 Bi-linear interpolation

To obtain an accurate phase pair correspondence between the CCD plane and the LCD plane, we firstly present bi-linear sub-pixel interpolation between the first CCD panel and the LCD panel. In this bi-linear interpolation scheme, we have the phase information (i.e., the vertical phase value and the horizontal phase value) of any LCD pixel center and they are entitled as $(\Phi_{hLCD}, \Phi_{vLCD})$. Moreover, we also know the geometric positions of the centers of all LCD pixels, and they are written as (x_{LCD}, y_{LCD}). A 3×3 LCD pixel region is given in Figure 4-6 as an example with the studied pixel P_{LCD} and its 8 neighboring LCD pixels. In this case, the phase values of pixel P_{LCD} at its center $({x_{LCD}}^0, {y_{LCD}}^0)$ are $({\Phi_{hLCD}}^0, {\Phi_{vLCD}}^0)$. However, as its corresponding phase pair in the first CCD panel has the phase values as $(\Phi_{hCCD1}, \Phi_{vCCD1})$, and $(\Phi_{hCCD1}, \Phi_{vCCD1})$ are different from $({\Phi_{hLCD}}^0, {\Phi_{vLCD}}^0)$ according to the quantization error, we need to find in this LCD pixel P_{LCD} another point position (x,y) with its phase values as $(\Phi_{hCCD1}, \Phi_{vCCD1})$. In other words, we let the phase values at position (x,y) in the LCD

panel (i.e., the purple point in Figure 4-6) be the same as phase values ($\Phi_{hCCD1}, \Phi_{vCCD1}$) in the first CCD plane.

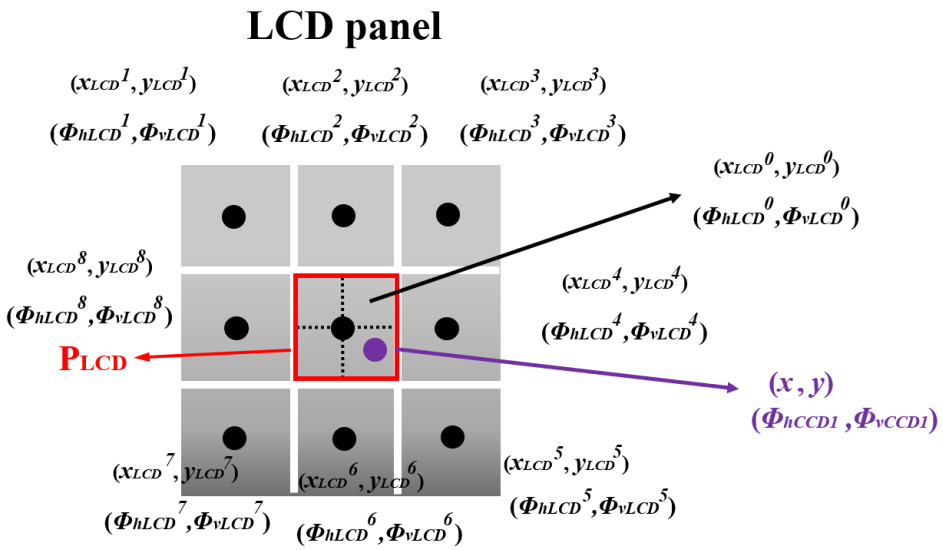

Figure 4-6. Scheme of sub-pixel phase pair correspondence using bi-linear interpolation.

To calculate the geometric position of (x,y) in LCD pixel P_{LCD}, we assume its position follows a linear tendency with respect to the phase values of the LCD pixel as:

$$x(\Phi_{hLCD}, \Phi_{vLCD}) = a_x + b_x \cdot \Phi_{hLCD} + c_x \cdot \Phi_{vLCD} + d_x \cdot \Phi_{hLCD} \cdot \Phi_{vLCD}, \tag{4.2}$$

$$y(\Phi_{hLCD}, \Phi_{vLCD}) = a_y + b_y \cdot \Phi_{hLCD} + c_y \cdot \Phi_{vLCD} + d_y \cdot \Phi_{hLCD} \cdot \Phi_{vLCD}, \tag{4.3}$$

where (a_x, b_x, c_x, d_x) and (a_y, b_y, c_y, d_y) are the linear coefficients of both X and Y directions; Φ_{hLCD} and Φ_{vLCD} are the horizontal and the vertical phase values of the LCD pixel; $x(\Phi_{hLCD}, \Phi_{vLCD})$ and $y(\Phi_{hLCD}, \Phi_{vLCD})$ are the sub-pixel geometric position in the LCD plane. Here, we write $x(\Phi_{hLCD}, \Phi_{vLCD})$ as x and $y(\Phi_{hLCD}, \Phi_{vLCD})$ as y to simplify the mathematical expression. Moreover, we will only discuss the bi-linear interpolation in X direction, as bi-linear interpolation in Y direction follows the same calculation process as it of X direction.

Now, let ε be the tiny error occurs during the bi-linear interpolation, we have:

$$\varepsilon = a_x + b_x \cdot \Phi_{hLCD} + c_x \cdot \Phi_{vLCD} + d_x \cdot \Phi_{hLCD} \cdot \Phi_{vLCD} - x. \tag{4.4}$$

To obtain the coefficients in Eq. (4.4), we should minimize the addition of its square errors. Thus, we square Eq. (4.4) and then sum all 9 pixels shown in Figure 4-6 together, we have Eq. (4.5) as:

$$E = \sum_{n=1}^{9} (a_x + b_x \cdot \Phi_{hLCD} + c_x \cdot \Phi_{vLCD} + d_x \cdot \Phi_{hLCD} \cdot \Phi_{vLCD} - x)^2 \,. \tag{4.5}$$

Then, we calculate the derivatives of Eq. (4.5) with respect to all coefficients, and we let these derivatives be zero. In this case, the derivatives are given as:

$$\frac{\partial E}{\partial a_x} = 2\sum_{n=1}^{9} (a_x + b_x \cdot \Phi_{hLCD} + c_x \cdot \Phi_{vLCD} + d_x \cdot \Phi_{hLCD} \cdot \Phi_{vLCD} - x)\,, \tag{4.6}$$

$$\frac{\partial E}{\partial b_x} = 2\sum_{n=1}^{9} \Phi_{hLCD} \cdot (a_x + b_x \cdot \Phi_{hLCD} + c_x \cdot \Phi_{vLCD} + d_x \cdot \Phi_{hLCD} \cdot \Phi_{vLCD} - x)\,, \tag{4.7}$$

$$\frac{\partial E}{\partial c_x} = 2\sum_{n=1}^{9} \Phi_{vLCD} \cdot (a_x + b_x \cdot \Phi_{hLCD} + c_x \cdot \Phi_{vLCD} + d_x \cdot \Phi_{hLCD} \cdot \Phi_{vLCD} - x)\,, \tag{4.8}$$

$$\frac{\partial E}{\partial d_x} = 2\sum_{n=1}^{9} \Phi_{hLCD} \cdot \Phi_{vLCD} \cdot (a_x + b_x \cdot \Phi_{hLCD} + c_x \cdot \Phi_{vLCD} + d_x \cdot \Phi_{hLCD} \cdot \Phi_{vLCD} - x)\,. \tag{4.9}$$

The solution to the above four equations is obtained by solving the following linear equation system as:

$$\boldsymbol{A} \cdot (a_x, b_x, c_x, d_x)^T = \boldsymbol{B}\,, \tag{4.10}$$

where matrix A is obtained with Eq. (4.6) to Eq. (4.9), and it is equal to:

$$A = \begin{pmatrix} n & \sum_{n=1}^{9} \Phi_{hLCD} & \sum_{n=1}^{9} \Phi_{vLCD} & \sum_{n=1}^{9} \Phi_{hLCD} \cdot \Phi_{vLCD} \\ \sum_{n=1}^{9} \Phi_{hLCD} & \sum_{n=1}^{9} (\Phi_{hLCD})^2 & \sum_{n=1}^{9} \Phi_{hLCD} \cdot \Phi_{vLCD} & \sum_{n=1}^{9} (\Phi_{hLCD})^2 \Phi_{vLCD} \\ \sum_{n=1}^{9} \Phi_{vLCD} & \sum_{n=1}^{9} \Phi_{hLCD} \cdot \Phi_{vLCD} & \sum_{n=1}^{9} (\Phi_{vLCD})^2 & \sum_{n=1}^{9} (\Phi_{vLCD})^2 \Phi_{hLCD} \\ \sum_{n=1}^{9} \Phi_{hLCD} \cdot \Phi_{vLCD} & \sum_{n=1}^{9} (\Phi_{hLCD})^2 \Phi_{vLCD} & \sum_{n=1}^{9} (\Phi_{vLCD})^2 \Phi_{hLCD} & \sum_{n=1}^{9} (\Phi_{hLCD})^2 (\Phi_{vLCD})^2 \end{pmatrix}. \tag{4.11}$$

On the other side, B of Eq. (4.10) is also calculated by Eq. (4.5) to Eq. (4.9), and it is equal to:

$$B = \left(\sum_{n=1}^{9} x, \sum_{n=1}^{9} x \cdot \Phi_{hLCD}, \sum_{n=1}^{9} x \cdot \Phi_{vLCD}, \sum_{n=1}^{9} x \cdot \Phi_{hLCD} \cdot \Phi_{vLCD} \right)^{T} . \tag{4.12}$$

At this moment, as we know the center point of each LCD pixel (i.e., term x in Eq. (4.12) is the central position for each LCD pixel) and their corresponding phase values (i.e., Φ_{hLCD} and Φ_{vLCD}), we can calculate any element in both Eqs. (4.11) and (4.12). Therefore, we can easily solve Eq. (4.10) and obtain the bi-linear coefficients (a_x, b_x, c_x, d_x) to determine the bi-linear interpolation function in Eq. (4.2).

Finally, as we want to find the accurate geometric point position x in the LCD pixel whose phase value is equal to its corresponding point in the first CCD, we can simply load the phase value of its corresponding point on the first CCD as $(\Phi_{hCCD1}, \Phi_{vCCD1})$ to Eq. (4.2) to calculate the sub-pixel LCD point position. Then, this LCD point position x is later used to perform the accurate sub-pixel LCD-CCD1 correspondence. By repeating the above-discussed process but to Y direction, we also get the sub-pixel LCD point position y.

Above we discuss the bi-linear sub-pixel interpolation for LCD-CCD1 phase pair correspondence, from which we can obtain the geometric position of a point (x,y) in the LCD panel with respect to its phase pair point on the first CCD plane. On the other hand, for LCD-CCD2 phase pair correspondence, we know the geometric position of a pixel in the second CCD plane and the geometric position of its corresponding pixel in the LCD plane, and we want to calculate the accurate phase values at these two points. In this case, we still use bi-linear interpolation principle, but now we assume the phase values on the LCD follow a linear tendency with respect to the LCD point positions, and the relations are written as:

$$\Phi_{hLCD}(x,y) = a_h + b_h \cdot x_{LCD} + c_h \cdot y_{LCD} + d_h \cdot x_{LCD} \cdot y_{LCD} , \tag{4.13}$$

$$\Phi_{vLCD}(x,y) = a_v + b_v \cdot x_{LCD} + c_v \cdot y_{LCD} + d_v \cdot x_{LCD} \cdot y_{LCD} , \tag{4.14}$$

where (a_h, b_h, c_h, d_h) and (a_v, b_v, c_v, d_v) are the linear coefficients; x_{LCD} and y_{LCD} are the geometric positions of the intersection point on the LCD panel; $\Phi_{hLCD}(x,y)$ and $\Phi_{vLCD}(x,y)$ are the sub-pixel phase values of the LCD intersection point. Now, by repeating the same bi-linear interpolation process, we can solve these two above equations and get the sub-pixel phase values in the LCD panel.

Finally, we repeat the bi-linear interpolation to the second CCD panel, that we assume the phase values on the second CCD panel follow a linear tendency with

respect to the intersection point positions on the second CCD panel, and such relations are written as:

$$\Phi_{hCCD2}(x,y) = a_h' + b_h' \cdot x_{CCD2} + c_h' \cdot y_{CCD2} + d_h' \cdot x_{CCD2} \cdot y_{CCD2}\,, \tag{4.15}$$

$$\Phi_{vCCD2}(x,y) = a_v' + b_v' \cdot x_{CCD2} + c_v' \cdot y_{CCD2} + d_v' \cdot x_{CCD2} \cdot y_{CCD2}\,, \tag{4.16}$$

where (a_h',b_h',c_h',d_h') and (a_v',b_v',c_v',d_v') are the linear coefficients; x_{CCD2} and y_{CCD2} are the geometric positions of the intersection point on the second CCD panel; $\Phi_{hCCD2}(x,y)$ and $\Phi_{hCCD2}(x,y)$ are the sub-pixel phase values of the second CCD panel intersection points. Again, by performing bi-linear interpolation, we get the sub-pixel phase values in the second CCD panel.

The above-discussed bi-linear interpolation method allows us to establish the accurate phase pair correspondence between the LCD and the camera image planes with sub-pixel accuracy. Therefore, the inverse ray tracing can be performed with a better performance, and we can obtain an accurate surface normal calculation.

4.3.2 Bi-cubic interpolation

In this section, we will introduce a bi-cubic interpolation method for LCD-CCD sub-pixel correspondence. In particular, we initially consider the sub-pixel correspondence between the LCD and the first CCD panel. Here, the LCD sub-pixel positions as a function of the phase values are described by the following equations as:

$$x(\Phi_{hLCD},\Phi_{vLCD}) = \sum_{i=0}^{3}\sum_{j=0}^{3} a_{xij} \cdot (\Phi_{hLCD})^i \cdot (\Phi_{vLCD})^j\,, \tag{4.17}$$

$$y(\Phi_{hLCD},\Phi_{vLCD}) = \sum_{i=0}^{3}\sum_{j=0}^{3} a_{yij} \cdot (\Phi_{hLCD})^i \cdot (\Phi_{vLCD})^j\,. \tag{4.18}$$

Here, $x(\Phi_{hLCD},\Phi_{vLCD})$ and $y(\Phi_{hLCD},\Phi_{vLCD})$ are sub-pixel point positions in the LCD panel obtained from bi-cubic interpolation, and they are later written as (x,y) for a simple mathematical expression. Moreover, a_{xij} and a_{yij} are bi-cubic interpolation coefficients; Φ_{hLCD} and Φ_{vLCD} are phase values of any LCD pixel. Again, we only discuss bi-cubic interpolation in X direction, since bi-cubic interpolation in Y direction shares a same calculation process as it of X direction.

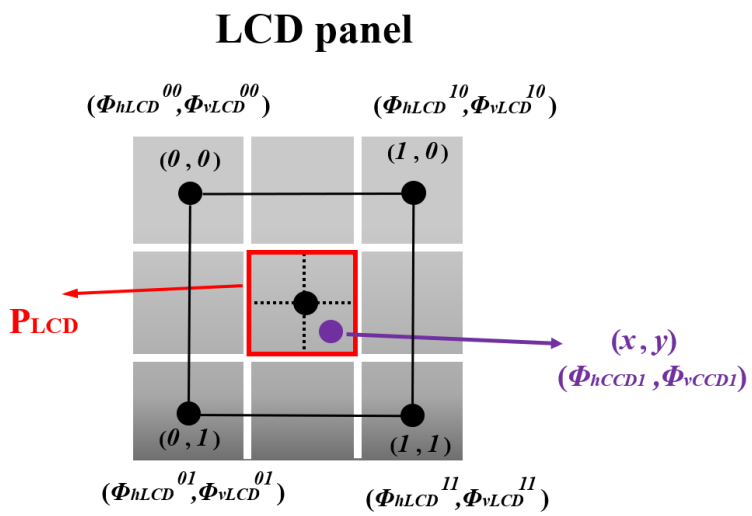

Figure 4-7. Scheme of sub-pixel phase pair correspondence using bi-cubic interpolation.

To calculate the sub-pixel point position in the LCD panel using bi-cubic interpolation, we need to obtain all 16 coefficients in Eq. (4.17). Thus, to obtain all these coefficients, we introduce a grid coordinate to represent a 3×3 LCD pixel region in Figure 4-7. Here, the studied LCD point (x,y) is in the middle pixel P_{LCD}, the phase values and the geometric positions of the surrounding pixel centers are known. Here, note that the pixels are unit squares, we then write the upper left corner pixel as (0,0), the upper right corner pixel as (1,0), the lower left corner pixel as (0,1), and the lower right corner pixel as (1,1). Then, by matching x with the function values, we obtain four equations at these four corners as:

$$x(0,0) = a_{x00}\,, \tag{4.19}$$

$$x(1,0) = a_{x00} + a_{x10} + a_{x20} + a_{x30}\,, \tag{4.20}$$

$$x(0,1) = a_{x00} + a_{x01} + a_{x02} + a_{x03}\,, \tag{4.21}$$

$$x(1,1) = \sum_{i=0}^{3}\sum_{j=0}^{3} a_{xij}\,. \tag{4.22}$$

We can also get eight equations for the derivatives in Φ_{hLCD} and Φ_{vLCD} directions as:

$$x^{h}(0,0) = \frac{\partial x}{\partial \Phi_{hLCD}}(0,0) = a_{x10}\,, \tag{4.23}$$

$$x^h(1,0) = \frac{\partial x}{\partial \Phi_{hLCD}}(1,0) = a_{x10} + 2a_{x20} + 3a_{x30}\,, \tag{4.24}$$

$$x^h(0,1) = \frac{\partial x}{\partial \Phi_{hLCD}}(0,1) = a_{x10} + a_{x11} + a_{x12} + a_{x13}\,, \tag{4.25}$$

$$x^h(1,1) = \frac{\partial x}{\partial \Phi_{hLCD}}(1,1) = \sum_{i=1}^{3}\sum_{j=0}^{3} a_{xij} i\,. \tag{4.26}$$

and,

$$x^v(0,0) = \frac{\partial x}{\partial \Phi_{vLCD}}(0,0) = a_{x01}\,, \tag{4.27}$$

$$x^v(1,0) = \frac{\partial x}{\partial \Phi_{vLCD}}(1,0) = a_{x01} + a_{x11} + a_{x21} + a_{x31}\,, \tag{4.28}$$

$$x^v(0,1) = \frac{\partial x}{\partial \Phi_{vLCD}}(0,1) = a_{x01} + 2a_{x02} + 3a_{x03}\,, \tag{4.29}$$

$$x^v(1,1) = \frac{\partial x}{\partial \Phi_{vLCD}}(1,1) = \sum_{i=0}^{3}\sum_{j=1}^{3} a_{xij} j\,. \tag{4.30}$$

We also have another four equations for the mixed partial derivatives as:

$$x^{hv}(0,0) = \frac{\partial^2 x}{\partial \Phi_{hLCD}\partial \Phi_{vLCD}}(0,0) = a_{x11}\,, \tag{4.31}$$

$$x^{hv}(1,0) = \frac{\partial^2 x}{\partial \Phi_{hLCD}\partial \Phi_{vLCD}}(1,0) = a_{x11} + 2a_{x21} + 3a_{x31}\,, \tag{4.32}$$

$$x^{hv}(0,1) = \frac{\partial^2 x}{\partial \Phi_{hLCD}\partial \Phi_{vLCD}}(0,1) = a_{x11} + 2a_{x12} + 3a_{x13}\,, \tag{4.33}$$

$$x^{hv}(1,1) = \frac{\partial^2 x}{\partial \Phi_{hLCD}\partial \Phi_{hLCD}}(1,1) = \sum_{i=1}^{3}\sum_{j=1}^{3} a_{xij} ij\,. \tag{4.34}$$

By grouping the coefficients to be calculated together, we obtain a vector as:

$$\begin{aligned}\alpha_x = [&a_{x00}, a_{x10}, a_{x20}, a_{x30}, a_{x01}, a_{x11}, a_{x21}, a_{x31}, ... \\ &a_{x02}, a_{x12}, a_{x22}, a_{x23}, a_{x03}, a_{x13}, a_{x23}, a_{x33}]^T.\end{aligned} \tag{4.35}$$

We can also forge another vector by using the previous calculated 16 equations as:

$$\begin{aligned}\beta_x = [&x(0,0), x(1,0), x(0,1), x(1,1), x^h(0,0), x^h(1,0), x^h(0,1), x^h(1,1), \ldots \\ &x^v(0,0), x^v(1,0), x^v(0,1), x^v(1,1), x^{hv}(0,0), x^{hv}(1,0), x^{hv}(0,1), x^{hv}(1,1)]^T .\end{aligned} \tag{4.36}$$

By combining Eqs. (4.35) and (4.36) together, we obtain a following equation as:

$$A\alpha_x = \beta_x \, . \tag{4.37}$$

Later, by inverting this equation, we can calculate all coefficients for Eq. (4.37) as:

$$\alpha_x = A^{-1}\beta_x \, , \tag{4.38}$$

where matrix A^{-1} is given as [120, 121]:

$$A^{-1} = \begin{pmatrix} 1 & 0 & 0 & 0 & 0 & 0 & 0 & 0 & 0 & 0 & 0 & 0 & 0 & 0 & 0 & 0 \\ 0 & 0 & 0 & 0 & 1 & 0 & 0 & 0 & 0 & 0 & 0 & 0 & 0 & 0 & 0 & 0 \\ -3 & 3 & 0 & 0 & -2 & -1 & 0 & 0 & 0 & 0 & 0 & 0 & 0 & 0 & 0 & 0 \\ 2 & -2 & 0 & 0 & 1 & 1 & 0 & 0 & 0 & 0 & 0 & 0 & 0 & 0 & 0 & 0 \\ 0 & 0 & 0 & 0 & 0 & 0 & 0 & 0 & 1 & 0 & 0 & 0 & 0 & 0 & 0 & 0 \\ 0 & 0 & 0 & 0 & 0 & 0 & 0 & 0 & 0 & 0 & 0 & 0 & 1 & 0 & 0 & 0 \\ 0 & 0 & 0 & 0 & 0 & 0 & 0 & 0 & -3 & 3 & 0 & 0 & -2 & -1 & 0 & 0 \\ 0 & 0 & 0 & 0 & 0 & 0 & 0 & 0 & 2 & -2 & 0 & 0 & 1 & 1 & 0 & 0 \\ -3 & 0 & 3 & 0 & 0 & 0 & 0 & 0 & -2 & 0 & -1 & 0 & 0 & 0 & 0 & 0 \\ 0 & 0 & 0 & 0 & -3 & 0 & 3 & 0 & 0 & 0 & 0 & 0 & -2 & 0 & -1 & 0 \\ 9 & -9 & -9 & 9 & 6 & 3 & -6 & -3 & 6 & -6 & 3 & -3 & 4 & 2 & 2 & 1 \\ -6 & 6 & 6 & -6 & -3 & -3 & 3 & 3 & -4 & 4 & -2 & 2 & -2 & -2 & -1 & -1 \\ 2 & 0 & -2 & 0 & 0 & 0 & 0 & 0 & 1 & 0 & 1 & 0 & 0 & 0 & 0 & 0 \\ 0 & 0 & 0 & 0 & 2 & 0 & -2 & 0 & 0 & 0 & 0 & 0 & 1 & 0 & 1 & 0 \\ -6 & 6 & 6 & -6 & -4 & -2 & 4 & 2 & -3 & 3 & -3 & 3 & -2 & -1 & -2 & -1 \\ 4 & -4 & -4 & 4 & 2 & 2 & -2 & -2 & 2 & -2 & 2 & -2 & 1 & 1 & 1 & 1 \end{pmatrix} . \tag{4.39}$$

Once the coefficients are obtained, we can perform bi-cubic sub-pixel interpolation. However, we still do not know those derivatives in Eq. (4.36). But this is easy to be solved, as they are typically approximated from the values at the neighboring points. For instance, we can use LCD pixels at (-1,0) and (1,0) to calculate the derivatives of LCD pixel (0,0) as:

$$\frac{\partial x}{\partial \Phi_{hLCD}}(0,0) = \frac{x(1,0) - x(-1,0)}{\Phi_{hLCD}(1,0) - \Phi_{hLCD}(-1,0)} \, , \tag{4.40}$$

where the pixel center positions and the phase values at LCD pixel (-1,0) and (1,0) are obtainable.

Then, for the mixed derivative, we use 4 neighboring points and we give one example as the following equation:

$$\frac{\partial^2 x}{\partial \Phi_{hLCD} \partial \Phi_{vLCD}}(0,0) = \frac{[x(1,1) + x(-1,-1)] - [x(1,-1) + x(-1,1)]}{[\Phi_{hLCD}(1,1) - \Phi_{hLCD}(-1,-1)] \cdot [\Phi_{vLCD}(1,-1) - \Phi_{vLCD}(-1,1)]}. \tag{4.41}$$

Once we determine the bi-cubic coefficients in Eq. (4.17), we can use such bi-cubic interpolation function to calculate the accurate geometric point position x in the LCD panel, whose phase values are equal to phase values $(\Phi_{hCCD1}, \Phi_{vCCD1})$ of its corresponding point on the first CCD plane. Later, by performing the same process to Y direction, we also get the sub-pixel interpolation point position y. Finally, for sub-pixel interpolation between the LCD panel and the second CCD panel, we also use this bi-cubic interpolation principle to establish the sub-pixel correspondence.

Bi-cubic interpolation guarantees a higher accuracy as such interpolation is smoother compared to bi-linear interpolation. However, bi-linear method gives a faster calculation speed, as bi-linear interpolation only needs to calculate 4 coefficients, but bi-cubic interpolation requires 16 coefficients. Under this scenario, a trade-off between the calculation speed and the sub-pixel correspondence accuracy has to be considered. For surface measurement discussed in this thesis, we focus on high accuracy measurement, and thus, we use bi-cubic interpolation to conduct the sub-pixel interpolation.

4.4 2D Fourier integration based surface reconstruction

In this section, we introduce a 2D Fourier integration method to reconstruct the specular surface. In particular, surface reconstruction is performed by using the surface derivative information [122]. The derivative distribution of the whole surface is calculated from the surface normal distribution. Under this scenario, different methods such as finite-difference-based least-squares integration [123–125], radial basis functions based integration [126], and Fourier transform based integration [127, 128] have been proposed. In this thesis, we use 2D Fourier transform integration method as it provides a high surface reconstruction accuracy with a relatively fast surface reconstruction speed.

To perform the surface reconstruction with 2D Fourier transform integration, we need to use the surface derivatives and its corresponding surface point positions.

Nevertheless, the experimental measurement only gives us the surface normal, and thus, we need to calculate the surface derivatives from the surface normal. To do so, we entitle the specular surface shape as $f(x,y)$, we also give the surface normal as $\boldsymbol{n}=[n_x,n_y,n_z]$ ($\boldsymbol{n}$ is a unit vector), and the surface derivatives are $f^x(x,y)$ and $f^y(x,y)$ in X and Y directions, respectively. Thus, the surface derivatives are calculated as:

$$f^x(x,y)=\frac{n_x}{n_z}, \tag{4.42}$$

$$f^y(x,y)=\frac{n_y}{n_z}. \tag{4.43}$$

From Eqs. (4.42) and (4.43), we obtain the surface derivative distributions in two directions. However, as the distance between any two adjacent surface points from the experimental measurement may not share an equal distance, the surface derivative distribution matrix is not homogeneous. Here, a homogeneous matrix means that the distance between any two adjacent surface point should be equal, and the derivatives are periodically distributed. Note that as 2D Fourier integration requires the derivative matrices to be homogeneous, we perform an interpolation at the very beginning to make the surface derivative distributions homogeneous matrices.

To do so, we can introduce different methods such as linear interpolation, cubic spline interpolation, or reflection interpolation. Once the derivatives in the matrices are modified to be periodically distributed, the edge effect during the digital Fourier transform is greatly reduced. In this thesis, we use cubic spline interpolation as it provides a high accuracy.

Once we get the homogeneous derivative distributions of the surface through interpolation, we transform these surface derivatives to the Fourier domain, and we obtain:

$$\mathcal{F}\{f^x(x,y)\}=F^u(u,v)=(i2\pi u)F(u,v), \tag{4.44}$$

$$\mathcal{F}\{f^y(x,y)\}=F^v(u,v)=(i2\pi v)F(u,v). \tag{4.45}$$

We can also perform the Fourier transform to the second order derivatives, and we obtain:

$$\mathcal{F}\{f^{xx}(x,y)\}=F^{uu}(u,v)=-(2\pi u)^2F(u,v), \tag{4.46}$$

$$\mathcal{F}\{f^{yy}(x,y)\} = F^{vv}(u,v) = -(2\pi v)^2 F(u,v). \tag{4.47}$$

To simplify the expression, we name $f^x(x,y)$ as f^x, $f^y(x,y)$ as f^y, $f(x,y)$ as f; we also entitle $F^u(u,v)$ as F^u, $F^v(u,v)$ as F^v, $F(u,v)$ as F; and we finally note $F^{uu}(u,v)$ as F^{uu}, $F^{vv}(u,v)$ as F^{vv}. Then, we have the following relations as:

$$F^{uu} = (i2\pi u)F^u = -(2\pi u)^2 F, \tag{4.48}$$

$$F^{vv} = (i2\pi v)F^v = -(2\pi v)^2 F. \tag{4.49}$$

Now, we introduce the Laplacian operator to emerge the two parameters in Eqs. (4.48) and (4.49) into one equation, and by using Fourier transform we can obtain:

$$\mathcal{F}\{\nabla^2 f\} = F^{uu} + F^{vv}. \tag{4.50}$$

Eq. (4.50) can be further expanded into another form as:

$$\begin{aligned} &\mathcal{F}\{\nabla^2 f\} = F^{uu} + F^{vv} = (i2\pi u)F^u + (i2\pi v)F^v \\ &= -(2\pi u)^2 F - (2\pi v)^2 F = -[(2\pi u)^2 + (2\pi v)^2]F. \end{aligned} \tag{4.51}$$

From Eq. (4.51), we extract the final surface shape as:

$$F = -\frac{i\left[(2\pi u)F^u + (2\pi v)F^v\right]}{(2\pi u)^2 + (2\pi v)^2}, \tag{4.52}$$

where u and v are the surface point coordinates in the Fourier domain, which can be obtained by using Fourier transform; F^u and F^v are the derivatives of the surface in the Fourier domain, which are calculated by Fourier transforming the homogeneous surface derivative matrices. Under this scenario, F is obtainable, and later by using inverse Fourier transform to F, the final surface shape $f(x,y)$ is reconstructed.

The above-discussed Fourier transform algorithm allows us to get the specular surface shape. To better visualize 2D Fourier integration-based surface reconstruction, we scheme the 2D Fourier integration process in Figure 4-8.

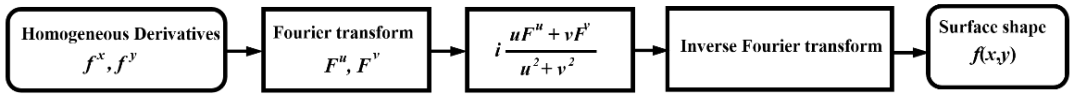

Figure 4-8. Diagram of the 2D integration method based on Fourier transform.

In Step 1, we calculate the surface derivative distributions from the experimental measured normal. Then, we interpolate the surface derivative distributions into two homogeneous matrices. In Step 2, we transform these two homogeneous derivative distributions into the Fourier domain. In Step 3, we introduce Eq. (4.52) to combine the derivative distributions and we obtain F in the Fourier domain. In Step 4, by simply introducing inverse Fourier transform, we get the integrated surface shape in the spatial domain.

The above-discussed method instructs us to theoretically calculate the surface shape through 2D Fourier integration. Nevertheless, in the real implementation, the derivatives are not consistent because of the noise, in addition, edge effects are generated when we apply Fourier transform to the real discrete data that do not maintain periodicity. Therefore, such non-periodic data may affect the 2D Fourier integration result. Under this scenario, we use an iteration method proposed in [129] to obtain a more accurate surface shape. Here, the iteration number is entitled as the convergent criteria. We describe the iteration method in Figure 4-9.

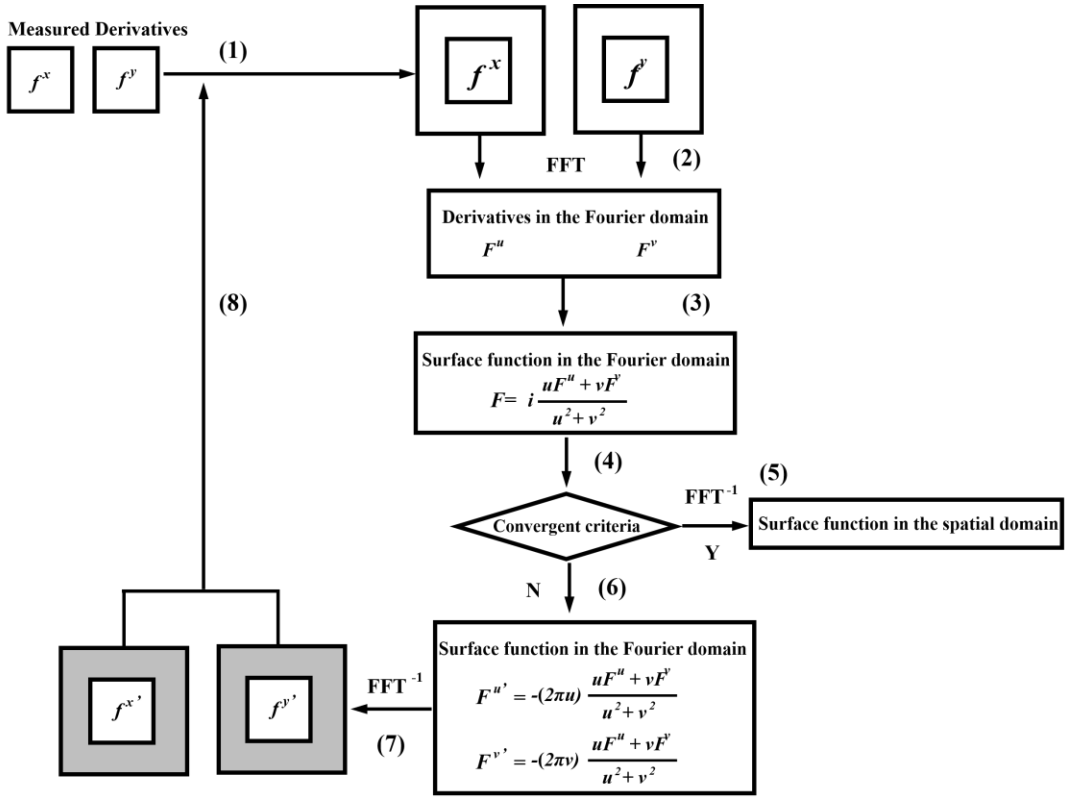

Figure 4-9. Iterative method of the 2D Fourier transform based integration for surface reconstruction.

The experimentally obtained derivatives are firstly stored in two matrices of larger dimensions (double size for each direction) surrounded by zeroes. In this manner, we can reduce the edge effects produced by the discrete Fourier transform, and this is entitled as Step 1. In Step 2, these two matrices are Fourier transformed to get F^u and F^v. Then, in Step 3, we use Eq. (4.52) to get the original surface function in the Fourier domain. If the iteration number exceeds the convergent criteria, we directly calculate the inverse Fourier transform of F and regard this result as the final surface function (see Step 5 in Figure 4-9). If the iteration number does not exceed the convergent criteria, we use this F to calculate the new derivatives in the form of Eqs. (4.44) and (4.45), and we have the new derivatives as $F^{u'}$ and $F^{v'}$ (see Step 6 in Figure 4-9). Now, we continue Step 7 to recalculate the inverse Fourier transform of the new derivatives back to the spatial domain as $f^{x'}$ and $f^{y'}$. The new derivatives are modified closer to the experimentally measured derivatives. Finally, in Step 8, we maintain the values obtained in the extension section of the matrices (i.e., the shaded part in two matrices with respect to Step 7 in Figure 4-9), and then we reintroduce the original derivatives obtained from the experimental measurements (i.e., f^x and f^y) to replace $f^{x'}$ and $f^{y'}$, then we go back to Step 2, so that we regain the newly refined derivative matrices. By repeating this process until the iteration number satisfies the convergent criteria (see Step 5), we output the final surface shape.

Here, we have to pay attention to Step 1, as in fact we introduce a larger dimension matrix to express the derivative distributions. In Figure 4-9, we simply fill the empty space with zeroes. However, it is necessary to extrapolate the surrounding areas of these larger matrices with periodical derivative values as it provides a better integration result than simply filling the matrix with zeroes. Specifically, we introduce spline extrapolation in this case.

To better visualize the extrapolation process, we present the extrapolation with Figure 4-10, that Figure 4-10 (a) is the extrapolation by rows and Figure 4-10 (b) is the extrapolation by columns. The shaded gray zone is used to represent the original experimentally measured derivative data surrounded by zeroes (i.e., zeroes are represented as white).

We firstly discuss the extrapolation in the horizontal direction (see Figure 4-10 (a)). To accomplish the extrapolation in this direction, we assume that the interpolated derivative values in both matrices are periodical, and we construct two copies of such matrices as *A'B'C'D'* and *A''B''C''D''*. Later, we impose the periodical condition and fill the matrix row by row shown as the red sections in Figure 4-10 (a). For instance,

we record both the derivatives from A to B, and the derivatives from A' to B' in Figure 4-10 (a). Then, we use these derivatives to extrapolate the empty section from B to A'. On the other side, we record the derivatives from A to B, and the derivatives from A'' to B'', and we use these derivatives to extrapolate the empty section from A to B''. Finally, we only remain the derivative information in the central expanded matrix (see the two red sections and the gray section in Figure 4-10 (a)).

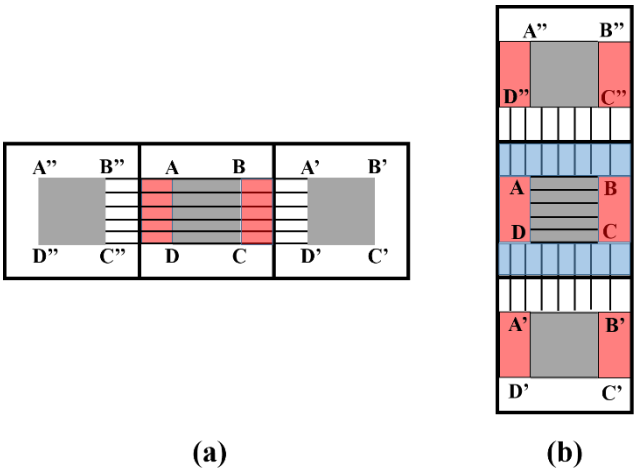

Figure 4-10. 2D derivative matrix extrapolation: (a) extrapolation within rows and (b) extrapolation within columns.

Once we accomplish the extrapolation within the rows, we extrapolate the matrix by column using the experimentally measured derivative values (i.e., gray sections in Figure 4-10 (b)) combined with the horizontal extrapolated values (i.e., red sections in Figure 4-10 (b)). By using the same manner, we fill the matrix column by column as shown in the blue sections in Figure 4-10 (b). For instance, we record both the derivatives from A to D, and the derivatives from A' to D' in Figure 4-10 (b). Then, we use these derivatives to extrapolate the empty section from D to A'. On the other side, we record the derivatives from A to D, and the derivatives from A'' to D'', and we use these derivatives to extrapolate the empty section from A to D''. Finally, we remain the derivative information in the central expanded matrix (see the two blue sections, two red sections and the gray section in Figure 4-10 (b)). At this moment, the whole enlarged matrix is filled by using 2D extrapolation.

Chapter 5 Experimental measurement using the stereoscopic phase measuring deflectometry system

In this chapter, we present the experimental measurement of specular surfaces using the stereoscopic phase measuring deflectometry (SPMD) system. We preliminarily show the SPMD system calibration, from which we can obtain the whole geometric scheme of an SPMD system. Specifically, three characteristics are calibrated as: (*i*) the gamma calibration of the LCD screen, (*ii*) the calibration of the stereoscopic camera, and (*iii*) the geometric calibration of the complete SPMD system (i.e., hand-eye calibration and LCD screen position calibration). Once the SPMD system is well calibrated, we send different sinusoidal fringe patterns (SFPs) to the LCD screen to illuminate the specular surface and then we capture the reflected SFPs with the stereoscopic camera. Now, we use phase shifting (see Section 3.2) combined with phase unwrapping (see Section 3.3) to calculate the phase map on the measured specular surface. Finally, to verify the feasibility of the proposed SPMD system, we measured different specular surfaces as a flat mirror, a spherical mirror and a discontinuous specular disk. The experimental measurement process and the results are discussed in Section 5.4.

5.1 LCD gamma calibration

In a stereoscopic phase measuring deflectometry system, the sinusoidal fringe patterns are generated on the LCD screen and later being captured by the stereoscopic camera through the specular surface reflection. Thus, the gray level-intensity response should follow a linear tendency for an accurate phase extraction. Here, the gray level is controlled by the LCD screen, and the intensity is characterized by the photons entering the camera. Nevertheless, the LCD screen used in our SPMD system (HP Elite Display E231, resolution of 1920×1080, pixel size of 0.265×0.265 mm^2) presents gamma nonlinearity, from which it deteriorates the gray level-intensity linear response and therefore the phase retrieval accuracy is deteriorated. Thus, the LCD illumination nonlinearity has to be corrected to present a linear gray level-intensity response. In this case, we accomplished the gamma correction by building an inverse look up table (LUT), which is previously discussed in Section 3.5. To be more specific, we sent constantly increasing gray levels from 0 to 255 with a step of 5 to all LCD pixels. Later, we placed the stereoscopic camera directly facing the LCD screen, and we captured the intensity images on the LCD with both cameras. Here, the first camera was inspecting the LCD screen with an angle β, and β is the angle between the first camera optical axis and the LCD screen axis. On the other hand, the second camera was inspecting the LCD screen with an angle -β, and -β is the angle between the second camera optical axis and the LCD screen axis. In this case, we let both cameras inspect the LCD screen with a same angle, so both cameras will give us a similar gray level-intensity response. On the contrary, if the two cameras are not inspecting the LCD with a same angle, then the gray level-intensity responses will be different within these two cameras, and this will bring phase retrieval error during phase shifting and phase unwrapping. Once the intensity image was captured in both cameras, we selected a central section of 10×10 pixels in each camera frame, then the average intensity of this 10×10 pixel central area was calculated and regarded as the experimentally measured intensity. Once we obtained the intensities corresponding to the whole gray level range (i.e., 0 to 255), they were fitted to a third order polynomial function. Two polynomial functions are given in Figure 5-1 with the blue curve represents the first camera and the red curve represents the second camera, respectively. The numerical functions are also given in Figure 5-1 with respect to their gray level-intensity responses.

Afterwards, as the two gray level-intensity curves in Figure 5-1 follow a same tendency and they are nearly identical, we calculated an average curve using these two fitted curves, and we built an inverse look up table (LUT) based on this averaged

curve. This inverse LUT represents the intensity-gray level response, and it means the gray level is a function with respect to the intensity in the LCD. Once we obtained this inverse LUT, we used it to perform the gamma correction. To do so, we artificially let the LCD intensities range from 0 to 255 with the intensity step as 5, and then we used the inverse LUT to calculate the gray levels g_i corresponding to these intensities, and we recorded these gray levels. Afterwards, we sent these gray levels g_i to the LCD screen, and we experimentally recorded the intensities on the LCD screen with both cameras now. The captured intensities corresponding to gray levels g_i are presented in Figure 5-2 with the first camera being shown in blue and the second camera being shown in red, respectively. The linear tendency in Figure 5-2 obviously demonstrates the feasibility of the inverse LUT-based nonlinearity gamma calibration.

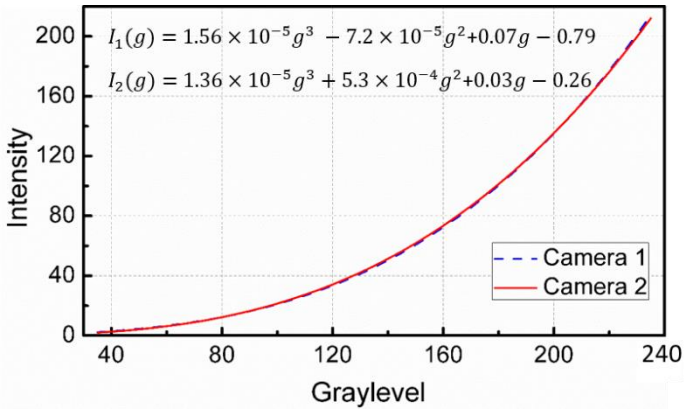

Figure 5-1. The gray level-intensity responses of both cameras before the nonlinearity calibration.

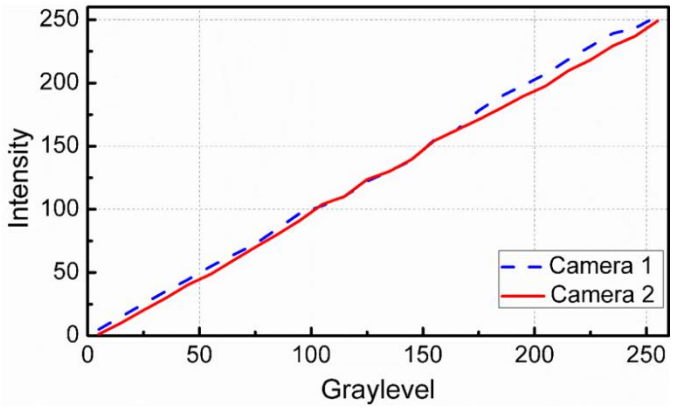

Figure 5-2. The gray level-intensity responses of both cameras after the nonlinearity calibration using the inverse look up table.

5.2 Stereoscopic camera calibration

Once the gamma calibration is completed, the stereoscopic camera calibration is subsequently performed. In stereoscopic camera calibration, we focus on two different calibrations as: (*i*) the intrinsic parameters of both cameras, and (*ii*) the extrinsic parameters between the stereoscopic camera. The camera intrinsic parameters contain the focal length of the camera objective lens, the principle point of the camera system, and the lens distortion of the camera objective lens. The extrinsic parameter of the stereoscopic camera is referred as the geometric transformation between the two cameras. To be more specific, the stereoscopic camera extrinsic calibration gives us the rotation matrix and the shifting vector from the first camera coordinate system to the second camera coordinate system.

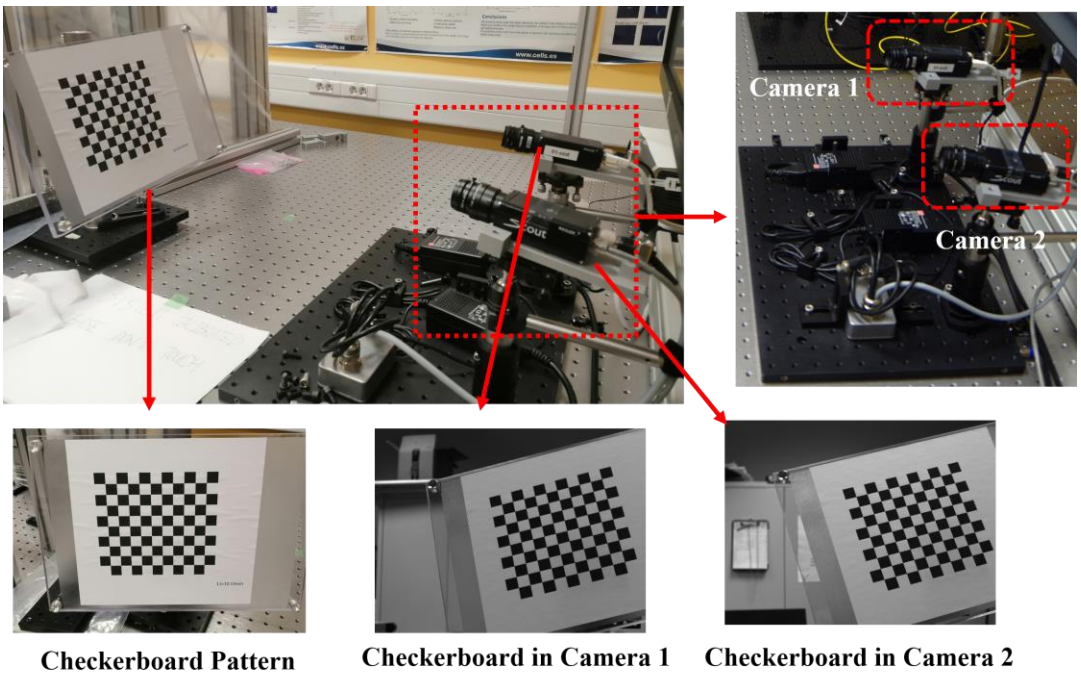

Figure 5-3. Stereoscopic camera calibration scheme using a checkerboard pattern.

Before we perform the camera calibration, let us firstly introduce the cameras used in our SPMD system. Here, as we use two cameras of the same type to construct the stereoscopic camera, we only present the characteristics of one camera. The camera consists a CCD and an objective lens. The charged-coupled devices (CCDs) is provided by Basler (Basler Scout scA1000-30gc), it has a resolution of 1034×779 and a pixel size of 4.65×4.65 μm^2. The objective lens is provided by Thorlabs (MVL12M23) with a focal length of 12 *mm*. The calibration scheme is given in Figure 5-3.

For camera intrinsic parameter calibration, we used Camera Calibration Toolbox developed by Jean-Yves Bouguet [108]. Here, we printed a checkerboard pattern on a piece of paper with its dimension as 11×10 (let us say the horizontal direction has 11 squares and the vertical direction has 10 squares, these squares are sequentially printed as black or white). The size of each square in the checkerboard is 13×13 mm^2. Later, this checkerboard was carefully stuck to a plane board to guarantee the checkerboard pattern is flat (see the left lower sub-figure in Figure 5-3). On the other side, both cameras were fixed on a flat iron board, and this iron board was located nearly 930 mm to the checkerboard to guarantee the cameras were placed in focus to capture the checkerboard pattern. Now, we let the cameras fixed on the iron board never move, but we only moved the checkerboard pattern to different locations with respect to the cameras. Then, we used both cameras to capture the checkerboard pattern at different positions so that we can perform the camera calibration with Camera Calibration Toolbox. In the real implementation, we moved the checkerboard to 104 different places, and we recorded all these 104 checkerboard frames with both cameras. Finally, we introduced Camera Calibration Toolbox [108] to calibrate the cameras using these 104 captured images, and we obtained the intrinsic parameters of each camera. The camera intrinsic parameters are given in Table 5-1 and Table 5-2:

Intrinsic parameters of the first camera	
Focal length (unit: pixel)	**2754.86, 2750.99**
Principle point (unit: pixel)	**516.72, 362.05**
Distortion coefficients	**-0.0869, 0.6799, -0.0012**

Table 5-1. The first camera intrinsic parameters obtained through camera calibration.

Intrinsic parameters of the second camera	
Focal length (unit: pixel)	**2763.55, 2760.66**
Principle point (unit: pixel)	**526.61, 368.78**
Distortion coefficients	**-0.1169, 0.7132, -0.0020**

Table 5-2. The second camera intrinsic parameters obtained through camera calibration.

Here, we need to note that the focal length and the principle point are represented with the unit of CCD pixel, and the side length of a CCD pixel is 4.65 μm.

Apart from the intrinsic parameter calibration, the geometric relation calibration between the stereoscopic camera is also required. From this calibration, we will know the rotation and the shifting from one camera to another camera. Here, we use the already captured checkerboard frames (i.e., the 104 checkerboard patterns) to perform the stereoscopic camera extrinsic calibration with Camera Calibration Toolbox [108]. The calibrated result is given by the following matrix as:

$$\boldsymbol{RT_{C1tC2}} = \begin{pmatrix} 0.9580 & -0.0052 & -0.2866 & 241.0125 \\ 0.0052 & 0.9999 & -0.0009 & -1.5536 \\ 0.2866 & -0.0007 & 0.9581 & 35.5967 \\ 0 & 0 & 0 & 1 \end{pmatrix}, \tag{5.1}$$

where $\boldsymbol{RT_{C1tC2}}$ is the transformation matrix from the first camera coordinate system to the second camera coordinate system. The first 3×3 elements represent the rotation, whereas the first three elements in the last column represent the shifting (unit in mm). Thus, we can tell from $\boldsymbol{RT_{C1tC2}}$ that the geometric distance between the two cameras is greater than 241 mm. What is more, by using $\boldsymbol{RT_{C1tC2}^{-1}}$, which is the inverse matrix of $\boldsymbol{RT_{C1tC2}}$, we can also transform any point from the second camera coordinate system to the first camera coordinate system.

5.3 Stereoscopic phase measuring deflectometry system calibration

Now, we have the intrinsic parameters of both cameras as well as the extrinsic parameter between the stereoscopic camera. To perform SPMD measurement, we also need to know the geometric relation between the LCD screen and the first camera of the stereoscopic camera system. In other words, the coordinate system transformation between the LCD coordinate system and the first camera coordinate system has to be known. Only in this way we can implement the inverse ray tracing for surface normal determination. Hence, to accomplish the SPMD system setup calibration, we sequentially perform 4 calibration steps.

In Step 1, we fixed both cameras on an iron board, and we placed this iron board close to the LCD screen (see the sub-figure in the lower right corner in Figure 5-4 (a)).

The cameras and the LCD screen were facing the same direction to fulfill the specular surface inspection. The location where the iron board sits now is registered as the initial position A in the world coordinate system (the world coordinate system of the SPMD system is defined as the first camera coordinate system which is mentioned in Section 3.6). Later, we put 6 fiducials on the cameras and traced these 6 fiducials positions using a laser tracker (3 fiducials on the first camera and 3 fiducials on the second camera, see the sub-figure in the lower left corner in Figure 5-4 (a)). Once all fiducial positions were recorded, we calculated the geometric center $\boldsymbol{O_P}$ of these 6 fiducials (see Figure 5-4 (d)) and this geometric center was used to describe the iron board located at the initial position A. Here, we need to emphasize again that the coordinate system of the iron board is not the coordinate system of the first camera, as these two coordinate systems are connected through the hand-eye calibration.

In Step 2, we moved the whole iron board, which is carrying the stereoscopic camera, to position B where both cameras can inspect the LCD screen (see Figure 5-4 (b)). In particular, the iron board was located nearly 930 mm away from the LCD screen. Again, the laser tracker was introduced to track the spatial positions of 6 fiducials at position B, and the geometric center of these 6 fiducials at position B was calculated as $\boldsymbol{O_P'}$. Now, as the fiducial positions in both position A and position B were already experimentally obtained, we can calculate the geometric transformation matrix of the iron board from position B to position A as $\boldsymbol{RT_{BtA}}$ (see Figure 5-4 (d)).

On the other hand, while the cameras were placed at position B, we generated a digital checkerboard pattern on the LCD so that the first camera can inspect this checkerboard pattern. This digital checkerboard pattern on the LCD contains a dimension as 11×10 with a square size as 12.985×12.985 mm^2. What is more, we intentionally made the digital checkerboard origin (the upper left corner grid intersection in the checkerboard pattern in Figure 5-4 (b)) coincide with the LCD screen geometric center. By now, we used the first camera at position B to capture this digital checkerboard pattern. Afterwards, we repeated this process as we moved the cameras to 39 more different positions to inspect this digital checkerboard pattern. Now, we record all these 40 images, and then we use these 40 checkerboard pattern images to perform the "inverse" camera calibration with Camera Calibration Toolbox. Therefore, we get 40 geometric transformation matrices (i.e., camera extrinsic parameters) from the LCD coordinate system to the first camera coordinate system.

Finally, as we have all these 40 transformation matrices, we select the camera at position B, and we obtained the geometric relation between the first camera coordinate

system at position B and the LCD screen coordinate system as $\boldsymbol{RT}_{LCDtC1'}$ (see the purple curve Figure 5-4 (d)).

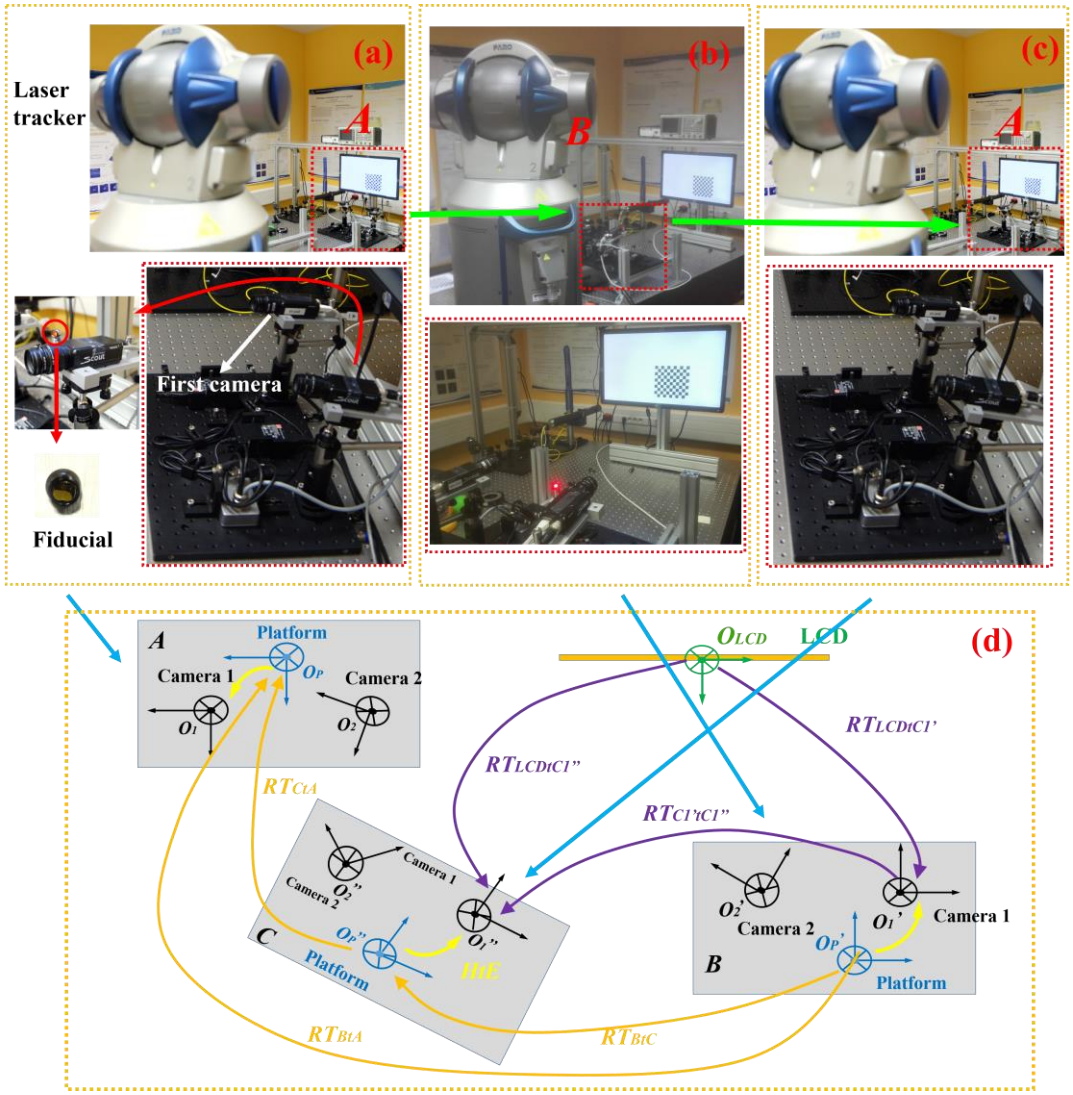

Figure 5-4. SPMD system setup calibration scheme: (a) The iron board which is carrying the stereoscopic camera is located at the initial position A close to the LCD screen. Six fiducials are mounted on both cameras for laser tracking. (b) The stereoscopic camera is moved to position B to inspect the digital checkerboard pattern generated on the LCD screen. (c) The stereoscopic camera is moved back to position A. (d) The simplified calibration process diagram for the SPMD system.

At this moment, we have two experimentally obtained transformation matrices as $\boldsymbol{RT}_{BtA}$ and $\boldsymbol{RT}_{LCDtC1'}$. Nevertheless, these two matrices still cannot let us establish

the geometric relation between the camera at position A and the LCD screen, because the hand-eye calibration is not performed. Therefore, we launched a third calibration to extract the hand-eye calibration matrix $\boldsymbol{HtE}$.

In Step 3, we moved the iron board to another position C, where the first camera can still inspect the digital checkerboard pattern on the LCD but from another position. Then, we again traced 6 fiducials at position C with laser tracker, and we calculated the fiducial geometric center at position C as $\boldsymbol{O_P''}$. Therefore, we experimentally obtained the transformation matrix of the iron board from position C to position A as $\boldsymbol{RT_{CtA}}$. At this moment, as we have the experimentally measured $\boldsymbol{RT_{BtA}}$ and $\boldsymbol{RT_{CtA}}$, we can calculate the transformation matrix $\boldsymbol{RT_{BtC}}$, which is the inner coordinate system transformation matrix of the iron board from position B to position C. Specifically, $\boldsymbol{RT_{BtC}}=\boldsymbol{RT_{CtA}}^{-1} \cdot \boldsymbol{RT_{BtA}}$.

On the other side, as we had already moved the camera to 40 different positions in Step 2, and position C is one of these 40 movements, we can also get $\boldsymbol{RT_{LCDtC1''}}$ from the "inverse" camera calibration. Here, $\boldsymbol{RT_{LCDtC1''}}$ is the transformation matrix from the LCD screen to the first camera at position C. Once we obtained $\boldsymbol{RT_{LCDtC1''}}$ and we previously have $\boldsymbol{RT_{LCDtC1'}}$, we used these two matrices to calculate the first camera transformation matrix from position B to position C as $\boldsymbol{RT_{C1'tC1''}}$. Here, $\boldsymbol{RT_{C1'tC1''}}=\boldsymbol{RT_{LCDtC1''}} \cdot \boldsymbol{RT_{LCDtC1'}}^{-1}$.

Now, we have both $\boldsymbol{RT_{C1'tC1''}}$ and $\boldsymbol{RT_{BtC}}$, we can establish a coordinate system transformation as $\boldsymbol{RT_{C1'tC1''}} \cdot \boldsymbol{HtE} = \boldsymbol{HtE} \cdot \boldsymbol{RT_{BtC}}$, where matrix $\boldsymbol{HtE}$ is the hand-eye calibration matrix. This equation can be analogous as Eq. (3.55) in Section 3.6.3 (which has the form of $\boldsymbol{AX}=\boldsymbol{XB}$), from which we can calculate the hand-eye calibration matrix $\boldsymbol{HtE}$. Moreover, to enhance the hand-eye calibration precision, we fully used all 40 different camera locations (such as position B or position C) to calculate the final hand-eye calibration matrix $\boldsymbol{HtE}$. This calculation was performed with the Matlab Toolbox developed by Christian Wengert [116].

In Step 4, as the hand-eye calibration matrix $\boldsymbol{HtE}$ was experimentally obtained, we moved the iron board, which is carrying the stereoscopic camera, back to the initial position A. Once the cameras were recovered to the initial position A, we can calculate the complete transformation matrix from the LCD screen coordinate system to the first camera coordinate system at the initial position A. To do so, we used the calibration route from the LCD to position B and then to position A as an example (i.e., $\boldsymbol{RT_{LCDtC1'}}$ to $\boldsymbol{HtE}^{-1}$ to $\boldsymbol{RT_{BtA}}$ to $\boldsymbol{HtE}$, see Figure 5-4 (d)). Here, $\boldsymbol{RT_{LCDtC1'}}$ is the LCD-first camera calibration matrix, and it was experimentally obtained from the

"inverse" camera calibration with locating the first camera at position B. Secondly, $\boldsymbol{HtE^{-1}}$ is the inverse hand-eye calibration at position B, because we need to transform from the iron board coordinate system back to the first camera coordinate system. Thirdly, $\boldsymbol{RT_{BtA}}$ is the geometric transformation matrix of the iron board from position B to position A, which we can experimentally calculate through laser tracking measurement. Finally, $\boldsymbol{HtE}$ is the hand-eye calibration matrix, which was acquired by moving the first camera to 40 different positions.

From the above four steps, we can decide the geometric relation between the LCD screen and the first camera at position A (i.e., the world coordinate system) with the transformation matrix defined as $\boldsymbol{RT_{LCDtCCD1} = HtE \cdot RT_{BtA} \cdot HtE^{-1} \cdot RT_{LCDtC1}}$. Nevertheless, it is easily noticed that $\boldsymbol{RT_{LCDtCCD1}}$ can be acquired by different routes such as from the LCD to position B then to position A, or from the LCD to position C then to position A. In fact, we have 40 different routes for SPMD system calibration as we moved the iron board to 40 different positions. Theoretically, these 40 routes should give us the same transformation matrix $\boldsymbol{RT_{LCDtCCD1}}$ because the initial position (i.e., position A) and the LCD position is fixed. However, the calibration error (i.e., laser tracking error or "inverse" camera calibration error) introduced within these 40 measurements will deteriorate the consistency of the calibration results slightly, and it is difficult to decide which calibration route we should use. Thus, to obtain a universal transformation matrix between the LCD screen and the first camera at position A, we calculate all these 40 matrices with respect to 40 iron board movements, and their averaged matrix is regarded as the final universal system calibration matrix. The final system geometric calibration matrix (from the LCD to the first camera at position A) is obtained as:

$$\boldsymbol{RT_{LCDtCCD1}} = \begin{pmatrix} -0.0058 & -0.9859 & 0.1672 & -156.7718 \\ 0.9930 & 0.0142 & 0.1177 & -253.1874 \\ -0.1184 & 0.1667 & 0.9789 & -93.9295 \\ 0 & 0 & 0 & 1 \end{pmatrix}. \tag{5.2}$$

In matrix $\boldsymbol{RT_{LCDtCCD1}}$, the first 3×3 elements represent the rotation from the LCD coordinate system to the first camera coordinate system at position A, whereas the first three elements in the last column represent the shifting (unit as mm). To better visualize the calibration result, we present the already calibrated SPMD system by labeling the coordinate systems of the LCD and the first camera in Figure 5-5.

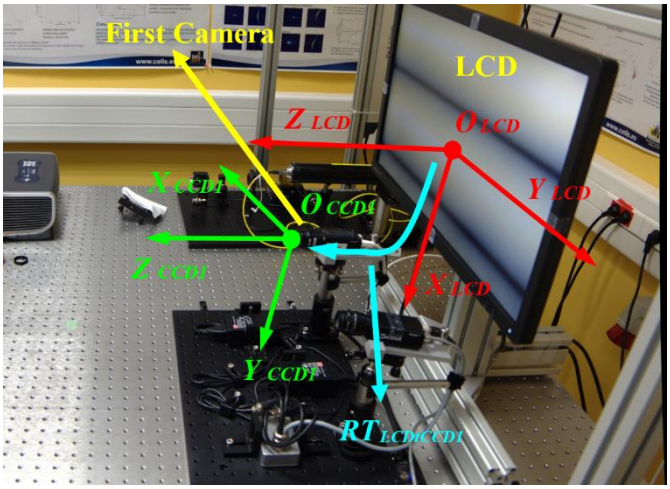

Figure 5-5. The calibrated stereoscopic phase measuring deflectometry system. The first camera coordinate system (i.e., world coordinate system) is demonstrated as (O_{CCD1}-X_{CCD1},Y_{CCD1},Z_{CCD1}), the LCD coordinate systems is demonstrated as (O_{LCD}-X_{LCD},Y_{LCD},Z_{LCD}), and the system calibration matrix is shown as $\boldsymbol{RT}_{LCD1CCD1}$.

5.4 Experimental measurements

Section 5.1 to Section 5.3 enable us to acquire all system calibration parameters in a stereoscopic phase measuring deflectometry system. In this section, we used the already calibrated SPMD system to measure different specular surfaces. In particular, we measured a flat mirror, a spherical mirror and a discontinuous specular disk. By measuring these three different objects, we would like to justify that our SPMD system is not only accurate to measure continuous specular objects with different shapes, but this system is also valid to measure discontinuous surfaces.

5.4.1 Flat mirror measurement

In flat specular mirror measurement, we selected a broadband dielectric mirror with its diameter as 50.8 *mm* (Thorlabs-BB1-E02). The mirror flatness is $\lambda/10$ at 633 *nm*. The mirror was firstly located nearly 930 *mm* to the LCD screen, and we placed its reflective surface facing the cameras. Afterwards, we adjusted the mirror position so that the sinusoidal fringe patterns on the LCD screen can be reflected by this mirror and later being captured by both cameras. In particular, the fringe patterns were

reflected to the nearly central section in both camera image planes. The experimental implementation is represented in Figure 5-6.

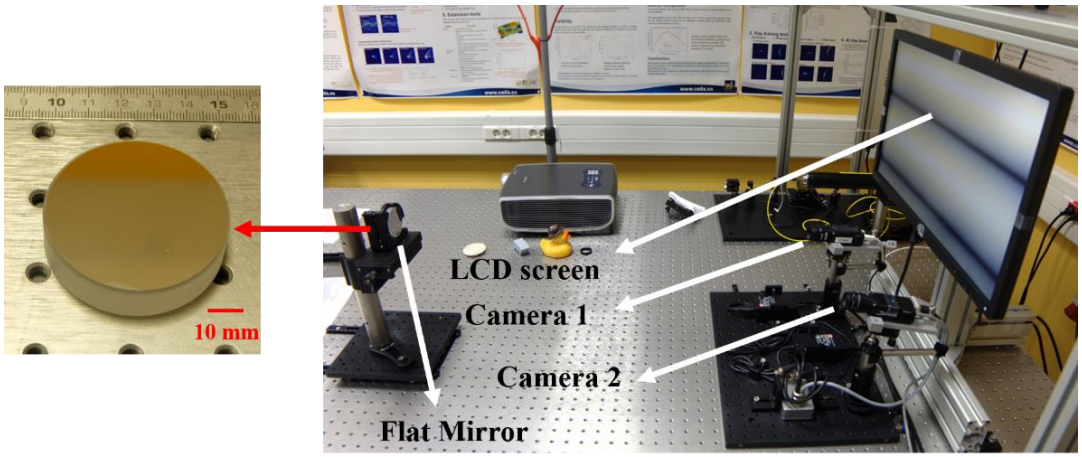

Figure 5-6. Experimental setup of the SPMD system for flat mirror measurement.

In the LCD screen, both horizontal and vertical sinusoidal fringe patterns (SFPs) were sequentially imaged by the measured mirror. Within the horizontal SFPs, three different frequencies were shown by the LCD (i.e., the resolution of the LCD is 1920×1080) with their frequencies being gradually increasing. In particular, the period of the horizontal SFPs were 540 pixels, 120 pixels and 30 pixels, respectively. Moreover, within each frequency, we introduced four different patterns with the phase-shift of $\pi/2$ for phase shifting (see Eq. (3.1)). Therefore, for horizontal SFPs, we projected in total 12 different SFPs from the LCD screen, as they are shown in Figure 5-7. On the other side, for vertical SFPs, we also sent 3 different frequencies set as 480 pixels, 120 pixels and 30 pixels to the LCD screen. Similar to the horizontal SFPs, each frequency contains four different patterns with the phase-shift of $\pi/2$.

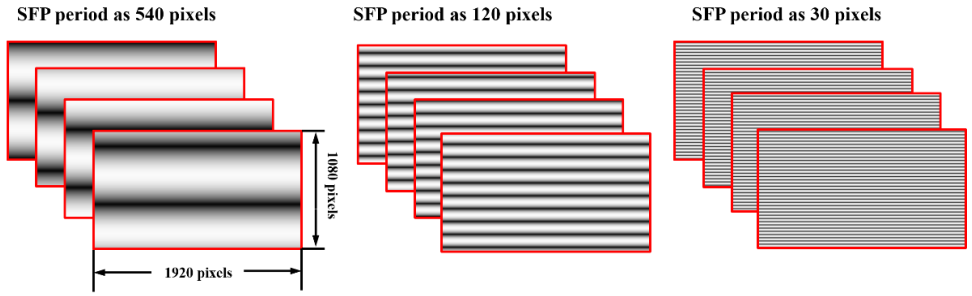

Figure 5-7. A set of 12 horizontal sinusoidal fringe patterns with 3 different frequencies used for the flat mirror measurement.

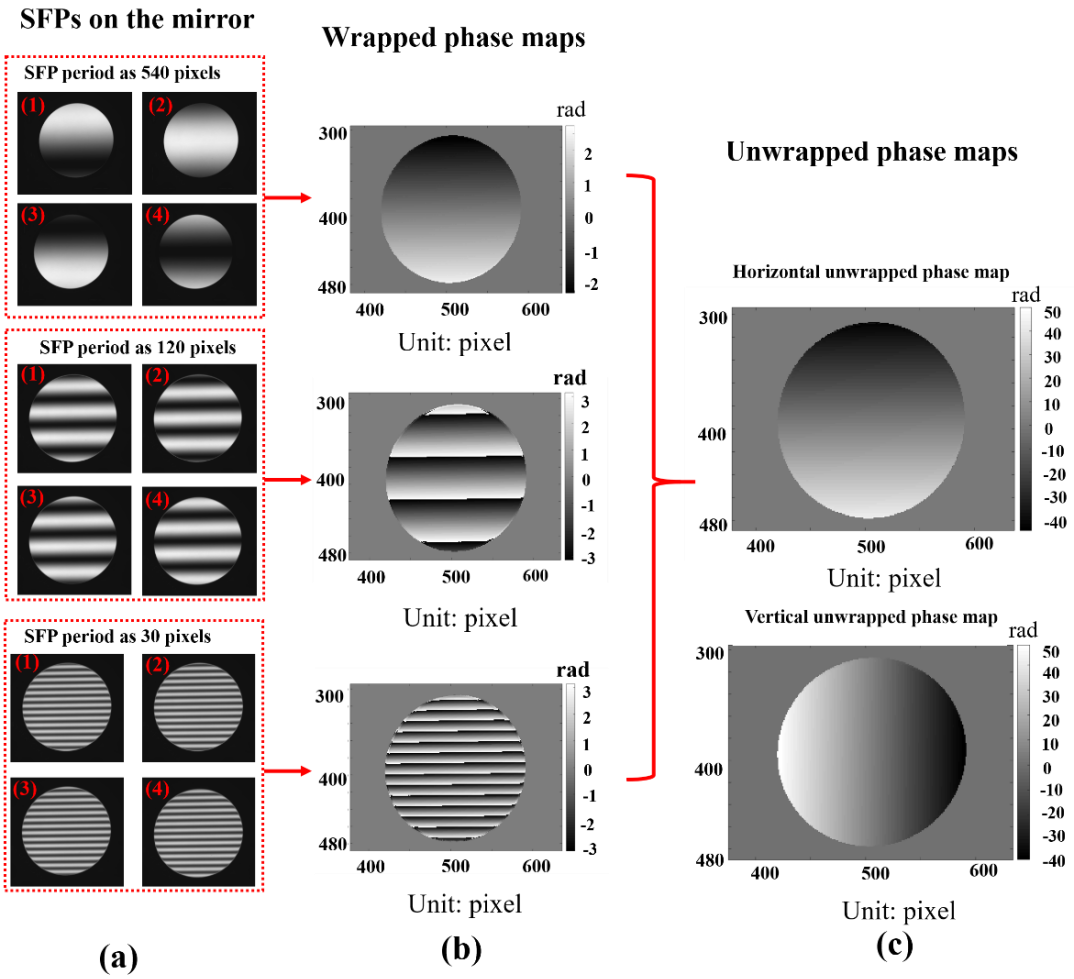

Figure 5-8. The phase unwrapping process by using the SFPs: (a) Horizontal SFPs with three frequencies are captured by the first camera. The three frequencies are 540, 120, 30 pixels, respectively. (b) By introducing phase shifting, we get three wrapped phase maps corresponding to each frequency. (c) By using all wrapped maps in (b), we get the unwrapped horizontal phase map in the first camera. Later, by performing the same phase unwrapping process to the vertical SFPs, we get the vertical unwrapped phase map.

Later, we captured these 24 fringe patterns reflected by the mirror with both cameras. Here, the LCD has a projection frequency of 60 Hz. Thus, we adjusted the exposure time and the frame rate of the stereoscopic camera, so that both cameras can capture the SFPs with the same frequency of 60 Hz. Here, the same frequency in both the LCD and the cameras guarantees us to avoid the LC flicker effect [130]. Moreover, to eliminate the random LCD illumination noise, we moved a step further

by capturing 300 images of any single frame and calculated their average intensity. This averaged intensity image is regarded as the real reflected pattern. Afterwards, the camera distortion coefficients were introduced to correct the distortion of all these averaged intensity images. At last, these averaged intensity images with their distortion corrected were regarded as the final reflected fringe patterns for phase shifting and phase unwrapping.

To present the phase unwrapping process, we use the horizontal SFPs reflected by the mirror and being captured by the first camera as an example (see Figure 5-8 (a)). Note that we have already corrected the distortion of these averaged intensity SFPs. At the beginning, by introducing phase shifting, we obtain three wrapped phase maps corresponding to each frequency shown in Figure 5-8 (b). It is obvious that the lowest frequency (i.e., SFP period as 540 pixels) shows a phase map without phase jump (i.e., the uppermost sub-figure in Figure 5-8 (b)), whereas the other phase maps present phase jumps. Moreover, the phase map related to the highest frequency (i.e., SFP period as 30 pixels, the bottom sub-figure in Figure 5-8 (b)) shows the greatest phase jump effect. Now, by unwrapping the phase maps in Figure 5-8 (b) from the lowest frequency to the highest frequency, we obtained the horizontal unwrapped phase map as the upper sub-figure shown in Figure 5-8 (c). Later, by performing the same phase unwrapping process but implemented to the vertical SFPs, we can also obtain the vertical unwrapped phase map (see the lower sub-figure in Figure 5-8 (c)). Here, Figure 5-8 (c) represents the orthogonal phase maps in the first camera.

With the above-discussed process, we get the vertical and the horizontal unwrapped phase maps within the first camera. Then, by executing the same process to the images captured by the second camera, we can also acquire the vertical and the horizontal unwrapped phase maps in the second camera. At this moment, as the orthogonal phase patterns in both cameras were experimentally obtained, we then used the second order polynomial fitting method discussed in Section 4.2 to perform the surface normal determination. The phase minimization criteria ε was set as 0.01 to establish the preliminarily phase pair correspondence. Then, bi-cubic sub-pixel interpolation was performed to further enhance the phase pair correspondence accuracy (see Section 4.3.2). Finally, by scanning all pixels on the first camera phase map, we collected the complete surface normal distributions. Then, we calculated the derivative distributions in both X and Y directions from the obtained normal information. At this time, we interpolated the obtained derivative distributions to homogeneous matrices with cubic spline interpolation. Then, we extrapolated the derivative distribution matrices into larger matrices which are twice the size of the original derivative matrices. Finally, we

performed 2D Fourier transform integration with the extrapolated derivative matrices (see Section 4.4), and the iteration loop was set as 50. The final reconstructed surface shape of the measured flat mirror is shown in Figure 5-9 (a).

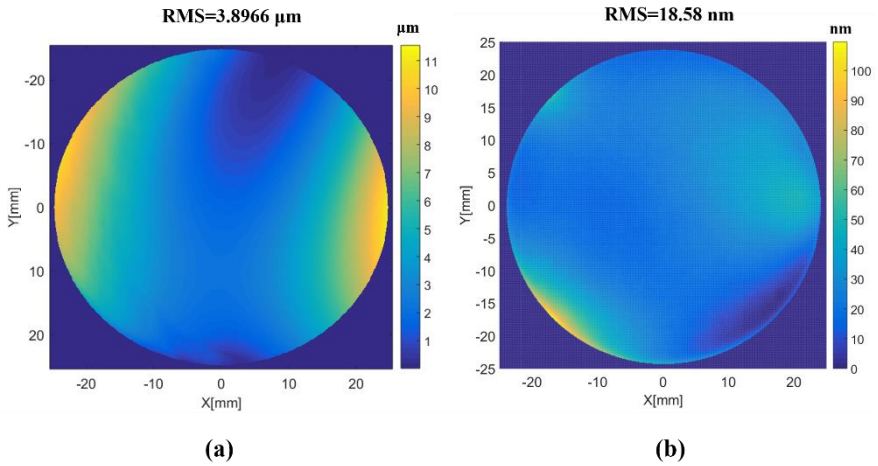

Figure 5-9. Surface shapes of the measured flat mirror (i.e., Thorlabs-BB1-E02). (a) The shape of the mirror obtained through SPMD measurement, the surface is reconstructed through 2D Fourier transform integration. (b) The surface shape of the flat mirror measured by an interferometer (Zygo Corp., MiniFiz 100).

The flat mirror measured by the SPMD system shows a smooth flatness as the root mean square (RMS) of the surface is only 3.8966 μm, whereas its peak-to-valley (PV) value is 11.5431 μm. If we further examine the reconstructed surface, it can be easily deduced that the central section of the reconstructed surface presents greater flatness whereas only the mirror edges show a slight bending.

To determine the measurement accuracy, we used an interferometer (Zygo Corp., MiniFiz 100) to measure this same flat mirror and the measured surface shape is provided in Figure 5-9 (b). The flat mirror measured by the interferometer presents the PV as 113.2 nm and the RMS as 18.58 nm. Thus, the measurement accuracy of the SPMD system, by considering the RMS value as criteria, could reach 3.878 μm by comparing the SPMD result with the interferometer result.

Even though the surface shape measured by the SPMD system presents smooth flatness, we can tell that the SPMD measured surface (Figure 5-9 (a)) shows surface bending at the mirror edge compared to the interferometer measured result (Figure 5-9 (b)). We want to note that such surface bending is in fact introduced by the system calibration error and the LCD screen inhomogeneity. Here, the system calibration error contains the laser tracker-based hand-eye calibration error and the checkerboard-

based camera calibration error. On the other hand, the LCD screen inhomogeneity can be described as the LCD panel is not flat but it is bended owing to the mechanical stress introduced during the fabrication [40,131]. In fact, by applying a more homogeneous LCD screen and by performing a more precise calibration, the surface measurement accuracy could be further enhanced.

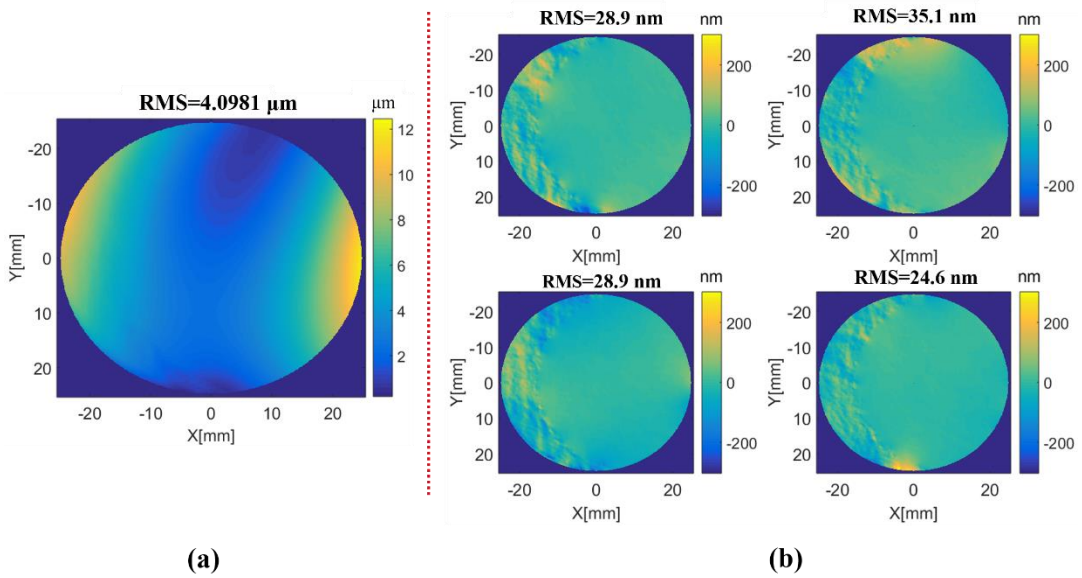

Figure 5-10. Repeatability measurement of the flat mirror: (a) The average surface shape of the four measured surfaces. (b) The surface shape differences between each individually measurement and the averaged surface.

Apart from the measurement accuracy, the measurement robustness is also critical. Hence, to examine the SPMD measurement robustness, we performed the repeatability measurement with this same flat mirror. In particular, the mirror was located at the same position and we performed the measurement for four times using the same sinusoidal fringe patterns under the same experimental condition. Once we obtain these four measured surface shapes, their averaged surface shape is calculated, and this averaged surface shape is given in Figure 5-10 (a). Moreover, the differences between the four measured surfaces and this averaged surface are also compared. The surface differences of each measured surface to this averaged surface are presented in Figure 5-10 (b).

The averaged surface in Figure 5-10 (a) gives us an RMS as 4.0981 μm, which is identical to the result demonstrated in Figure 5-9 (a) as 3.8966 μm. Moreover, note that the four figures in Figure 5-10 (b) are the surface shape differences between the four distinct measured mirror shapes and their average surface shape. So, we calculate

the RMS of each sub-figure in Figure 5-10 (b) to represent the system repeatability. The maximum RMS within all these four sub-figures is presented as only 35.1 *nm*. Thus, it is obvious that the SPMD system has great measurement repeatability and robustness.

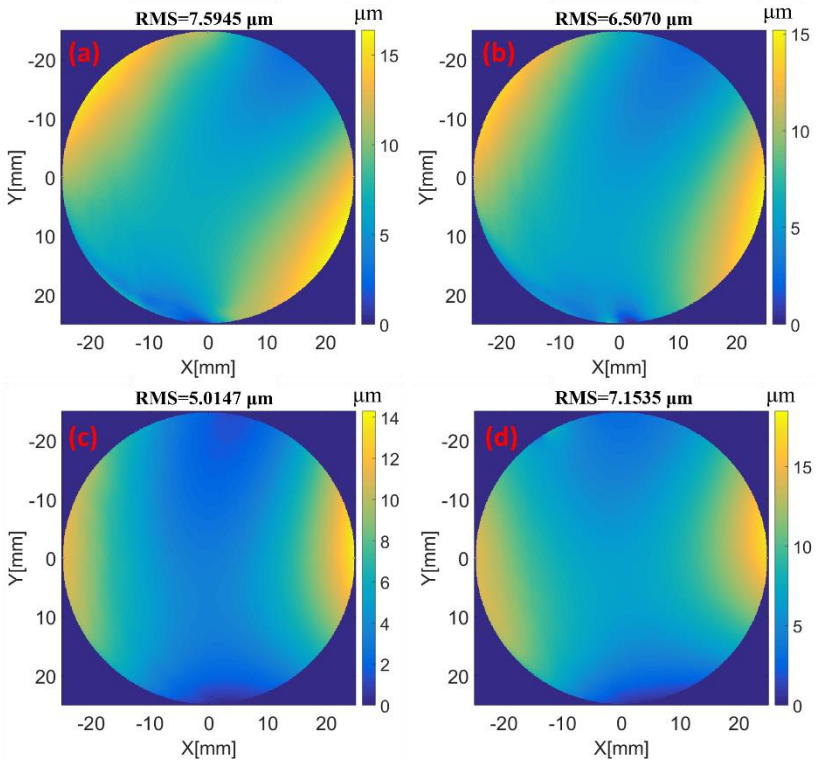

Figure 5-11. Surface shapes of the flat mirror measured by the SPMD system at different locations. The flat mirror is shifted from the original position for: (a) +2 *mm*, (b) +1 *mm*, (c) -1 *mm*, and (d) -2 *mm*.

Finally, we shifted the flat mirror position and measured the surface shapes at different locations. Here, we shifted the mirror along X axis with respect to the SPMD coordinate system origin (see Figure 5-5) for +2 *mm*, +1 *mm*, -1 *mm* and -2 *mm*, respectively. In this case, by locating the mirror away from the system origin, the mirror was not being illuminated by the central section of the LCD screen, but it was gradually being illuminated by the LCD screen edges. Moreover, the fringe patterns reflected by the mirror were not imaged to the central section in the camera image plane, but the reflected images were shifted away from the image plane center, where the lens distortion will affect the captured images a bit more seriously. We performed the surface reconstruction to these four cases, and the measured surface profiles are given in Figure 5-11.

From Figure 5-11, we can clearly tell that the measurement accuracy is slightly deteriorated when we shift the flat mirror farther from the coordinate system origin. When the flat mirror is shifted for +2 *mm* from the original position, the surface RMS is increased from 3.8966 μm to 7.5945 μm, whereas the surface RMS is only deteriorated to 6.5070 μm when the shifted distance is +1 *mm*. On the other side, the surface RMS is deteriorated to 7.1535 μm when the mirror is shifted for -2 *mm*. Here, we can see that the shifting distances of ± 2 *mm* give us nearly the same surface RMS values (i.e., 7.5945 μm and 7.1535 μm), and the surface RMS values with shifting distances of ± 2 *mm* are greater than the RMS values of shifting distances of ± 1 *mm*.

5.4.2 Spherical mirror measurement

In Section 5.4.1, the flat mirror measurement results demonstrate the feasibility and robustness of the stereoscopic phase measuring deflectometry system. In this section, we further measure a spherical mirror, to justify that the proposed SPMD system is not only able to measure the flat surface, but also it is feasible to measure the curved specular surface.

Here, the spherical mirror we measured is a dielectric-coated spherical concave mirror (Thorlabs, CM750-500-E02). The mirror provides a focal length of 500 *mm* (curvature radius of 1000 *mm*) with a diameter of 75 *mm*. The surface irregularity is $\lambda/4$ at 633 *nm* and the thickness tolerance is ± 0.2 *mm*. This spherical mirror was as well located nearly 930 *mm* to the LCD screen and the orthogonal sinusoidal fringe patterns with three frequencies were sent to the LCD screen. In this case, the horizontal SFP periods were 120 pixels, 30 pixels and 24 pixels, whereas the vertical SFP periods were set as 120 pixels, 30 pixels and 24 pixels as well. By capturing the sinusoidal fringe patterns reflected by the spherical mirror with both cameras, we can perform phase shifting and then phase unwrapping to obtain the unwrapped phase maps in both cameras. Here, note that we again captured 300 images of any frame and later calculated their average intensity to eliminate the random LCD illumination noise. Then, the distortion of these averaged images was corrected using the lens distortion coefficients. After these two steps, we performed phase unwrapping. For this spherical mirror measurement, the orthogonal unwrapped phase maps corresponding to each camera are presented in Figure 5-12. The first phase map group in Figure 5-12 (a) corresponds to the first camera, and the second phase map group in Figure 5-12 (b) corresponds to the second camera.

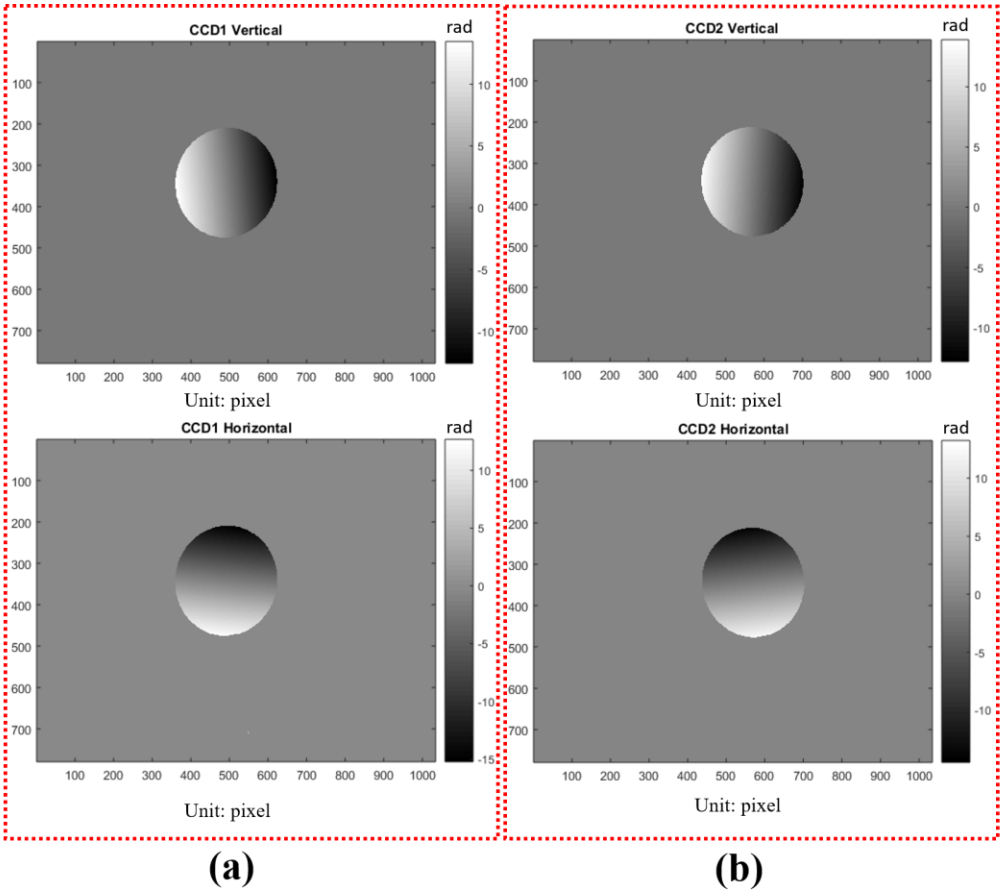

Figure 5-12. The phase maps on the spherical mirror in both cameras: (a) the orthogonal unwrapped phase patterns in the first camera, and (b) the orthogonal unwrapped phase patterns in the second camera.

Once we obtained all unwrapped phase maps on the spherical mirror, we again used the second order polynomial fitting method to calculate the surface derivative distributions. Here, the phase minimization criteria ε in Eq. (4.1) was set as 0.0225 for the preliminary phase pair correspondence, and bi-cubic sub-pixel interpolation was later introduced to enhance the phase pair correspondence accuracy. Then, we used the phase pair correspondence information to calculate the surface normal, and these normal distributions are later calculated into surface derivatives. With the surface derivative distributions, we firstly interpolated these derivative distributions into homogeneous matrices, and then we extrapolated these homogeneous derivative matrices. Afterwards, we used these extrapolated homogeneous surface derivatives in both X and Y directions to perform 2D Fourier transform integration, and the

iteration loop was set as 50 times. The final reconstructed surface shape of the measured spherical mirror is shown in Figure 5-13 (a).

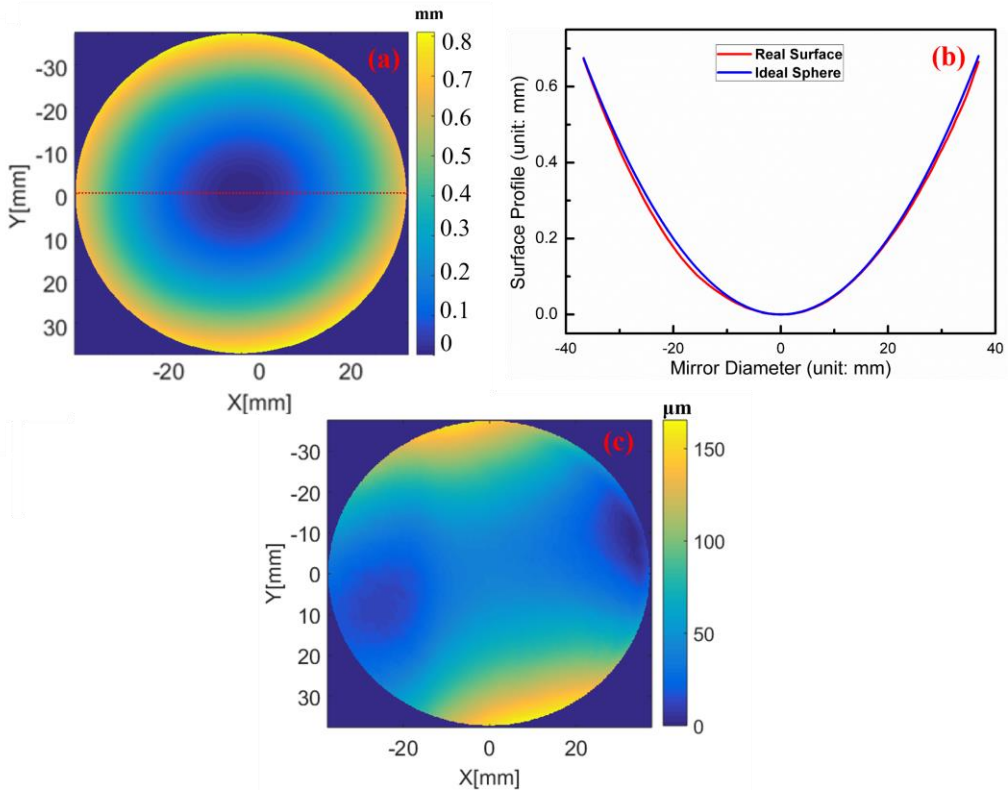

Figure 5-13. Surface shape of the measured spherical mirror (i.e., Thorlabs, CM750-500-E02): (a) The shape of the spherical mirror obtained through the SPMD measurement, the surface is reconstructed through 2D Fourier transform integration. (b) The surface shape represented by a central horizontal line. (c) The surface shape difference between the experimentally measured spherical mirror and an ideal spherical surface (i.e., radius as 1000 *mm*).

The reconstructed spherical surface in Figure 5-13 (a) shows great smoothness. The curvature radius of this mirror given by Thorlabs is 1000 *mm*, whereas the curvature radius of this measured spherical mirror is calculated as 1001.40 *mm* by selecting a central surface line in Figure 5-13 (a) (from the middle of the mirror left edge to the middle of the mirror right edge, see the red dashed line in Figure 5-13 (a)).

Moreover, we also compare this experimentally measured horizontal cross line to an ideal spherical curve, and these two curves are given in Figure 5-13 (b). It is obvious that the experimentally measured surface line (i.e., the red curve in Figure 5-13 (b), which is the same red dashed line in Figure 5-13 (a)) precisely coincides with an ideal

spherical line (i.e., blue curve in Figure 5-13 (b)), whereas only a slight difference is presented.

Finally, we construct an ideal spherical surface with a radius as 1000 *mm*, and we compare this ideal spherical surface with the experimentally obtained spherical surface, the surface difference is given in Figure 5-13 (c). From Figure 5-13 (c), we see that the measured spherical surface is bended compared to the ideal spherical surface only at the very edge, and the central section shows nearly no surface difference. Here, we need to note that the surface difference at the edges is introduced by the system calibration error as well as the LCD screen inhomogeneity.

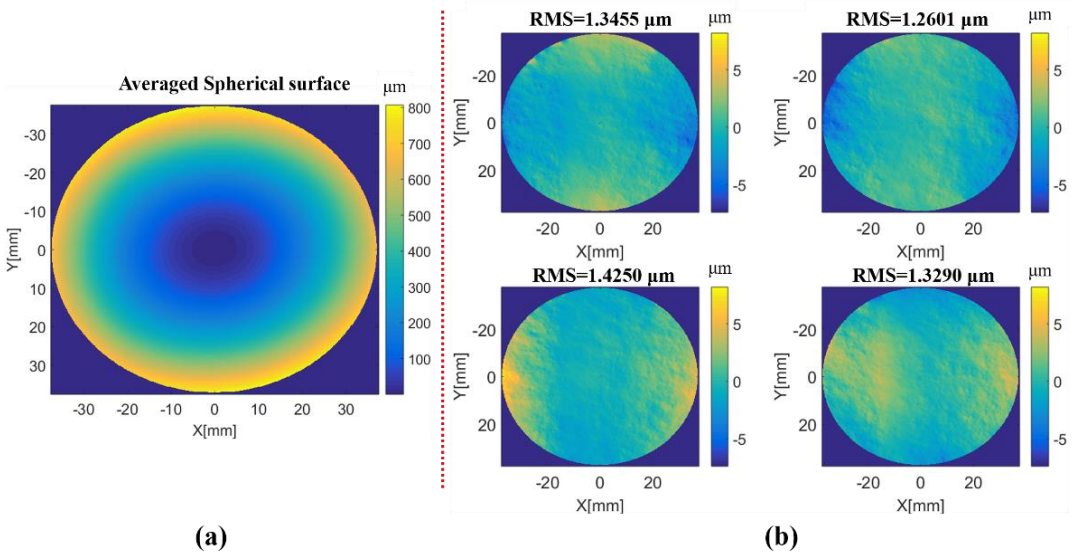

Figure 5-14. Repeatability measurement of the spherical mirror with the highest SFP frequencies as 24 pixels: (a) The average surface shape of the four measurements. (b) The surface shape difference maps between each individually measured surface and the averaged surface.

Apart from the surface shape measurement, we as well conducted the repeatability measurement of this spherical mirror. Similar to the flat mirror measurement case, we measured the spherical mirror located at the same position using the same sinusoidal fringe patterns for four times. Once these four surface shapes are obtained, we firstly calculate their average shape and this averaged spherical surface is given in Figure 5-14 (a). We can see that this averaged surface is identical to the spherical surface in Figure 5-13 (a). Furthermore, the surface differences between each measured spherical surface to this averaged surface are calculated, and the four surface difference maps are given in Figure 5-14 (b).

To verify the measurement repeatability, we calculate the RMS values of these four sub-figures shown in Figure 5-14 (b). The maximum RMS within all surface difference maps in Figure 5-14 (b) is presented as 1.4250 μm, whereas the minimum RMS value is 1.2601 μm. Here, as the four measured spherical surfaces have nearly the same surface shape, we can tell that the SPMD system has great measurement repeatability and robustness to measure the curved specular surface.

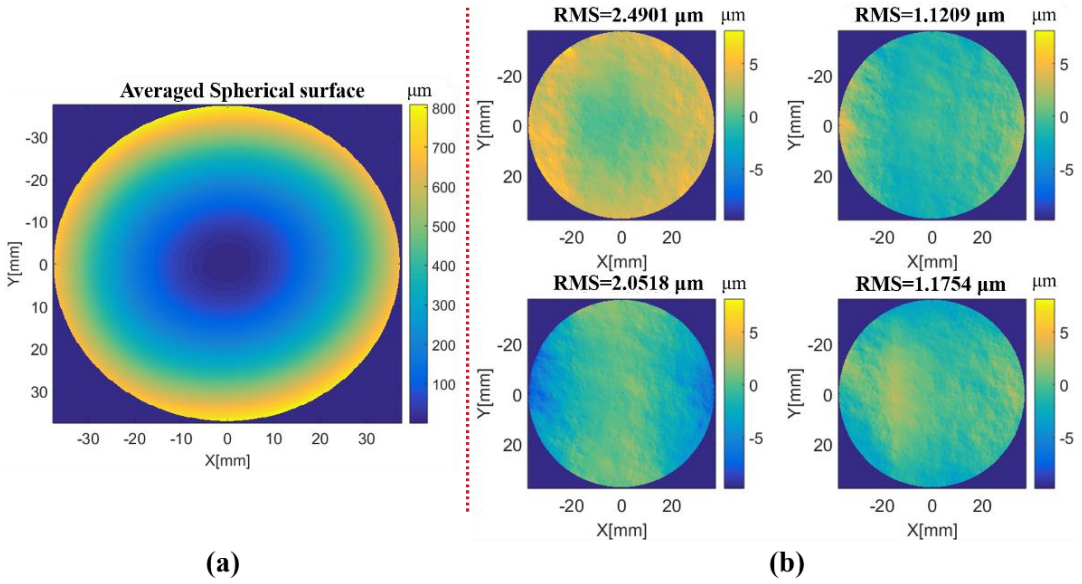

Figure 5-15. Repeatability measurement of the spherical mirror with the highest SFP frequencies as 20 pixels: (a) The average surface shape of the four measurements. (b) The surface shape difference maps between each individually measured surface and the averaged surface.

The above-discussed spherical surface measurement was performed by using the highest sinusoidal fringe pattern (SFP) frequency as 24 pixels to both horizontal and vertical directions. However, by only using one series of SFPs, we still cannot comprehensively study the SPMD system measurement robustness, as how the variation of the SFP frequencies will influence the measurement result is still not studied yet. Therefore, to more comprehensively verify the SPMD measurement robustness, we used another series of SFPs with different frequencies to perform the spherical mirror measurement. Here, we want to emphasize that it is the highest SFP frequency who determines the final unwrapped phase map distribution, so we only modified the highest frequencies in the new SFP series, as we increased the highest SFP frequency to 20 pixels in both horizontal and vertical directions to perform a secondary spherical surface measurement (the previous measurement used the SFP

series frequency of 24 pixels). Under this scenario, we measured this same spherical mirror for four times at the same position but by using the new SFPs with its highest frequency as 20 pixels. The averaged surface shape of these four measurements with respect to the new SFP frequency is given in Figure 5-15 (a), and the surface differences between each measured spherical surface to this averaged surface are compared and given in Figure 5-15 (b).

The averaged spherical surface shown in Figure 5-15 (a), which is obtained using the second series of SFP (i.e., highest frequency as 20 pixels), demonstrates an identical surface shape to that in Figure 5-14 (a). Moreover, the maximum RMS of the surface difference maps in Figure 5-15 (b) is 2.4901 μm, and the minimum RMS is 1.1209 μm. Such results are also identical to the results in Figure 5-14 (b) with only a small variation. Thus, it is obvious that the SPMD system demonstrates great robustness to measure the spherical surface even with different SFP frequencies. More importantly, by considering the accurate measurement results of both the flat mirror and the spherical mirror, we can make a conclusion that our proposed SPMD system is able to measure various specular surfaces of different shapes with great robustness.

5.4.3 Discontinuous specular surface measurement

The previous two sub-sections discuss the measurements of regular specular surfaces (i.e., a flat mirror or a spherical mirror) with the stereoscopic phase measuring deflectometry system. What is more, the experimental results prove both a reasonable measurement accuracy and a great measurement robustness. Nevertheless, in the real industrial applications, irregular specular objects are also widely used, and the surface measurement of such objects is also mandatory. Therefore, we discuss the measurement of a discontinuous specular disk in this section, from which we can justify the feasibility of using the SPMD system to measure irregular specular surfaces.

The specular disk is an almost flat round disk with its diameter of 95 mm. In this disk, it contains a hollow circle that this circle has a diameter of 26.23 mm. The whole specular disk and the hollow circle share the same geometric center, and the photograph of the nearly flat disk is given in Figure 5-16 (a). This disk also demonstrates great reflective ability, as it can reflect the sinusoidal fringe patterns to the camera as shown in Figure 5-16 (b) and Figure 5-16 (c).

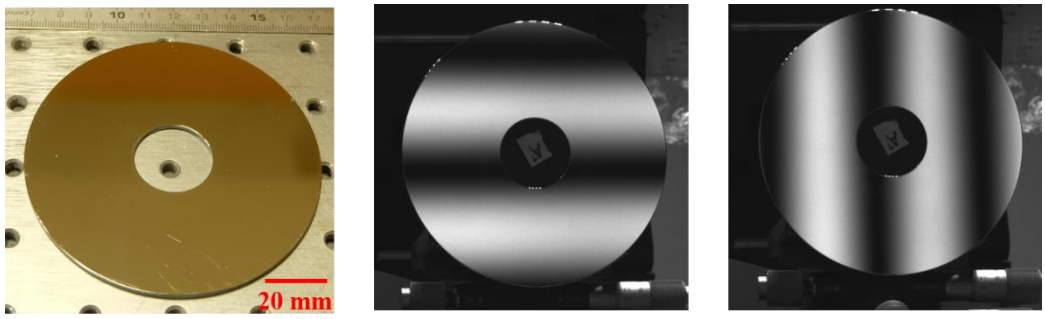

Figure 5-16. (a) The photograph of the specular disk. (b) The horizontal SFP reflected by the specular disk and captured by the camera. (c) The vertical SFP reflected by the specular disk and captured by the camera.

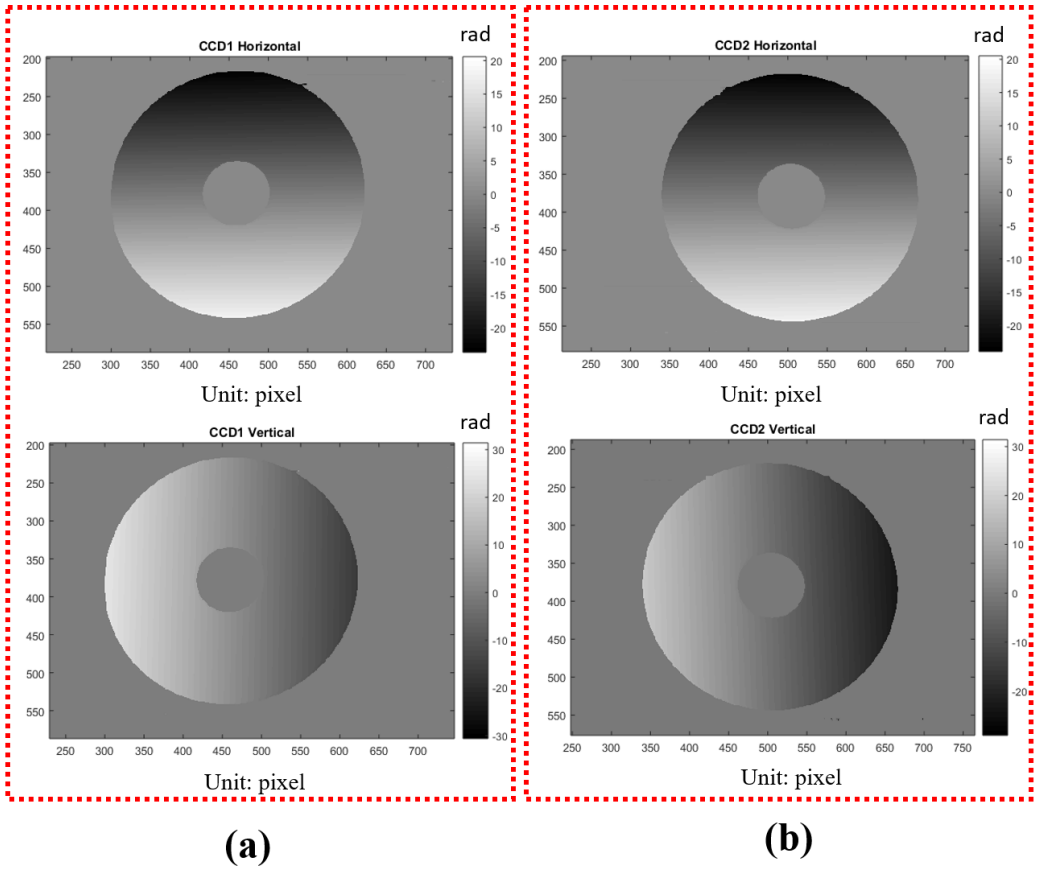

Figure 5-17. The unwrapped phase maps of the specular discontinuous disk obtained using SFPs (with its highest frequency as 120 pixels): (a) the orthogonal phase patterns obtained through phase unwrapping in the first camera, and (b) the orthogonal phase patterns in the second camera.

This disk was also located nearly 930 *mm* to the LCD screen and the orthogonal SFPs with three frequencies were sent to the LCD screen. For the SFPs, the horizontal SFP periods were 1080 pixels, 360 pixels and 120 pixels, whereas the vertical SFP periods were set as 960 pixels, 320 pixels and 120 pixels. Similar to the flat mirror or the spherical mirror measurement, we again captured 300 images of any frame and later calculated their average intensity to eliminate the random LCD illumination noise. Here, we need to emphasize that even though the specular disk shows discontinuity, the phase maps can still be unwrapped because we used temporal phase unwrapping, and therefore, polynomial fitting method is still available for surface derivative determination. In particular, the unwrapped phase maps calculated through the averaged SFPs are given in Figure 5-17. Here, we want to note that the image distortion has been corrected in these figures.

Once we obtain all unwrapped phase maps on the discontinuous disk, we again performed the second order polynomial fitting phase minimization to calculate the surface derivative distributions. The phase minimization criteria ε in Eq. (4.1) was set as 0.0225 for the preliminary phase pair correspondence, and bi-cubic sub-pixel interpolation was later introduced to enhance the correspondence accuracy. Once we got the derivative matrices, we performed interpolation and then extrapolation to the derivative matrices, and we used these matrices to perform 2D Fourier transform integration. Here, the iteration loop was set as 50. The final reconstructed surface shape of the measured discontinuous specular disk is shown in Figure 5-18.

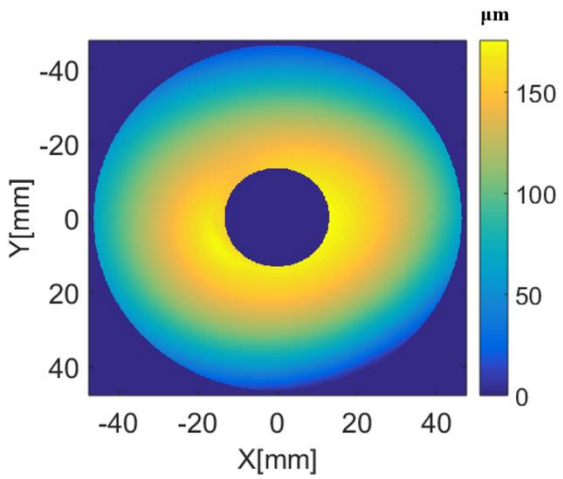

Figure 5-18. Surface shape of the discontinuous specular disk through the SPMD measurement, the surface is reconstructed through 2D Fourier transform integration.

The reconstructed discontinuous disk in Figure 5-18 shows a nearly flat surface shape with an RMS as 92.37 μm, and a PV as 175.61 μm. Here, we need to emphasize that the most severe surface shape variation is introduced at the central section. In particular, the central section presents a greater surface curvature than the rest of the specular surface. Nevertheless, such surface deformation is reasonable, because the central section cutting during the specular disk fabrication will definitely introduce surface deformation, and such deformation will deteriorate the cutting section flatness (i.e., the central section in Figure 5-18). Apart from the central curvature, we can also tell that the reconstructed specular disk is not symmetrically curved in the horizontal and the vertical directions. Specifically, we can find out from Figure 5-18 that the horizontal direction is slightly more curved than the vertical direction. Such surface asymmetry is introduced by the LCD screen inhomogeneity and camera calibration error, as they are also shown in the flat mirror and the spherical mirror measurement cases.

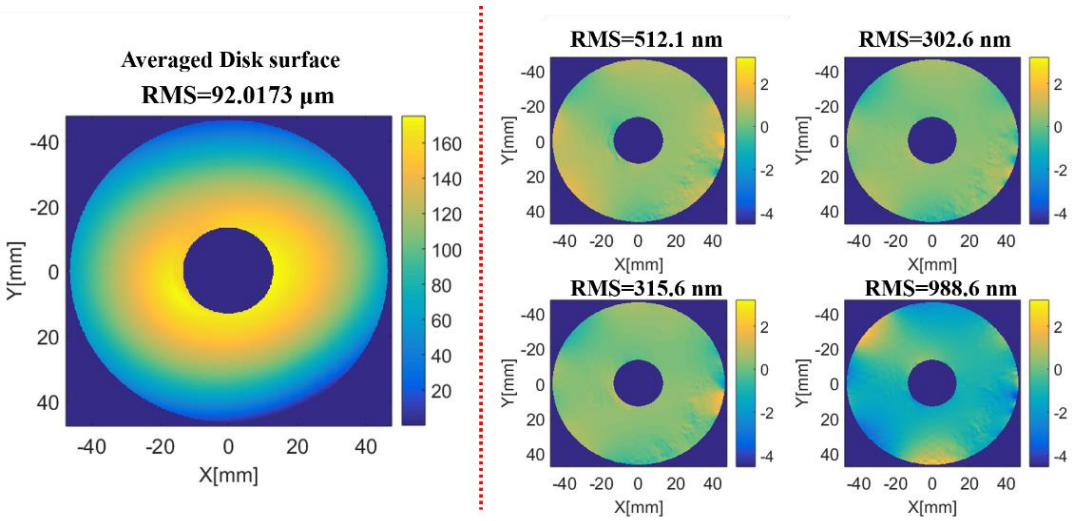

Figure 5-19. Repeatability measurement of the discontinuous specular disk with the highest SFP frequencies as 120 pixels: (a) The average surface shape of the four measurements. (b) The surface shape differences between each individually measured surface and the averaged surface.

Later, we as well conducted the repeatability measurement of this discontinuous specular disk to examine the robustness of the SPMD system for discontinuous surface measurement. Similar to the flat mirror or the spherical mirror case, we measured this disk located at the same position using the same SFPs for four times. Once the four surface shapes are obtained, we preliminarily calculate their average surface shape and

the averaged specular disk shape is given in Figure 5-19 (a). Here, the RMS of this averaged discontinuous disk surface is 92.0173 μm. Furthermore, the surface differences between each measured disk surface to this averaged surface are compared and the four surface differences are given in Figure 5-19 (b).

In Figure 5-19 (b), the maximum RMS within all these four sub-figures is presented as 988.6 nm, and the minimum RMS is 302.6 nm. For the discontinuous disk repeatability measurement, the RMS errors of all surface difference maps are ranging within micrometer scale, from which we can tell that the SPMD system presents great measurement repeatability to measure even the discontinuous specular surface.

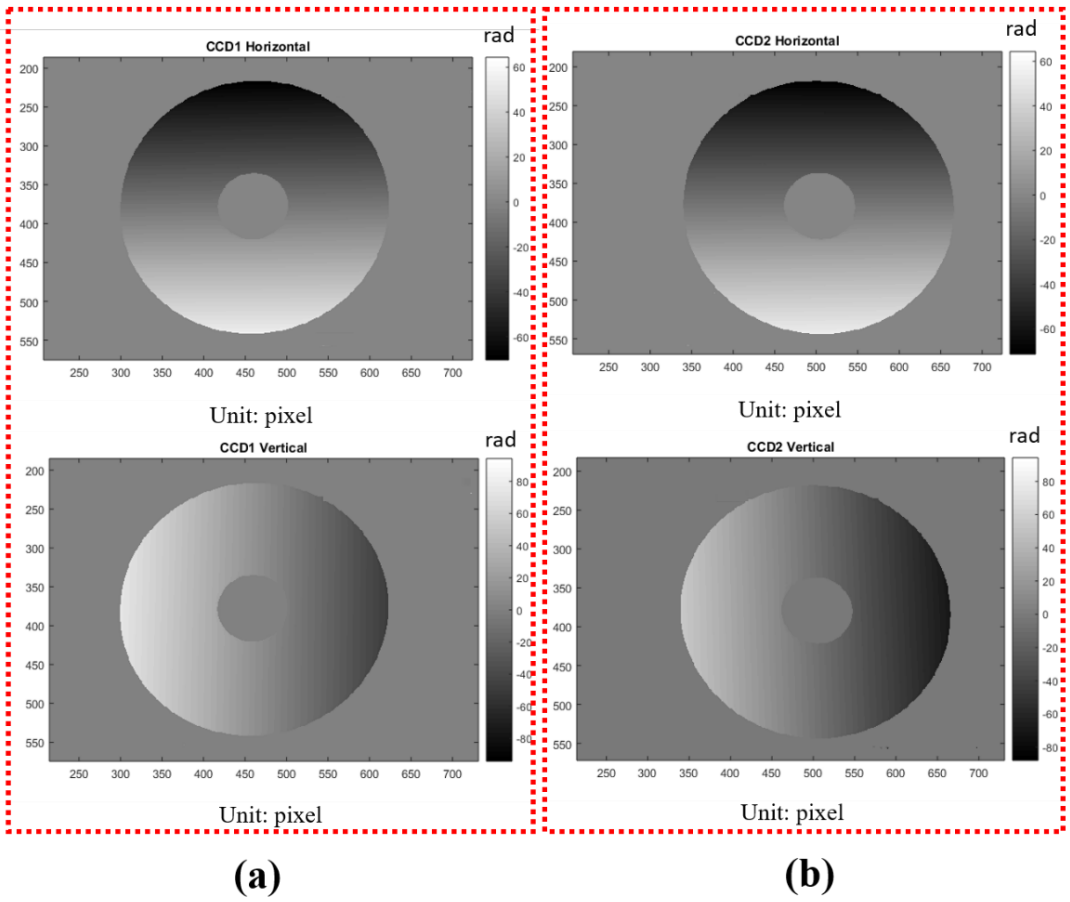

Figure 5-20. The unwrapped phase maps of the specular discontinuous disk obtained by using the new SFPs (with its highest frequency as 40 pixels) in the stereoscopic camera: (a) the orthogonal phase patterns obtained through phase unwrapping in the first camera, and (b) the orthogonal phase patterns in the second camera.

The above-discussed discontinuous disk measurement is performed by using the highest SFP frequency as 120 pixels to both the horizontal and the vertical directions. However, such frequency (i.e., 120 pixels) is relatively low, so the phase difference between any two adjacent pixels in the phase map is also relatively small. Note that such small phase difference may introduce difficulties in both the phase pair correspondence and the further sub-pixel interpolation. Thus, to study the influence of the phase difference between two adjacent pixels to the final surface measurement, we performed another measurement with different SFP frequencies. Here, instead of using the previous three frequencies, we introduced SFPs with four frequencies. For the new SFP series, the horizontal SFP periods were set as 1080 pixels, 360 pixels, 120 pixels and 40 pixels, whereas the vertical SFP periods were set as 960 pixels, 320 pixels, 120 pixels and 40 pixels. To obtain the unwrapped phase maps corresponding to the new SFP series, we used the same phase unwrapping principle, but to implement with four frequencies. To be more specific, we firstly obtained the continuous unwrapped phase maps of the SFP period of 120 pixels, then we used this unwrapped phase map to further unwrap the SFP with the period of 40 pixels. The new phase maps corresponding to the SFP period of 40 pixels are given in Figure 5-20.

At this moment, the phase values in the horizontal phase map in the first camera range from -70.4 radians to 64.4 radians, whereas the phase values in the vertical direction range from -94.2 to 94.2 radians. By comparing the four frequencies-based phase maps to the previous three frequencies-based phase maps, we obviously detect that the phase range is increased, and thus, the phase difference between each two adjacent pixels is greater. In this case, the phase pair correspondence is easier to be established. At this moment, we still measured the same disk at the same location under the same experimental condition for four times, but this time we used the phase minimization criteria ε as 0.36 to perform the primary phase pair correspondence. Here, we need to note that we only used a different ε for the primary phase pair correspondence, but we still used the same bi-cubic method for sub-pixel interpolation. Then, we obtained the surface derivative matrices through this new SFP frequency scheme, and the derivative matrices are interpolated and then extrapolated, so that we can use them to accomplish 2D Fourier transform integration. Once we reconstruct the surface shapes of the four measurements, their averaged surface shape is calculated, and it is presented in Figure 5-21 (a). Note that this averaged disk surface is obtained through the four frequencies-based SFPs measurement. Afterwards, the surface differences between each newly measured specular disk surface to this averaged surface are compared and the four surface differences are presented in Figure 5-21 (b).

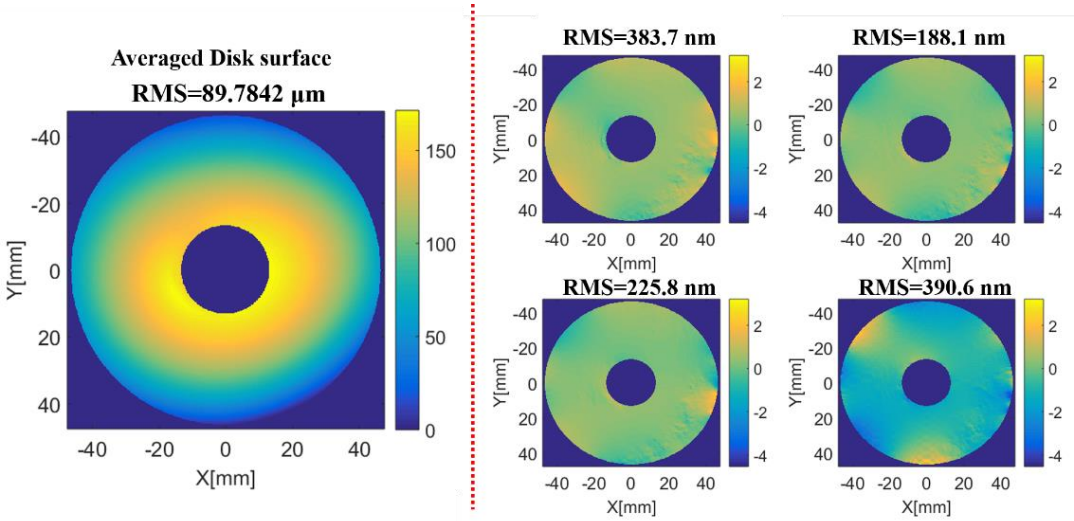

Figure 5-21. Repeatability measurement of the discontinuous specular disk with the highest SFP frequencies as 40 pixels: (a) The average surface shape of the four measurements. (b) The surface shape difference maps between each individually measured surface and the averaged surface.

In Figure 5-21 (a), the RMS of the averaged disk surface, which is obtained through the four-frequencies SFPs, is calculated as 89.7842 μm. On the other hand, the previous averaged surface obtained through the three-frequencies SFPs presents an RMS as 92.0173 μm. The two averaged surfaces demonstrate nearly a same surface shape with a tiny RMS difference as 2.2331 μm. Thus, we can verify the robustness of the SPMD system, as it provides nearly the same surface measurement results with different SFP frequencies even for the discontinuous specular surface. What is more, the maximum RMS within all surface difference maps for the four-frequencies based measurement is 390.6 nm, and the minimum RMS value is 188.1 nm (see Figure 5-21 (b)). On the other hand, the surface shape differences obtained from the three-frequencies SFPs based measurement give a maximum RMS as 988.6 nm, and a minimum RMS as 302.6 nm (see Figure 5-19 (b)). Here, as both the four-frequencies based measurement and the three-frequencies based measurement give a nearly identical surface shape difference, we can further prove the SPMD measurement robustness. Moreover, by comparing the surface shape differences obtained through the four-frequencies SFPs and the previous discussed three-frequencies SFPs (i.e., maximum RMS as 988.6 nm for the three-frequencies SFPs based measurement and maximum RMS as 390.6 nm for the four-frequencies SFPs based measurement), we can also tell that a greater phase difference between the two adjacent pixels guarantees a better measurement robustness.

Chapter 6 Stereoscopic fringe projection profilometry

In Chapter 5, we described the experimental measurements of different specular surfaces using a stereoscopic phase measuring deflectometry system. In this chapter, we present the stereoscopic fringe projection profilometry (SFPP) system, which is able to measure the surface shapes of diffuser objects.

At the beginning, we mathematically describe the SFPP measurement principle in Section 6.1, which is based on geometric triangulation. Afterwards, we introduce the SFPP system calibration in Section 6.2, from which the system parameters are obtained. Once the SFPP system is calibrated, we present the experimental measurement process and give the measurement results in Section 6.3. In particular, we use the calibrated SFPP system to measure the surface shapes of three different diffuser objects as a "stair" structure object, a spherical structure object and a more complicated irregular structure object. In the experimental measurements, we still use sinusoidal fringe patterns (SFPs) to illuminate the objects and then we capture the distorted SFPs on the measured objects with the stereoscopic camera. Here, to illuminate the diffuser objects, a video projector is used instead of an LCD screen to provide the illumination. Once the distorted SFPs on the diffuser objects are captured by the stereoscopic camera, we again introduce phase shifting (see Section 3.2) combined with phase unwrapping (see Section 3.3) to obtain the unwrapped phase maps in both cameras, from which the triangulation can be performed, and the surface

shapes then can be obtained. Finally, we want to emphasize that as SFPP is a direct measurement system, it is feasible to measure diffuser objects with complex shapes.

6.1 Mathematical principle of the stereoscopic fringe projection profilometry measurement

Stereoscopic fringe projection profilometry (SFPP) is a diffuser surface shape measurement system based on structured light illumination. The principle of SFPP measurement is briefly explained in Section 1.3.3. Here, we again review the SFPP measurement process. In an SFPP system, a video projector is used to project sinusoidal fringe patterns (SFPs). The projected SFPs are distorted by the diffuser object, and then we use the stereoscopic camera to capture these distorted SFPs on the diffuser objects. Now, by modulating the captured SFPs with phase shifting and phase unwrapping, we obtain the unwrapped phase maps on the measured object in both cameras. Finally, by establishing the phase correspondence between the unwrapped phase maps in both cameras, we obtain the surface depth information through geometric triangulation. This surface depth information directly gives us the surface shape of the measured diffuser object.

In this section, as we intend to mathematically describe the geometric triangulation for SFPP measurement, we initially establish the basic geometric SFPP scheme. In particular, as we use the same stereoscopic camera used in the SPMD system (see Chapter 5) for this SFPP measurement, we directly use the calibration results in Table 5-1 and Table 5-2 as the camera intrinsic parameters, and we use the calibrated matrix $\boldsymbol{RT}_{C1tC2}$ presented in Section 5.2 as the extrinsic parameter between the stereoscopic camera.

Now, we choose one certain point $\boldsymbol{A}$ on the first camera image plane, its coordinate position in the world coordinate system (i.e., the first camera coordinate system) is presented by three tuples in a vector notation as $\boldsymbol{A}=(x_A,y_A,z_A)$. Here, (x_A,y_A,z_A) is the geometric position of point $\boldsymbol{A}$ with respect to the world coordinate system origin, and its phase values are (Φ_h,Φ_v). On the other side, we find on the second camera image plane a correspondent point $\boldsymbol{B}$ which has the same phase values as (Φ_h,Φ_v). The coordinate position of point $\boldsymbol{B}$ in the world coordinate system is also presented by three tuples in a vector notation as $\boldsymbol{B}=(x_B,y_B,z_B)$. Here, (x_B,y_B,z_B) is the geometric position of point $\boldsymbol{B}$ with respect to the world coordinate system origin. Moreover, by regarding both cameras as pinhole cameras, their pinholes are entitled as

$\boldsymbol{O_1}=(O_{x1},O_{y1},O_{z1})$ and $\boldsymbol{O_2}=(O_{x2},O_{y2},O_{z2})$ in the world coordinate system. The SFPP diagram is presented in Figure 6-1.

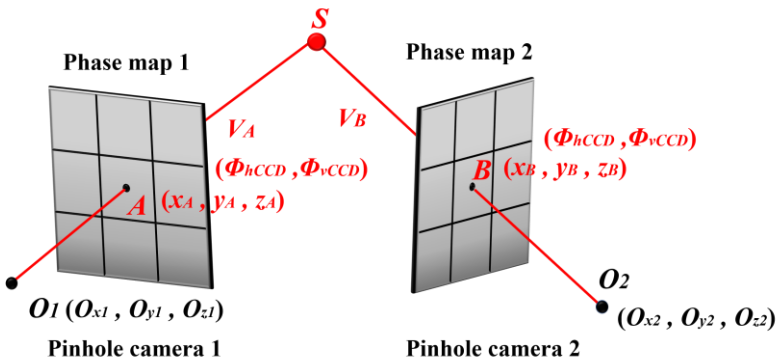

Figure 6-1. The diagram of the stereoscopic fringe projection profilometry system for surface point determination through geometric triangulation.

At this moment, by using the first camera pinhole $\boldsymbol{O_1}$ and point $\boldsymbol{A}$, we can obtain a primary normalized vector as $\boldsymbol{V_A}=[V_{Ax},V_{Ay},V_{Az}]$ in the world coordinate system, and $\boldsymbol{V_A}$ is calculated as:

$$[V_{Ax},V_{Ay},V_{Az}]=\frac{(x_A,y_A,z_A)-(O_{x1},O_{y1},O_{z1})}{\sqrt{(x_A-O_{x1})^2+(y_A-O_{y1})^2+(z_A-O_{z1})^2}}. \tag{6.1}$$

We can also get a secondary unit vector as $\boldsymbol{V_B}=[V_{Bx},V_{By},V_{Bz}]$ in the world coordinate system by connecting $\boldsymbol{O_2}$ to point $\boldsymbol{B}$, and $\boldsymbol{V_B}$ is calculated as:

$$[V_{Bx},V_{By},V_{Bz}]=\frac{(x_B,y_B,z_B)-(O_{x2},O_{y2},O_{z2})}{\sqrt{(x_B-O_{x2})^2+(y_B-O_{y2})^2+(z_B-O_{z2})^2}}. \tag{6.2}$$

Then, two lines corresponding to these two unit vectors are described in the world coordinate system as below:

$$P_{\boldsymbol{A}}=\boldsymbol{V_A}\cdot t+\boldsymbol{A}, \tag{6.3}$$

$$P_{\boldsymbol{B}}=\boldsymbol{V_B}\cdot u+\boldsymbol{B}, \tag{6.4}$$

where t and u are real numbers.

Now, by setting $P_{\boldsymbol{A}}$ equal to $P_{\boldsymbol{B}}$, we can calculate the value of t and u, and therefore, we can easily obtain the intersection point $\boldsymbol{S}$ of these two lines in the world coordinate system. Finally, by implementing such triangulation to all pixels on the first camera image plane, we can obtain the full surface depth information of the measured object.

Nevertheless, the camera calibration in the real experimental implementation introduces calibration uncertainty to both the intrinsic parameters and the extrinsic parameter. Therefore, the camera pinhole positions and the focal lengths of both cameras may not be accurately determined, as the tiny calibration uncertainty will inevitably deteriorate the calibration accuracy. Thus, it is almost certain that the two lines (i.e., P_A and P_B) will not intersect with each other in the space, but they are separated for a tiny distance even at the real surface point position, which is shown in Figure 6-2 (see the black dashed square, where $\boldsymbol{S}$ is the real surface point, but the two lines are not intersecting at $\boldsymbol{S}$). These two lines are also mentioned as skew lines. Under this scenario, the surface point is taken as a particular point in the space (i.e., $\boldsymbol{S'}$ in Figure 6-2) which can provide a minimum distance between the skew lines.

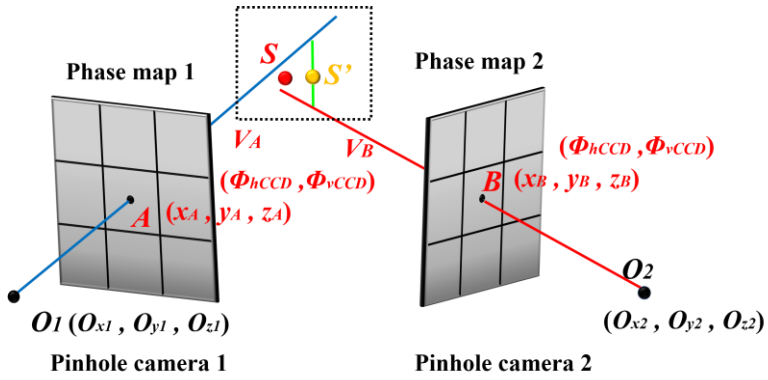

Figure 6-2. The diagram of the SFPP system for surface point determination using the skew lines-based triangulation.

To obtain the point that gives the minimum separation distance between the skew lines, we proceed the following steps: first of all, we calculate the cross product of $\boldsymbol{V_A}$ and $\boldsymbol{V_B}$, as their cross product $\boldsymbol{n}$ is perpendicular to both vectors,

$$\boldsymbol{n} = \boldsymbol{V_A} \times \boldsymbol{V_B} . \tag{6.5}$$

Next, we forge a plane which contains line P_B and vector $\boldsymbol{n}$, and this plane is perpendicular to a second cross product $\boldsymbol{n_2}$, where $\boldsymbol{n_2}$ is:

$$\boldsymbol{n_2} = \boldsymbol{V_B} \times \boldsymbol{n} . \tag{6.6}$$

Therefore, the intersecting point of line P_A with this above-mentioned plane, which is also the point on line P_A that is nearest to line P_B, is given as:

$$\boldsymbol{S_1} = \boldsymbol{A} + \frac{(\boldsymbol{B} - \boldsymbol{A}) \cdot \boldsymbol{n_2}}{\boldsymbol{V_A} \cdot \boldsymbol{n_2}} \boldsymbol{V_A} . \tag{6.7}$$

Similarly, the triangulated surface point on line P_B nearest to line P_A is given as:

$$\boldsymbol{S_2} = \boldsymbol{B} + \frac{(\boldsymbol{A} - \boldsymbol{B}) \cdot \boldsymbol{n_1}}{\boldsymbol{V_B} \cdot \boldsymbol{n_1}} \boldsymbol{V_B}\,, \tag{6.8}$$

where $\boldsymbol{n_1}$ is calculated as:

$$\boldsymbol{n_1} = \boldsymbol{V_A} \times \boldsymbol{n}\,. \tag{6.9}$$

At this moment, point $\boldsymbol{S_1}$ and point $\boldsymbol{S_2}$ form the shortest line segment linking line P_A and line P_B. Then, we calculate the middle point between point $\boldsymbol{S_1}$ and point $\boldsymbol{S_2}$, and we regard this middle point as the real surface point. Finally, we perform such triangulation to all pixels of the experimentally obtained unwrapped phase map on the first camera image plane, and the complete surface shape is determined. Note that in this thesis, we use the skew lines intersection method to perform the geometric triangulation.

6.2 Experimental calibration of a stereoscopic phase measuring profilometry system

To perform surface reconstruction with a stereoscopic phase measuring profilometry system, we need to know the geometric relation of the stereoscopic camera, and we also have to properly calibrate the video projector to provide the optimal sinusoidal fringe patterns. Thus, in this section, we comprehensively show the SFPP system calibration. In particular, we firstly discuss the video projector calibration, and then we briefly discuss the stereoscopic camera calibration. In fact, we use exactly the same stereoscopic camera scheme previously used in the SPMD system to perform the SFPP measurement. Thirdly, we also discuss the geometric position between the video projector and the stereoscopic camera, as it affects the illumination homogeneity, and therefore influences the final phase extraction (i.e., through phase shifting and phase unwrapping).

For video projector calibration in an SFPP system, we let the camera capturing frequency and the video projector projecting frequency be equal, so we can avoid the LC flicker in the video projector (this video projector has a LCoS phase modulator).

Even though we adjust the video projector and the camera to have the same frequency, the video projector still demonstrates a nonlinear gray level-intensity response, which is also referred as the gamma effect. Specifically, it presents the

gamma nonlinearity characteristic similar to that of an LCD screen, which shares a similar tendency as Figure 5-1. However, we need to emphasize that in an SFPP system, the gamma effect does not influence the surface reconstruction result, so it is not necessary to correct the gamma nonlinearity of the video projector. This is because the gamma nonlinearity is simultaneously introduced into both cameras when we use them to capture the same SFPs, and therefore, the same nonlinearity error is introduced to both cameras during phase unwrapping. Thus, the phase maps into both cameras are affected by the same gamma error. Note that such consistent phase error in both cameras is in fact not affecting the phase pair correspondence if we select a proper sub-pixel interpolation method (i.e., bi-cubic sub-pixel interpolation), so we can still obtain the correct phase correspondence for geometric triangulation.

Now, as video projector calibration has been accomplished, we focus on stereoscopic camera calibration. Again, in our proposed SFPP system, the triangulation is performed between the stereoscopic camera, so the geometric relation between these two cameras is critical. Nevertheless, as the stereoscopic camera system has already been implemented in the previous SPMD system, we directly use that already calibrated stereoscopic scheme to perform SFPP measurement. More importantly, the separation distance between the stereoscopic camera (i.e., see $\boldsymbol{RT}_{C1tC2}$ in Eq. (5.1)) is large enough to achieve an accurate geometric triangulation. Thus, we directly use the already calibrated stereoscopic camera in Section 5.2 for SFPP measurement.

Finally, we also have to pay attention to the geometric relation between the video projector and the stereoscopic camera. Nevertheless, the video projector position calibration is flexible, and it is not mandatory to obtain the geometric relation between the video projector and the stereoscopic camera. This is because the triangulation is only performed within the cameras, whereas the video projector is only used to provide the sinusoidal fringe patterns. Under this scenario, we can flexibly locate the video projector only if it can guarantee: (*i*) a homogeneous illumination on the measured object, and (*ii*) the SFPs projected on the measured object can be seen by both cameras. In fact, the flexibility of the video projector position calibration is one of the main advantages of a stereoscopic fringe projection profilometry system compared to a single-camera based fringe projection profilometry system.

By considering the above-discussed conditions, we calibrated an SFPP system, and the calibrated system is given below in Figure 6-3. In this SFPP system, the video projector was located behind the stereoscopic camera, where the distance from the video projector to any camera was set nearly equal (see Figure 6-3 (b)). Later, we

located the measured diffuser object in front of the cameras, so both cameras can capture the image of the measured object (see Figure 6-3 (a)). In the SFPP system, we also implemented a linear polarizer in front of the video projector. This linear polarizer was introduced to only decrease the illumination intensity, so that the intensity captured by both cameras will not be saturated.

Figure 6-3. Experimental setup of the stereoscopic fringe projection profilometry system for diffuser object measurement.

6.3 Experimental measurements using a stereoscopic fringe projection profilometry system

In this section, we used this calibrated stereoscopic fringe projection profilometry (SFPP) system to measure the surface shapes of different diffuser objects. In particular, we measured a "stair" structure object, a spherical structure object and a complex surface structure object. By measuring these three different objects, we would like to justify that our SFPP system is available to accurately measure the surface shapes of different diffuser objects even with complex surface profiles.

6.3.1 "Stair" structure object measurement

To verify the feasibility of the SFPP system, we firstly select a "stair" structure diffuser object to measure. This "stair" contains three steps, the stair height between each step is nearly 15 mm, the distance between each stair face is nearly 10 mm, and the size of each stair is 25 $\times$25 mm^2. The surface of each stair is nearly flat, and the "stair" photograph is given in Figure 6-4 (a). This "stair" structure object is placed nearly 650 mm to the stereoscopic camera.

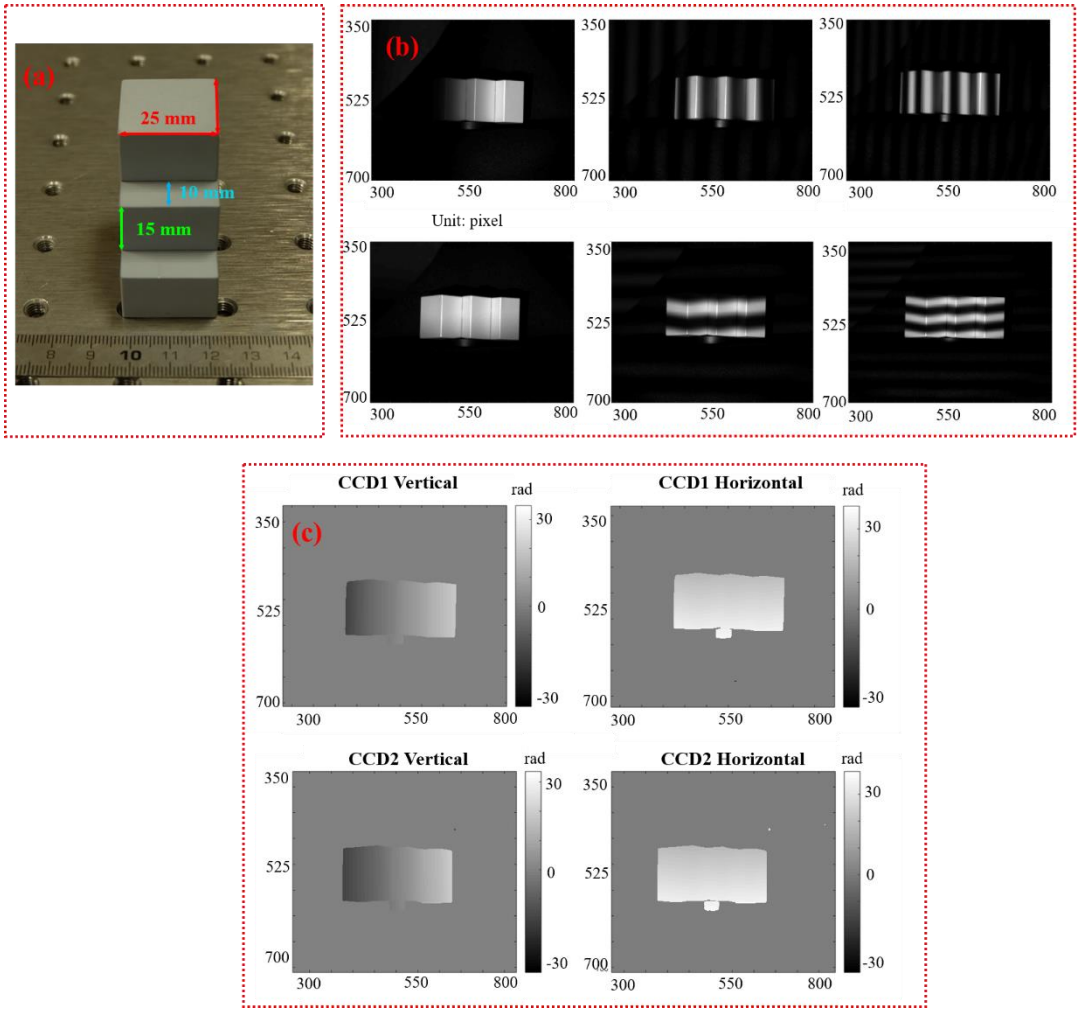

Figure 6-4. The "stair" structure object measured by the SFPP system: (a) the photograph of the "stair" structure object, (b) the "stair" structure object with projecting different SFPs to its surface, and (c) the phase maps of the measured object in both cameras.

By using a video projector, we sequentially projected both horizontal and vertical sinusoidal fringe patterns (SFPs) to the measured object. Within these SFPs, three different frequencies were used, and their frequencies were gradually increasing. In particular, the periods of both the horizontal and the vertical SFPs were set as 350 pixels, 50 pixels and 30 pixels. Moreover, within each frequency, we introduced four different patterns with the phase-shift as $\pi/2$ for phase shifting (see Eq. (3.1)). Therefore, we projected in total 24 different SFPs from the video projector and captured these images within both cameras. To better visualize the measured "stair" structure object, we give an intensity image series captured by the first camera in

Figure 6-4 (b) as an example. The images in Figure 6-4 (b) contain the vertical and the horizontal SFPs on the "stair", and the phase-shift value is $\pi/2$. Later, to eliminate the random video projector illumination noise, we further captured 300 images of any frame and calculated their average intensity. Afterwards, the camera distortion coefficients were introduced to correct the image distortion in all averaged images. Finally, these average intensity images with their distortion corrected were regarded as the final intensity patterns for phase shifting and phase unwrapping. For an SFPP system, it shares the same phase shifting and phase unwrapping principle as an SPMD system, so we directly used the same phase modulation principle to get the unwrapped phase maps on the "stair", and the phase maps are given in Figure 6-4 (c).

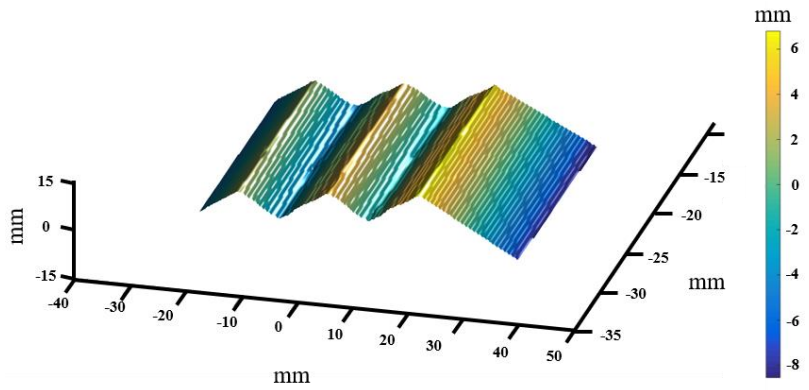

Figure 6-5. The surface shape of the "stair" measured by the SFPP system using direct triangulation.

The above-discussed process provides us the vertical and the horizontal unwrapped phase maps within the stereoscopic camera. Then, by executing the geometric triangulation using the unwrapped phase maps from the first camera to the second camera, we can get the surface shape of the "stair". Here, to perform geometric triangulation, we have to find the phase pair correspondence between the two cameras. More specifically, we selected one phase pixel in the first camera image plane and recorded its orthogonal phase values. Then, we searched along the whole phase maps in the second camera image plane and find a particular phase pixel whose orthogonal phase values are the closest to that phase pixel in the first camera, and then we used such two phase pixels to construct the phase pair correspondence. Nevertheless, the phase values in these two pixels may not be equal. In fact, it is most certainly that the two pixels share slightly different phase values due to pixel quantization error and SFP illumination error. By using this direct phase pair correspondence method to perform the geometric triangulation, we obtain a "stair" surface profile in Figure 6-5.

The reconstructed surface of the “stair” structure shown in Figure 6-5 correctly reveals the shape of the measured object, from which we can distinguish the three steps of the “stair”. Nevertheless, the quality of the reconstructed surface is poor, and the reconstructed surface is not smooth. We want to note that such surface error is introduced by the phase pair correspondence error. Specifically, direct phase pair correspondence leaves the phase values between the correspondent phase pixels being slightly different, and such phase difference deteriorates the triangulation accuracy.

Therefore, to enhance the reconstruction accuracy, sub-pixel interpolation has to be performed. For SFPP measurement, we firstly implemented bi-linear sub-pixel interpolation for surface shape enhancement. In the bi-linear sub-pixel interpolation, we used the method comprehensively discussed in Section 4.3.1, and the interpolation was performed by using a 3×3 pixel region in the phase maps. The reconstructed surface shape obtained through bi-linear sub-pixel interpolation is given below in Figure 6-6.

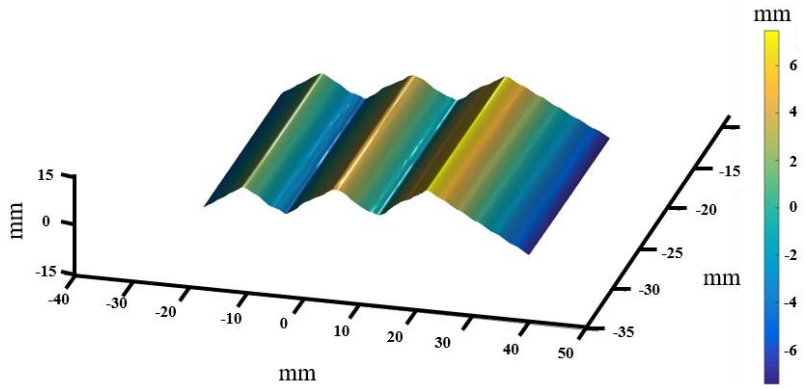

Figure 6-6. The surface shape of the “stair” measured by the SFPP system by using bi-linear sub-pixel interpolation.

By implementing bi-linear sub-pixel interpolation, the quality of the reconstructed “stair” surface (i.e., Figure 6-6) is enhanced. Specifically, the surface smoothness is greatly improved, from which we can tell that the stair face in Figure 6-6 is nearly flat. Nevertheless, the “stair” surface still presents a tiny surface bump (see the rightmost reconstructed “stair” surface section in Figure 6-6) and it degenerates the surface reconstruction accuracy. The reason to such surface bump is that bi-linear interpolation still cannot precisely compensate the phase pair correspondence error.

Under this scenario, to further enhance the measurement accuracy, we introduced bi-cubic sub-pixel interpolation for surface reconstruction. In the bi-cubic sub-pixel interpolation scheme, we used the method comprehensively discussed in Section 4.3.2,

and the interpolation was performed by using a 3×3 pixel region in the phase maps. The reconstructed surface shape obtained by using bi-cubic sub-pixel interpolation is given below in Figure 6-7.

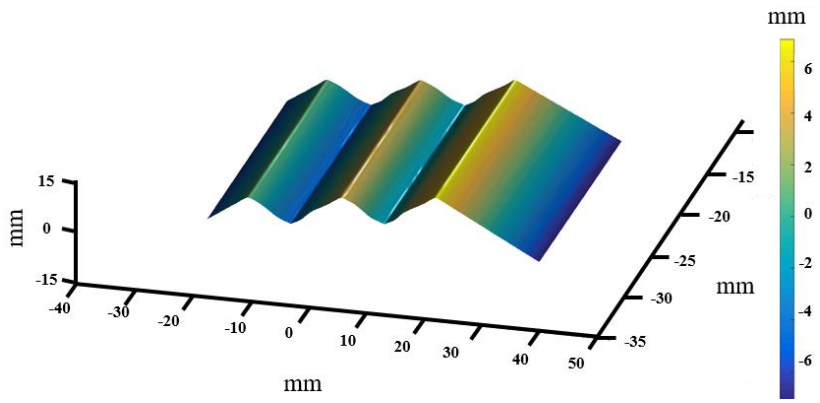

Figure 6-7. The surface shape of the "stair" measured by the SFPP system by using bi-cubic sub-pixel interpolation.

By implementing bi-cubic sub-pixel interpolation, the reconstructed surface of the "stair" (i.e., Figure 6-7) is further enhanced. Specifically, the surface is smooth at this moment, and the stair face in Figure 6-7 is extremely flat. Moreover, we calculated the stair height from this reconstructed surface as 14.98 *mm* (by measuring 10 times the stair heights at different positions and calculate their average stair height), and such distance coincides with the real stair height (i.e., as nearly 15 *mm*). We also calculated the distance between each stair face as 9.97 *mm* (by measuring 10 times the distance at different positions and calculate their average distance), which is also identical to the real stair face distance. Thus, it is obvious that bi-cubic sub-pixel interpolation guarantees a high surface reconstruction accuracy.

Apart from the surface shape, we also obtained the distance from the measured object to the first camera. In particular, we select a central surface point on the reconstructed surface, and we get the distance from this point to the camera optical center as 656.822 *mm*. Therefore, our proposed SFPP system is not only feasible to measure the surface shape, but it also gives an accurate distance measurement from the first camera to the diffuser object.

From the above-mentioned three reconstructed surfaces, we can deduce that direct phase correspondence gives the poorest surface reconstruction result, whereas bi-linear sub-pixel interpolation method improves the surface reconstruction accuracy, and bi-cubic sub-pixel interpolation guarantees a best surface reconstruction result. Thus, it is recommended to perform sub-pixel interpolation in SFPP measurements. Here, bi-

cubic sub-pixel interpolation requires a more complicated calculation, and therefore, it cannot compete with bi-linear method when the measurement speed is required (i.e., real-time 3D surface measurement [132–134]). Therefore, a trade-off between the measurement accuracy and efficiency has to be considered. In this thesis, as we focus on the measurement accuracy, we use bi-cubic sub-pixel interpolation to perform all SFPP surface reconstructions.

6.3.2 Spherical object measurement

In the previous sub-section, we measured a "stair" structure object with the SFPP system. The "stair" measurement results justify the feasibility of using such system to measure the flat surface with sharp surface variation (i.e., the corners at the "stair" edges). In this sub-section, we measured a spherical diffuser object, to further demonstrate that the SFPP system is also able to measure curved surfaces. The spherical object we measured is shown below in Figure 6-8 (a).

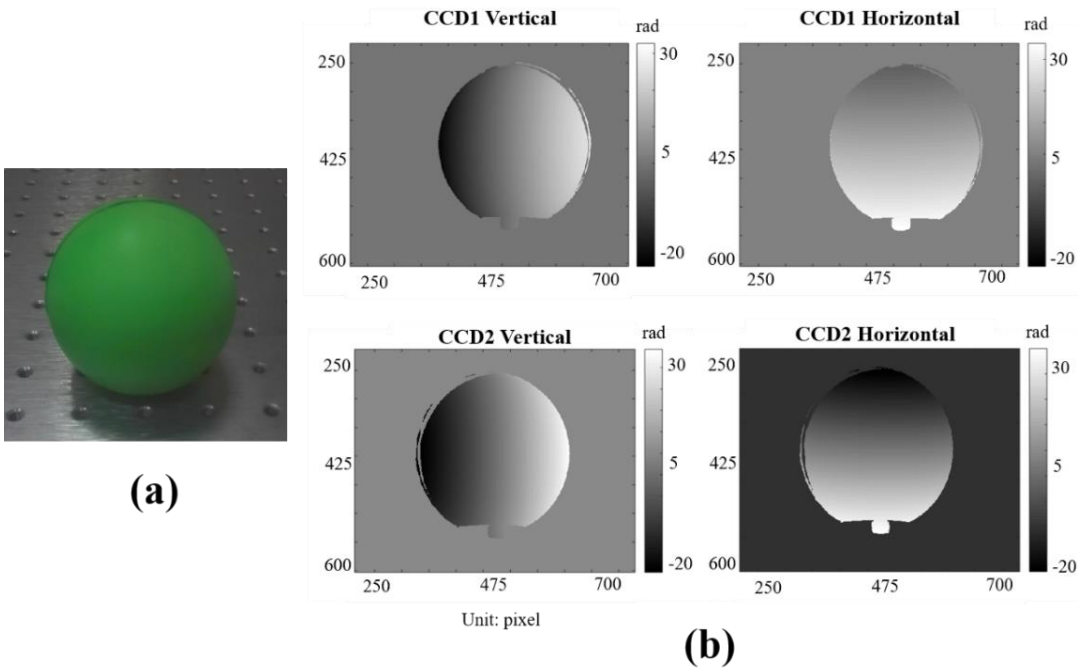

Figure 6-8. The spherical object measured through the SFPP system: (a) photograph of the ball, (b) the phase maps on the sphere ball in both cameras.

The diameter of this spherical ball is nearly 68 *mm*, and the surface of this sphere presents the diffuser characteristic. We again placed this spherical ball nearly 650 *mm*

to the stereoscopic camera, and we sent different SFPs through the video projector to illuminate this sphere. In particular, the frequencies of the SFPs were set the same as those used to measure the "stair", as the SFP periods in both horizontal and vertical directions were set as 350 pixels, 50 pixels and 30 pixels. Moreover, within each frequency, four different patterns with phase-shift as $\pi/2$ were introduced for phase shifting. Afterwards, we captured 300 images of any frame and calculated their average intensity to eliminate the video projector illumination noise. Then, camera distortion coefficients were introduced to correct the image distortion of all averaged images. At last, these average intensity images with their distortion corrected, were regarded as the final object intensity patterns to perform phase shifting and phase unwrapping. The unwrapped phase maps on the spherical object are shown in Figure 6-8 (b).

As we had obtained the vertical and the horizontal unwrapped phase maps in the stereoscopic camera, we executed the geometric triangulation from the first camera to the second camera to calculate the surface shape of this sphere. In particular, geometric triangulation was performed using direct triangulation, bi-linear interpolation based triangulation and bi-cubic interpolation based triangulation, respectively. The reconstructed surface shapes corresponding to each triangulation method are given in Figure 6-9, as Figure 6-9 (a) is the reconstructed surface obtained from direct triangulation, Figure 6-9 (b) is the reconstructed surface obtained from bi-linear interpolation, and Figure 6-9 (c) is the reconstructed surface obtained by using bi-cubic interpolation. To better visualize the reconstructed surfaces, we give the surface shapes from two different perspectives.

The spherical object reconstructed through direct triangulation demonstrates very weak surface smoothness (see Figure 6-9 (a)), as the discontinuous bumps can be seen throughout the whole surface. The reason to such surface bump is that the phase pair correspondence obtained by direct triangulation is not accurate. Then, the sphere surface reconstructed through bi-linear sub-pixel interpolation was obtained and we can easily find that the surface smoothness is enhanced (see Figure 6-9 (b)), as we can tell the smooth spherical shape of the measured object. Nevertheless, the reconstructed surface still contains the tiny bump and it degenerates the surface reconstruction accuracy. The reason to such surface bump is that bi-linear interpolation still cannot provide a precise sub-pixel correspondence. Finally, the reconstructed spherical surface through bi-cubic sub-pixel interpolation shows great surface smoothness (see Figure 6-9 (c)). Thus, it is obvious that bi-cubic sub-pixel interpolation provides the highest surface reconstruction accuracy. The distance from the central point of this spherical

object to the optical center of the first camera is measured as 646.724 *mm* through bi-cubic interpolation.

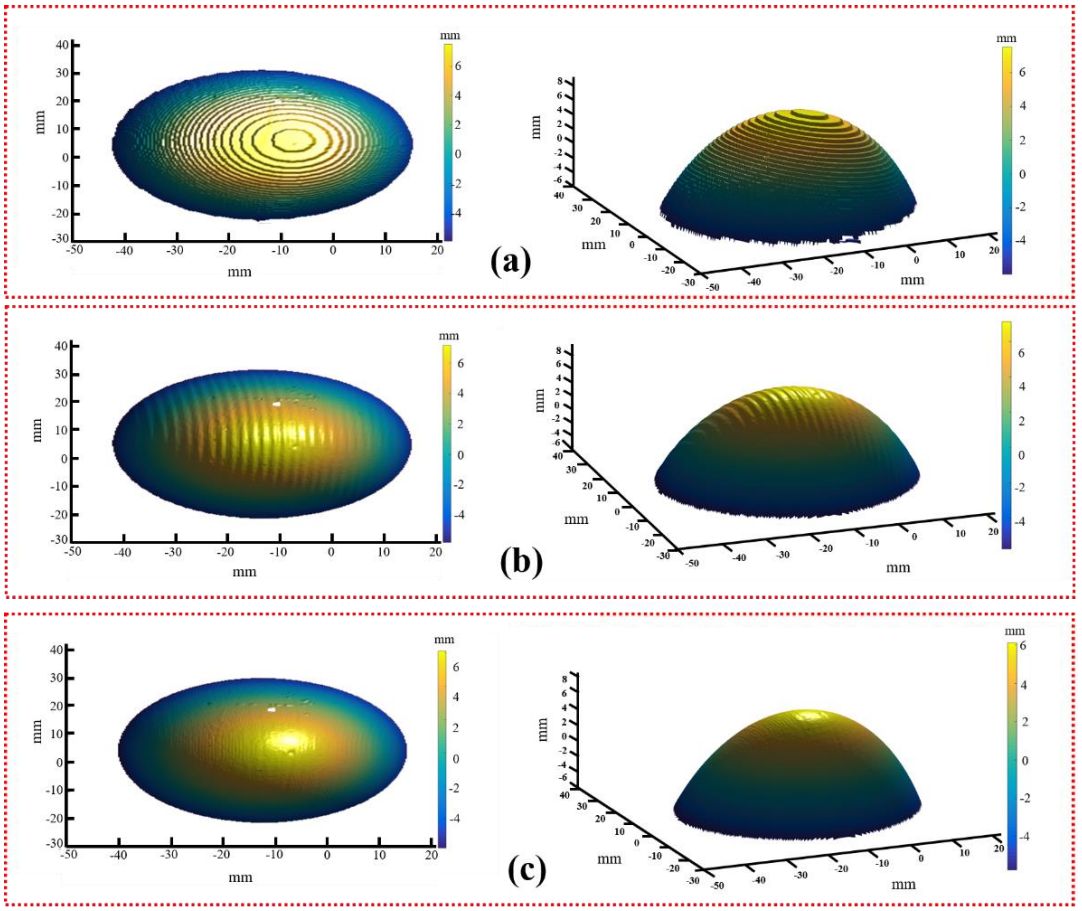

Figure 6-9. The spherical surface reconstructed by different geometric triangulation methods: (a) direct geometric triangulation, (b) bi-linear sub-pixel interpolation method, and (c) bi-cubic sub-pixel interpolation method.

Finally, we need to note that even though a tiny hole (see the tiny white section in Figure 6-9) is presented in the reconstructed surfaces, it is in fact introduced by the surface defect on the spherical object, but it is not introduced during the triangulation.

6.3.3 Irregular surface object measurement

In Section 6.3.1 and Section 6.3.2, we used the proposed SFPP system to measure the surface shape of both a “stair” structure object and a spherical structure object.

Both results demonstrate great measurement accuracy using bi-cubic sub-pixel interpolation. Nevertheless, the "stair" contains a nearly flat surface and the spherical object is mildly curved, and therefore, they only represent regular surfaces. However, in the real industrial applications, the objects with irregular surface shapes are more commonly seen, and their surfaces show more complex surface shapes rather than a simple flat or curve characteristic. Under this scenario, to further verify the wide application of the SFPP system, we finally measured an irregular diffuser object. In particular, the object we measured is a plastic toy duck, and this object is presented in Figure 6-10 (a).

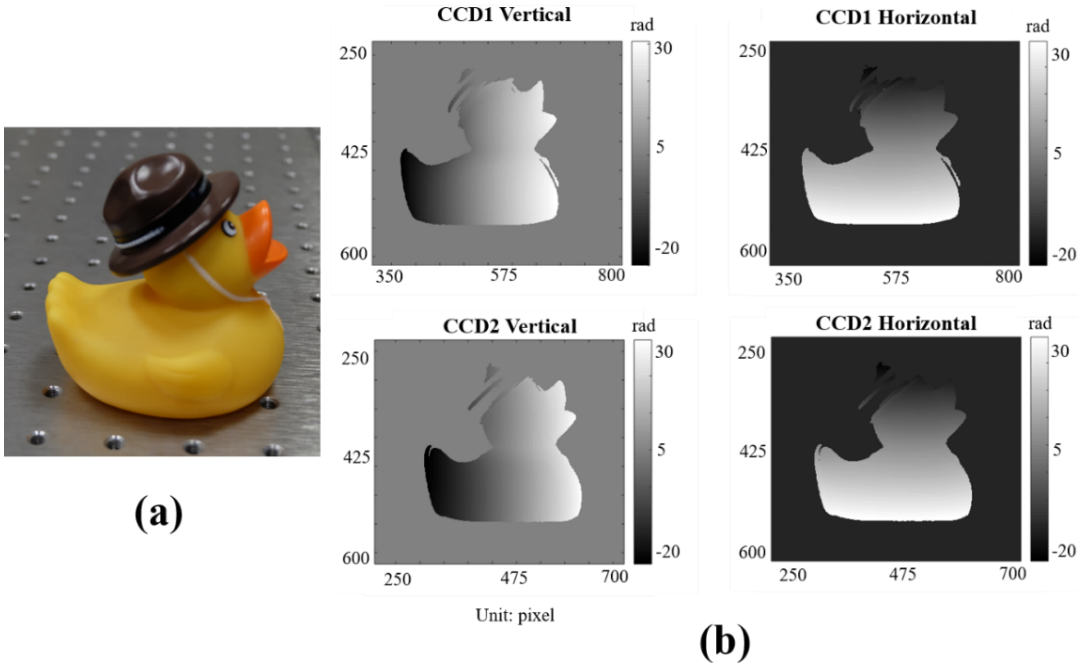

Figure 6-10. The irregular object (i.e., toy duck) measured through the SFPP system: (a) the photograph of the irregular object, (b) the phase maps on the irregular object in both cameras.

The measured object has a length of nearly 80 *mm* and a height of nearly 65 *mm*. Now, this irregular toy duck was located about 650 *mm* to the stereoscopic camera, and different SFPs were sent to illuminate this object. The frequencies of both the horizontal and vertical SFPs were set as 350 pixels, 50 pixels and 30 pixels, and the phase-shift was set as $\pi/2$ for phase shifting. What is more, the video projector illumination noise and the distortion correction were eliminated by using the same method presented in the previous measurements, the unwrapped phase maps in both

cameras were obtained and presented in Figure 6-10 (b). Note that in Figure 6-10 (b), the phase values at the "duck hat" section is not calculable in any of the phase maps. This is because the "duck hat" section presents great reflective characteristic rather than diffuser characteristic, and therefore, the saturated intensity captured at this section cannot be used to perform phase unwrapping.

Once we obtained the vertical and the horizontal unwrapped phase maps of this toy duck within both cameras, we performed the geometric triangulation from the first camera to the second camera to reconstruct its surface shape. Similar to the previous two cases (i.e., the "stair" structure object and the spherical object), the geometric triangulation was performed using direct triangulation, bi-linear interpolation based triangulation and bi-cubic interpolation based triangulation, respectively. The reconstructed surface shapes corresponding to each triangulation method are given below in Figure 6-11. Figure 6-11 (a), (b) and (c) are the reconstructed surface obtained through direct triangulation, bi-linear interpolation and bi-cubic interpolation, respectively. These reconstructed toy duck surfaces are shown from two aspects for a better visualization.

The toy duck surface reconstructed through direct triangulation demonstrates weak surface smoothness and low resolution. In fact, it is unlikely to tell the specific structured such as the "wing" section or the "ribbon" section from Figure 6-11 (a). Later, we introduced bi-linear sub-pixel interpolation to surface reconstruction and the surface smoothness is enhanced. At this moment, we can distinguish the duck structure with detail, but still we see the "string" error throughout the surface. Such surface bump is introduced by the inadequacy of bi-linear interpolation. Finally, the reconstructed toy duck surface obtained through bi-cubic sub-pixel interpolation shows great surface smoothness without the undesired surface bump. Specifically, we can easily distinguish the two inward strings in the "wing" section and the nods in the "ribbon" section. These two particular sections are given in Figure 6-11 (d) for a better visualization. Here, the measured depths of these two strings in the "wing" section is smaller than 1 mm, and the nod height is around 200 μm.

By now, we experimentally demonstrated that our proposed SFPP system can reach a high measurement accuracy even with a complex irregular surface object. We also would like to mention that in the duck surface reconstruction case, bi-cubic sub-pixel interpolation was performed with a 3×3 phase pixel section. Nevertheless, if higher measurement accuracy is required, we can expand the interpolation section so that we can use more phase data to perform bi-cubic interpolation, and then the sub-pixel interpolation accuracy could be further enhanced. Note that if we expand the

intersection section, the calculation time will be longer as more data are used for interpolation.

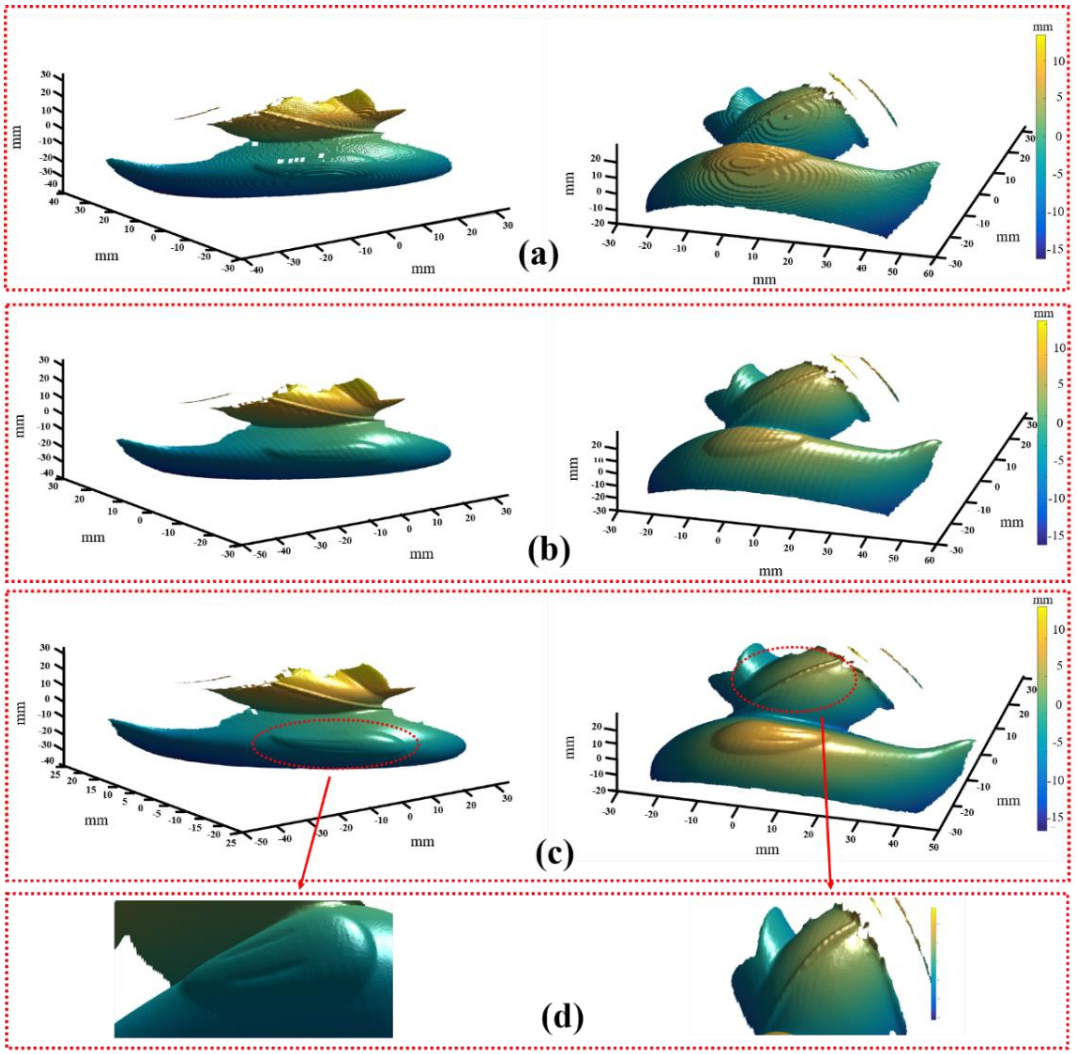

Figure 6-11. The toy duck surface reconstructed through different geometric triangulation methods as: (a) direct geometric triangulation, (b) bi-linear sub-pixel interpolation based triangulation, (c) bi-cubic sub-pixel interpolation based triangulation, and (d) the zoomed "wing" section and "ribbon" section of the measured toy duck.

Chapter 7 Stereoscopic deflectometry-profilometry hybrid structured light measurement system

In Chapter 5, we described the experimental measurement of different specular surfaces with a stereoscopic phase measuring deflectometry system. In Chapter 6, we presented the experimental measurement of diffuser surfaces with a stereoscopic fringe projection profilometry system. In this chapter, we combine stereoscopic deflectometry with stereoscopic profilometry to measure the surface shape of a specular-diffuser hybrid object.

In Section 7.1, we describe the measurement principle of a stereoscopic deflectometry-profilometry hybrid (SDPH) structured light system. In particular, by combining stereoscopic deflectometry with stereoscopic profilometry, this hybrid system can measure both the specular section and the diffuser section of an object at the same time. Then, in Section 7.2, we present the specular-diffuser hybrid surface reconstruction. Specifically, we obtain the specular surface shape with deflectometry, and we obtain the diffuser surface shape with profilometry. Hence, by considering the geometric relation between these two sections and their corresponding spatial positions, we merge these two surfaces together to get a complete hybrid surface. In Section 7.3, we experimentally test the feasibility of our proposed stereoscopic deflectometry-profilometry hybrid structured light system by measuring a specular-diffuser hybrid object. Here, we want to note that we use both a separate projection method and a combined projection method to measure this object. Separate projection method is defined as we firstly project the sinusoidal fringe patterns from the LCD

screen to measure the specular section, and then we project the sinusoidal fringe patterns from the video projector to measure the diffuser section. In this case, we have to project the fringe patterns sequentially by an LCD and a video projector. On the other hand, combined projection method is defined as we project the sinusoidal fringe patterns with the LCD and the video projector at the same time, and we simultaneously measure both the specular section and the diffuser section, from which we can enhance the measurement efficiency. Finally, the reconstructed surfaces with respect to these two projection measurements are obtained and compared.

7.1 Principle of stereoscopic deflectometry-profilometry hybrid structured light measurement

As specular-diffuser hybrid objects are widely used in industrial applications, we propose a structured light system to measure the surface shapes of such objects. Here, note that the stereoscopic deflectometry system discussed in Chapter 4 and Chapter 5 enables us to measure the specular surfaces, whereas the stereoscopic profilometry system discussed in Chapter 6 allows us to measure the diffuser surfaces. So, we fully take advantage of the stereoscopic camera scheme by combining such two systems together, and we use this combined system to measure the specular-diffuser hybrid objects. We entitle this combined structured light system as stereoscopic deflectometry-profilometry hybrid (SDPH) system.

In an SDPH system, it has the stereoscopic camera, an LCD screen and a video projector. The stereoscopic camera is the key component, as these two cameras capture the sinusoidal fringe patterns reflected by both the specular section and the diffuser section of the measured object. On the other hand, the LCD and the video projector are implemented to provide sinusoidal fringe patterns (SFPs), and these SFPs are used to illuminate the measured specular-diffuser hybrid object.

We firstly discuss the measurement of the specular section of a specular-diffuser hybrid object. To do so, we project the SFPs with an LCD and capture the reflected fringe pattern with the stereoscopic camera. Then, once we capture the reflected SFPs, we use exactly the same method discussed in Chapter 4 to accomplish the specular section measurement. To be more specific, by projecting the SFPs to the measured object with an LCD, only the specular section reflects the SFPs from the LCD to the stereoscopic camera (see the green lines in Figure 7-1), but the diffuser section cannot reflect the SFPs from the LCD to the cameras. Thus, we can separate the specular

section from the diffuser section of the measured object, and it is shown in Figure 7-1, as the red part is the specular section, and the blue part is the diffuser section. Here, we need to emphasize that the specular-diffuser section separation is the most critical issue in SDPH measurement. Afterwards, we use phase shifting and phase unwrapping to calculate the phase maps corresponding to the specular section in both cameras. Once we obtain the unwrapped phase maps of the specular surface in both cameras, we use these phase maps combined with the phase pattern on the LCD screen to perform phase minimization (see Section 4.2). Finally, the surface shape of the specular section can be obtained by following the same surface reconstruction process presented in Section 4.3 and Section 4.4.

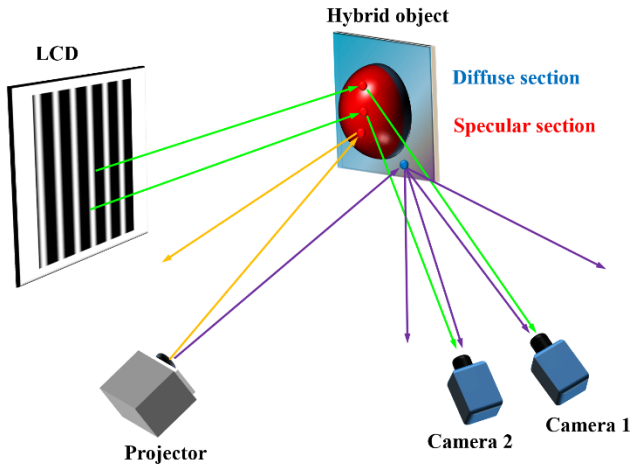

Figure 7-1. Projection diagram of a stereoscopic deflectometry-profilometry hybrid structured light system.

Above we present the measurement of the specular section with the stereoscopic deflectometry-profilometry hybrid system, now we discuss the measurement of the diffuser section. To do so, we project the SFPs with a video projector, and then we capture the reflected fringe patterns with the stereoscopic camera. Here, we need to emphasize that the SFPs projected by the video projector can be reflected by both the specular section (see the yellow lines in Figure 7-1) and the diffuser section (see the purple lines in Figure 7-1). Thus, to only measure the surface shape of the diffuser section, we should separate the diffuser section illumination from the specular section illumination, as we should only allow the video projector light reflected by the diffuser section to enter the cameras. In other words, the video projector light reflected by the specular section should not enter any camera (see how the yellow light is reflected to another direction and does not enter the cameras in Figure 7-1). To accomplish such purpose, we need to properly calibrate the geometric position among the stereoscopic

camera, the measured object and the video projector. With a proper positioning, we let the video projector light reflected by the specular section goes into a certain direction, and the light within this direction cannot be detected by both cameras.

Once we accomplish the above-mentioned positioning, we use the video projector to illuminate the measured object with sinusoidal fringe patterns. Now, as the cameras only capture the reflected SFPs with respect to the diffuser section, we then perform phase shifting and phase unwrapping to obtain the unwrapped phase maps of this diffuser section. Finally, as we have the phase maps in each camera with respect to the diffuser section, we perform the geometric triangulation discussed in Chapter 6 to accomplish the diffuser section surface reconstruction.

Now, we have both the specular section surface and the diffuser section surface, we need to combine these two parts together to reconstruct a complete surface. This is easy to be accomplished, because we not only measure the surface shapes, but we also obtain the geometric position of any point on both measured surfaces with respect to the first camera optical center. Therefore, by extracting the spatial position information of both the diffuser section and the specular section, and then combining these two sections together, we have the complete specular-diffuser object surface. Such surface reconstruction is later more comprehensively discussed in Section 7.2.

At last, we want to emphasize the advantage of using our proposed stereoscopic deflectometry-profilometry hybrid system to accomplish the specular-diffuser object surface measurement. The core element in our proposed system is the stereoscopic camera, and the introduction of these two cameras is the main advantage of our system. Here, by introducing two cameras, we can eliminate the height-normal ambiguity in deflectometry measurement and obtain the surface shape of a specular surface. On the other hand, by introducing two cameras to perform the profilometry measurement, we can avoid both the video projector gamma calibration and the video projector position calibration (i.e., the video projector position calibration means the spatial position between the video projector and the cameras), and this will ease the calibration complexity. Most importantly, the stereoscopic camera guarantees a great system flexibility, because we can change the video projector location (see Section 6.2). By changing the video projector position, we can always let the video projector light being reflected by the specular section not enter the cameras. Therefore, we can always separate the illumination on the specular section and the diffuser section by simply modifying the video projector illumination position. On the contrary, let us assume that we only used one camera in a deflectometry-profilometry hybrid system.

If we only use one camera, the video projector location cannot be changed once it is calibrated, and this will enormously restrict the measurement flexibility. Hence, we may fail to separate the illumination between the specular section and the diffuser section.

7.2 Specular-diffuser hybrid surface reconstruction

To perform the specular-diffuser hybrid object surface reconstruction, the most critical issue is the specular-diffuser section separation (this is to be presented in Section 7.3 with the experimental measurement results). Now, let us assume we have separated the illumination on these two sections with a proper system calibration. Then, we have the specular region and the diffuser region, respectively. So, we can separately perform the surface shape measurement with respect to these two surface regions.

For specular section measurement, we use an LCD to project the sinusoidal fringe patterns (SFPs), and such SFPs will be reflected only by the specular section and enter the cameras. Then, we use the same process in Chapter 4 to obtain the specular surface shape. Here, we want to emphasize that the surface reconstruction process discussed in Chapter 4 not only allows us to get the surface normal, but it also enables us to obtain the surface point position.

Afterwards, we use this same system to perform the diffuser section measurement. For diffuser section measurement, we use a video projector to project sinusoidal fringe patterns (SFPs), and such SFPs will be reflected by the diffuser section and enter the cameras, whereas these SFPs reflected by the specular section cannot enter the cameras. Then, we collect the sinusoidal fringe patterns on the measured diffuser region, and we use the same triangulation process in Chapter 6 to get the surface shape with respect to this diffuser region.

Finally, we have the surface shapes of both the diffuser section and the specular section, and the coordinate of any surface point in these two surfaces are presented in a same coordinate system (i.e., the first camera coordinate system). So, we get the complete surface shape of the specular-diffuser hybrid object by simply stitching these two regions together.

7.3 Experimental measurements with a stereoscopic deflectometry-profilometry hybrid structured light system

In this section, we present the experimental measurement of a specular-diffuser hybrid object with our proposed stereoscopic deflectometry-profilometry hybrid system. To do so, we firstly calibrate the whole system, as we determine the geometric relation among the video projector, the LCD screen, and the stereoscopic camera. Then, we use both separate projection method and combined projection method to measure the specular-diffuser hybrid object. Here, the specular section in the hybrid object is the same specular disk we measured in Section 5.4.3, and the diffuser section is a "stair" structure object similar to that we measured in Section 6.3.1.

7.3.1 Experimental set-up calibration

The calibration of a stereoscopic defleceometry-profilometry hybrid system contains three terms as: (*i*) the calibration of the stereoscopic camera, (*ii*) the geometric calibration of the LCD screen to the stereoscopic camera, and (*iii*) the geometric calibration of the video projector.

We firstly discuss the stereoscopic camera calibration. Here, as we have already presented the stereoscopic camera calibration process in Section 3.4.1, and we have also experimentally implemented the camera calibration in Section 5.2, we directly use that same stereoscopic camera system shown in Figure 5-5 to perform this experiment.

Afterwards, we present the LCD screen position calibration. Here, we use the same stereoscopic phase measuring deflectometry (SPMD) scheme presented in Figure 5-5 to achieve the specular section measurement in a stereoscopic deflectometry-profilometry hybrid (SDPH) system. So, the coordinate system transformation matrix between the LCD coordinate system and the first camera coordinate system is the same matrix $\boldsymbol{RT}_{LCDtCCD1}$ given in Section 5.3.

Finally, we discuss the video projector calibration. In an SDPH system, it is not mandatory to calibrate the gamma nonlinearity of a video projector. However, the video projector cannot be flexibly located at any location, because we need to guarantee the light from the video projector, which is later reflected by the specular section, will not enter any camera. Under this scenario, we locate the video projector away from the stereoscopic camera, and we let the video projector illuminate the whole

specular-diffuser hybrid object with a tilt angel. In this case, the light from the video projector will be reflected by the specular section and goes to another direction, where the stereoscopic camera is not located in this direction. The geometric position between the video projector and the stereoscopic camera is presented in Figure 7-2. Moreover, we give one reflection example presented by the red dash lines, from which we can see that the video projector light is reflected by the specular section and then goes outside of the cameras.

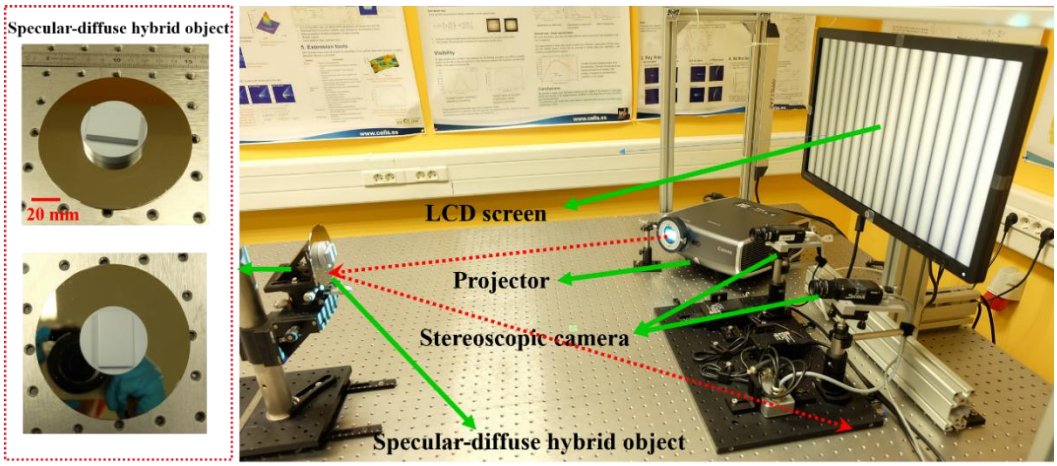

Figure 7-2. Experimental set-up of the stereoscopic deflectometry-profilometry hybrid structured light measurement system, and the measured specular-diffuser hybrid object.

7.3.2 Separate projection measurement

To verify the feasibility of the stereoscopic deflectometry-profilometry hybrid system, we measured a specular-diffuser hybrid object. The specular section of this object is the nearly flat disk that we previously measured in Section 5.4.3. The diffuser section is a "stair", that the bottom is a cylinder and the top is a cuboid. This hybrid object is shown in the left part of Figure 7-2. The diameter of the specular disk is 95 *mm*, the dimeter of the diffuser cylinder is 39.92 *mm*, and the side lengths of the cuboid are 30.55 *mm* and 20.06 *mm*. The height from the disk surface to the cylinder surface is 8.53 *mm*, and the height from the cylinder surface to the cuboid surface is 5.99 *mm*. We located this specular-diffuser hybrid object nearly 930 *mm* to the LCD screen, and we adjusted its position so that the cameras can see this object. Then, we used separate projection to measure the surface shape.

First of all, we projected the sinusoidal fringe patterns from the LCD screen to the measured object, so the cameras only captured the fringe patterns reflected by the specular section. To prove that only the specular section reflected the LCD light, but the diffuser section cannot reflect the LCD light, we give an example of the experimentally captured images in both cameras in Figure 7-3 (a). In Figure 7-3 (a), we can find that the fringe patterns projected from the LCD was only reflected by the specular section, whereas the diffuser section does not present any fringe pattern.

Now, let us discuss the sinusoidal fringe patterns (SFPs) projected from the LCD screen. Here, we use the same process presented in Section 5.4 to measure this specular section, and the SFP series used here have the same frequencies as those presented in Section 5.4. Finally, we again calculate the unwrapped phase maps through phase shifting and phase unwrapping, and the final unwrapped phase maps in each camera are given in Figure 7-3 (b) and Figure 7-3 (c).

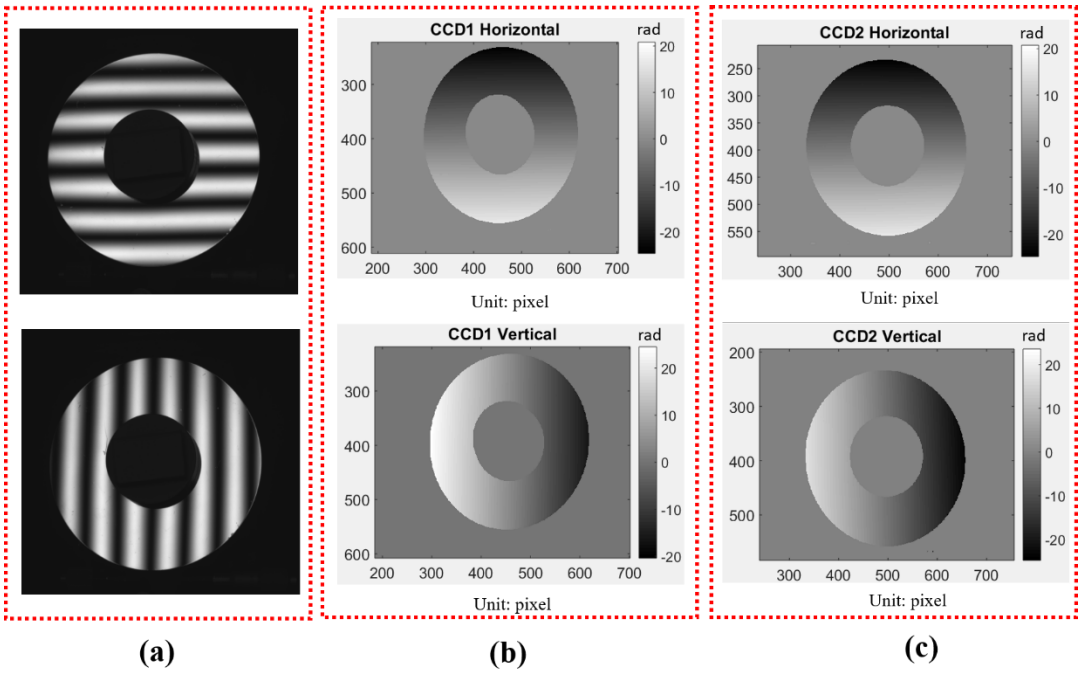

Figure 7-3. Images obtained through the specular section of the object when the LCD is switched on: (a) The photographs of the fringe images. The upper sub-figure is the image captured by the first camera, and the lower sub-figure is the image captured by the second camera. Here, the sinusoidal fringe patterns projected from the LCD have a horizontal period of 360 pixels and a vertical period of 320 pixels. (b) The orthogonal unwrapped phase maps in the first camera. (c) The orthogonal unwrapped phase maps in the second camera.

Once we obtained all unwrapped phase maps of the specular section, we performed the specular surface reconstruction (see Chapter 4), and we got the reconstructed surface shape of the specular section in Figure 7-4. Moreover, the distance from the specular section to the first camera optical center was also obtained.

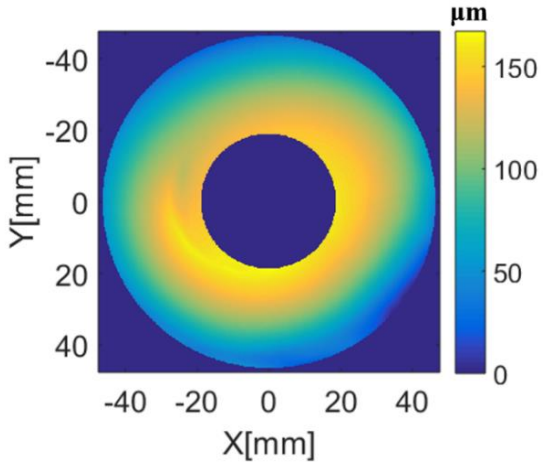

Figure 7-4. Surface shape of the specular section in the specular-diffuser hybrid object measured by the stereoscopic deflectometry-profilometry hybrid system.

The reconstructed discontinuous disk in Figure 7-4 demonstrates a nearly flat surface shape. Moreover, it has an identical surface shape to the disk measured by the stereoscopic phase measuring deflectometry system (see Figure 5-18 in Section 5.4). The nearly same surface shapes provided by both the stereoscopic defleceometry-profilometry hybrid (SDPH) system and the stereoscopic phase measuring deflectometry (SPMD) system prove that the diffuser section will not influence the specular section measurement result in a specular-diffuser hybrid object.

Above we provided the specular section measurement of the specular-diffuser hybrid object. Now, we project the sinusoidal fringe patterns from the video projector to the measured object, so that we can measure the diffuser section. Here, we need to note that as we provided the video projector illumination after we finished all the specular surface measurements with the LCD screen, this is a separate projection measurement.

Note that by using a video projector to illuminate the specular-diffuser hybrid object, both the specular section and the diffuser section will reflect the light. Nevertheless, as we had already performed a proper system positioning, the light will be separated by the specular section (that the light reflected by the specular region will not enter the camera), and we only have the light reflected by the diffuser section

entering the camera. To prove this, we present an example of the experimentally captured images in both cameras in Figure 7-5 (a). In Figure 7-5 (a), we can obviously find that the fringe patterns reflected by the specular section go out of the camera, whereas only the central diffuser section shows the fringe patterns sent from the video projector.

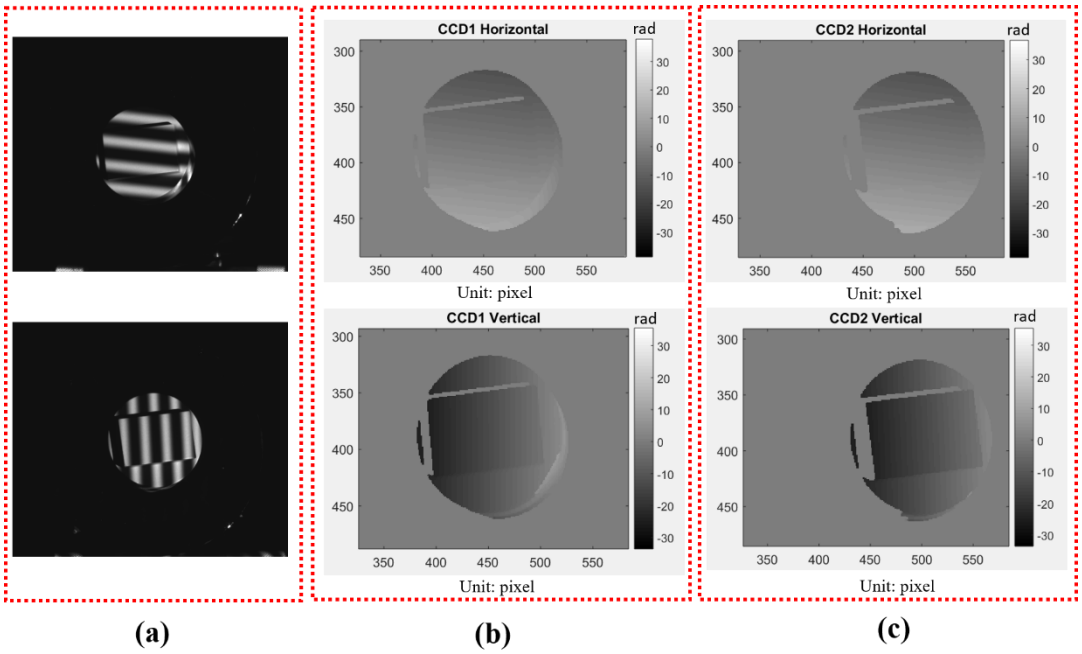

Figure 7-5. Video projector illumination on the specular-diffuser hybrid object: (a) The photographs of the hybrid object being illuminated by the video projector. The upper sub-figure is the image captured by the first camera, and the lower sub-figure is the image captured by the second camera. Here, the sinusoidal fringe pattern projected from the video projector has the horizontal and vertical periods of 50 pixels. (b) The orthogonal unwrapped phase maps in the first camera. (c) The orthogonal unwrapped phase maps in the second camera.

Now, let us discuss the sinusoidal fringe patterns (SFPs) projected from the video projector. Here, we sequentially sent both horizontal and vertical SFPs with their periods as 350, 50 and 30 pixels. Then, we use exactly the same phase unwrapping process in Chapter 3 to acquire the unwrapped phase maps of the diffuser section, and they are given in Figure 7-5 (b) and Figure 7-5 (c). In these unwrapped phase maps, we can find hollow sections without phase information. Nevertheless, it is reasonable that such sections do not provide phase information, because the video projector light

was blocked by the geometric structure of the object and the light was not illuminating these sections.

Once we obtained all unwrapped phase maps of the diffuser section, we performed geometric triangulation between the stereoscopic camera, which is previously described in Section 6.1, to obtain the reconstructed diffuser surface shape. During the geometric triangulation, we only used bi-cubic interpolation to establish the phase pair correspondence as it gives the best reconstruction accuracy. The reconstructed surface shape of the diffuser section is given in Figure 7-6. Moreover, to better visualize the reconstructed diffuser section, we give the reconstructed surface from two different perspectives.

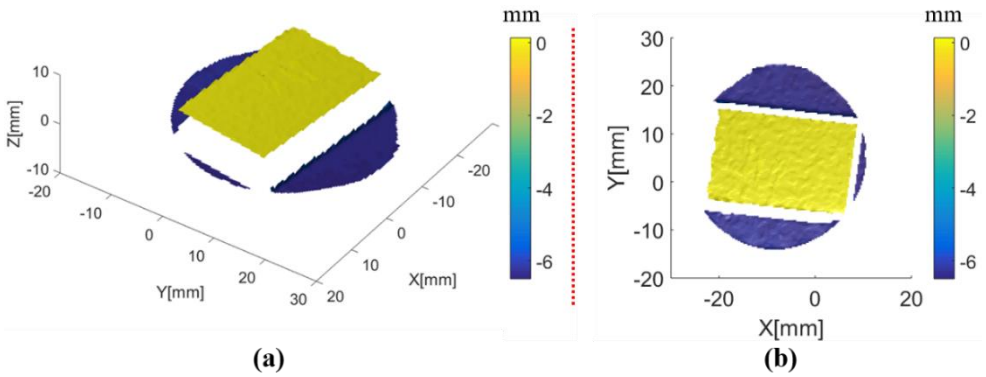

Figure 7-6. Surface shape of the diffuser section in the specular-diffuser hybrid object measured by the stereoscopic deflectometry-profilometry hybrid system: (a) the reconstructed surface shape from the side view, and (b) the reconstructed surface shape from the top view.

At this moment, we have reconstructed the surface shapes of both the specular section and the diffuser section. Apart from the surface shapes, the spatial coordinate of any point in these two surfaces can also be obtained. More importantly, all surface points of both the specular surface and the diffuser surface are represented with respect to the first camera optical center. In other words, all surface points are located in the same coordinate system. Thus, we directly combine the specular surface with the diffuser surface, and we get the complete surface of the specular-diffuser hybrid object as Figure 7-7. In Figure 7-7, we present the reconstructed specular-diffuser hybrid object surface from two perspectives. Here, the purple section is the specular disk, the green section is the diffuser cylinder, and the yellow section is the diffuser cuboid. Moreover, these different colors represent surface heights with respect to the color bar in Figure 7-7.

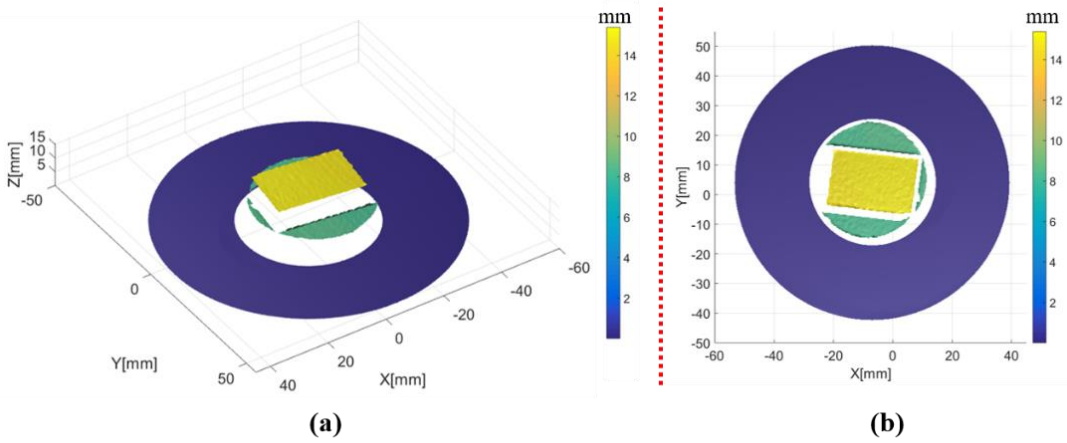

Figure 7-7. Surface shape of the specular-diffuser hybrid object measured by the stereoscopic deflectometry-profilometry hybrid system: (a) the reconstructed surface shape from the side view, and (b) the reconstructed surface shape from the top view.

Finally, we extract the surface heights between any two surfaces. In particular, the surface height from the cuboid surface to the cylinder surface was measured as 6.05 *mm* (i.e., we measured this height at 10 different locations and calculated their average height), whereas the real height measured by a caliper is 5.99 *mm*. Moreover, we also get the height from the specular disk to the cylinder surface as 8.43 *mm* (i.e., we measured this height at 10 different locations and calculated their average height), and the real height between these two surfaces is 8.53 *mm*. Thus, we prove that our proposed stereoscopic deflectometry-profilometry hybrid system can measure the complete surface shape of a specular-diffuser hybrid object with a separate projection.

7.3.3 Combined projection measurement

In Section 7.3.2, we demonstrated the feasibility of using a stereoscopic deflectometry-profilometry hybrid system to measure the surface shape of a specular-diffuser hybrid object. Nevertheless, the measurement was performed by separately illuminating the specular section and the diffuser section. Specifically, we used an LCD to preliminarily illuminate the specular section, and then we used a video projector to illuminate the diffuser section. In this way, the measurement is not efficient because we need to separately illuminate a same object. Hence, we look forward to developing a combined measurement method, from which we can illuminate the hybrid object with both an LCD screen and a video projector at the same time. In this way, by

projecting with an LCD and a video projector simultaneously, we can save the measurement time and therefore enhance the efficiency.

The key to accomplish the combined measurement is how to separate the illumination on the specular section and the diffuser section. From the previous discussion, we know that with a proper system positioning, we can let only the video projector light reflected by the diffuser section enter the camera, whereas we also let the LCD light reflected by the specular section enter the camera. What is more, the light reflected by both sections will not be mixed together, as the video projector light reflected by the specular section will never enter the camera. Under this scenario, we simultaneously illuminate the whole hybrid object, and the image captured by the cameras contains the sinusoidal fringe patterns from both the video projector and the LCD. We give a principle scheme in Figure 7-8, from which we use both cameras to catch the whole sinusoidal fringe pattern distribution on a specular-diffuser hybrid object.

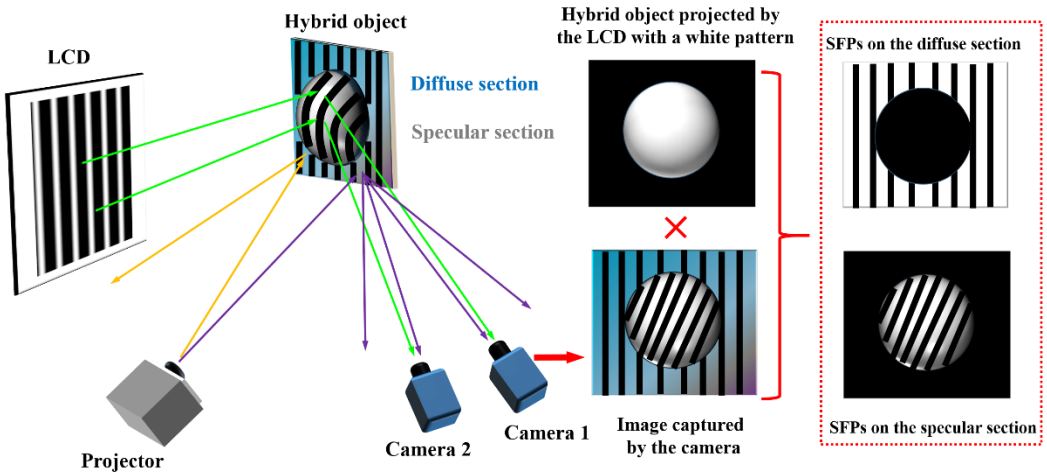

Figure 7-8. The combined measurement diagram of a stereoscopic deflectometry-profilometry hybrid structured light system. Here, the LCD and the video projector illuminate the specular-diffuser object at the same time, and we use Camera 1 to capture a sinusoidal fringe pattern distribution on the object as "Image captured by the camera". Afterwards, we generate a white pattern on the LCD to illuminate the hybrid object, and the intensity distribution captured by Camera 1 at this moment is shown as "Hybrid object projected by the LCD with a white pattern". Finally, we multiplex these two figures together to separate the specular section from the diffuser section. The separated figures are given in the right part.

Now, as both the LCD generated SFPs and the video projector generated SFPs are simultaneously captured by the camera (see "Image captured by the camera" in Figure 7-8), we need to separate these two sections. To do so, we use the LCD to generate a white pattern (i.e., all LCD pixels have the gray level as 255), and we project this white pattern to the specular-diffuser hybrid object. Then, the cameras are used to capture the intensity distribution on this hybrid object. Here, as the specular section will reflect this white board, we can see the profile of the specular section, and we regard the captured image pixels with non-zero intensity as "1". On the other hand, as the diffuser section cannot reflect the light from the LCD to the cameras, we find the diffuser section as totally black, and we regard the camera image pixels with zero intensity as "0". In this way, we construct a binary pattern that reveals the specular and diffuser sections in each camera, and we entitle this pattern as the "principle pattern". One example of a "principle pattern" is given in Figure 7-8 as "Hybrid object projected by the LCD with a white pattern". Here, we need to emphasize that we only consider an ideal condition at this moment, that the diffuser section will not reflect any light at all. Nevertheless, the diffuser section may still reflect a tiny amount of light in the real implementation, and thus, the intensities at these pixels are not zero. However, this is not a problem, as the intensity contrast between the specular section and the diffuser section is high, we can always set a threshold intensity to determine the "principle pattern".

Now, as we have obtained the "principle pattern", and it was modulated to a binary distribution pattern, we simply multiplex this "principle pattern" with the captured images, so we can separate the specular section from the diffuser section. Specifically, by multiplexing the "principle pattern" with a captured image, we obtain the SFP distribution only on the specular section (i.e., see the right lower corner sub-figure in Figure 7-8). Here, the specular section only contains the sinusoidal fringe patterns from the LCD screen. Then, we use the original captured image (i.e., an image with SFPs on both the specular and diffuser sections) to subtract this already separated specular section, and we get the SFP distribution on the diffuser section (i.e., see the right upper corner sub-figure in Figure 7-8). Here, the diffuser section only contains the sinusoidal fringe patterns from the video projector. At this moment, as we have already separated these two sections, we can use the same methods discussed in Section 7.2 to reconstruct the surface.

To verify the feasibility of our proposed method, we again measured the same specular-diffuser hybrid object (see Figure 7-2) with combined projection. Here, we projected the sinusoidal fringe patterns (SFPs) to the object with an LCD and a video

projector at the same time. In the LCD screen, the horizontal SFP periods were 1080 pixels, 360 pixels and 120 pixels, whereas the vertical SFP periods were set as 960 pixels, 320 pixels and 120 pixels. On the other hand, in the video projector, the SFP periods in both the horizontal and vertical directions were set as 350 pixels, 50 pixels and 30 pixels. The captured images are given in Figure 7-9 (a).

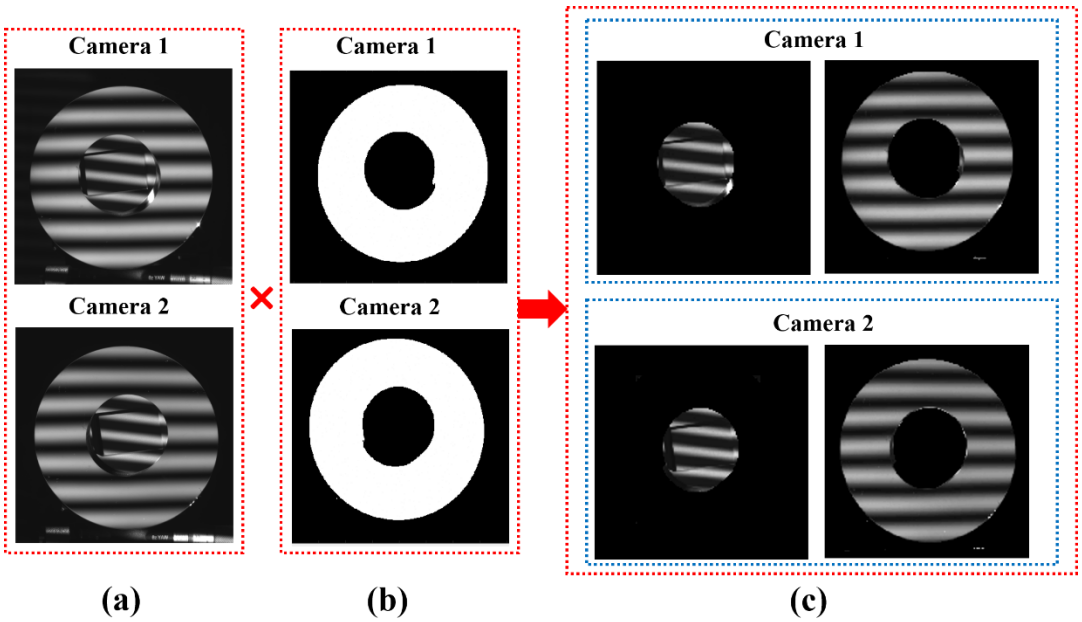

Figure 7-9. Combined illumination on the specular-diffuser hybrid object: (a) The photographs of the hybrid object being illuminated by both the LCD screen and the video projector at the same time. The upper sub-figure is the image captured by the first camera, and the lower sub-figure is the image captured by the second camera. (b) The "principle patterns" with respect to both cameras. (c) The images separated by using the "principle patterns". The SFP patterns on the diffuser section are given in the left part, and the SFP patterns on the specular section are given in the right part.

Later, we used the LCD to project a white pattern, and thus we obtained the "principle patterns" with respect to both cameras shown as Figure 7-9 (b). In Figure 7-9 (b), we can easily distinguish the specular section, as the diffuser section cannot reflect the light from the LCD screen. Finally, by modulating the "principle patterns" into binary patterns, and by multiplexing the original images with these binary "principle patterns", we got the SFPs only on the specular section, and they are shown as the right part figures in Figure 7-9 (c). Hence, we successfully separated the specular sections in both cameras. Then, we subtracted the specular section patterns with the

original images, we obtained the SFPs on the diffuser sections, as they are shown as the left part figures in Figure 7-9 (c).

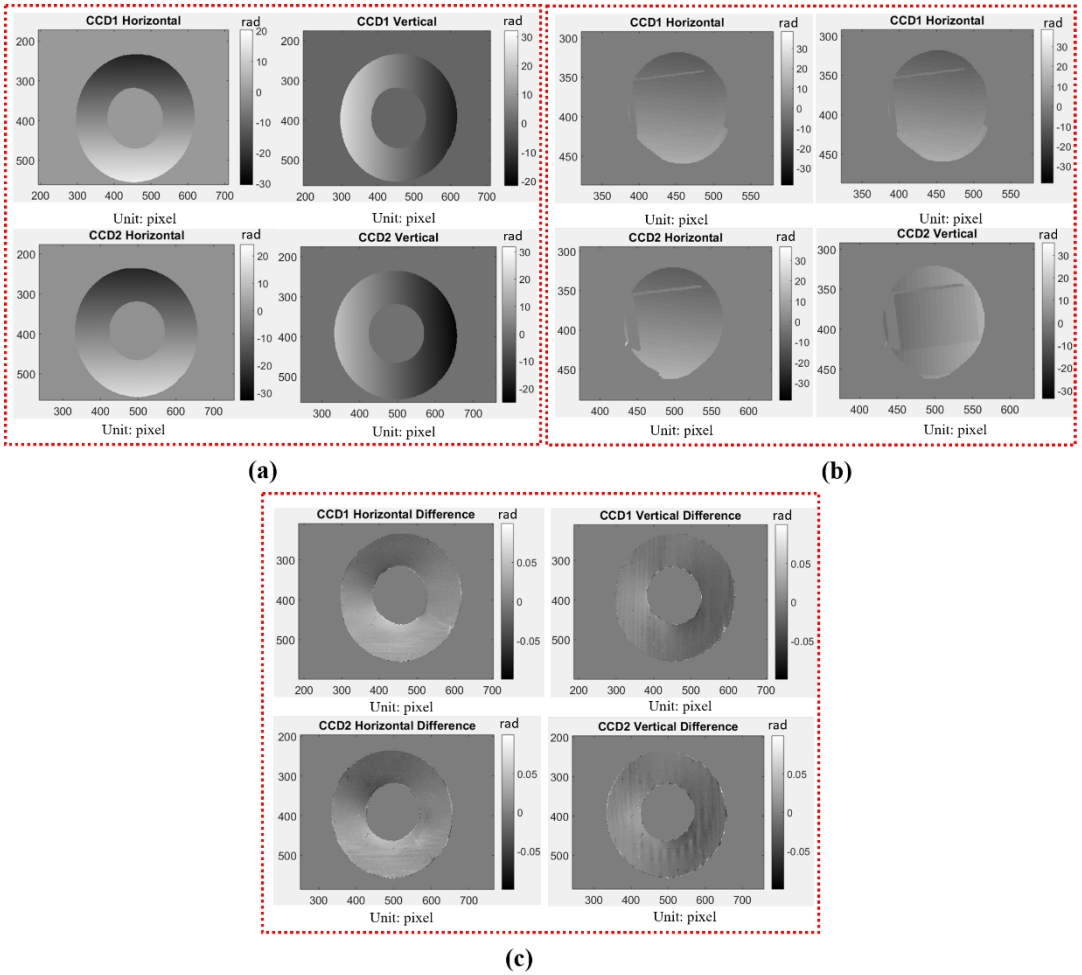

Figure 7-10. Phase maps obtained by combined projection. (a) The phase maps of the specular section in both cameras. The phase maps are calculated by separating the specular section and the diffuser section with "principle patterns". (b) The phase maps of the diffuser section in both cameras. (c) The phase difference maps of the specular section between combined projection and separate projection.

At this moment, as we have the specular section images and the diffuser section images, we again performed phase shifting and phase unwrapping, and the unwrapped phase maps corresponding to both cameras are given in Figure 7-10, where Figure 7-10 (a) are the unwrapped phase maps of the specular section, and Figure 7-10 (b) are the unwrapped phase maps of the diffuser section. To further examine the illumination separation performance, we compare the phase maps on the specular section, which

were obtained through combined projection, with the corresponding phase maps obtained from separate projection (see Figure 7-3 in Section 7.3.2). The unwrapped phase map differences are given in Figure 7-10 (c). From the unwrapped phase difference maps, we find that the maximum phase difference is ranging within only nearly 0.05. Finally, as we used the phase minimization criteria ε as 0.0225 (i.e., 0.15^2=0.0225), such small phase difference (i.e., nearly 0.05) is unlikely to influence the phase pair correspondence.

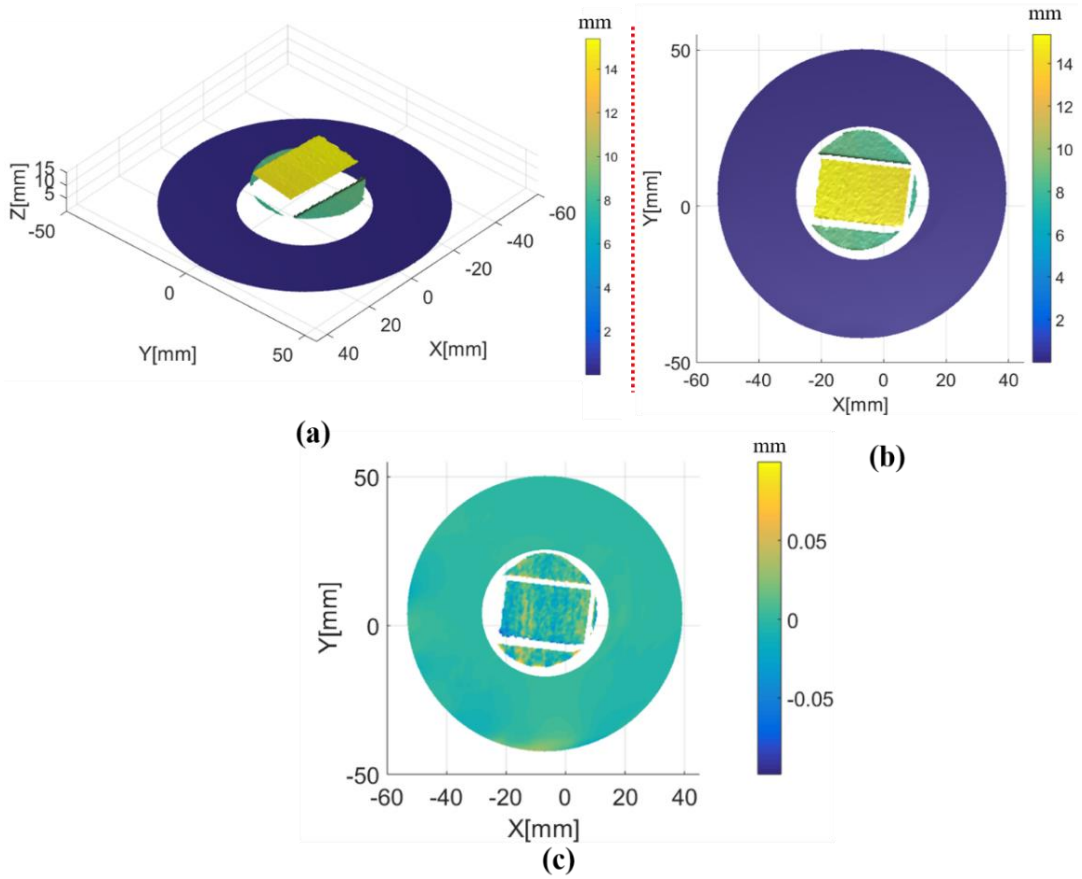

Figure 7-11. Surface shape of the specular-diffuser hybrid object measured by the stereoscopic deflectometry-profilometry hybrid system with combined projection. (a) The reconstructed surface shape from the side view. (b) The reconstructed surface shape from the top view. (c) The surface difference map between separate projection and combined projection.

Finally, we again use the same surface reconstruction method, which is used in the previous discussed separate projection measurement, to reconstruct the surface shape of this specular-diffuser hybrid object. The surface reconstructed by combined

projection method is given in Figure 7-11 (a) and Figure 7-11 (b), from which we can find that it is identical to the reconstructed surface with separate projection (see Figure 7-7). Afterwards, we moved a step further by comparing the separation projection reconstructed surface with the combined projection reconstructed surface. The surface shape difference is given in Figure 7-11 (c). From Figure 7-11 (c), we distinguish a maximum surface difference as 67.3 μm, and it appears on the diffuser section. On the other hand, the specular section presents a smaller surface difference compared to the diffuser section, as the maximum surface difference in the specular section is 34.3 μm. Moreover, the majority of the surface difference map only demonstrates a tiny variation, from which we justify the feasibility of combined projection measurement. So, by properly separating the illumination on both the specular and diffuser sections, combined projection provides a nearly identical measurement result as separate projection, but it will enhance the measurement efficiency.

Chapter 8 Conclusions

8.1 Summary of contributions

In this thesis, we have developed three structured light systems to perform 3D surface shape measurement with high accuracy and robustness. In this case, our proposed systems can measure specular, diffuser and specular-diffuser hybrid objects. This thesis has made the following contributions:

- **We have proposed a phase minimization algorithm to obtain the specular surface shape with a stereoscopic phase measuring deflectometry system.** In this thesis, we presented a stereoscopic phase measuring deflectometry (SPMD) system to measure the surface shapes of specular objects. We initially demonstrated the advantages of using stereoscopic camera based deflectometry to perform the specular surface measurement. In particular, the advantages of an SPMD system can be summarized as: (*i*) it can solve the height-normal ambiguity without shifting the LCD screen position, (*ii*) it does not require any initial surface estimation, and this makes an SPMD system robust to measure different surface shapes. Once we have demonstrated the advantages of SPMD measurement, we propose a phase minimization method to perform the specular surface normal calculation. To be more specific, such phase minimization is accomplished by minimizing the phase difference square value between the phase maps on the LCD screen and the CCD planes. Afterwards, we proposed a polynomial fitting algorithm to perform the phase minimization, and we also presented an iterative method to guarantee that the minimization can be efficiently

fulfilled. From phase minimization, we can calculate the partial derivative distribution of the measured specular surface. Later, we proposed a sub-pixel interpolation method to improve the phase pair correspondence, from which we can further improve the surface derivative calculation accuracy. Here, we showed both a bi-linear interpolation method and a bi-cubic interpolation method. Finally, we discussed a 2D Fourier transform integration process to reconstruct the surface from the measured derivatives. The advantages of the stereoscopic phase measuring deflectometry is discussed in Chapter 1, and the specular surface measurement with an SPMD system is shown in Chapter 4.

- **We have developed and calibrated a stereoscopic phase measuring deflectometry system to perform the specular surface measurement.** Once we have presented the complete surface measurement process, then we experimentally demonstrated the feasibility of using our proposed stereoscopic phase measuring deflectometry (SPMD) system to measure the surface shapes of different specular objects. The SPMD system was firstly calibrated, from which we sequentially performed the LCD gamma correction, the camera calibration, and the LCD position calibration. Once the system was well calibrated, we introduced the proposed polynomial fitting method combined with 2D Fourier transform integration to experimentally obtain the surface shapes of a flat mirror, a spherical mirror and a discontinuous specular disk. The measurement results of the flat mirror demonstrate a surface error RMS as 3.90 μm and a repeatability RMS as 35.1 nm. Later, by comparing the SPMD measurement result with the interferometer result for this flat mirror, we determined the SPMD measurement accuracy (i.e., by using the surface error RMS value as criteria) as 3.88 μm. Apart from the flat mirror, we also measured a spherical mirror. The measurement results of the spherical mirror also demonstrate great accuracy and robustness, as the measured radius is 1001.4 mm compared to the radius of 1000 mm given by Thorlabs. What is more, we also obtained the identical spherical surface shapes by using sinusoidal fringe pattern series with different frequencies, and thus we further justified the robustness of the SPMD system. Finally, we measured a discontinuous specular disk, and the results also show great repeatability by using two different SFP series. Therefore, we have proved that the proposed SPMD system is feasible to perform the accurate and robust measurement of both regular and irregular specular surfaces.

- **We have developed and calibrated a stereoscopic fringe projection profilometry system to perform the diffuser surface measurement.** In this thesis, we systematically demonstrated the feasibility of using our proposed stereoscopic fringe projection profilometry (SFPP) system to measure the surface shapes of different diffuser objects. In particular, we firstly justified that the surface shape reconstruction can be accomplished by using the skew lines to perform the geometric triangulation between the stereoscopic camera. Later, the SFPP system was calibrated, as the exact same stereoscopic camera system, which was also used in the SPMD system, was implemented in the SFPP system. Moreover, as we proved that the gamma nonlinearity will not influence the triangulation accuracy, the video projector was implemented without correcting the gamma effect. Once the SFPP system was well calibrated, we experimentally measured three different diffuser objects as a "stair" structure object, a spherical structure object and a more complex irregular surface structure object. The measurement result of the "stair" object proves that the SFPP system we proposed is feasible to measure the flat surface even with a sharp surface variation; the sphere measurement result demonstrates the practicability of SFPP for curved surface measurement; and the irregular object (i.e., toy duck) measurement result finally verifies that the SFPP system is also available to perform the complex surface measurement. More importantly, in surface reconstruction, we applied direct triangulation, bi-linear sub-pixel interpolation triangulation and bi-cubic sub-pixel interpolation triangulation to reconstruct the surface shape, respectively. Direct triangulation is the fastest, but it provides the poorest surface reconstruction accuracy. Later, bi-linear sub-pixel interpolation provides an improved surface reconstruction accuracy, but it still contains a surface reconstruction error. Finally, bi-cubic sub-pixel interpolation guarantees the most accurate surface reconstruction, with the price of increasing the calculation time. Thus, for SFPP measurement, sub-pixel interpolation technique is recommended for surface reconstruction, and we have to consider the trade-off between the calculation speed and the sub-pixel interpolation accuracy. At last, if a higher measurement accuracy is required, sub-pixel interpolation can be implemented with using more pixel data, with the price of further decrease the calculation efficiency.

- **We have developed and calibrated a stereoscopic deflectometry-profilometry hybrid system to perform the specular-diffuser object**

surface measurement. Finally, we combined the stereoscopic deflectometry system with the stereoscopic profilometry system to obtain a stereoscopic deflectometry-profilometry hybrid (SDPH) system to measure the surface shape of the specular-diffuser hybrid object. In this case, we use the same principle of stereoscopic phase measuring deflectometry (SPMD) to measure the specular section of the hybrid object, and we use the same principle of stereoscopic fringe projection profilometry (SFPP) to measure the diffuser section of the hybrid object. Finally, as we obtain both the specular surface and the diffuser surface, we simply combine these two sections together to obtain the complete specular-diffuser hybrid object surface shape. Here, we want to note that the most critical issue in SDPH measurement is the specular-diffuser section separation. Thus, we proposed both (*i*) a separate projection and (*ii*) a combined projection to measure the hybrid object. Separate projection method is described as we project the sinusoidal fringe patterns from the LCD and the video projector separately, so we can automatically separate the specular section and the diffuser section. Combined projection method is described as we project the sinusoidal fringe patterns from the LCD and the video projector at the same time. Then, we generate a white pattern on the LCD to illuminate the measured specular-diffuser hybrid object, so we obtain a "principle pattern". Finally, we used the obtained "principle pattern" to separate the specular section from the diffuser section for further measurement. As we have proposed two measurement methods, we calibrated the SDPH system and performed the experimental measurement of a specular-diffuser hybrid object. In particular, we used both separate projection and combined projection to measure the studied object. The proposed SDPH demonstrated its feasibility to measure the specular-diffuser hybrid object, and we further examined that both separate projection and combined projection provide an identical measurement result. Thus, we experimentally verified the feasibility of our proposed stereoscopic deflectomety-profilometry hybrid system.

8.2 Future prospects

Structured light measurement is a promising technique to achieve high accuracy 3D surface shape measurement. Specific improvements that can be made in the future are listed below:

- **GPU assisted calculation.** In this thesis, we used Matlab to perform: (*i*) the surface normal calculation for specular surface measurement and (*ii*) the surface point triangulation for diffuser surface measurement. In this way, we perform the calculation point by point, and this is time consuming. Nevertheless, the recently proposed GPU-assisted calculation can avoid the point by point calculation, as it can directly calculate all studied points at the same time, so it guarantees a parallel calculation. As a result, the calculation time will be dramatically decreased, and thus, the measurement efficiency can be improved.

- **Flexible system calibration.** In our stereoscopic phase measuring deflectometry system, the calibration between the LCD coordinate system and the camera coordinate system is complex. In particular, we have to move the cameras to numerous locations to accomplish the calibration, and this will inevitably complex the system calibration and decrease the calibration accuracy. Nevertheless, there is still room to simplify the system calibration between the LCD and the camera. For instance, by implementing a high precision robotic arm, we can easily determine the spatial position relation between the LCD screen and the camera without moving the camera to numerous different locations.

- **Adaptive fringe pattern projection.** In our stereoscopic deflectometry or stereoscopic profilometry system, fixed-pitch sinusoidal fringe patterns (SFPs) are projected to the measured object to perform the surface measurement. However, note that in the case of measuring an extremely complex irregular surface (i.e., large curvature with a steep surface variation), a fixed-pitch sinusoidal fringe pattern may overlap at the irregular section, and thus influence the phase retrieving accuracy. Thus, an adaptive sinusoidal fringe projection can be generated to compensate the fringe overlap in the irregular surface section. At this moment, the structured light measurement system could be used to measure more complex objects.

- **Multi-perspective 3D surface reconstruction.** In this thesis, the structured light systems allow us to obtain the 3D surface shape of the measured object. Here, we measured the object with our proposed systems from only one perspective. Now, let us assume we rotate the measured object, so we can measure the 3D surface shape of other sections of the

measured object. Then, by performing a multi-perspective 3D surface reconstruction, we can reconstruct the complete 3D surface shape of the measured object (i.e., the toy duck we measured in Chapter 6).

Appendix

Mathematical description of surface normal calculation in an SPMD system

In Section 4.1, we present a phase minimization principle to obtain the specular surface normal in the stereoscopic phase measuring deflectometry system. However, the mathematical description for surface normal calculation is not presented in that section. Thus, in this Appendix, we will comprehensively present a complete mathematical description of surface normal calculation in the stereoscopic phase measuring deflectometry system.

To describe the mathematics for surface normal calculation, we need to initially give the unwrapped phase maps on the image plane of both cameras. Here, we assume that the phase map distortion, which is introduced by camera distortion, has already been corrected. Therefore, we have the ideal phase maps, and the phase value at any camera image plane pixel is known.

On the other hand, we give the SPMD system component parameters and all coordinate systems. For system component parameters, we have the following three parameters as: (*i*) the intrinsic parameters of the first camera, (*ii*) the intrinsic parameters of the second camera, and (*iii*) the parameters of the LCD screen. For coordinate systems, we have: (*i*) the world coordinate system, (*ii*) the coordinate

system transformation from the second camera coordinate system to the first camera coordinate system, and (*iii*) the coordinate system transformation from the LCD screen coordinate system to the first camera coordinate system.

We present the three above-mentioned SPMD system component parameters here:

(1) As the lens distortion has already been corrected, the intrinsic parameters of the first camera contain the camera focal length and the principle point. The focal length of the first camera is entitled as f_1. The principle point of this camera is entitled as (u_{O1},v_{O1}). Here, the CCD pixel is a square pixel with its side length as s.

(2) Similar to the first camera, we have the parameters of the second camera as: the focal length of f_2, the principle point of (u_{O2},v_{O2}), the CCD pixel side length of s.

(3) For the LCD screen, we have the dimension of the LCD screen, and we also have the size of an LCD pixel. Here, the LCD dimension is $M\times N$, its geometric center is (M_0,N_0), and the LCD pixel is a square pixel with its side length as l.

Next, we present three coordinate systems used in the SPMD system, they are presented as follow:

(1) The coordinate system of the first camera is entitled as $(O_1\text{-}X_1,Y_1,Z_1)$, where $\boldsymbol{O_1}$ is the camera optical center (i.e., the pinhole), and Z_1 axis is the optical axis of the first camera. The first camera coordinate follows a right hand distribution. Here, we want to emphasize that the first camera coordinate system is also the world coordinate system in our SPMD system. This means that we transform all points and vectors into this coordinate system to perform the further calculation.

(2) The coordinate system of the second camera is entitled as $(O_2\text{-}X_2,Y_2,Z_2)$, where $\boldsymbol{O_2}$ is the camera optical center (i.e., the pinhole), and Z_2 axis is the optical axis of the second camera. The second camera coordinate follows a right hand distribution. Here, the coordinate transformation from the second camera coordinate to the first camera coordinate is accomplished by introducing $\boldsymbol{RT_{C2tC1}}$. Specifically, $\boldsymbol{RT_{C2tC1}}$ is a 4×4 matrix and it is written as:

$$\boldsymbol{RT_{C2tC1}} = \begin{pmatrix} \boldsymbol{R_{C2tC1}} & \boldsymbol{T_{C2tC1}} \\ 0 & 1 \end{pmatrix}, \tag{A.1}$$

where $\boldsymbol{R_{C2tC1}}$ is a 3×3 matrix representing the rotation from the second camera to the first camera, and $\boldsymbol{T_{C2tC1}}$ is a 1×3 column representing the shifting in the same direction.

(3) The coordinate system of the LCD screen is entitled as $(O_{LCD}\text{-}X_{LCD}, Y_{LCD}, Z_{LCD})$, where $\boldsymbol{O_{LCD}}$ is the geometric center of the LCD screen, and Z_{LCD} axis is a vector perpendicular to the LCD plane. The LCD screen coordinate system follows a right hand distribution, and the origin of this coordinate system is at the geometric center of the LCD plane. Here, the coordinate transformation from the LCD screen coordinate system to the first camera coordinate system is accomplished by introducing $\boldsymbol{RT_{LCDtC1}}$. Specifically, $\boldsymbol{RT_{LCDtC1}}$ is a 4×4 matrix, and it is written as:

$$\boldsymbol{RT_{LCDtC1}} = \begin{pmatrix} \boldsymbol{R_{LCDtC1}} & \boldsymbol{T_{LCDtC1}} \\ 0 & 1 \end{pmatrix}, \tag{A.2}$$

where $\boldsymbol{R_{LCDtC1}}$ is a 3×3 matrix representing the rotation from the LCD screen to the first camera, and $\boldsymbol{T_{LCDtC1}}$ is a 1×3 column representing the shifting in the same direction.

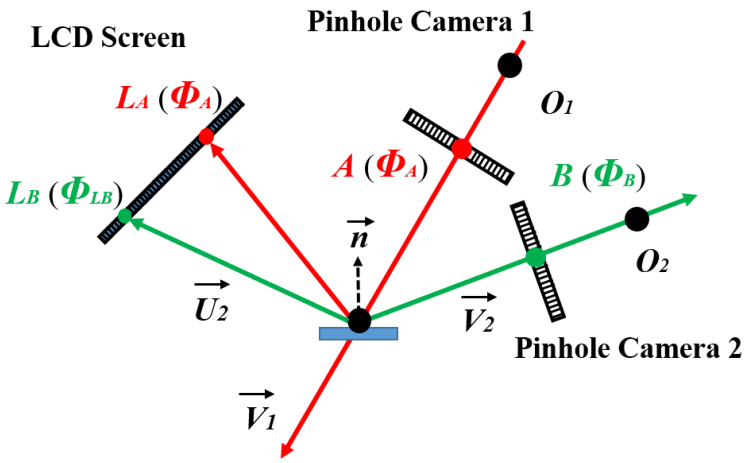

Figure A: Principle scheme of the stereoscopic phase measuring deflectometry system for surface normal determination.

Now, as we are equipped with the system parameters and the coordinate system information, we perform the surface normal calculation. To better visualize the calculation process, we give Figure A to depict the surface normal calculation, and the studied pixel is $\boldsymbol{A}$ on the first camera image plane. The surface normal calculation can be listed as nine sequential steps, and they are discussed as follow:

(1) Determine the basic vector $\boldsymbol{V_1}$

We select pixel $\boldsymbol{A}$ on the first camera image plane, this pixel is located at (u_1, v_1) in the first camera image plane, and its phase value is Φ_A. Note that in the real

implementation, a pixel has two phase values (i.e., orthogonal phase). However, here we only use one phase value so we can simplify the discussion. Then, the coordinate of this pixel $\boldsymbol{A}$ in the first camera coordinate system is calculated as three tuples as follow:

$$x_1 = s(u_1 - u_{O1})\,, \tag{A.3}$$

$$y_1 = s(v_1 - v_{O1})\,, \tag{A.4}$$

$$z_1 = f_1\,, \tag{A.5}$$

where s is the CCD pixel side length, (u_{O1},v_{O1}) is the first camera principle point, and f_1 is the camera focal length.

Once we get the three-dimensional coordinate of this pixel in the first camera coordinate system, we connect it to the first camera optical center to forge a vector $\boldsymbol{v_1}$ in the first camera coordinate system. This vector is then mathematically described as:

$$\boldsymbol{v_1} = \left[x_1, y_1, z_1\right]. \tag{A.6}$$

Finally, we calculate its normalized vector $\boldsymbol{V_1}$, and this normalized vector is calculated as:

$$\boldsymbol{V_1} = \frac{\left[x_1, y_1, z_1\right]}{\sqrt{{x_1}^2 + {y_1}^2 + {z_1}^2}}\,. \tag{A.7}$$

(2) Find the correspondent phase pair $\boldsymbol{L_1}$ on the LCD

Now, as we have determined the basic vector $\boldsymbol{V_1}$ in the first camera coordinate system, we search on the LCD screen a particular pixel $\boldsymbol{L_A}$ that has the same phase value as Φ_A. Here, Φ_A is the phase value of point $\boldsymbol{A}$ on the first camera image plane. After we search the phase map on the LCD panel, we find pixel $\boldsymbol{L_A}$ and it is located at pixel (m_1,n_1) in the LCD plane, so its position in the LCD coordinate system can be calculated as three tuples as follow:

$$X_{LA} = l(m_1 - M_0)\,, \tag{A.8}$$

$$Y_{LA} = l(n_1 - N_0)\,, \tag{A.9}$$

$$Z_{LA} = 0\,. \tag{A.10}$$

where l is the LCD pixel side length, (M_0,N_0) is the LCD geometric center.

Now, we use $\boldsymbol{RT_{LCDtC1}}$ to transform this point from the LCD coordinate system to the first camera coordinate system, and this point $\boldsymbol{L_A}$ is presented as:

$$(x_{LA}, y_{LA}, z_{LA}, 1)^T = \boldsymbol{RT_{LCDtC1}} \cdot (X_{LA}, Y_{LA}, Z_{LA}, 1)^T , \tag{A.11}$$

where (x_{LA}, y_{LA}, z_{LA}) is the coordinate of point $\boldsymbol{L_A}$ in the first camera coordinate system.

(3) Determine a potential surface point

Now, as we have the corresponding phase pair on both the first camera and the LCD, we need to select a potential point on the basic vector $\boldsymbol{V_1}$. To do so, we use $\boldsymbol{V_1}$ to forge a line P_1 which passes through the first camera optical center $\boldsymbol{O_1}$. This line is determined as:

$$P_1 = \boldsymbol{V_1} \cdot t , \tag{A.12}$$

where t is a real number, and this line is described in the first camera coordinate system.

In this case, we select any t, and the three tuples representing the potential surface point $\boldsymbol{P}$ is calculated as:

$$x = \frac{x_1 \cdot t}{\sqrt{{x_1}^2 + {y_1}^2 + {z_1}^2}} , \tag{A.13}$$

$$y = \frac{y_1 \cdot t}{\sqrt{{x_1}^2 + {y_1}^2 + {z_1}^2}} , \tag{A.14}$$

$$z = \frac{z_1 \cdot t}{\sqrt{{x_1}^2 + {y_1}^2 + {z_1}^2}} . \tag{A.15}$$

Here, this potential surface point $\boldsymbol{P}$ is represented as $\boldsymbol{P}$=(x,y,z), and it is represented in the first camera coordinate system.

(4) Calculate the surface normal to the potential surface point

At this moment, we have used the first camera and the LCD screen to estimate a potential surface point $\boldsymbol{P}$. Then, we need to calculate the surface normal to this potential point. To do so, we firstly connect $\boldsymbol{P}$ with $\boldsymbol{L_A}$ to forge an inverse vector $\boldsymbol{u_1}$, and this vector can be calculated as:

$$\boldsymbol{u_1} = \left[x_{LA} - x, y_{LA} - y, z_{LA} - z \right]. \tag{A.16}$$

where (x_{LA}, y_{LA}, z_{LA}) is the coordinate of the LCD point $\boldsymbol{L_A}$ in the first camera coordinate system, and (x,y,z) is the coordinate of the potential surface point $\boldsymbol{P}$ in the same coordinate system.

Then, we calculate its unit vector $\boldsymbol{U_1}$, and this unit vector is calculated as:

$$\boldsymbol{U_1} = \frac{\left[x_{LA} - x, y_{LA} - y, z_{LA} - z\right]}{\sqrt{(x_{LA} - x)^2 + (y_{LA} - y)^2 + (z_{LA} - z)^2}}. \tag{A.17}$$

Finally, as we have both $\boldsymbol{V_1}$ and $\boldsymbol{U_1}$, we can calculate the surface normal to this potential point $\boldsymbol{P}$ as:

$$\boldsymbol{N} = \boldsymbol{U_1} - \boldsymbol{V_1}. \tag{A.18}$$

Then, we normalize normal $\boldsymbol{N}$, and we have the normalized normal $\boldsymbol{n}$ to the potential surface point $\boldsymbol{P}$.

(5) Calculate the second inverse ray to the second camera

Until this step, we have performed all the calculation with respect to the first camera, Later, we introduce the second camera to execute phase minimization. To do so, we need to find the correspondent points on the LCD panel and the second camera image plane with respect to this potential surface point $\boldsymbol{P}$.

So, we connect point $\boldsymbol{P}$ with the second camera optical center $\boldsymbol{O_2}$, and we can forge another vector $\boldsymbol{v_2}$. Here, the second camera optical center $\boldsymbol{O_2}$ is transformed into the first camera coordinate system as:

$$(x_{O2}, y_{O2}, z_{O2}, 1)^T = \boldsymbol{RT_{C2tC1}} \cdot (0,0,0,1)^T, \tag{A.19}$$

Then, $\boldsymbol{v_2}$ is calculated as:

$$\boldsymbol{v_2} = \left[x_{O2} - x, y_{O2} - y, z_{O2} - z\right]. \tag{A.20}$$

By calculating its normalized vector, we have $\boldsymbol{V_2}$ as:

$$\boldsymbol{V_2} = \frac{\left[x_{O2} - x, y_{O2} - y, z_{O2} - z\right]}{\sqrt{(x_{O2} - x)^2 + (y_{O2} - y)^2 + (z_{O2} - z)^2}}. \tag{A.21}$$

(6) Calculate the intersection pixel on the second camera image plane

Now, we use $\boldsymbol{V_2}$ to calculate its intersection point with the second camera image plane. To do so, we need to firstly transform the second camera coordinate system to

the first camera coordinate system. Specifically, the normal of the second camera image plane in the first camera coordinate system is:

$$\boldsymbol{N_2}^T = \boldsymbol{R_{C2tC1}} \cdot (0,0,1)^T \,, \tag{A.22}$$

where $\boldsymbol{R_{C2tC1}}$ is the rotation matrix from the second camera to the first camera.

Then, we normalize vector $\boldsymbol{N_2}$, and we get the normalized vector $\boldsymbol{n_2}$.

Afterwards, we also transform the second camera image center to the first camera coordinate system as:

$$\boldsymbol{C_2} = \boldsymbol{T_{C2tC1}}^{\boldsymbol{T}} \,, \tag{A.23}$$

where $\boldsymbol{C_2}$ is the coordinate of the second camera image center in the first camera coordinate system.

Now, we can calculate the intersection point from $\boldsymbol{V_2}$ to the second camera image plane, and we obtain this intersection point $\boldsymbol{B}$=(x_B,y_B,z_B) as:

$$\boldsymbol{B} = \boldsymbol{V_2} \frac{(\boldsymbol{C_2} - \boldsymbol{P}) \cdot \boldsymbol{n_2}}{\boldsymbol{V_2} \cdot \boldsymbol{n_2}} + \boldsymbol{P} \,, \tag{A.24}$$

where (x_B,y_B,z_B) is the coordinate of the intersection point $\boldsymbol{B}$ in the first camera coordinate system.

Finally, we transfer this point back to the second camera coordinate system, and we have the following equation as:

$$(X_B, Y_B, Z_B, 1)^T = \boldsymbol{R}\boldsymbol{T_{C2tC1}}^{\boldsymbol{-1}} \cdot (x_B, y_B, z_B, 1)^T \,, \tag{A.25}$$

where the three tuples (X_B, Y_B, Z_B) mean the coordinate of point $\boldsymbol{B}$ in the second camera coordinate system.

From this information, we can finally transform this point to the image plane of the second camera, and we have the pixel position of this point presented as:

$$u_2 = X_B \big/ s + u_{O2} \,, \tag{A.26}$$

$$v_2 = Y_B \big/ s + v_{O2} \,, \tag{A.27}$$

where s is the CCD pixel side length of the second camera, and (u_{O2},v_{O2}) is the principle point of the second camera.

Once we know this intersection pixel (u_2,v_2) on the second camera image plane, we can easily find the phase value Φ_B of this pixel on the phase map in the second camera image plane.

(7) Calculate the second inverse ray to the LCD

Now, we have the intersection pixel on the second camera, and we also know the phase value of this pixel. Thus, we need to find on the LCD its correspondent pixel and determine its phase value, so that we can perform the phase minimization. To do so, we establish a second inverse ray tracing, which connects the potential surface point $\boldsymbol{P}$ to the LCD panel.

Here, as we have previously calculated the normal to the potential surface point $\boldsymbol{P}$, we then use its normal $\boldsymbol{n}$ to perform the second inverse ray tracing. By knowing the potential surface point normal $\boldsymbol{n}$ and the incident vector $\boldsymbol{V_2}$, we can calculate the reflection vector $\boldsymbol{u_2}$, and it is calculated as:

$$\boldsymbol{u_2} = \boldsymbol{V_2} - 2(\boldsymbol{V_2} \cdot \boldsymbol{n_2})\boldsymbol{n_2}\,. \tag{A.28}$$

Finally, we normalize vector $\boldsymbol{u_2}$, and we have the normalized vector $\boldsymbol{U_2}$ in the first camera coordinate system (see Figure A).

(8) Calculate the second intersection pixel on the LCD

For this step, we need to use $\boldsymbol{U_2}$ to calculate its intersection pixel on the LCD panel. To do so, we need to firstly transform the LCD coordinate system to the first camera coordinate system. Specifically, the normal of the LCD panel in the first camera coordinate system is:

$$\boldsymbol{N_{LCD}}^T = \boldsymbol{R_{LCDtC1}} \cdot (0,0,1)^T\,, \tag{A.29}$$

where $\boldsymbol{R_{LCDtC1}}$ is the rotation matrix from the LCD coordinate system to the first camera coordinate system. Then we normalize $\boldsymbol{N_{LCD}}$ and we get the normalized LCD panel normal as $\boldsymbol{n_{LCD}}$.

Afterwards, we transform the geometric center of the LCD to the first camera coordinate system as:

$$\boldsymbol{C_{LCD}}^T = \boldsymbol{T_{LCDtC1}}^T\,, \tag{A.30}$$

where $\boldsymbol{C_{LCD}}$ is the coordinate of the LCD geometric center in the first camera coordinate system.

Now, we can calculate the intersection point from $\boldsymbol{U_2}$ to the LCD plane, and we obtain this intersection point $\boldsymbol{L_B}$=(x_{LB},y_{LB},z_{LB}) as:

$$\boldsymbol{L_B} = \boldsymbol{U_2}\frac{(\boldsymbol{C_{LCD}} - \boldsymbol{P}) \cdot \boldsymbol{n_{LCD}}}{\boldsymbol{U_2} \cdot \boldsymbol{n_{LCD}}} + \boldsymbol{P}\,, \tag{A.31}$$

where (x_{LB},y_{LB},z_{LB}) is in the first camera coordinate system.

Finally, we transfer this point back to the LCD coordinate system, and we have the following equation as:

$$(X_{LB}, Y_{LB}, Z_{LB}, 1)^T = \boldsymbol{RT_{LCDtC1}}^{-1} \cdot (x_{LB}, y_{LB}, z_{LB}, 1)^T\,, \tag{A.32}$$

where the three tuples mean the coordinate of point $\boldsymbol{L_B}$ in the LCD coordinate system.

From this information, we can finally represent this point in the unit of LCD pixel, and we have the pixel position of this point presented as:

$$u_{LCD} = X_{LB}\big/l + M_0\,, \tag{A.33}$$

$$v_{LCD} = Y_{LB}\big/l + N_0\,, \tag{A.34}$$

where l is the LCD pixel side length, and (M_0,N_0) is the center pixel in the LCD panel.

Once we know this intersection pixel on the LCD panel, we can easily find the phase value Φ_{LB} of this pixel on the phase map in the LCD panel.

(9) Calculate the square of the phase difference

Finally, we get the correspondent phase pixels on the LCD and the second camera image plane, respectively. The second camera image plane pixel is (u_2,v_2), and its phase value is Φ_B; whereas the corresponding pixel on the LCD plane is (u_{LCD},v_{LCD}), and its phase value is Φ_{LB}. Thus, we can calculate the phase difference square between these two pixels as:

$$(\Phi_B - \Phi_{LB})^2 = \delta\,, \tag{A.35}$$

where δ is the square of the phase difference.

Moreover, by introducing sub-pixel interpolation with respect to these two pixels, we can get a more accurate phase pair correspondence. The sub-pixel interpolation is comprehensively discussed in Section 4.3.

List of acronyms

Acronym	Meaning
SFP	Sinusoidal Fringe Pattern
PMD	Phase Measuring Deflectometry
FPP	Fringe Projection Profilometry
SFPP	Stereoscopic Fringe Projection Profilometry
SPMD	Stereoscopic Phase Measuring Deflectometry
SDPH	Stereoscopic Deflectometry-Profilometry Hybrid
LCD	Liquid Crystal Display
LCoS	Liquid Crystal on Silicon

Bibliography

[1] F.A.R. Martins, J.G. García-Bermejo, E.Z. Casanova, and J.R. Perán González. *Automated 3D surface scanning based on CAD model*. Mechatronics **15** (7), pp. 837–857 (2005).

[2] M. Germani, F. Mandorli, M. Mengoni, and R. Raffaeli. *CAD-based environment to bridge the gap between product design and tolerance control*. Precis. Eng. **34** (1), pp. 7–15 (2010).

[3] D. Malacara. *Optical Shop Testing. 3th Ed*. John Wiley & Sons (2007).

[4] H. Kawasaki, R. Furukawa, R. Sagawa, and Y. Yagi. *Dynamic scene shape reconstruction using a single structured light pattern*. Proc. IEEE Comput. Soc. Conf. Comput. Vis. Pattern Recognit., pp. 1-8 (2008).

[5] O.V. Olesen, R.R. Paulsen, L. Højgaard, B. Roed, and R. Larsen. *Motion tracking for medical imaging: A nonvisible structured light tracking approach*. IEEE Trans. Med. Imaging **31** (1), pp. 79–87 (2012).

[6] J.E. Krist, R.N. Hook, and F. Stoehr. *20 years of Hubble Space Telescope optical modeling using Tiny Tim*. Proc. SPIE **8127**, Opt. Model. Perform. Predict. V, 81270J (2011).

[7] W.L. Freedman, B.F. Madore, B.K. Gibson, L. Ferrarese, D.D. Kelson, S. Sakai, J.R. Mould, R.C. Kennicutt, H.C. Ford, J.A. Graham, J.P. Huchra, S.M.G. Hughes, G.D. Illingworth, L.M. Macri, and P.B. Stetson. *Final results from the Hubble Space Telescope Key Project to measure the Hubble constant*. Astrophys. J. **553** (1), pp. 47 (2001).

[8] J.P. Gardner, J.C. Mather, M. Clampin, R. Doyon, M.A. Greenhouse, H.B. Hammel, J.B. Hutchings, P. Jakobsen, S.J. Lilly, K.S. Long, J.I. Lunine, M.J. McCaughrean, M. Mountain, J. Nella, G.H. Rieke, M.J. Rieke, H.W. Rix, E.P. Smith, G. Sonneborn, M. Stiavelli, H.S. Stockman, R.A. Windhorst, and G.S. Wright. *The James Webb Space Telescope*. Space Sci. Rev. **123** (4), pp. 485–606 (2006).

[9] C.J. Walsh, A.J. Leistner, J. Seckold, B.F. Oreb, and D.I. Farrant. *Fabrication and measurement of optics for the Laser Interferometer Gravitational Wave Observatory*. Appl. Opt. **38** (13), pp. 2870-2879 (1999).

[10] A. Abramovici, W.E. Althouse, R.W.P. Drever, Y. Gürsel, S. Kawamura, F.J. Raab, D. Shoemaker, L. Sievers, R.E. Spero, K.S. Thorne, R.E. Vogt, R. Weiss, S.E. Whitcomb, and M.E. Zucker. *LIGO: The laser interferometer gravitational-wave observatory*. Science **256** (5055), pp. 325-333 (1992).

[11] P. Su, R.E. Parks, L. Wang, R.P. Angel, and J.H. Burge. *Software configurable optical test system: a computerized reverse Hartmann test*. Appl. Opt. **49** (23), pp. 4404-4412 (2010).

[12] P. Su, Y. Wang, J.H. Burge, K. Kaznatcheev, and M. Idir. *Non-null full field X-ray mirror metrology using SCOTS: a reflection deflectometry approach*. Opt. Express **20** (11), pp. 12393-12406 (2012).

[13] L. Ren, X. Wei, Z. Lu, W. Yu, W. Xu, and Z. Shen. *A review of available methods for the alignment of mirror facets of solar concentrator in solar thermal power system*. Renew. Sustain. Energy Rev. **32**, pp. 76–83 (2014).

[14] J. Xiao, X. Wei, Z. Lu, W. Yu, and H. Wu. *A review of available methods for surface shape measurement of solar concentrator in solar thermal power applications*. Renew. Sustain. Energy Rev. **16**, pp. 2539–2544 (2012).

[15] D. Fontani, F. Francini, D. Jafrancesco, L. Mercatelli, and P. Sansoni. *Mirror shape detection by reflection grating moire method with optical design validation*. Proc. SPIE **5856**, Opt. Meas. Syst. Ind. Insp. IV, pp. 377-384 (2005).

[16] S. Ulmer, P. Heller, and W. Reinalter. *Slope Measurements of Parabolic Dish Concentrators Using Color-Coded Targets*. J. Sol. Energy Eng. **130** (1), pp. 011015 (2008).

[17] B. Belhomme, R. Pitz-Paal, P. Schwarzbözl, and S. Ulmer. *A New Fast Ray Tracing Tool for High-Precision Simulation of Heliostat Fields*. J. Sol. Energy Eng. **131** (3), pp. 031002 (2009).

[18] H. G. Maas. *Robust Automatic Surface Reconstruction with Structured Light*. ISPRS J. Photogramm. Remote Sens. **29**, pp. 709–713 (1993).

[19] J.M. Fitts. *High-speed 3-D surface measurement surface inspection and reverse-CAD system*. US 5175601 (1992).

[20] J. Straub. *Initial work on the characterization of additive manufacturing (3D Printing) using software image analysis*. Machines **3** (2), pp. 55–71 (2015).

[21] E. Brinksmeier, and J. Sölter. *Prediction of shape deviations in machining*. CIRP Ann. - Manuf. Technol. **58** (1), pp. 507–510 (2009).

[22] K.C. Fan, F. Cheng, W. Wang, Y. Chen, and J.Y. Lin. *A scanning contact probe for a micro-coordinate measuring machine (CMM)*. Meas. Sci. Technol. **21** (5), pp. 054002 (2010).

[23] V. Carbone, M. Carocci, E. Savio, G. Sansoni, and L. De Chiffre. *Combination of a vision system and a coordinate measuring machine for the reverse engineering of freeform surfaces.* Int. J. Adv. Manuf. Technol. **17** (4), pp. 263–271 (2001).

[24] T.L. Zobrist, J.H. Burge, and H.M. Martin. *Laser tracker surface measurements of the 8.4 m GMT primary mirror segment.* Proc. SPIE **7426**, Opt. Manuf. Test. VIII, 742613 (2009).

[25] J.H. Burge, P. Su, C. Zhao, and T. Zobrist. *Use of a commercial laser tracker for optical alignment.* Proc. SPIE **6676**, Opt. Syst. Alignment Toler., 66760E (2007).

[26] G. Sansoni, and F. Docchio. *Three-dimensional optical measurements and reverse engineering for automotive applications.* Robot. Comput. Integr. Manuf. **20** (5), pp. 359–367 (2004).

[27] J. Xu, N. Xi, C. Zhang, J. Zhao, B. Gao, and Q. Shi. *Rapid 3D surface profile measurement of industrial parts using two-level structured light patterns.* Opt. Lasers Eng. **49** (7), pp. 907–914 (2011).

[28] J. Xu, N. Xi, C. Zhang, Q. Shi, and J. Gregory. *Real-time 3D shape inspection system of automotive parts based on structured light pattern.* Opt. Laser Technol. **43** (1), pp. 1–8 (2011).

[29] K. Zhong, Z. Li, X. Zhou, Y. Li, Y. Shi, and C. Wang. *Enhanced phase measurement profilometry for industrial 3D inspection automation.* Int. J. Adv. Manuf. Technol. **76** (9–12), pp. 1563–1574 (2015).

[30] H. Lin, J. Gao, Q. Mei, G. Zhang, Y. He, and X. Chen. *Three-dimensional shape measurement technique for shiny surfaces by adaptive pixel-wise projection intensity adjustment.* Opt. Lasers Eng. **91**, pp. 206–215 (2017).

[31] J. Geng. *Structured-light 3D surface imaging: a tutorial.* Adv. Opt. Photonics **3** (2), pp. 128 (2011).

[32] M.C. Knauer, J. Kaminski, and G. Hausler. *Phase measuring deflectometry: a new approach to measure specular free-form surfaces.* Proc. SPIE **5457**, Opt. Metrol. Prod. Eng., pp. 366-376 (2004).

[33] K. Schlüns, and R. Klette. *Local and global integration of discrete vector fields.* Adv. Comput. Vis. Springer, pp.149-158 (1997).

[34] M. Petz, and R. Tutsch. *Measurement of optically effective surfaces by imaging of gratings.* Proc. SPIE **5144**, Opt. Meas. Sys. Ind. Insp. III, pp. 288–294 (2003).

[35] Y. Tang, X. Su, Y. Liu, and H. Jing. *3D shape measurement of the aspheric mirror by advanced phase measuring deflectometry.* Opt. Express **16** (19), pp. 15090–15096 (2008).

[36] Y. Tang, X. Su, F. Wu, and Y. Liu. *A novel phase measuring deflectometry for aspheric mirror test.* Opt. Express **17** (22), pp. 19778–19784 (2009).

[37] Y. Liu, S. Huang, Z. Zhang, N. Gao, F. Gao, and X. Jiang. *Full-field 3D shape measurement of discontinuous specular objects by direct phase measuring deflectometry.* Sci. Rep. **7** (1), pp. 10293 (2017).

[38] Z. Zhang, Y. Wang, S. Huang, Y. Liu, C. Chang, F. Gao, and X. Jiang. *Three-dimensional shape measurements of specular objects using phase-measuring deflectometry.* Sensors **17** (12), pp. 2835 (2017).

[39] C. Li, Y. Li, Y. Xiao, X. Zhang, and D. Tu. *Phase measurement deflectometry with refraction model and its calibration.* Opt. Express **26** (26), pp. 33510-33522 (2018).

[40] R. Huang. *High precision optical surface metrology using deflectometry.* PhD thesis, the University of Arizona (2015).

[41] L. Huang, J. Xue, B. Gao, C. McPherson, J. Beverage, and M. Idir. *Modal phase measuring deflectometry.* Opt. Express **24** (21), pp. 24649-24664 (2016).

[42] I. Mochi, and K.A. Goldberg. *Modal wavefront reconstruction from its gradient.* Appl. Opt. **54** (12), pp. 3780-3785 (2015).

[43] P.C.L. Stephenson. *Recurrence relations for the Cartesian derivatives of the Zernike polynomials.* J. Opt. Soc. Am. A **31** (4), pp. 708-715 (2014).

[44] F. Brunet. *Contributions to parametric image registration and 3D surface reconstruction.* PhD thesis, Université d'Auvergne (2010).

[45] V. Srinivasan, H.C. Liu, and M. Halioua. *Automated phase-measuring profilometry of 3-D diffuse objects.* Appl. Opt. **23** (18), pp. 3105-3108 (1984).

[46] S. Toyooka, and Y. Iwaasa. *Automatic profilometry of 3-D diffuse objects by spatial phase detection.* Appl. Opt. **25** (10), pp. 1630-1633 (1986).

[47] Q. Hu, P.S. Huang, Q. Fu, F. Chiang. *Calibration of a three-dimensional shape measurement system.* Opt. Eng. **42** (2), pp. 487-493 (2003).

[48] P.S. Huang, Q. Hu and F. Chiang. *Error compensation for a three-dimensional shape measurement system.* Opt. Eng. **42** (2), pp. 482-487 (2003).

[49] C. Zhang, P.S. Huang, and F. Chiang. *Microscopic phase-shifting profilometry based on digital micromirror device technology.* Appl. Opt. **41** (28), pp. 5896-5904 (2002).

[50] H. Takasaki. *Moiré topography.* Appl. Opt. **9** (6), pp. 1467–1472 (1970).

[51] D.M. Meadows, W.O. Johnson, and J.B. Allen. *Generation of Surface Contours by Moiré Patterns.* Appl. Opt. **9** (4), pp. 942-947 (1970).

[52] J.J.J. Dirckx, J.A.N. Buytaert, and S.A.M. Van der Jeught. *Implementation of phase-shifting moiré profilometry on a low-cost commercial data projector.* Opt. Lasers Eng. **48** (2), pp. 244–250 (2010).

[53] J. Kato, I. Yamaguchi, T. Nakamura, and S. Kuwashima. *Video-rate fringe analyzer based on phase-shifting electronic moiré patterns.* Appl. Opt. **36** (32), pp. 8403-8412 (1997).

[54] F. Mohammadi, K. Madanipour, and A.H. Rezaie. *Accuracy enhancement of 3D profilometric human face reconstruction using undecimated wavelet analysis*. Appl. Opt. **51** (16), pp. 3120-3131 (2012).

[55] B. Münch, P. Trtik, F. Marone, and M. Stampanoni. *Stripe and ring artifact removal with combined wavelet-Fourier filtering*. Opt. Express **17** (10), pp. 8567–8591 (2009).

[56] P. Jia, J. Kofman, and C. English. *Comparison of linear and nonlinear calibration methods for phase-measuring profilometry*. Opt. Eng. **46** (4), pp. 043601 (2007).

[57] F. Mohammadi. *3D optical metrology by digital moiré : Pixel-wise calibration refinement, grid removal, and temporal phase unwrapping*. PhD thesis, the University of Waterloo (2017).

[58] M. Takeda, and K. Mutoh. *Fourier transform profilometry for the automatic measurement of 3-D object shapes*. Appl. Opt. **22** (24), pp. 3977-3982 (1983).

[59] X. Mao, W. Chen, and X. Su. *Improved Fourier-transform profilometry*. Appl. Opt. **46** (5), pp. 664-668 (2007).

[60] J. Li, X. Su, and L. Guo. *Improved Fourier transform profilometry for the automatic measurement of three-dimensional object shapes*. Opt. Eng. **29** (12), pp. 1439–1444 (1990).

[61] J. Lin, and X. Su. *Two-dimensional Fourier transform profilometry for the automatic measurement of three-dimensional object shapes*. Opt. Eng. **34** (11), pp. 3297–3302 (1995).

[62] Q. Kemao. *Windowed Fourier transform for fringe pattern analysis*. Appl. Opt. **43** (13), pp. 2695-2702 (2004).

[63] Q. Kemao, S.H. Soon, and A. Asundi. *Instantaneous frequency and its application to strain extraction in moire interferometry*. Appl. Opt. **42** (32), pp. 6504-6513 (2003).

[64] S. Zhang. *Recent progresses on real-time 3D shape measurement using digital fringe projection techniques*. Opt. Lasers Eng. **48** (2), pp. 149–158 (2010).

[65] P. Sandoz. *Wavelet transform as a processing tool in white-light interferometry*. Opt. Lett. **22** (14), pp. 1065-1067 (1997).

[66] J. Zhong, and J. Weng. *Spatial carrier-fringe pattern analysis by means of wavelet transform: wavelet transform profilometry*. Appl. Opt. **43** (26), pp. 4993-4998 (2004).

[67] J. Zhong, and J. Weng. *Phase retrieval of optical fringe patterns from the ridge of a wavelet transform*. Opt. Lett. **30** (19), pp. 2560-2562 (2005).

[68] P.S. Huang, C. Zhang, and F. Chiang. *High-speed 3-D shape measurement based on digital fringe projection*. Opt. Eng. **42** (1), pp. 163-168 (2003).

[69] S. Zhang, and P.S. Huang. *Novel method for structured light system calibration*.

Opt. Eng. **45** (8), pp. 083601 (2006).

[70] C. Zuo, L. Huang, M. Zhang, Q. Chen, and A. Asundi. *Temporal phase unwrapping algorithms for fringe projection profilometry: A comparative review.* Opt. Laser Eng. **85**, pp. 84-103 (2016).

[71] S. Zhang, and P.S. Huang. *High-resolution, real-time three-dimensional shape measurement.* Opt. Eng. **45** (12), pp. 123601 (2006).

[72] H. Du, and Z. Wang. *Three-dimensional shape measurement with an arbitrarily arranged fringe projection profilometry system.* Opt. Lett. **32** (16), pp. 2438-2440 (2007).

[73] S. Zhang. *Comparative study on passive and active projector nonlinear gamma calibration.* Appl. Opt. **54** (13), pp. 3834-3841 (2015).

[74] K. Liu, Y. Wang, D.L. Lau, Q. Hao, and L.G. Hassebrook. *Gamma model and its analysis for phase measuring profilometry.* J. Opt. Soc. Am. A **27** (3), pp. 553-562 (2010).

[75] L. Zhang, B. Curless, and S.M. Seitz. *Spacetime stereo: shape recovery for dynamic scenes.* Proc. IEEE Comput. Soc. Conf. Comput. Vis. Pattern Recognit. **2**, pp. II-367 (2003).

[76] F. Bruno, G. Bianco, M. Muzzupappa, S. Barone, and A.V. Razionale. *Experimentation of structured light and stereo vision for underwater 3D reconstruction.* ISPRS J. Photogramm. Remote Sens. **66** (4), pp. 508–518 (2011).

[77] D. Scharstein, and R. Szeliski. *High-accuracy stereo depth maps using structured light.* Proc. IEEE Comput. Soc. Conf. Comput. Vis. Pattern Recognit. **1**, pp. I-1 (2003).

[78] J. Davis, R. Ramamoorthi, and S. Rusinkiewicz. *Spacetime stereo: A unifying framework for depth from triangulation.* IEEE Trans. Pattern Anal. Mach. Intell. **27** (2), pp. 296–302 (2003).

[79] B.D. Lucas, and T. Kanade. *An iterative image registration technique with an application to stereo vision.* Proc. 7th Int. Joint Conf. Artif. Intell. (IJCAI), pp. 674-679 (1981).

[80] U.R. Dhond, and J.K. Aggarwal. *Structure from stereo - A review.* IEEE Trans. Syst. Man Cybern. **19** (6), pp. 1489-1510 (1989).

[81] T. Kanade, and M. Okutomi. *A stereo matching algorithm with an adaptive window: theory and experiment.* IEEE Trans. Pattern Anal. Mach. Intell. **16** (9), pp. 920-932 (1994).

[82] S.M. Seitz, B. Curless, J. Diebel, D. Scharstein, and R. Szeliski. *A comparison and evaluation of multi-view stereo reconstruction algorithms.* IEEE Comput. Soc. Conf. Comput. Vis. Pattern Recognit. **1**, pp. 519–528 (2006).

[83] J. Salvi, J. Pagès, and J. Batlle. *Pattern codification strategies in structured light systems.* Pattern Recognit. **37** (4), pp. 827–849 (2004).

[84] F. Gary. *Pulse code communication*. US 2632058 (1953).

[85] B. Li, Y. Wang, J. Dai, W. Lohry, and S. Zhang. *Some recent advances on superfast 3D shape measurement with digital binary defocusing techniques*. Opt. Lasers Eng. **54**, pp. 236–246 (2014).

[86] C. Jiang, B. Li, and S. Zhang. *Pixel-by-pixel absolute phase retrieval using three phase-shifted fringe patterns without markers*. Opt. Lasers Eng. **91**, pp. 232–241 (2017).

[87] Y. Li, Y.P. Cao, Z.F. Huang, D.L. Chen, and S.P. Shi. *A three dimensional on-line measurement method based on five unequal steps phase shifting*. Opt. Commun. **285** (21–22), pp. 4285–4289 (2012).

[88] B. Pan, Q. Kemao, L. Huang, and A. Asundi. *Phase error analysis and compensation for nonsinusoidal waveforms in phase-shifting digital fringe projection profilometry*. Opt. Lett. **34** (4), pp. 416–418 (2009).

[89] B. Zhao, and Y. Surrel. *Effect of quantization error on the computed phase of phase-shifting measurements*. Appl. Opt. **36** (10), pp. 2070-2075 (1997).

[90] B. Zhao. *A statistical method for fringe intensity-correlated error in phase-shifting measurement: The effect of quantization error on the N-bucket algorithm*. Meas. Sci. Technol. **8** (2), pp. 147–153 (1997).

[91] A. Lizana, I. Moreno, A. Márquez, C. Iemmi, E. Fernández, J. Campos, and M.J. Yzuel. *Time fluctuations of the phase modulation in a liquid crystal on silicon display: characterization and effects in diffractive optics*. Opt. Express **16** (21), pp. 16711-16722 (2008).

[92] R.M. Goldstein, H.A. Zebker, and C.L. Werner. *Satellite radar interferometry: Two-dimensional phase unwrapping*. Radio Sci. **23** (4), pp. 713–720 (1988).

[93] H. Lim, W. Xu, and X. Huang. *Two new practical methods for phase unwrapping*. IEEE Trans. Geosci. Remote Sens., Quant. Remote Sens. Sci. Appl., pp. 196–198 (1995).

[94] T.J. Flynn. *Two-dimensional phase unwrapping with minimum weighted discontinuity*. J. Opt. Soc. Am. A **14** (10), pp. 2692-2701 (1997).

[95] D.C. Ghiglia, and L.A. Romero. *Minimum L^P-norm two-dimensional phase unwrapping*. J. Opt. Soc. Am. A **13** (10), pp. 1999-2013 (1996).

[96] J.M. Huntley, and H. Saldner. *Temporal phase-unwrapping algorithm for automated interferogram analysis*. Appl. Opt. **32** (17), pp. 3047-3052 (1993).

[97] H.O. Saldner, and J.M. Huntley. *Temporal phase unwrapping: application to surface profiling of discontinuous objects*. Appl. Opt. **36** (13), pp. 2770–2775 (1997).

[98] H. Zhao, W. Chen, and Y. Tan. *Phase-unwrapping algorithm for the measurement of three-dimensional object shapes*. Appl. Opt. **33** (20), pp. 4497-4500 (1994).

[99] C. Zuo, Q. Chen, G. Gu, S. Feng, F. Feng, R. Li, and G. Shen. *High-speed three-dimensional shape measurement for dynamic scenes using bi-frequency tripolar pulse-width-modulation fringe projection.* Opt. Lasers Eng. **51** (8), pp. 953–960 (2013).

[100] C. Reich, R. Ritter, and J. Thesing. *3-D shape measurement of complex objects by combining photogrammetry and fringe projection.* Opt. Eng. **39** (1), pp. 224-231 (2002).

[101] G. Sansoni, S. Corini, S. Lazzari, R. Rodella, and F. Docchio. *Three-dimensional imaging based on Gray-code light projection: characterization of the measuring algorithm and development of a measuring system for industrial applications.* Appl. Opt. **36** (19), pp. 4463–4472 (1997).

[102] G. Sansoni, M. Carocci, and R. Rodella. *Three-dimensional vision based on a combination of gray-code and phase-shift light projection: analysis and compensation of the systematic errors.* Appl. Opt. **38** (31), pp. 6565-6573 (1999).

[103] C. Zuo, L. Huang, M. Zhang, Q. Chen, and A. Asundi. *Temporal phase unwrapping algorithms for fringe projection profilometry: A comparative review.* Opt. Lasers Eng. **85**, pp. 84–103 (2016).

[104] C. Zuo, Q. Chen, G. Gu, S. Feng, and F. Feng. *High-speed three-dimensional profilometry for multiple objects with complex shapes.* Opt. Express **20** (17), pp. 19493-19510 (2012).

[105] Y. Wang, S. Zhang, and J.H. Oliver. *3D shape measurement technique for multiple rapidly moving objects.* Opt. Express **19** (9), pp. 8539-8545 (2011).

[106] J. Heikkilä, and O. Silvén. *A four-step camera calibration procedure with implicit image correction.* Proc. IEEE Comput. Soc. Conf. Comput. Vis. Pattern Recognit. **97**, pp. 1106 (1997).

[107] Z. Zhang. *Flexible camera calibration by viewing a plane from unknown orientations.* Proc. IEEE Int. Conf. Comput. Vis. **99**, pp. 666-673 (1999).

[108] J.Y. Bouguet. (2004) *Camera calibration toolbox for matlab*, retrieved from https://www.vision.caltech.edu/bouguet/calib_doc/index.html.

[109] J.G. Fryer. *Lens distortion for close range photogrametry.* Photogramm. Eng. Remote Sensing **52**(1), pp. 51-58 (1986).

[110] D.B. Gennery. *Stereo-camera calibration.* Proc. ARPA/US Workshop, pp. 101-107 (1979).

[111] H. Rapp. *Reconstruction of specular reflective surfaces using auto-calibrating deflectometry.* PhD thesis, Karlsruher Institut für Technologie (2012).

[112] R.Y. Tsai, and R.K. Lenz. *A new technique for fully autonomous and efficient 3D robotics hand/eye calibration.* IEEE Trans. Robot. Autom. **5** (3), pp. 345–358 (1989).

[113] R. Horaud, and F. Dornaika. *Hand-eye Calibration.* Int. J. Rob. Res. **14** (3),

pp. 195–210 (1995).

[114] F.C. Park, and B.J. Martin. *Robot sensor calibration: solving AX=XB on the Euclidean group*. IEEE Trans. Robot. Autom. **10** (5), pp. 717–721 (1994).

[115] K. Daniilidis. *Hand-eye calibration using dual quaternions*. Int. J. Rob. Res. **18** (3), pp. 286–298 (1999).

[116] C. Wengert. *Hand-eye calibration addon*, retrieved from https://github.com/christianwengert/calib_toolbox_addon.

[117] A.K.C. Wong, P. Niu, and X. He. *Fast acquisition of dense depth data by a new structured light scheme*. Comput. Vis. Image Underst. **98** (3), pp. 398–422 (2005).

[118] K. Takita, T. Aoki, Y. Sasaki, T. Higuchi, and K. Kobayashi. *High-accuracy subpixel image registration based on phase-only correlation*. IEICE Trans. Fundam. Electron. Commun. Comput. Sci. **E86-A** (8), pp. 1925–1934 (2003).

[119] B. Pan, H.M. Xie, B.Q. Xu, and F.L. Dai. *Performance of sub-pixel registration algorithms in digital image correlation*. Meas. Sci. Technol. **17** (6), pp. 1615–1621 (2006).

[120] M. Giassa. *IV-Generalized bicubic interpolation*, retrieved from gissa.net/?page_id=371.

[121] W.H. Press, S.A. Teukolsky, W.T. Vetterling, and B.P. Flannery. *Numerical recipes in C the art of scientific computing. 2nd Ed.* Cambridge University Press (1992).

[122] L. Huang, M. Idir, C. Zuo, K. Kaznatcheev, L. Zhou, and A. Asundi. *Comparison of two-dimensional integration methods for shape reconstruction from gradient data*. Opt. Lasers Eng. **64**, pp. 1–11 (2015).

[123] W.H. Southwell. *Wave-front estimation from wave-front slope measurements*. J. Opt. Soc. Am. **70** (8), pp. 998-1006 (1980).

[124] L. Huang, and A. Asundi. *Improvement of least-squares integration method with iterative compensations in fringe reflectometry*. Appl. Opt. **51** (31), pp. 7459-7465 (2012).

[125] G. Li, Y. Li, K. Liu, X. Ma, and H. Wang. *Improving wavefront reconstruction accuracy by using integration equations with higher-order truncation errors in the Southwell geometry*. J. Opt. Soc. Am. A **30** (7), pp. 1448-1459 (2013).

[126] S. Ettl, J. Kaminski, M.C. Knauer, and G. Häusler. *Shape reconstruction from gradient data*. Appl. Opt. **47**(12), pp. 2091-2097 (2007).

[127] R.H. Hudgin. *Wave-front reconstruction for compensated imaging*. J. Opt. Soc. Am. **67** (3), pp. 375-378 (1977).

[128] C. Kottler, C. David, F. Pfeiffer, and O. Bunk. *A two-directional approach for grating based differential phase contrast imaging using hard x-rays*. Opt. Express **15** (3), pp. 1175-1181 (2007).

[129] F. Roddier, and C. Roddier. *Wavefront reconstruction using iterative Fourier transforms*. Appl. Opt. **30** (11), pp. 1325-1327 (1991).

[130] K. Liu, Y. Wang, D.L. Lau, Q. Hao, and L.G. Hassebrook. *Dual-frequency pattern scheme for high-speed 3-D shape measurement*. Opt. Express **18** (5), pp. 5229-5244 (2010).

[131] H. Zhang, A. Lizana, C. Iemmi, F.A. Monroy-Ramirez, A. Marquez, I. Moreno, and J. Campos. *LCoS display phase self-calibration method based on diffractive lens schemes*. Opt. Lasers Eng. **106**, pp. 147–154 (2018).

[132] L. Zhu, Y. Cao, D. He, and C. Chen. *Grayscale imbalance correction in real-time phase measuring profilometry*. Opt. Commun. **376**, pp. 72–80 (2016).

[133] B. Li, and S. Zhang. *Superfast high-resolution absolute 3D recovery of a stabilized flapping flight process*. Opt. Express **25** (22), pp. 27270-27282 (2017).

[134] V. Suresh, Y. Wang, and B. Li. *High-dynamic-range 3D shape measurement utilizing the transitioning state of digital micromirror device*. Opt. Lasers Eng. **107**, pp. 176–181 (2018).